

Université Paris Cité

ECOLE DOCTORALE D'ASTRONOMIE ET D'ASTROPHYSIQUE D'ILE-DE-FRANCE (ED127)

Département d'Astrophysique du CEA Saclay

Laboratoire Cosmologie et Evolution des Galaxies (LCEG)

Unveiling the hidden side of the first 3 billion years of galaxy formation.

Presenté par **LUCAS LEROY**

Thèse de doctorat en **ASTRONOMIE ET ASTROPHYSIQUE**

Dirigée par **David ELBAZ**

Présentée et soutenue publiquement le 23 Octobre 2023

JOHAN RICHARD	PROFESSEUR	UNIVERSITÉ DE LYON	Président du jury
LAURENCE TRESSE	PROFESSEUR	AIX-MARSEILLE UNIVERSITÉ	Rapportrice
AMÉLIE SAINTONGE	PROFESSEUR	UNIVERSITY COLLEGE LONDON	Rapportrice
LAURE CIESLA	CHARGÉ DE RECHERCHE	AIX-MARSEILLE UNIVERSITÉ	Examinateuse
SIMONA MEI	PROFESSEUR	UNIVERSITÉ PARIS CITÉ	Examinateuse (Absent)
DAVID ELBAZ	DIRECTEUR DE RECHERCHE	UMR AIM - CEA PARIS SACLAY	DIRECTEUR DE THÈSE
BENJAMIN MAGNELLI	CHARGÉ DE RECHERCHE	UMR AIM - CEA PARIS SACLAY	INVITÉ

RÉSUMÉ EN FRANÇAIS

Des questions clés de l’astrophysique sont de savoir comment les galaxies se développent au fil du temps et quels sont les moteurs de leur évolution. À l’heure actuelle, de nombreuses questions restent sans réponse : Quelle quantité d’étoiles se forment au tout début de l’Univers, c’est à dire à un décalage vers le rouge élevé (c.-à-d. $z \geq 4$) ? Quel type de galaxie contribue le plus à la densité de formation d’étoiles dans le cosmos ? Sont-elles principalement massives, brillantes dans l’infrarouge (IR), ou rien de tout cela ? Qu’est-ce qui est responsable du midi cosmique (c.-à-d. lorsque le nombre d’étoiles formées par unité de volume mobile atteint son maximum à $z \sim 2$) ? Les galaxies sont-elles toujours aussi efficaces à transformer le gaz en étoiles ? Comment les propriétés des galaxies sont-elles liées les unes aux autres ? Comment les galaxies massives se sont-elles formées si tôt dans l’Univers ?

Depuis une dizaine d’années, la communauté scientifique est parvenue à réaliser des relevés profonds de galaxies sur des champs couverts de l’ultraviolet au millimétrique. La collaboration Cosmic Assembly Near-infrared Deep Extragalactic Legacy Survey (CANDELS) visait à l’origine, en 2009, à réaliser les observations les plus profondes en utilisant les nouvelles caméras du *Hubble Space Telescope (HST)*: WFC3 (Wide Field Camera 3) dans le proche infrarouge et ACS (Advanced Camera for Surveys) dans le visible. Les champs CANDELS restent à ce jour les grands champs les plus profonds étudiés. Ils ont été observés par de nombreux télescopes, notamment par *Herschel* dans l’infrarouge lointain (FIR). Ces champs sont aujourd’hui couverts dans une large gamme de longueurs d’onde allant de l’ultraviolet (UV) au millimétrique. Les spécificités de ces champs les rendent exceptionnellement bien adaptés à une étude visant à sonder les propriétés globales de l’évolution des galaxies jusqu’à des décalages vers le rouge élevés. De plus, via Atacama Large Millimeter/submillimeter Array (ALMA), le programme GOODS-ALMA a récemment permis à la communauté de bénéficier de l’observation d’un champ profond CANDELS dans le millimétrique. L’ensemble permet de pousser notre compréhension de l’évolution des galaxies à des décalages vers le rouge plus élevés et de sonder des galaxies de masse stellaire (M_\star) encore plus faible.

Cette thèse est basée sur l’étude des galaxies dans ces champs. Je combine pour la première fois les relevés *Herschel* (GOODS-South, GOODS-North, COSMOS et USD) et ALMA (GOODS-South) les plus profonds. L’objectif de l’étude que j’ai menée pendant mon doctorat est d’obtenir une vue globale de l’histoire cosmique de la formation d’étoiles. En particulier je contrains le taux de formation d’étoiles (SFR), la masse de poussière (M_{dust}), la température de poussière (T_{dust}) et la masse de gaz (M_{gas}) en fonction de leur M_\star à l’aide d’une analyse cohérente. Ce travail est rendu possible par l’accès aux dernières versions des catalogues de galaxies dans les champs CANDELS, ainsi que par le programme GOODS-ALMA, qui étend l’étude des galaxies au domaine millimétrique.

Une partie importante de mon doctorat a consisté à utiliser une méthode d’empilement d’images dans le FIR. La méthode d’empilement d’images consiste à empiler les images photométriques, d’une seule bande, de plusieurs galaxies afin d’augmenter le rapport signal sur bruit (S/N) sur cette population. L’objectif est de déduire la densité de flux caractéristique d’une population de galaxies qui n’ont pas pu être détectées individuellement. A cette fin, j’ai étudié en profondeur la méthode d’empilement et ses biais. En particulier, je m’intéresse au biais de clustering qui apparaît dans les bandes *Herschel* lorsque l’on empile des galaxies ensemble. Je compare deux méthodes qui visent à l’annuler. Je compare également différentes méthodes de fit de la distribution d’énergie spectrale et j’étudie leurs biais potentiels.

En effectuant cette analyse d’empilement d’image sur plus de 105 000 galaxies sélectionnées dans la bande H du *HST*, je retrouve l’évolution, de $z = 5$ à $z = 0$, des propriétés clés des galaxies

à formation d'étoiles (SFG) telles que leur SFR, T_{dust} et M_{gas} . Tout au long de l'étude, je m'intéresse également aux galaxies H -dropout qui ne sont pas prises en compte dans l'échantillon initial. Je déduis la contribution relative des galaxies à l'histoire cosmique de la formation d'étoiles en fonction de M_{\star} et la compare avec la simulation TNG100. J'étudie l'évolution des galaxies dans le plan $\Sigma_{\text{SFR}} - \Sigma_{\text{gaz}}$ en fonction du décalage vers le rouge et de M_{\star} .

Avec cette étude, je montre qu'ALMA est un complément utile à une étude basée uniquement sur *Herschel* en permettant d'atteindre des M_{\star} plus faibles et des décalages vers le rouge plus élevés. Je confirme que la séquence principale de formation d'étoiles suit une évolution linéaire avec une pente proche de l'unité, et qu'une courbure apparaît aux masses élevées à $z < 2$. Je confirme que la moyenne T_{dust} des galaxies de la séquence principale évolue linéairement avec le décalage vers le rouge, sans corrélation apparente avec M_{\star} .

De plus, j'ai mis en évidence que, jusqu'à $z = 5$, les galaxies les plus massives (c.-à-d. $M_{\star} \geq 10^{10} M_{\odot}$) contribuent pour la majeure partie de la densité de SFR (ρ_{SFR}) totale, tandis que la somme des étoiles formées par les galaxies les moins massives (c.-à-d. $M_{\star} \leq 10^{10} M_{\odot}$) est plutôt constante. La simulation cosmologique TNG100 ne reproduit pas la contribution relative des galaxies au ρ_{SFR} en fonction de M_{\star} . Je donne, pour la première fois, une estimation de la contribution des galaxies H -dropout à la ρ_{SFR} des galaxies de masse stellaire similaire : à $z \sim 5$, les galaxies H -dropout représentent $\sim 23\%$ des étoiles formées dans les galaxies massives (c'est-à-dire, $M_{\star} \geq 10^{10.3} M_{\odot}$). Enfin, je présente des preuves que les galaxies à fort décalage vers le rouge, comparées aux galaxies à faible décalage vers le rouge, sont intrinsèquement plus efficaces à former des étoiles, par rapport à ce qui est attendu de la relation locale de Kennicutt-Schmidt.

Mots-clés: galaxies, formation-d'étoile, température-de-poussière, masse-de-gaz, empilement, *Herschel*, ALMA, densité-de-formation-d'étoiles.

ABSTRACT

Key questions in astrophysics are how galaxies develop over time and what drives their evolution. At present, many questions remain unanswered: How many stars form at the very beginning of the Universe, i.e. at a high redshift (i.e. $z \geq 4$)? What type of galaxy contributes most to the density of star formation in the cosmos? Are they predominantly massive, bright in the infrared (IR), or none of these? What is responsible for the cosmic noon (i.e. when the number of stars formed per unit of comoving volume peaks at $z \sim 2$)? Are galaxies always as efficient at transforming gas into stars? How are the properties of galaxies related to each other? How did massive galaxies form so early in the universe?

Over the last decade or so, the scientific community has succeeded in carrying out deep surveys of galaxies in fields ranging from the ultraviolet to the millimetre. In 2009, the Cosmic Assembly Near-infrared Deep Extragalactic Legacy Survey (CANDELS) collaboration originally set out to make the deepest observations using the *Hubble Space Telescope* (*HST*) new cameras: WFC3 (Wide Field Camera 3) in the near infrared and ACS (Advanced Camera for Surveys) in the visible. The CANDELS fields remain the deepest large fields studied to date. They have been observed by numerous telescopes, notably by *Herschel* in the far infrared (FIR). These fields are now covered in a wide range of wavelengths from the ultraviolet (UV) to the millimetre. The specific features of these fields make them exceptionally well suited to a study aimed at probing the global properties of galaxy evolution down to high redshifts. In addition, via the Atacama Large Millimeter/submillimeter Array (ALMA), the GOODS-ALMA programme has recently enabled the community to benefit from the observation of a CANDELS deep field in the millimetre range. All of this will enable us to improve our understanding of galaxy evolution at higher redshifts and to probe galaxies with even lower stellar mass.

This thesis is based on the study of galaxies in these fields. I am combining, for the first time, the deepest surveys *Herschel* (GOODS-South, GOODS-North, COSMOS and USD) and ALMA (GOODS-South). The aim of the study I carried out during my PhD was to obtain a global view of the cosmic history of star formation. In particular, I constrained the star formation rate (SFR), dust mass (M_{dust}), dust temperature (T_{dust}) and gas mass (M_{gas}) as a function of their M_{\star} using coherent analysis. This work is made possible by access to the latest versions of galaxy catalogues in the CANDELS fields, as well as by the GOODS-ALMA programme, which extends the study of galaxies to the millimetre range.

An important part of my PhD involved using an image stacking method in the FIR. The image stacking method consists of stacking the photometric images, from a single band, of several galaxies in order to increase the signal to noise ratio (S/N) on this population. The aim is to deduce the characteristic flux density of a population of galaxies that could not be detected individually. To this end, I have studied the stacking method and its biases in depth. In particular, I am interested in the clustering bias that appears in the *Herschel* bands when galaxies are stacked together. I compare two methods that aim to cancel this bias. I also compare different methods of fitting the spectral energy distribution and study their potential biases.

By performing this stacking analysis on more than 105,000 galaxies selected from *HST H*-band, I recover the evolution, from $z = 5$ to $z = 0$, of key properties of star-forming galaxies (SFG) such as their SFR, T_{dust} and M_{gas} . Throughout the study, I am also interested in *H*-dropout galaxies that are not taken into account in the initial sample. I deduce the relative contribution of galaxies to the cosmic history of star formation as a function of M_{\star} and compare it with the TNG100 simulation. I study the evolution of galaxies in the $\Sigma_{\text{SFR}} - \Sigma_{\text{gas}}$ plane as a function of redshift and M_{\star} .

With this study, I show that ALMA is a useful complement to a study based solely on *Herschel* by making it possible to reach lower M_\star and higher redshifts. I confirm that the main sequence of star formation follows a linear evolution with a slope close to unity, and that a curvature appears at high masses at $z < 2$. I confirm that the mean T_{dust} of the main sequence galaxies evolves linearly with redshift, with no apparent correlation with M_\star .

Furthermore, I have shown that, up to $z = 5$, the most massive galaxies (i.e. $M_\star \geq 10^{10} M_\odot$) contribute most to the total SFR density (ρ_{SFR}), while the sum of stars formed by the least massive galaxies (i.e. $M_\star \leq 10^{10} M_\odot$) is rather constant. The TNG100 cosmological simulation does not reproduce the relative contribution of galaxies to the ρ_{SFR} as a function of M_\star . I give, for the first time, an estimate of the contribution of H -dropout galaxies to the ρ_{SFR} of galaxies of similar stellar mass: at $z \sim 5$, H -dropout galaxies account for $\sim 23\%$ of the stars formed in massive galaxies (i.e., $M_\star \geq 10^{10.3} M_\odot$). Finally, I present evidence that high-redshift galaxies, compared to low-redshift galaxies, are intrinsically more efficient for star formation, compared to what is expected from the local Kennicutt-Schmidt relation.

Key words: galaxies, star-formation, dust-temperature, gas-mass, stacking, Herschel, ALMA, star-formation-rate-density.

RÉSUMÉ SUBSTANTIEL EN FRANÇAIS

Des questions clés de l’astrophysique sont de savoir comment les galaxies se développent au fil du temps et quels sont les moteurs de leur évolution. À l’heure actuelle, de nombreuses questions restent sans réponse : Quelle quantité d’étoiles se forment au tout début de l’Univers, c’est à dire à un décalage vers le rouge élevé (c.-à-d. $z \geq 4$) ? Quel type de galaxie contribue le plus à la densité de formation d’étoiles dans le cosmos ? Sont-elles principalement massives, brillantes dans l’infrarouge (IR), ou rien de tout cela ? Qu’est-ce qui est responsable du midi cosmique (c.-à-d. lorsque le nombre d’étoiles formées par unité de volume mobile atteint son maximum à $z \sim 2$) ? Les galaxies sont-elles toujours aussi efficaces à transformer le gaz en étoiles ? Comment les propriétés des galaxies sont-elles liées les unes aux autres ? Comment les galaxies massives se sont-elles formées si tôt dans l’Univers ?

Depuis une dizaine d’années, la communauté scientifique est parvenue à réaliser des relevés profonds de galaxies sur des champs couverts de l’ultraviolet au millimétrique. La collaboration Cosmic Assembly Near-infrared Deep Extragalactic Legacy Survey (CANDELS) visait à l’origine, en 2009, à réaliser les observations les plus profondes en utilisant les nouvelles caméras du *Hubble Space Telescope (HST)*: WFC3 (Wide Field Camera 3) dans le proche infrarouge et ACS (Advanced Camera for Surveys) dans le visible. Les champs CANDELS restent à ce jour les grands champs les plus profonds étudiés. Ils ont été observés par de nombreux télescopes, notamment par *Herschel* dans l’infrarouge lointain (FIR). Ces champs sont aujourd’hui couverts dans une large gamme de longueurs d’onde allant de l’ultraviolet (UV) au millimétrique. Les spécificités de ces champs les rendent exceptionnellement bien adaptés à une étude visant à sonder les propriétés globales de l’évolution des galaxies jusqu’à des décalages vers le rouge élevés. De plus, via Atacama Large Millimeter/submillimeter Array (ALMA), le programme GOODS-ALMA a récemment permis à la communauté de bénéficier de l’observation d’un champ profond CANDELS dans le millimétrique. L’ensemble permet de pousser notre compréhension de l’évolution des galaxies à des décalages vers le rouge plus élevés et de sonder des galaxies de masse stellaire (M_\star) encore plus faible.

Cette thèse est basée sur l’étude des galaxies dans ces champs. Je combine pour la première fois les relevés *Herschel* (GOODS-South, GOODS-North, COSMOS et USD) et ALMA (GOODS-South) les plus profonds. L’objectif de l’étude que j’ai menée pendant mon doctorat est d’obtenir une vue globale de l’histoire cosmique de la formation d’étoiles. En particulier je contrains le taux de formation d’étoiles (SFR), la masse de poussière (M_{dust}), la température de poussière (T_{dust}) et la masse de gaz (M_{gas}) en fonction de leur M_\star à l’aide d’une analyse cohérente basé sur de l’empilement d’images. Ce travail est rendu possible par l’accès aux dernières versions des catalogues de galaxies dans les champs CANDELS possédant les dernières versions des décalages vers le rouge et masses stellaires; ainsi que par le programme GOODS-ALMA, qui étend l’étude des galaxies au domaine millimétrique.

Une partie importante de mon doctorat a consisté à utiliser une méthode d’empilement d’images dans le FIR. La méthode d’empilement d’images consiste à empiler les images photométriques, d’une seule bande, de plusieurs galaxies afin d’augmenter le rapport signal sur bruit (S/N) sur cette population. L’objectif est de déduire la densité de flux caractéristique d’une population de galaxies qui n’ont pas pu être détectées individuellement. A cette fin, j’ai étudié en profondeur la méthode d’empilement et ses biais. En particulier, je m’intéresse de manière approfondie au biais de clustering qui apparaît dans les bandes *Herschel* lorsque l’on empile des galaxies ensemble.

Je compare deux méthodes qui visent à annuler le biais de clustering en empilant les images dans les bandes *Herschel* : la méthode de [Schreiber et al. \(2015\)](#) et celle de [Béthermin et al. \(2015\)](#). Je

compare l'efficacité des deux méthodes à supprimer le biais de clustering. En conclusion, bien que la méthode de [Béthermin et al. \(2015\)](#) puisse, en théorie, offrir une meilleure caractérisation du biais de clustering en identifiant précisément le terme et en le distinguant du signal de fond et du signal venant de la galaxie, il possède en pratique et dans le cas de mon échantillon de travail, une certaine incertitude à distinguer précisément les termes de biais de clustering et celui de signal de fond, et cela au détriment de mesurer robustement le signal de la galaxie. Par ailleurs, la méthode de [Schreiber et al. \(2015\)](#), bien que ne pouvant pas clairement identifier la contribution du biais de clustering qui est en partie enfouie dans le terme de signal de fond, parvient à déduire en moyenne le signal de la galaxie de façon robuste.

Je compare également différentes méthodes de fit de la distribution d'énergie spectrale (SED): la bibliothèque des modèles de [Schreiber et al. \(2018\)](#) et le modèle de distribution d'énergie spectrale de [Draine & Li \(2007\)](#). La première a l'avantage de définir des modèles de SED de galaxies de la séquence principale avec seulement cinq paramètres: $T_{\text{dust}}, M_{\text{dust}}$, le décalage vers le rouge, la fraction d'hydrocarbure polycyclique aromatique (f_{PAH}) et l'IR8; ce qui la rend extrêmement bien adaptée à mon étude. Par ailleurs, cette bibliothèque se base sur un modèle de grain de poussière différent de celui majoritairement utilisé dans la littérature (celui du modèle de [Draine & Li 2007](#)). L'impact principal est que la masse de poussière (M_{dust}) des modèles de SED de la bibliothèque de [Schreiber et al. \(2018\)](#) sont plus faibles d'un facteur deux (en moyenne) en comparaison avec le modèle de [Draine & Li \(2007\)](#). Ceci n'a, par ailleurs, pas d'impact sur les masses de gaz car le facteur s'annule lors de la conversion de M_{dust} à M_{gas} . J'ai testé que cette différence et que l'utilisation de l'un ou l'autre des deux modèles n'avait pas d'impact majeur sur les propriétés des galaxies déduites et mes conclusions. Par soucis de consistance avec la littérature, j'ai choisi de travailler avec la bibliothèque des modèles de [Schreiber et al. \(2018\)](#) mais en utilisant les masses de poussières de [Draine & Li \(2007\)](#). Pour cela j'ai établi une table de conversion entre les deux type de M_{dust} . En pratique, l'établissement ce cette table de conversion consistait à associer les modèles de [Schreiber et al. \(2018\)](#) à un modèle de [Draine & Li \(2007\)](#).

J'ai aussi réalisé plusieurs tests afin de vérifier que ma méthode ne biaisait pas les propriétés moyennes des galaxies déduites. En particulier, j'ai effectué une simulation visant à identifier des potentiels biais de moyenne en simulant ma méthode d'empilement d'images et de déduction du SED sur des galaxies simulées. La comparaison des "vraies" moyennes et moyennes "observées" des propriétés n'ont révélé aucun biais dû à ma méthode. J'ai aussi vérifié que les noyaux actifs de galaxies (AGN) n'avaient pas d'impact majeur dans le signal des galaxies résultant des empilements d'images.

En effectuant cette analyse d'empilement d'images sur plus de 105 000 galaxies sélectionnées dans la bande H du HST , je retrouve l'évolution, de $z = 5$ à $z = 0$, des propriétés clés des galaxies à formation d'étoiles (SFG) telles que leur SFR, T_{dust} et M_{gas} . Tout au long de l'étude, je m'intéresse également aux galaxies H -dropout qui ne sont pas prises en compte dans l'échantillon initial. En particulier, je fais attention à inclure leur contribution dans les propriétés déduites de l'analyse d'empilement effectuées sur les galaxies détectées en bande-H. Ceci permet d'avoir une vision complète de ces propriétés.

Je montre également qu'ALMA est un complément important à une étude basée uniquement sur *Herschel* en permettant d'atteindre des masses stellaires plus faibles et des décalages vers le rouge plus élevés. ALMA est aussi crucial pour mieux contraindre le pic de SED d'une galaxie et permet aussi d'avoir accès à une méthode supplémentaire pour déduire la masse de gaz associée à une galaxie. De manière générale, je mets en avant qu'ALMA est la pierre angulaire de l'étude menée lors de cette

thèse qui permet de faire gagner les conclusions et résultats en pertinence et robustesse.

Ce travail de thèse permet l'étude de nombreuses propriétés. En particulier, en s'intéressant à la température de poussièrée, je confirme que la moyenne des T_{dust} des galaxies de la séquence principale évolue linéairement avec le décalage vers le rouge, dont je donne une estimation. J'observe aussi que la température de poussière n'a pas de corrélation apparente avec la masse stellaire. La longueur d'onde correspondant au pic de SED, avait été observée comme diminuant avec la luminosité infrarouge (L_{IR}) par [Drew & Casey \(2022\)](#). Lors de mon étude je ne retrouve pas cette propriété. Je ne vois pas d'évolution claire de λ_{peak} avec L_{IR} . Je conclus que l'évolution observée par [Drew & Casey \(2022\)](#) est en réalité une évolution en redshift interprétée par erreur en une évolution en L_{IR} en raison de l'échantillon et méthode de visualisation choisie par [Drew & Casey \(2022\)](#).

Lors de l'étude du SFR, je confirme que la séquence principale de formation d'étoiles suit une évolution linéaire avec une pente proche de l'unité, et qu'une courbure apparaît aux masses élevées à $z < 2$. Mon travail permet d'étendre le domaine de connaissance de la séquence principale de la formation d'étoiles jusqu'à un décalage vers le rouge de $z = 5$ et aussi d'atteindre des masses stellaires plus faible aux $z \leq 5$. Je montre aussi que la courbure à hautes masses stellaires et faible décalage vers le rouge est plus importante que ce qui est prévu par [Schreiber et al. \(2015\)](#) et se rapproche plus de [Leslie et al. \(2020\)](#).

En étudiant l'évolution de la densité de formation d'étoiles au cours du temps, j'ai montré qu'une étude statistique consistante retrouvait une estimation du ρ_{SFR} proche de celle donnée par [Madau & Dickinson \(2014\)](#), et donc en contradiction avec des estimations récentes montrant des ρ_{SFR} bien plus important à hauts décalages vers le rouge. J'ai aussi mis en évidence que, jusqu'à $z = 5$, les galaxies les plus massives (c.-à-d. $M_{\star} \geq 10^{10} M_{\odot}$) contribuent pour la majeure partie du ρ_{SFR} totale, tandis que la somme des étoiles formées par les galaxies les moins massives (c.-à-d. $M_{\star} \leq 10^{10} M_{\odot}$) est plutôt constante. Je présente une vision globale du ρ_{SFR} en donnant la contribution de différentes galaxies suivant, notamment, leur masse stellaire et L_{IR} .

Ayant déduit la contribution relative des galaxies à l'histoire cosmique de la formation d'étoiles en fonction de la masse stellaire, je la compare avec la simulation cosmologique TNG100 ([Nelson et al. 2019, 2018; Springel et al. 2018; Marinacci et al. 2018; Naiman et al. 2018; Pillepich et al. 2018b,a; Weinberger et al. 2017](#)). J'observe que la simulation TNG100 arrive, globalement, bien à reproduire la valeur absolue des galaxies de faible masse stellaire (c.-à-d. $M_{\star} \leq 10^{10} M_{\odot}$) au ρ_{SFR} total. Par ailleurs, la simulation TNG100 échoue à reproduire la valeur absolue des galaxies de haute masse stellaire (c.-à-d. $M_{\star} \geq 10^{10} M_{\odot}$) qui est largement sous estimée à tous les décalages vers le rouge. Cela se traduit par une sous-estimation systématique du ρ_{SFR} total à tous les décalages vers le rouge. En étudiant l'évolution de la séquence principale de la formation d'étoiles et des fractions de gaz issues de la simulation TNG100 et en les comparant à mon étude, j'identifie que le problème vient de la méthode utilisée pour réguler la formation d'étoiles dans les galaxies massives de la simulation TNG100: par retro-action d'AGN.

Au cours de ce manuscrit je m'attarde aussi sur l'étude de l'évolution des masses de gaz en fonction du décalage vers le rouge et de la masse stellaire des galaxies. Je retrouve une évolution similaire à celle déjà présenté dans la littérature: une augmentation de la masse de gaz avec la masse stellaire, et une augmentation de la masse de gaz avec le décalage vers le rouge jusqu'à $z \sim 2$. Néanmoins, pour $z \geq 2$, je n'observe pas d'évolution des masses de gaz (à masse stellaire fixée), et celles ci sont plus faibles que ce qui est rapporté dans la littérature pour des décalages vers le rouge $z \geq 2$ (e.g., [Tacconi et al. 2018; Wang et al. 2022](#)).

Suite à l'étude des masses de gaz, je m'intéresse à l'évolution de la densité de gaz (ρ_{gas}) au cours du temps. J'y retrouve des propriétés reflétant celles déjà observées lors de l'étude de l'évolution du ρ_{SFR} au cours du temps: les galaxies les plus massives (c.-à-d. $M_{\star} \geq 10^{10} M_{\odot}$) contribuent pour la majeure partie de ρ_{gas} totale, tandis que la somme des quantités de gaz dans les galaxies les moins massives (c.-à-d. $M_{\star} \leq 10^{10} M_{\odot}$) est plutôt constante. J'observe, par ailleurs, que ρ_{gas} chute plus rapidement que ce qui pourrait être déduit du ρ_{SFR} et d'une efficacité de formation d'étoiles ($SFE \equiv SFR/M_{\text{gas}}$) universelle. Ceci laisse supposer que la SFE n'est pas universelle et qu'elle évoluerait avec le décalage vers le rouge.

Pour creuser cette hypothèse, j'étudie l'évolution des galaxies dans le plan $\Sigma_{\text{SFR}} - \Sigma_{\text{gas}}$ ($\Sigma_{\text{SFR}} = SFR/(2\pi R_e^2)$ and $\Sigma_{\text{gas}} = M_{\text{gas}}/(2\pi R_e^2)$, où R_e est le rayon effectif) en fonction du décalage vers le rouge et de la masse stellaire. J'observe une corrélation globale linéaire avec une pente de $N = 1.21$ qui est consistante avec la littérature. Pour aller plus loin, j'étudie l'évolution de la corrélation en fonction du décalage vers le rouge. J'observe l'apparition de deux régimes. A $z \leq 2$, la normalisation de la corrélation n'évolue pas et j'en déduis que les variations observées dans le SFR résultent entièrement des variations des M_{gas} . A l'opposé, à $z > 2$, la normalisation de la corrélation dans le plan $\Sigma_{\text{SFR}} - \Sigma_{\text{gas}}$ augmente significativement. Dans ce cas, et en tenant compte des évolutions respectives de SFR et M_{gas} à $z > 2$, j'en déduis que pour les décalages vers le rouge de $z > 2$, la M_{gas} n'est plus la seule responsable d'une variation en SFR mais que la SFE impacte maintenant de façon non négligeable ces variations. Une conséquence directe suggérée par cette observation est que les galaxies à haut décalage vers le rouge étaient intrinsèquement plus efficaces à former des étoiles que les galaxies de plus faibles décalages vers le rouge.

En conclusion les principaux résultats de ce travail de doctorat peuvent être résumés ainsi: j'ai mis en évidence que, jusqu'à $z = 5$, les galaxies les plus massives (c.-à-d. $M_{\star} \geq 10^{10} M_{\odot}$) contribuent pour la majeure partie de la densité de SFR (ρ_{SFR}) totale, tandis que la somme des étoiles formées par les galaxies les moins massives (c.-à-d. $M_{\star} \leq 10^{10} M_{\odot}$) est plutôt constante. La simulation cosmologique TNG100 ne reproduit pas la contribution relative des galaxies au ρ_{SFR} en fonction de M_{\star} . Je donne, pour la première fois, une estimation de la contribution des galaxies H -dropout à la ρ_{SFR} des galaxies de masse stellaire similaire : à $z \sim 5$, les galaxies H -dropout représentent $\sim 23\%$ des étoiles formées dans les galaxies massives (c'est-à-dire, $M_{\star} \geq 10^{10.3} M_{\odot}$). Enfin, je présente des preuves que les galaxies à fort décalage vers le rouge, comparées aux galaxies à faible décalage vers le rouge, sont intrinsèquement plus efficaces à former des étoiles, par rapport à ce qui est attendu de la relation locale de Kennicutt-Schmidt.

Pour conclure ce manuscrit de thèse, je présente quelques perspectives d'études et questions toujours en suspens induites par mon travail. Je centre cette section sur les nouvelles opportunités ouvertes par le lancement du James Webb Space Telescope (*JWST*) il y a maintenant plus d'un an. *JWST* permettra, notamment de détecter de nouvelles galaxies à tous les décalages vers le rouge, d'atteindre des M_{\star} plus faibles; de dévoiler la morphologie des galaxies grâce à sa grande sensibilité à la faible luminosité de surface; de détecter davantage de raies d'émissions, ce qui permettra de mieux diagnostiquer la métallicité, l'âge de la population stellaire et les AGN. Une importante perspective de *JWST* en relation directe avec ce travail est une meilleure caractérisation de la population des galaxies *HST*-dark (e.g., [Barrufet et al. \(2023\)](#)). *JWST* étant le successeur du télescope spatial *Spitzer* avec lequel les galaxies *HST*-dark ont été découvertes et caractérisées, *JWST* est le mieux placé pour raffiner et étendre nos connaissances sur cette population de galaxies. Dans cette partie je présente aussi brièvement un travail que j'ai commencé à réaliser lors de ma thèse visant à empiler des images de galaxies dans les bandes de *JWST* pour essayer de contraindre la dispersion de la séquence principale

de la formation d'étoiles à bas décalages vers le rouge (c.-à-d. $z \leq 0.5$) et basses masses stellaires (c.-à-d. $M_\star \leq 10^8 M_\odot$). Je mentionne aussi une perspective d'étude de la contribution des galaxies appartenant à un amas de galaxies au ρ_{SFR} totale. Cette perspective est motivée par des simulations menées par [Chiang et al. \(2017\)](#) qui prédit une contribution importante de ce type de galaxies au ρ_{SFR} total. L'impact de l'environnement est une question induite par le travail de ce doctorat car il s'agit du point de vue manquant à cette étude. Cela pourrait notamment donner une explication au surplus d'efficacité à la formation d'étoile que j'observe à hauts décalages vers le rouge. C'est cependant une question qui ne pourra probablement pas être répondues par le *JWST* seul. En effet, cela nécessitera d'autres télescopes dont le télescope EUCLID pour l'étude de ces amas et proto-amas de galaxies.

CONTENTS

Résumé en Français	i
Abstract	iii
Résumé substantiel en Français	v
Table des matières	xiii
Liste des figures	xvi
Liste des tableaux	xvii
Acronyms and abbreviations	xx
1 Introduction	1
1.1 Global context and historic	2
1.2 The galaxy bimodality	2
1.3 The SFG population	5
1.3.1 Typical SED of SFGs	5
1.3.2 Stellar mass and mass function	6
1.3.3 The star formation in SFGs	6
1.3.4 The link between the SFR and the gas content of SFGs	9
1.4 The cosmic star formation history	10
1.5 The current understanding on how galaxies form through cosmic time	12
1.6 Problematic	14
2 Data set	17
2.1 Catalogues	18
2.1.1 Stellar masses	18
2.1.2 Completeness of the catalogues	19
2.1.3 The specificity of GOODS North catalogue	20
2.2 Observation maps	21
3 Galaxy stacking	25
3.1 The stacking method in theory	26
3.2 Mean or median stacking?	26
3.3 The mean stacking method in practice	27
3.3.1 How to group galaxies into bins?	27
3.3.2 How to deal with detected/undetected sources?	30
3.3.3 How to deal with a possible gradient in maps?	30
3.4 How to measure flux densities?	31
3.4.1 <i>Herschel</i> : Clustering bias and PSF fitting method	31
3.4.2 How to deal with clustering bias in <i>Herschel</i> bands	32
3.4.3 <i>Spitzer</i> and ALMA: the aperture photometry method	37
3.4.4 How to measure the signal-to-noise ratio?	39
3.5 The mean stacking developed programs	39

4 From flux density measurements to galaxy properties	41
4.1 The SED fitting procedure	42
4.2 The M_{dust} debate	45
4.3 Adding ALMA to <i>Herschel</i>	48
4.4 Looking for biases in the SED fitting procedure	50
4.4.1 Simulations to correct for averaging biases	50
4.4.2 Active galactic nuclei bias	51
5 Redshift evolution the dust-obscured star-forming properties of galaxies	55
5.1 Deducing the T_{dust} of SFGs	57
5.1.1 Influence of the CMB on T_{dust}	57
5.1.2 The T_{dust} of main sequence SFGs	57
5.1.3 The evolution of λ_{peak} as a function of L_{IR}	59
5.1.4 Influence of <i>H</i> -dropout galaxies on T_{dust}	61
5.2 Deducing the dust attenuation of SFGs	62
5.2.1 Deducing SFR for SFGs	63
5.2.2 The evolution of A_{UV}	63
5.2.3 The contribution of <i>H</i> -dropouts galaxies to A_{UV}	66
5.3 Deducing the main sequence of SFGs	67
5.3.1 Fitting the shape of the main sequence of SFGs	67
5.3.2 The contribution of <i>H</i> -dropouts galaxies to SFR	72
5.4 Deducing the gas mass of SFGs	72
5.4.1 From M_{dust} to M_{gas} and how to derive the metallicity	72
5.4.2 The contribution of <i>H</i> -dropout galaxies	75
5.4.3 Fitting the M_{gas} evolution of SFGs	75
5.4.4 Impact on M_{gas} of the dust grain model	76
5.5 Deducing the cosmic star formation history	77
5.6 Deducing the cosmic evolution of the gas mass density	79
5.7 Discussion	81
5.7.1 SFR, M_{gas} and SFE	81
5.7.2 ρ_{SFR} and ρ_{gas}	84
5.7.3 The Kennicutt-Schmidt relation	85
5.8 Retrospective: the impact of the clustering bias correction method on properties of galaxies	88
5.8.1 The T_{dust} evolution deduced from the method from B15	88
5.8.2 The $SFR - M_{\star}$ evolution deduced from the method from B15	90
5.8.3 The M_{gas} dependences deduced from the method from B15	90
6 Comparaison with the TNG100 cosmological simulation	93
6.1 The IllustrisTNG project	94
6.2 How to work with the TNG100 output data, and what to choose?	95
6.3 Galaxy properties of the TNG100 simulation	96
6.3.1 Deducing the stellar mass function of TNG100	96
6.3.2 SFR and f_{gas} in TNG100	97
6.3.3 The cosmic star formation history in TNG100	99
6.4 Discussion and conclusions on the TNG100 simulation	100

7 Conclusion	103
8 Perspectives	107
List of publications	117
Bibliographie	148

LIST OF FIGURES

1.1	51 Messier (The Whirlpool Galaxy) representation by Lord Rosse and <i>HST</i>	1
1.2	The Hubble galaxy classification	3
1.3	<i>UVJ</i> diagrams for the CANDELS sample of S15	4
1.4	Typical SED of a SFG	5
1.5	The stellar mass function of SFGs	7
1.6	The star formation main sequence	8
1.7	Starburstiness distribution of SFGs	9
1.8	The Kennicutt-Schmidt diagram	10
1.9	The cosmic star formation history	11
1.10	<i>H</i> -dropout galaxies contribution to the cosmic star formation history	12
2.1	Comparison of the stellar masses used in this work to the ones from the COSMOS2020 catalogue	19
2.2	Example of the completeness of catalogues	20
2.3	Examples of the CANDELS fields maps	23
3.1	Example of mean and median stacking	27
3.2	Evidence for a systematic bias in median stacking	28
3.3	Example of gradient in a stack in the COSMOS field	31
3.4	Comparison of flux density measurements obtained by aperture photometrie and PSF fitting	32
3.5	Example of results of flux density measurements with the method from B15, and the impact of the radius chosen	35
3.6	Comparison of flux density measured with the methods from (S15) and B15	36
3.7	The curve of growth for the ALMA PSF	38
4.1	Example of templates from the S18 library, and the influence of different variables	43
4.2	Example of a template from the S18 library, and the evolution with redshift	43
4.3	A representation of the transmission window considered in this work	45
4.4	Best fit SED for each bin of redshift and stellar mass	46
4.5	S18 to Draine & Li (2007) conversion factor for M_{dust} as a function of redshift	47
4.6	Comparison of the best fit SEDs with the template libraries from S18 and Draine & Li (2007)	48
4.7	Comparison of properties of stacked galaxies deduced from the best fit SED with Draine & Li (2007) model and S18 template library.	49
4.8	Comparison between the mean property value of the simulated galaxies, and the observed value retrieved after simulation	52
5.1	T_{dust} as a function of M_{\star} , colour-coded by redshift bin	58
5.2	T_{dust} and $\langle U \rangle$ as a function of redshift	60
5.3	λ_{peak} as a function of L_{IR}	61
5.4	Best fit SED for the stacked sample of <i>H</i> -dropout galaxies from Wang et al. (2019)	62
5.5	A_{UV} as a function of M_{\star} in different redshift bins	64
5.6	A_{UV} as a function of redshift, colour coded in different M_{\star} bin	65
5.7	Colour-magnitude diagram of the sample from Xiao et al. (2023) colour-coded by photometric redshift	67

5.8	SFR as a function of M_\star over different redshift bins	68
5.9	Comparison of SFR as a function of M_\star with the literature	70
5.10	SFR as a function of M_\star over different redshift bins following the evolution of the stellar mass knee	71
5.11	M_{gas} as a function of redshift for different M_\star	74
5.12	Comparison of M_{gas} as a function of redshift and M_\star with the literature	76
5.13	Cosmic star formation rate density as a function of redshift	78
5.14	Contributions over the whole range of stellar masses to the total ρ_{SFR} as a function of redshift for SFGs	79
5.15	The cosmic gas mass density as a function of redshift	80
5.16	The cosmic gas mass density as a function of redshift, comparison with Magnelli et al. (2020)	81
5.17	SFE as a function of M_\star , colour coded by redshift	82
5.18	Contribution to ρ_{SFR} , for SFGs, as a function of redshift	86
5.19	The Kennicutt-Schmidt relation, and redshift evolution	87
5.20	Comparison of T_{dust} and $\langle U \rangle$ as a function of redshift, deduced from the methods of S15 and B15	89
5.21	Comparison of SFR_{MS} as a function of M_\star over different redshift bins, deduced from the methods of S15 and B15	90
5.22	Comparison of M_{gas} as a function of redshift and M_\star , deduced from the methods of S15 and B15	91
6.1	The stellar mass function in TNG100	97
6.2	SFR as a function of M_\star for SFGs in TNG100	98
6.3	The gas fraction as a function of M_\star for SFGs in TNG100	98
6.4	Metallicity as a function of M_\star in IllustrisTNG simulations	99
6.5	Cosmic star formation rate density as a function of redshift in TNG100	100
6.6	Ratio of the ρ_{SFR} of high mass over low mass galaxies, as a function of redshift	101
8.1	Comparison of images between <i>Spitzer</i> -IRAC and <i>JWST</i> -MIRI	108
8.2	SFR as a function M_\star of <i>HST</i> -dark and <i>H</i> -dropout galaxies	109
8.3	Examples of SED fitting on galaxies detected with <i>JWST</i> -MIRI	111
8.4	Example of SED fitting on the stack of 103 galaxies on the first two MIRI pointings of CEERS observations in the EGS fields	112
8.5	Ratio of the effective radius for different galaxy types over those of the parent SFGs sample	113
8.6	Rest-optical to rest-MIR size ratios	114
8.7	Contribution of protocluster galaxies to the ρ_{SFR}	115

LIST OF TABLES

2.1	Number of galaxies in the final sample from each field	18
2.2	M_\star limit for 90% completeness	20
2.3	Differences in output flux with and without the GOODS North catalogue	21
3.1	Number of galaxies in each bin of M_\star and redshift	29
3.2	Clustering bias correction factor from S15	33
5.1	Best fit parameters of the A_{UV} of star-forming galaxies using Eq. 5.8	65
5.2	Best fit parameters of the main sequence of star-forming galaxies using Eq. 5.11	68
5.3	Best fit parameters of the main sequence of star-forming galaxies using Eq. 5.12	71
5.4	Best fit parameters of M_{gas} evolution of the main sequence using Eq. 5.19	75
5.5	ρ_{SFR} as a function of redshift	78
6.1	Specifics of the three TNG simulations	95

ACRONYMS AND ABBREVIATIONS

A_{UV}	Dust attenuation
HST	<i>Hubble</i> Space Telescope
H_2	Molecular gas
L_8	Luminosity at $8 \mu\text{m}$
L_{IR}	Infrared luminosity
L_{UV}	Ultraviolet luminosity
M/L	Mass-to-light ratio
M_{H_2}	Molecular gas mass
M_{HI}	Atomic gas mass
M_{dust}	Dust mass
M_{gas}	Gas mass
M_{\star}	Stellar mass
R_{SB}	Starburstiness
S/N	Signal-to-noise ratio
T_{dust}	Dust temperature
$T_{\text{dust}}^{\text{L}}$	Light weighted dust temperature
$T_{\text{dust}}^{\text{M}}$	Mass weighted dust temperature
Z	Metallicity
Σ_{SFR}	Star formation rate surface density
Σ_{gas}	Gas mass surface density
δ_{GDR}	Gas-to-dust mass ratio
λ_{peak}	Peak wavelength of the SED
$\langle U \rangle$	Mean starlight heating rate
ρ_{SFR}	Star formation rate density
ρ_{gas}	Gas mass density
τ_{dep}	Depletion time
f_{PAH}	Fraction of polycyclic aromatic hydrocarbon
f_{gas}	Gas fraction
$JWST$	<i>James Webb</i> Space Telescope
ACS	Advanced Camera for Surveys
AGN	Active galactic nuclei
ALMA	Atacama Large Millimeter/submillimeter Array
CANDELS	Cosmic Assembly Near-infrared Deep Extra-galactic Legacy Survey
CMB	Cosmic microwave background
FIR	Far-infrared
FMR	Fundamental metalicity relation
FoF	Friends-of-friends
FUV	Far-ultraviolet
FWHM	Full width half maximum

HI	Atomic gas
IMF	Initial mass function
IR	Infrared
IR8	L_{IR}/L_8
IRAC	Infrared Array Camera
LBG	Lyman-break galaxy
MIR	Mid-infrared
MS	Main sequence
MZR	Mass-metallicity relation
OFG	Optically faint galaxy
PAH	Polycyclic aromatic hydrocarbon
PSF	Point spread function
SED	Spectral energy distribution
SFE	Star formation efficiency
SFG	Star-forming galaxy
SFH	Star formation history
SFR	Star formation rate
SMG	Submillimetre galaxy
SSFR	Specific star formation rate
UV	Ultraviolet
WFC3	Wide Field Camera 3

CHAPTER 1

INTRODUCTION

1.1	Global context and historic	2
1.2	The galaxy bimodality	2
1.3	The SFG population	5
1.3.1	Typical SED of SFGs	5
1.3.2	Stellar mass and mass function	6
1.3.3	The star formation in SFGs	6
1.3.4	The link between the SFR and the gas content of SFGs	9
1.4	The cosmic star formation history	10
1.5	The current understanding on how galaxies form through cosmic time	12
1.6	Problematic	14



Figure 1.1: Left: Drawing of 51 Messier (The Whirlpool Galaxy) by Lord Rosse (W. Parsons Lord Rosse) in 1850. Credit: [Rosse \(1850\)](#). Right: Image of 51 Messier taken by the *Hubble* Space Telescope (*HST*) in 2017. Credits: NASA, ESA, S. Beckwith (STScI) and the Hubble Heritage Team (STScI/AURA).

1.1 Global context and historic

Galaxies have been studied for a long time. They were first mistaken for clouds within the Milky Way, later called nebulae. Historically, a nebula was often a star-forming region, where cold gas slowly collapses to form stars, a star cluster or a galaxy. In other words, a nebula was what had been identified as being too large to be a star and not originating from the solar system. One of the first significant attempts to identify nebulae was made by Charles Messier, who recorded 104 of them ([Messier 1781](#)). From this survey, we now know that around 40% of these nebulae are galaxies (i.e., non-galactic nebulae). William Herschel quickly surpassed this number with a survey of 2,500 nebulae ([Herschel 1786, 1789, 1802](#)).

From then on, learning more about these objects became a major driving force in astronomy. Among the first remarkable studies was that of Lord Rosse (W. Parsons Lord Rosse), who observed elliptical and spiral nebulae ([Rosse 1844, 1850](#)). In the 1910s, Vesto Slipher studied the radial velocities of these objects by studying their spectra ([Slipher 1912, 1913, 1915, 1917](#)). A few years later, the study of nebulae provided proof that certain nebulae such as the Andromeda Nebula are in fact galaxies located outside the Milky Way ([Opik 1922; Hubble 1925](#)).

The study of galaxies has also led to major discoveries in our current understanding of the universe. The expansion of the universe, which derives from Albert Einstein's theory of general relativity ([Einstein 1915](#)), is a great example. Friedmann and Georges Lemaître ([Lemaître 1927](#)) independently derive the expansion of the universe from Einstein theory of general relativity. Lemaître and Edwin Hubble ([Hubble 1929](#)) also gave an estimation of this expansion while using the radial velocities from Vesto Slipher ([Slipher 1912, 1913, 1915, 1917](#)). It showed that the further away the galaxy is from the Milky Way, the faster it escapes from it. Later on, Vera Rubin showed discrepancies between the observed and theorised rotation curves of stars in galaxies ([Rubin & Ford 1970, 1971; Rubin et al. 1980, 1982](#)), these observations will later on be explained by the dark matter.

Nowadays, galaxy surveys can count more than 300 million galaxies over 5000 deg^2 ([Sevilla-Noarbe et al. 2021](#)), or reach unprecedented depth by allowing for the detection of galaxies at incredibly large redshift: $z \sim 13.2$ ([Curtis-Lake et al. 2023](#)). While astronomers now have access to numerous ground- and space-based telescopes to study individual galaxies at almost any redshift, deducing the properties of galaxies as a whole population remains a challenge. This type of study requires a compromise between the surface and the depth of the survey. The inference of the properties of galaxies as a whole population will be the main topic of this manuscript.

1.2 The galaxy bimodality

Galaxies can be classified in different ways. The first depends on their morphology, as shown in Fig. 1.2 from [Hubble \(1936\)](#). Galaxies fall into two main groups: elliptical galaxies and spiral galaxies. A third group of "irregular galaxies" has been added to the classification, grouping together galaxies that are not clearly elliptical or spiral. Although this varies according to the study, the local universe is made up of approximately $\sim 22.7\%$ elliptical, $\sim 75.8\%$ spiral and $\sim 1.5\%$ irregular galaxies ([Oh et al. 2013](#)).

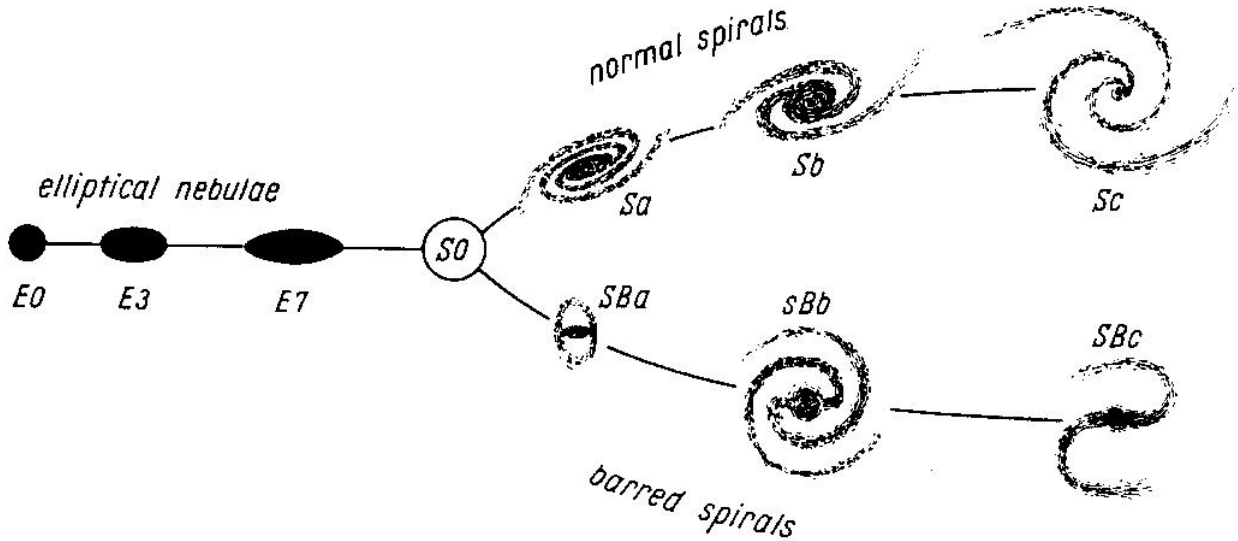


Figure 1.2: Galaxy classification from [Hubble \(1936\)](#). Credit: [Hubble \(1936\)](#).

Another way to sort galaxies is by their stellar population. The stellar population of galaxies can be divided into two categories according to whether they are short-lived (i.e., ≤ 100 Myr) or long-lived (i.e., ≥ 10 Gyr). Naturally, the presence of short-lived stars are a sign of active star formation within the galaxy. Short-lived stars are massive, bluer and dominate the ultraviolet/optical (UV/optical) spectral energy distribution (SED) of these galaxies, therefore called star-forming galaxies (SFGs). On the other hand, galaxies that have no signature of short-lived stars in their SED are, almost exclusively, constituted of long-lived redder stars, and are no longer forming stars (i.e., these galaxies are known as quiescent or passive galaxies). This classification of galaxies according to star formation reflects to some extent that of morphology, with SFGs tending to be spiral galaxies and quiescent galaxies tending to be elliptical galaxies. This tells us that in today's universe, a large proportion of galaxies are already dead.

The classification based on star formation is the one I will use in this manuscript in which galaxy morphology is not much studied. The method used in this thesis to differentiate SFGs from quiescent galaxies is based on two rest frame colour criteria and is called the *UVJ* method ([Wuyts et al. 2007](#); [Williams et al. 2009](#)). The first colour, the rest frame $U - V$, is a proxy for the specific star formation rate ($\text{SSFR} = \text{SFR}/M_\star$, where SFR is the star formation rate and M_\star the stellar mass) ([Salim et al. 2005](#); [Pannella et al. 2009](#)). The second colour, the rest frame $V - J$, breaks the age-dust attenuation degeneracy ([Wuyts et al. 2007](#); [Williams et al. 2009](#); [Whitaker et al. 2011](#)). In this manuscript, the *UVJ* criteria for quiescent galaxies are taken from ([Schreiber et al. 2015](#), hereafter S15) (see also [Williams et al. 2009](#)):

$$\text{Quiescent galaxies} = \begin{cases} U - V > 1.3, \\ V - J < 1.6, \\ U - V > 0.88 \times (V - J) + 0.49. \end{cases} \quad (1.1)$$

A representation of this classification in the $(U - V)_{\text{rest}} - (V - J)_{\text{rest}}$ plane is given in Fig. 1.3. In Fig. 1.3, quiescent galaxies are mostly found on the high M_\star end, and more common at lower redshift. In Fig. 1.3, 5% of the galaxies in the sample are classified as quiescent galaxies, of which a third

have more than a 20% probability of being misclassified due to uncertainties in the UVJ colours ([S15](#)). This shows that this method is not perfect and that classification errors can always occur. Misclassifications are mainly red-dusty galaxies identified as quiescent galaxies.

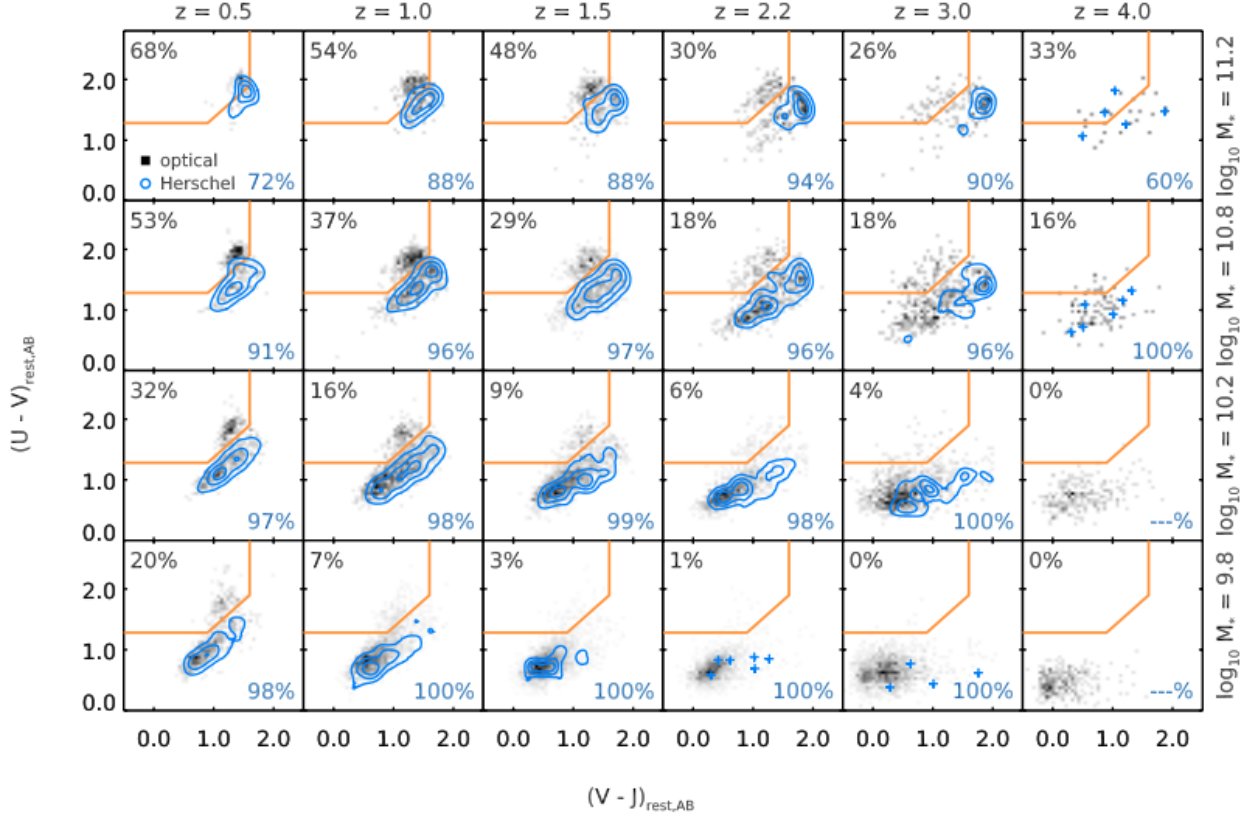


Figure 1.3: "UVJ diagrams in each bin of redshift (horizontally) and mass (vertically) of our Cosmic Assembly Near-infrared Deep Extragalactic Legacy Survey (CANDELS) sample. The central value of the redshift and mass bins are shown at the top and on right-hand side of the figure, respectively. The dividing line between active and passive galaxies is shown as a solid orange line on each plot, with passive galaxies located on the top-left corner. We show in the background the distribution of sources from the H -band catalogs in gray scale. We also overplot the position of sources detected with *Herschel* as blue contours or, when the source density is too low, as individual blue crosses. On the top-left corner of each plot, we give the fraction of H band-selected galaxies that fall inside the quiescent region, and on the bottom-right corner we show the fraction of *Herschel* sources that reside in the star-forming region." ([S15](#)). Credit: [S15](#).

A conclusion drawn from this classification is that the vast majority of galaxies appear to be SFGs. While some studies focus more on quiescent galaxies, in this manuscript I attempt to study the evolution of SFGs. I will now present the current understanding of the SFG population.

1.3 The SFG population

1.3.1 Typical SED of SFGs

The SED of a typical SFG (see Fig. 1.4) is constituted of several main components: the star emission, the dust emission and the gas emission. The rest frame stellar emission is mainly located in the UV and optical, it is dominated by young stars in SFGs. In the presence of dust within the galaxy, part of the stellar emission is absorbed by dust, and re-emitted in the infrared (IR) through some thermal emission (i.e., the dust emission in Fig. 1.4). The gas can even be ionised by the most energetic photons produced by stars, which translates into transition and free-free gas lines (see the main ones in Fig. 1.4) that can largely stand out of the global SED if properly resolved.

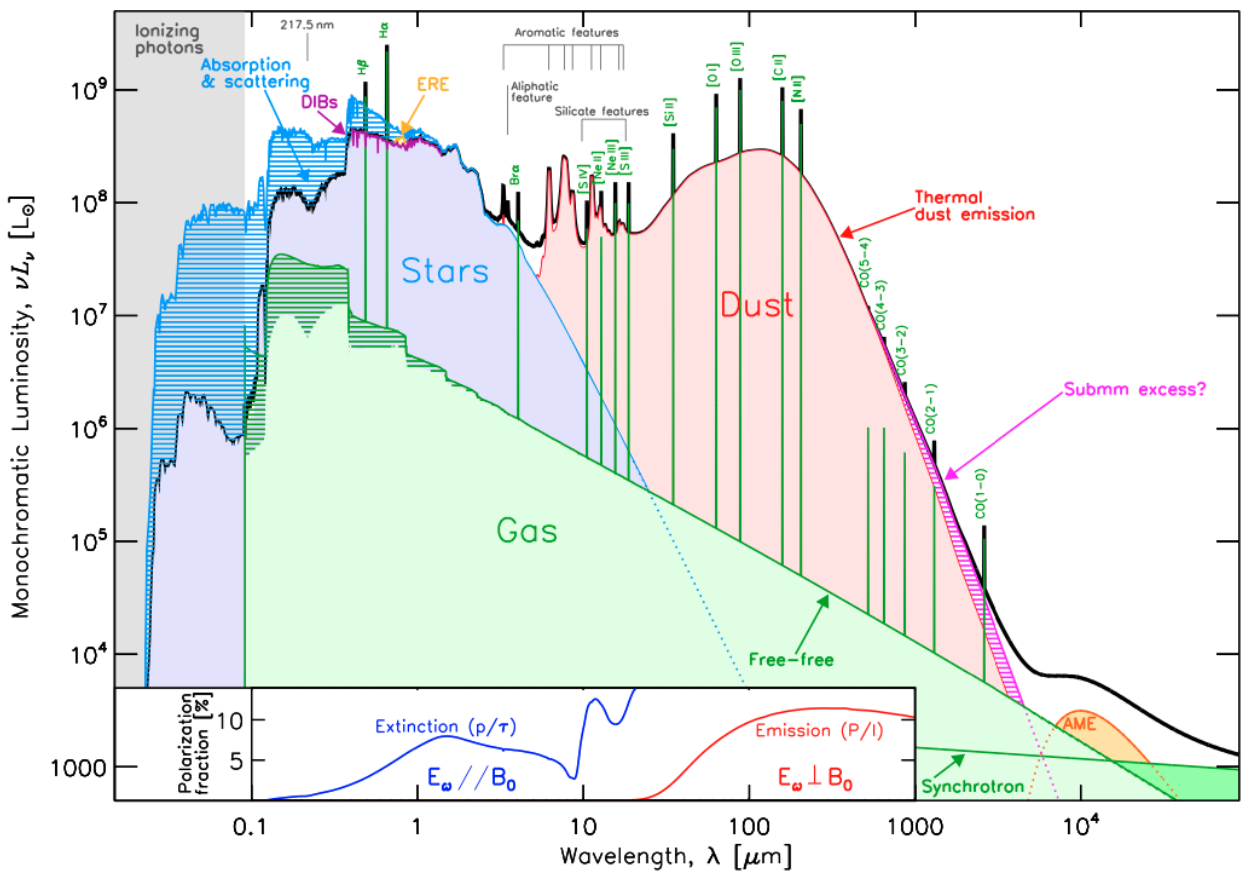


Figure 1.4: Typical SED of a SFG. The black line represent the total emission. The blue shaded area represents the stellar emission. The blue hatched area represents the portion of the stellar emission that is absorbed by dust. The red shaded area represents the dust emission. The green shaded area represents the gas emission and the most relevant gas lines. See [Galliano et al. \(2018\)](#) for more details. Credit: [Galliano et al. \(2018\)](#).

1.3.2 Stellar mass and mass function

One of the most important property of galaxies is their M_{\star} . Stellar masses are usually derived by the SED fitting of observed stellar emission (i.e., the blue shaded part of the SED on Fig. 1.4) with a model that will convert the light observed to estimate the M_{\star} through a mass to light ratio (M/L). Stellar models rely on several parameters to infer M/L : the initial mass function (IMF), the star formation history (SFH), the age of the stellar population, the metallicity and the dust attenuation.

The IMF represents the stellar mass distribution of stars being formed. The IMF is a quite important parameter to derive the stellar mass of a galaxy. Most of the UV light is due to these massive short-lived O B stars. But less massive stars, which dominate the mass, are dominating the optical, near-infrared emission. For this reason, a good way to infer the stellar mass, is to model the optical/near-infrared. The purpose of the IMF is thus to extrapolate the amount of mass that is not seen in the optical/near-infrared light emission, and is therefore crucial. Several forms of IMF exist (e.g., [Salpeter 1955](#); [Kroupa 2001](#); [Chabrier 2003](#)) and it is a topic still highly debated and hard to constrain due to its very nature. However, it is assumed that one can go from one to another by applying a conversion factor to both M_{\star} and SFR. For these reasons, studies usually assume a fixed IMF ([Salpeter 1955](#) or [Chabrier \(2003\)](#) most of the time) and carry they work with it, and leave the IMF debate for experts on the matter.

The SFH is needed to properly deduce the M/L to infer the stellar mass, but it is hard to characterise as the SFH might be complex and strongly vary on both short and long time scales. Parametric SFH are the most common type of SFH used to model the SED. This method possesses some strong bias (e.g., [Buat et al. 2014](#); [Ciesla et al. 2015, 2017](#); [Carnall et al. 2019](#); [Lower et al. 2020](#)). Nowadays, studies turn to non parametric SFH that are supposedly less biased (see e.g., [Iyer & Gawiser 2017](#); [Iyer et al. 2019](#); [Leja et al. 2019](#); [Lower et al. 2020](#)).

A direct visualisation of the evolution of the stellar mass distribution of galaxies is the stellar mass function, which represents the number of galaxies in a given mass range and per unit of comoving volume. The mass function for SFGs to which I choose to refer in this manuscript is that of [Davidzon et al. \(2017\)](#) and is shown in Fig. 1.5. In Fig. 1.5, the redshift evolution of the stellar mass function strongly varies at low M_{\star} , while the high mass end do not evolve much. This effect is known as the "downsizing" ([Cowie et al. 1996](#)), and suggests that massive galaxies formed earlier and evolved quicker compared to low-mass galaxies. This raises the question of what impact the M_{\star} of a galaxy has on its evolution and properties such as its SFR.

1.3.3 The star formation in SFGs

There are several ways of deducing the SFR of an SFG, of which I will briefly mention the main ones. The first is the direct study of the stellar emission continuum (i.e. the blue shaded area in Fig. 1.4). The stellar emission of massive short-lived O and B stars dominates the UV emission of galaxies, which thus provides a proxy for SFR on timescale less than 100 Myr, assuming a given IMF. As for the stellar mass the study of the stellar emission through SED model is dependent on the SFH. However, parametric SFH only allows to put constraints on the last few millions years for the SFR (e.g., [Ciesla et al. 2018](#); [Aufort et al. 2020](#); [Ciesla et al. 2021](#)). Then, by taking the observed rest-UV photometry of the galaxy and applying a simply conversion factor, one can deduce the observable

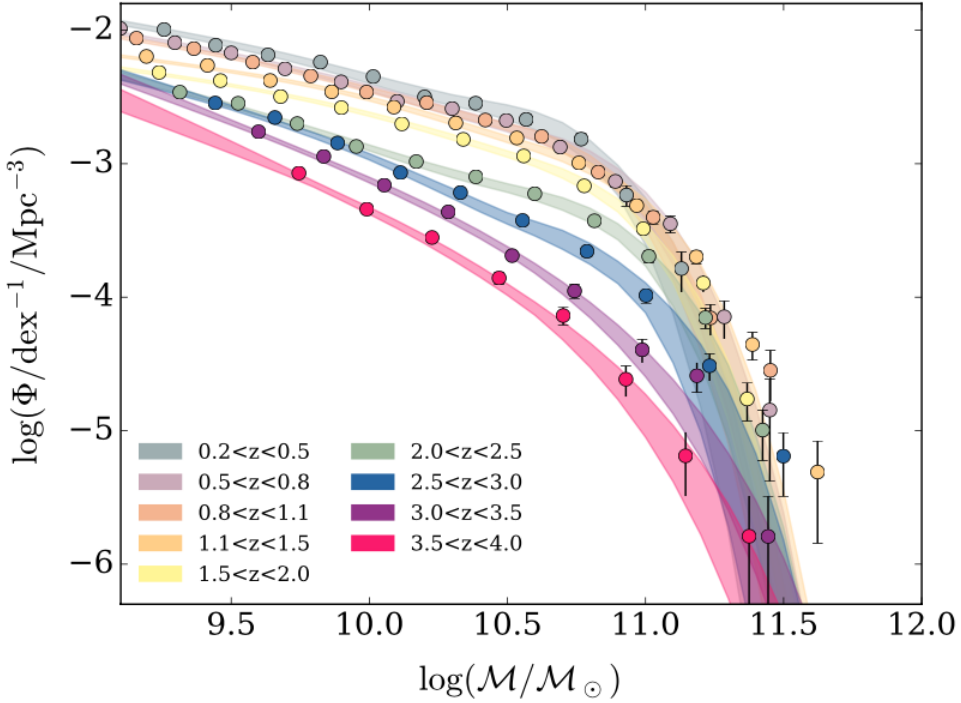


Figure 1.5: Stellar mass function from Davidzon et al. (2017). Different redshift bins are colour coded. Credit: Davidzon et al. (2017).

SFR after the dust has absorbed some of it (usually called $SFR_{\text{UV}}^{\text{obs}}$). From this, one can either correct for dust attenuation using attenuation models to deduce the total SFR. Another method is to combine $SFR_{\text{UV}}^{\text{obs}}$ directly with a SFR_{IR} , which is deduced from the dust emission (i.e., the red shaded area in Fig. 1.4) itself measured by fitting a dust SED model. SFR deduced from the study of the dust emission usually also probes the SFR on timescales less than 100 Myr. Another method consists of measuring the gas emission lines, such as H_{α} and H_{β} (i.e., the first two green lines, from the left, in Fig. 1.4) because they trace H_2 regions created by the ionising emission ($E > 13.6 \text{ eV}$) of O and B stars. Then, one can deduce the attenuation from the ratio of these lines. SFR is then deducted from the H_{α} line corrected for attenuation by applying a conversion factor. Although H_{α} is regarded as the most reliable SFR indicator, one could also infer SFR from the study of other nebula emission lines such as Ly α , [OII] and [OIII] (e.g., Moustakas et al. 2006). Usually SFR inferred from an emission line comes from the heaviest and hottest stars (i.e. $M_{\star} \geq 10 M_{\odot}$), and thus probes the SFR on timescales less than 10 Myr. Finally, the radio continuum emission can probe SFR on timescales less than 100 Myr (e.g., Murphy et al. 2011; Kennicutt & Evans 2012) as the result of the synchrotron emission and the thermal emission of warm HII region for frequency less than 20 GHz. One way to infer SFR from the radio is to use a IR-radio correlation (e.g., Helou et al. 1985; Yun et al. 2001; Molnár et al. 2021)

It has been shown that the SFR of SFGs is positively correlated with their stellar mass (M_{\star} ; e.g. Elbaz et al. 2007; Daddi et al. 2007; Whitaker et al. 2012, 2014; Speagle et al. 2014; S15; Lee et al. 2015; Delvecchio et al. 2021; Leslie et al. 2020; Popesso et al. 2023) with a small scatter of $\sim 0.2\text{--}0.3$ dex (e.g. Elbaz et al. 2007; Noeske et al. 2007; Rodighiero et al. 2011; Whitaker et al. 2012; Speagle et al. 2014; S15). This correlation is called the "main sequence" (MS) of SFGs (Noeske et al. 2007).

Although the specifics of this correlation remain a matter of debate, most recent studies tend to favour a linear main sequence in logarithmic space with a bending appearing at high M_\star and for $z \leq 2 - 3$ (e.g. Whitaker et al. 2014; Magnelli et al. 2014; S15; Delvecchio et al. 2021; Leslie et al. 2020, see Fig. 1.6), rather than a strictly linear correlation between SFR and M_\star (e.g. Whitaker et al. 2012; Speagle et al. 2014). The fact that such a strong correlation is found between the SFR and M_\star favours a scenario of stable star formation histories in galaxies (Noeske et al. 2007).

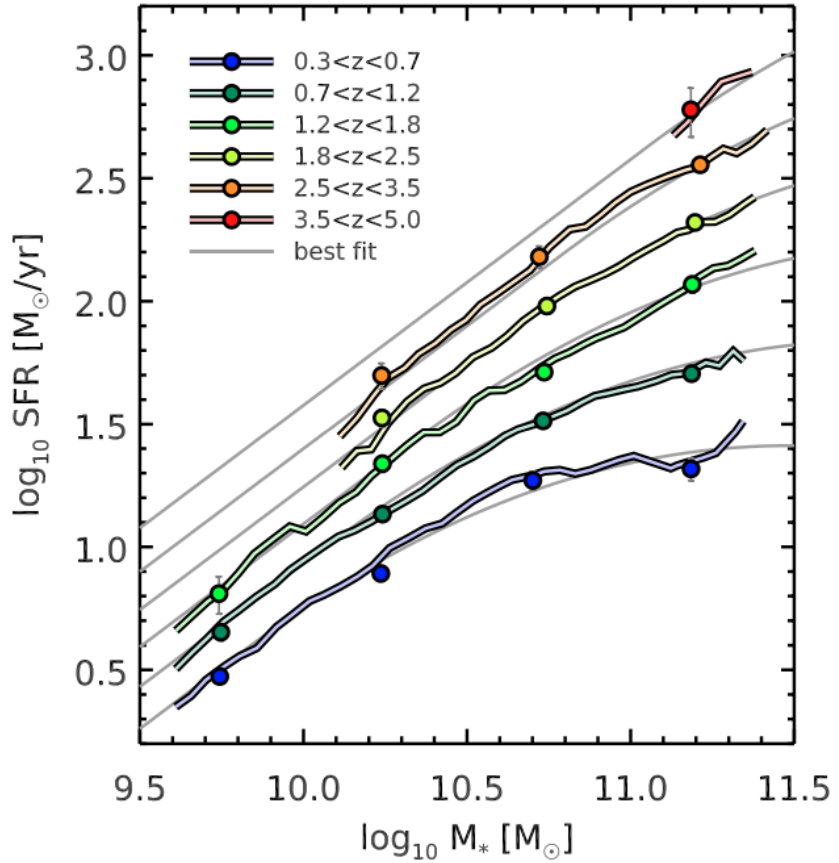


Figure 1.6: Evolution of the SFR as a function M_\star . Stacked results from S15 are displayed as points colour coded by redshift. Light grey line represents the best fit from S15. Credit: S15.

In Fig. 1.6, we can see the bending, discussed earlier, which illustrates the overall flattening in star formation in massive galaxies with redshift. This curvature and the evolution of normalisation observed in Fig. 1.6 raise some questions about the evolution of massive galaxies: what makes galaxies of a given mass produce ten times fewer stars today than at an earlier stage in the universe? Why do most massive galaxies appear to form even fewer stars per unit of their M_\star as the universe ages?

Although most SFGs reside by definition in the main sequence, there exists a small population of SFGs with a high SFR compared to main sequence galaxies, called starburst galaxies. In Fig. 1.7, we can see that the starburst galaxies do indeed form a second population of galaxies when we look at the distance of all the SFGs from the main sequence: the main sequence is distributed in a Gaussian, while the distribution of the starburst galaxies is distributed in a second Gaussian offset to higher SFR. Starburst galaxies are characterised by $\langle SFR_{\text{starburst}} \rangle \sim 5 \times SFR_{\text{MS}}$, where SFR_{MS} is the SFR

of the main sequence. However, Fig. 1.7 shows that starburst galaxies are much less numerous than normal SFGs which represent almost all SFGs ($\sim 97 - 98\%$ of SFGs, S15).

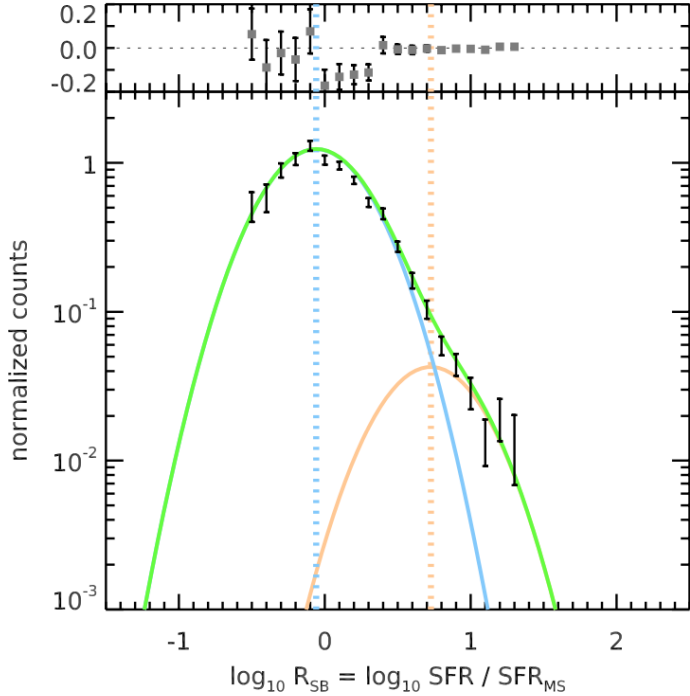


Figure 1.7: "Combined starburstiness ($R_{SB} = SFR/SFR_{MS}$) distributions normalised to the total number of SFGs in each bin. The green line shows our best-fit model, and the blue and orange lines show the contributions of main sequence and starburst galaxies, respectively. The residuals of the fit are shown at the top of the figure." S15 (see S15 for more details). Credit: S15.

1.3.4 The link between the SFR and the gas content of SFGs

Spatially resolved studies show that the SFR mostly correlates with molecular gas (H_2) surface density, and very little with atomic gas (HI) surface density (e.g. Bigiel et al. 2008; Leroy et al. 2008). The gas content of galaxies is usually probed through CO emission lines (see gas line on the left in Fig. 1.4) because of the difficulty of directly observing the H_2 molecules (e.g., Saintonge et al. 2017; Tacconi et al. 2018 ;see also Bolatto et al. 2013 for a review). However, other techniques have been developed to infer the gas content of galaxies through the study of multi-wavelength dust spectral energy distribution (i.e., the red shaded area in Fig. 1.4) fits, and by applying gas-to-dust ratio to infer the gas mass (M_{gas}) from the dust mass (M_{dust}) (e.g. Leroy et al. 2011; Magdis et al. 2011, 2012; Magnelli et al. 2012; Rémy-Ruyer et al. 2014; Genzel et al. 2015).

The relation between SFR and M_{gas} surface densities is the so called Kennicutt-Schmidt relation (i.e., Σ_{SFR} as a function of Σ_{gas} ; see Kennicutt 1998b). This relation has been shown to give a power law correlation, universal over redshift, with a slope of $\sim 1.0 - 2.0$ (e.g., Kennicutt 1998b; Bigiel et al. 2008; Liu et al. 2011; Bigiel et al. 2014; Morokuma-Matsui & Muraoka 2017; de los Reyes & Kennicutt 2019; Wang et al. 2022). An example of this relation is given in Fig. 1.8, where we can see that the relation follows a slope of ~ 1.41 . One of the consequences of this relation is that normal

SFGs appear to be all as efficient at converting gas into stars.

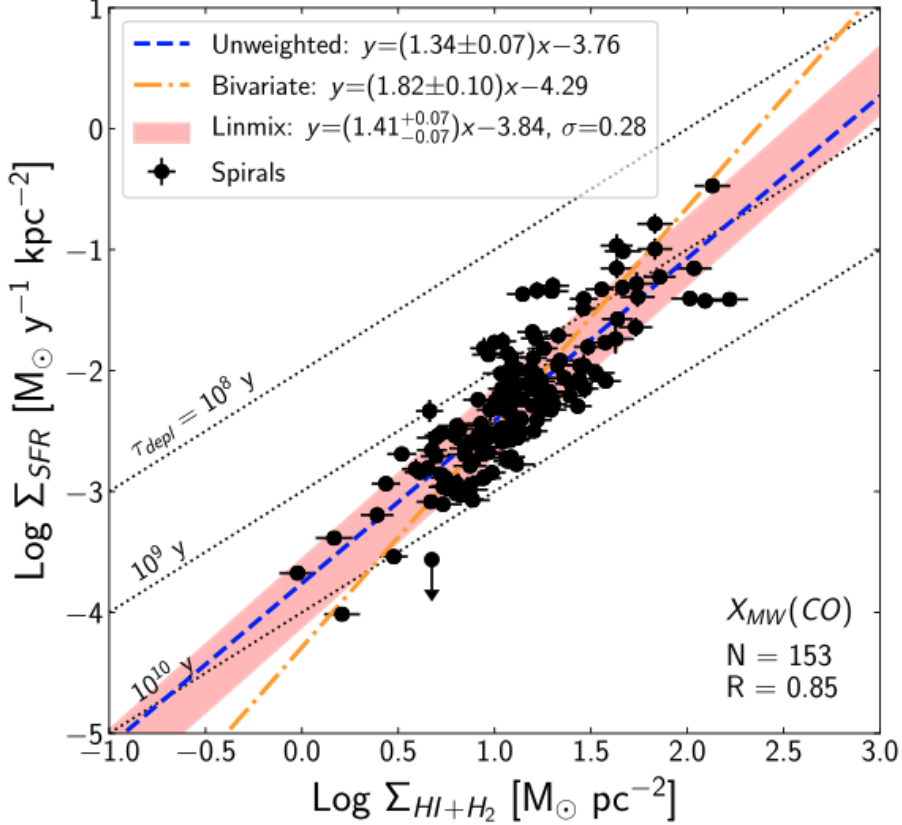


Figure 1.8: "The global star formation law for spirals (black circles), using a constant Milky Way $X(\text{CO})$. Dashed lines represent constant depletion time $\tau_{\text{dep}} = \Sigma_{\text{SFR}}/\Sigma_{\text{gas}}$. The lines of best fit are derived using different methods as described in the text: *unweighted* linear regression (blue dashed line), *bivariate* linear regression (orange dotted-dashed line), and an MCMC model using the *linmix* algorithm (the red shaded area marks the median of the posterior distributions for the linear slope, intercept, and intrinsic dispersion). Note that the correlation coefficient R shown on the bottom right is the Pearson correlation coefficient." [de los Reyes & Kennicutt \(2019\)](#). Credit: [de los Reyes & Kennicutt \(2019\)](#).

However, unlike the main sequence in Fig. 1.6, in this view all galaxies are packed together (regardless of the redshift and M_\star) and it raises a few questions: Do stars form with the same efficiency in all galaxies, regardless of their M_\star ? Is the relation redshift dependent?

1.4 The cosmic star formation history

The cosmic SFR density (ρ_{SFR}) is the total amount of stars formed in a comoving volume. The evolution of ρ_{SFR} over time, presented in Fig. 1.9, follows a gradual growth from the big bang to the cosmic noon (i.e. $z \sim 2$), followed by a continuous decline by a factor ~ 10 up to our time (e.g. [Madau & Dickinson 2014](#); [Bouwens et al. 2015b](#); [Liu et al. 2018](#); [Leslie et al. 2020](#) and [S15](#)). This evolution

alone raises many questions about the growth and death of galaxies. For example, the contribution to the ρ_{SFR} of galaxies of different M_* , or the ρ_{SFR} at high redshift (i.e. $z \geq 3$) are still largely uncertain. In Fig. 1.9, it is clear that our understanding of the high-redshift part (i.e. $z \geq 3$) is mainly built from the UV, and then deduced by correcting these UV measurements from dust attenuation (e.g. Bouwens et al. 2012b,a; Schenker et al. 2013; Bouwens et al. 2015a,b; Oesch et al. 2018).

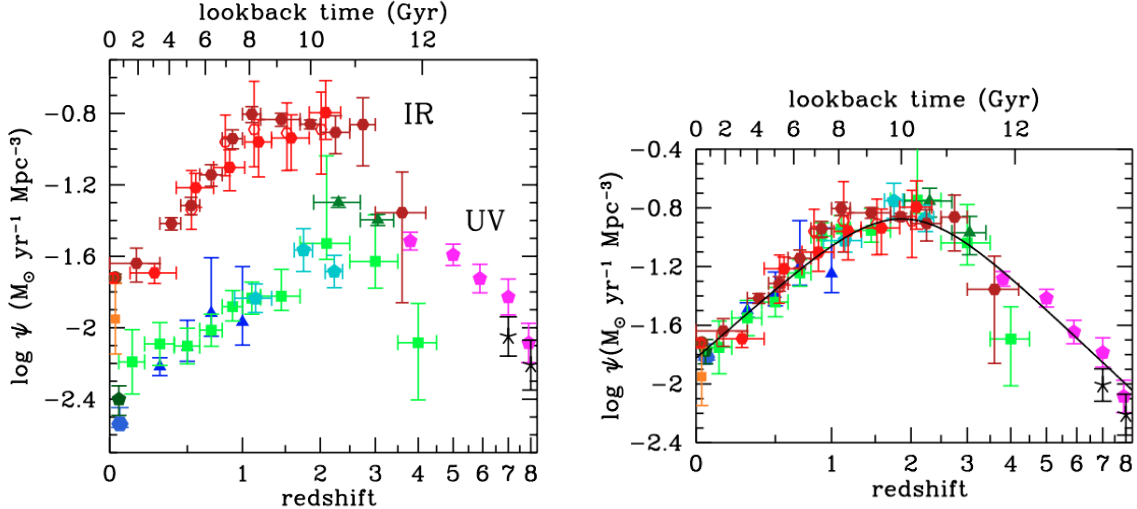


Figure 1.9: Left: SFR densities in the far-UV (FUV) (uncorrected for dust attenuation) and in the far-infrared (FIR). Right: The history of cosmic star formation from FUV+IR rest-frame measurements. Credit: Madau & Dickinson (2014).

However, it has recently been claimed, through studies using dust-unbiased measurements (i.e. radio or far-infrared emission), that ρ_{SFR} is actually higher at high redshift (e.g. Novak et al. 2017; Lagache 2018; Gruppioni et al. 2020). This shows that part of the star formation is obscured by dust and may still not be properly taken into account in UV-based measurements. The fraction of star formation obscured by dust is still highly uncertain at high redshift (i.e. $z \geq 3$), as it could be higher up to a factor of 10 above unobscured star formation (Casey et al. 2018). The correction factors for dust attenuation are quite large (e.g. Calzetti et al. 1994; Madau et al. 1998; Steidel et al. 1999), some studies have therefore attempted to combine SFR from the UV (uncorrected from dust attenuation) and SFR deduced directly from the IR using stacking (e.g. S15; Delvecchio et al. 2021) when seeking the total SFR and ρ_{SFR} .

Most of these studies are based on *Hubble* Space Telescope (*HST*) detected catalogues to infer the evolution of the SFR, they do not take into account the contribution of so-called *HST*-dark galaxies in the study of the ρ_{SFR} . *H*-dropout (Wang et al. 2019), *HST*-dark (Zhou et al. 2020) or optically-dark/faint (Gómez-Guijarro et al. 2022a; Xiao et al. 2023) galaxies, represent massive and highly obscured galaxies usually detected with low significance or not at all in the optical. Although initially thought to be a marginal population with little effect on the ρ_{SFR} , over time it was shown that such obscured galaxies could significantly contribute to the ρ_{SFR} above $M_* \sim 10^{10.5} M_\odot$ (e.g. Wang et al. 2019; Xiao et al. 2023). In Fig. 1.10, massive *H*-dropout galaxies (i.e., $M_* \geq 10^{10} M_\odot$) account for $\sim 10\%$ of the total ρ_{SFR} for $4 \lesssim z \lesssim 6$.

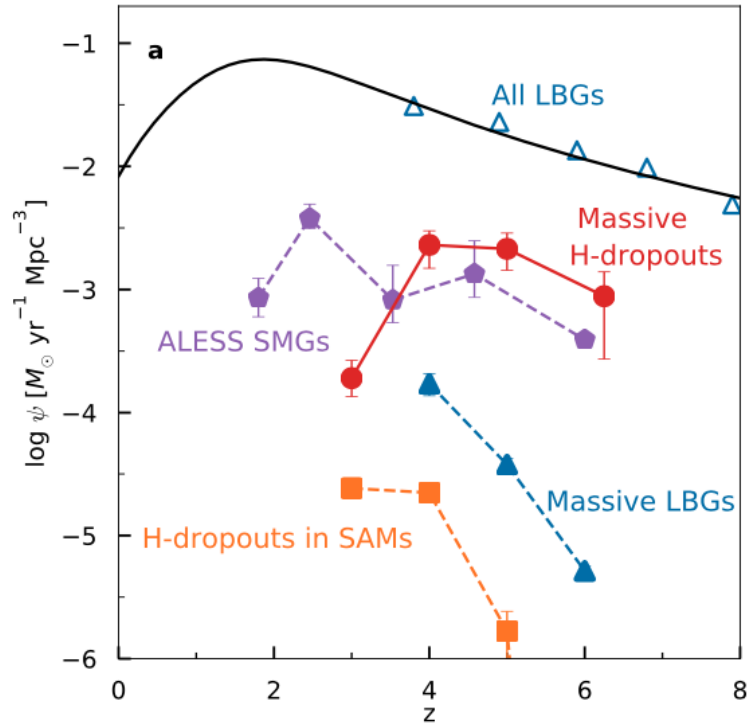


Figure 1.10: Contribution of H -dropouts to the cosmic SFR density and the stellar mass function. Credit: [Wang et al. \(2019\)](#).

These observations on the cosmic star formation history raise a number of questions: What controls the raise and fall of the ρ_{SFR} with redshift? What is the contribution to the total ρ_{SFR} of SFGs with different M_\star ? How much of the total ρ_{SFR} is missed by studies based on H -band detected galaxies?

1.5 The current understanding on how galaxies form through cosmic time

Our current understanding is that galaxies first formed within dark matter halos which trapped cold gas which then collapsed into star. From then, galaxy grew though different mechanisms such as cold gas accretion running from the filamentary streams of the cosmic web, minor and major mergers. The minor mergers usually follow the cold gas inflows ([Dekel et al. 2009](#)). Although, cold gas accretion and minor mergers seem to dominate the growth of SFG at $z \leq 2$, major mergers are more frequent at $z \geq 2$ and an important factor of mass growth of massive galaxies ([Le Borgne et al. 2009](#)). Mergers are also known to have an impact on triggering various effects such as star formation and quasar activity ([Hopkins et al. 2008b](#)). Once quenched, passive galaxies build they mass mostly through dry mergers (i.e., mergers that do not trigger any star formation event, [Hopkins et al. 2008b](#)).

An important behaviour of galaxy evolution is the fact that massive galaxies seem to build up their mass and evolve quicker compared to lower mass galaxies: this is called the downsizing effect ([Cowie et al. 1996](#)). There also seems to be a downsizing effect in the build up of the most massive black holes: most of them seem to be built up by $z \sim 2$ compared to less massive ones that form later on

(e.g., McLure & Dunlop 2004; Fine et al. 2006). This is however unclear whether the downsizing effect observed at the black hole level translates into a downsizing effect at the galaxy level (e.g., Hopkins et al. 2008b,a).

The number of galaxies that stop producing stars increases over time (e.g., Tomczak et al. 2014; Davidzon et al. 2017; Santini et al. 2022). This seems correlated to the evolution of their morphology from spiral to elliptical but whether these transitions in morphology and SFR happen simultaneously or not is still unclear. The role and relative impact of mergers and active galactic nuclei (AGN) events in the quenching process of a galaxy is still debated. There is, however, two types of quenching that can be distinguished: "mass quenching" depending on the galaxy mass and the close link observes between mass and the SFR through the main sequence (e.g., Elbaz et al. 2007; Santini et al. 2009, 2017), and an "environmental quenching". The environment in which the galaxy evolves plays an important role. For example, it has been shown that high density environments are dominated by early-type (i.e., elliptical and S0 nebulae in the Hubble (1936) classification) galaxies (e.g., Dressler 1980; Whitmore et al. 1993; Dressler et al. 1997; Postman et al. 2005) and quiescent galaxies (e.g., Lewis et al. 2002; Peng et al. 2010); that spiral galaxies in such environments tend to have lower HI and H_2 reservoirs, and, as a result, low SFR compared to field galaxies (e.g., Gavazzi et al. 1998; Boselli et al. 2014b, 2016). The reasons for the quenching of galaxies in dense environments are still unclear and debated but the main ones are the galaxy high velocity within the hot and dense intracluster medium (e.g., Sarazin 1986), galaxy harassment (e.g., Moore et al. 1996, 1998) and ram-pressure stripping (e.g., Gunn & Gott 1972). A more detailed presentation of the processes of galaxy quenching is depicted in Man & Belli (2018).

Overall, the mechanisms that trigger and regulate mass growth and star formation of a galaxy are complex, and their relative impact are still widely unknown. For example, AGN feedback is at times negative (e.g., Silk & Rees 1998; Fabian 2012; Harrison 2017) by pushing gas out of the galaxy and suppressing star formation and triggering the quenching of the galaxy; and at times positive (e.g., Silk 2013; Zubovas et al. 2013) by pressuring the gas within the galaxy (in the path of the outflow jets) and triggering star forming event. In addition, feedback both from AGN and stellar winds (i.e., supernovae) might play a role into regulating star formation within a galaxy (e.g., Silk 2011). Finally, the impact of the compactness of the galaxy inner morphology (i.e., presence of a bar and a bulge) is also an important factor in the galaxy future evolution (e.g., Saintonge et al. 2012; Boselli et al. 2014a; Saintonge & Catinella 2022). Altogether, and depending on the model considered, the evolution of star formation is expected to vary strongly on both short and long time scale which explain why it is such a complex topic to understand.

1.6 Problematic

A key question in astronomy is how baryonic matter comes together. The scientific community now has an insight into how this process works. Gravitation is the main player that glues matter together to form massive structures such as clusters of galaxies, galaxies and at a smaller scale giant molecular clouds. Again thanks to gravitation, we know that galaxies form supermassive black holes at their centres, and that stars form from the collapse of cold gas. On the other hand, feedback from supernovae and AGN influences the amount of cold gas available in the galaxy's reservoir, and the galaxy's environment can dictate the very evolution of this reservoir (e.g., gas accretion from the cosmic web or on the contrary harassment or ram-pressure depleting it). All these elements combine to form our overall understanding of galaxy evolution. These are deduced from a decade of diverse studies taking advantage of deep multi-wavelength surveys from UV to radio wavelengths over large deep fields. The aim is to understand how gas, environment, stellar mass, SFR, AGN and morphology are linked to explain the evolution of galaxies as a whole.

As a result, many questions remain unanswered: what is the true star formation activity of galaxies at redshifts $z > 3$ where the effect of dust attenuation is poorly known? What type of galaxy contributes most to the cosmic star formation density? Are they mostly massive, bright in the IR, or none of the above? What is responsible for cosmic noon (i.e. when the number of stars formed per unit of comoving volume reached its maximum)? Are galaxies always as efficient at forming stars? How are the properties of galaxies related to each other? How did massive galaxies form so early in the universe?

In an attempt to answer these questions, several surveys were carried out over the years. They focus on deep fields, first probed with *HST* in the optical and known as the Cosmic Assembly Near-infrared Deep Extragalactic Legacy Survey (CANDELS) fields. These fields were then observed with *Spitzer* and *Herschel* to cover the mid-to-far-infrared, and more recently with the Atacama Large Millimeter/submillimeter Array (ALMA) to cover submillimetre part of the spectra.

During my PhD, I had access to all these data with the aim of combining them to study the evolution of galaxy properties for the first time with a submillimeter view thanks to the ALMA GOODS-South map. This study is my main investigation during my PhD. This thesis manuscript summarises my best efforts to push our understanding of galaxy evolution a little further.

In Chap. 2 of this manuscript, I will present the dataset on which I have based my main study. I will take the time to present the flux density maps and galaxy catalogues that I have used.

In Chap. 3, I will introduce the stacking method that I have used throughout my main study. I will review the basics and the key steps of the stacking method. I will also explain how I applied it to the observations used in this study. I will then discuss how to measure flux densities from a stacked image as a function of wavelength. In particular, I will present the "clustering bias" that can appear in the *Herschel* bands, and how I corrected for this bias.

In Chap. 4, I will present the SED fitting method I used for my study. I will also present my analysis to look for biases in the SED fitting procedure such as stacking and AGN biases.

In Chap. 5, I will present how I deduced the dependence with redshift and M_\star of several galaxy properties, including: the dust temperature (T_{dust}), the dust attenuation (A_{UV}), SFR, M_{gas} , ρ_{SFR} and the

gas mass density (ρ_{gas}). For each of these properties, I will study the potential specific biases, as well as the contribution of the H -dropout population of galaxies from Wang et al. (2019), in an attempt to derive an unbiased, mass complete view of galaxy properties. I will end this chapter with a discussion that aims to place each galaxy property dependence in a global context.

In Chap. 6, I will compare the results of the previous chapter with the TNG100 simulation of the IllustrisTNG project. In particular, I will examine key properties such as SFR, M_{gas} and ρ_{SFR} . The aim of this chapter is to assess the extent to which current cosmological simulations are able to reproduce observational results and to highlight possible areas for improvement.

Finally, I will summarise my findings and discuss possible future prospects, including the use of MIRI on board the James Webb Space Telescope (*JWST*).

Throughout this thesis manuscript, I adopt a Salpeter (1955) IMF and the cosmological parameters $(\Omega_M, \Omega_\Lambda, h) = [0.30, 0.70, 0.70]$. I will use a factor of 1.7 to convert M_\star and SFR from a Chabrier (2003) to a Salpeter (1955) IMF whenever necessary (e.g. Reddy et al. 2006; Santini et al. 2012; Elbaz et al. 2018; Gómez-Guijarro et al. 2022b). When mentioned, magnitudes are in the AB system, such that $M_{\text{AB}} = 23.9 - 2.5 \log_{10}(S_\nu [\mu\text{Jy}])$.

CHAPTER 1

CHAPTER 2

DATA SET

2.1 Catalogues	18
2.1.1 Stellar masses	18
2.1.2 Completeness of the catalogues	19
2.1.3 The specificity of GOODS North catalogue	20
2.2 Observation maps	21

In this chapter, I will introduce all the data that I based my study on, namely, the catalogues of galaxies and the photometric maps.

My study take place in the CANDELS fields. The CANDELS collaboration originally aimed, in 2009, at creating the deepest observations using the new near-infrared WFC3 (Wide Field Camera 3) and visible-light ACS (Advanced Camera for Surveys) cameras of the *HST*. The CANDELS fields remain to this day the deepest large fields surveyed with a coverage in a wide range of wavelengths from the UV to the millimetre. The specifics of these fields made them exceptionally well fitted for a study aiming at probing global properties of galaxies evolution to high redshifts. In my study, I focus on 4 of the 5 CANDELS fields, namely: GOODS-South, GOODS-North, COSMOS and UDS.

2.1 Catalogues

In the study presented in this manuscript, I worked from catalogues of H -band selected SFGs on three fields: GOODS-South, COSMOS and UDS. I used the ultra-deep H -band catalogue of the CANDELS-*HST* team (Grogan et al. 2011; Koekemoer et al. 2011) for GOODS-South (Guo et al. 2013), COSMOS (Nayyeri et al. 2017) and UDS (Galametz et al. 2013) fields. In contrast, the GOODS North catalogue is from S15 and is K_s -band selected. The 5σ limiting magnitude ranges from $H \sim 27.4$ to 29.7 for GOODS-South, $H \sim 27.4$ to 28.8 for COSMOS, and $H \sim 27.1$ to 27.6 for UDS. The 5σ limiting magnitude for in the GOODS North catalogue is $K_s \sim 24.5$. The photometric redshifts and M_\star of all the galaxies in these catalogues were derived in S15. Photometric data were fitted up to the Infrared Array Camera (IRAC) $4.5\mu\text{m}$ band, with EAZY (Brammer et al. 2008), by assuming a delayed exponentially declining star formation history with the Bruzual & Charlot (2003) stellar population synthesis model. The SFGs are UVJ selected, following the definition from Muzzin et al. (2013). The final number of SFGs in the sample is given in Table 2.1. H -dropout galaxies are by definition not included in these samples, as they are not detected in H -band. However, their impact will be added and discussed in any necessary analyses.

Table 2.1: Number of galaxies in the final sample from each field.

Field	Number of galaxies	Area (arcmin 2)
GOODS South	26,811	134
GOODS North	11,492	142
COSMOS	34,124	388
UDS	32,695	412
Total	105,122	1,077

2.1.1 Stellar masses

For this study, M_\star were derived using FAST (Kriek et al. 2009), adopting a Salpeter (1955) IMF, the stellar population synthesis model of Bruzual & Charlot (2003) and assuming a delayed exponentially declining SFH for all galaxies (see S15 for more details).

I also compared the M_\star used in this study, in the COSMOS CANDELS field, to the ones from the COSMOS2020 catalogue (Weaver et al. 2022). The M_\star from the COSMOS2020 catalogue are deduced by fitting the SED of the galaxy using EAZY (Brammer et al. 2008) and log-normal SFH.

I cross-matched galaxies between the two catalogues and compared their M_\star in Fig 2.1. We can see in Fig 2.1 that both M_\star are consistent overall, that no offset nor systematic bias exists between the two distributions ($\log_{10}(M_\star^{\text{COSMOS2020}}/M_\star) = -0.04^{+0.26}_{-0.29}$). As a result, we conclude that the particular SED fit method used in this study to derive stellar masses should not have any particular bias to our results. The differences between the M_\star used in this study and the ones from COSMOS2020 catalogue (Weaver et al. 2022) might come down to the differences in the photometry, template models, SFH and redshifts used to fit the SED and deduce them.

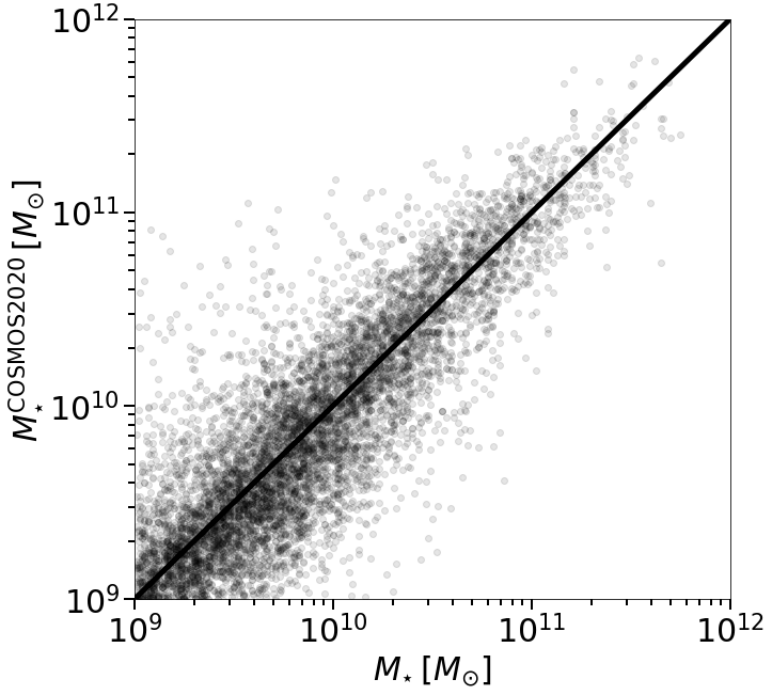


Figure 2.1: Stellar masses from the COSMOS2020 catalogue (Weaver et al. 2022) as a function of the ones used in this work (COSMOS CANDELS fields).

2.1.2 Completeness of the catalogues

In order to access the completeness of the catalogues that I stacked in this study, I followed the method of S15. In summary, I assumed, for each redshift bin, that the observed luminosity at $1.6\mu\text{m}$ ($L_{1.6\mu\text{m}-\text{obs}}$) can be related to M_\star simply by $M_\star = C \times L_{1.6\mu\text{m}-\text{obs}}^\alpha$ with a scatter. The relation and dispersion are fitted from the H -band photometry of the catalogues. I derive the completeness from Monte Carlo simulations by generating, from a uniform redshift distribution in the redshift bin and a given M_\star , the corresponding $L_{1.6\mu\text{m}-\text{obs}}$ taking into account the dispersion, and comparing it to the corresponding H -band detection limit for each catalogue. I assume that catalogues are complete when the detectability (i.e., $L_{1.6\mu\text{m}-\text{obs}} \geq L_D$, where L_D is the luminosity corresponding to the detection limit at the redshift of the mock galaxy) in a given stellar mass is above 90% (S15). The corresponding $M_\star^{90\%}$, above which all catalogues are assumed to be mass complete, are listed in Table 2.2. We will see in Chap. 4, that all but two of the bins which yield significant mid-to-submillimetre detection (i.e., with signal to noise ratio $S/N \geq 3\sigma$ in at least one band from $24\mu\text{m}$ to 1.13 mm) considered in this study are mass complete: for $10.0 \leq \log_{10}(M_\star/M_\odot) \leq 10.5$ at $3.1 \leq z \leq 3.9$ and $3.9 \leq z \leq 5.0$. These

two bins are, however, almost mass complete as $M_\star^{90\%} = 10^{10.1} M_\odot$.

Table 2.2: M_\star for which we obtain a completeness of 90% in the H -band catalogues used in this work.

Redshift bin	$\log_{10}(M_\star^{90\%}/M_\odot)$
$0.1 \leq z \leq 0.4$	7.7
$0.4 \leq z \leq 0.7$	8.1
$0.7 \leq z \leq 1.0$	8.5
$1.0 \leq z \leq 1.3$	8.5
$1.3 \leq z \leq 1.8$	8.6
$1.8 \leq z \leq 2.3$	9.3
$2.3 \leq z \leq 3.1$	9.7
$3.1 \leq z \leq 3.9$	10.1
$3.9 \leq z \leq 5.0$	10.1

2.1.3 The specificity of GOODS North catalogue

The GOODS North catalogue was not selected in the H -band like the other three catalogues but in the K_s -band. The main impact is on the completeness of the GOODS North catalogues, which is poorer than for the other three catalogues. Figure 2.2 shows the completeness of the four fields for $3.1 \leq z \leq 5$. Figure 2.2 shows that the GOODS North catalogue is significantly less complete than the other three catalogues. However, this does not have much impact on the results of my analysis because the missing galaxies in the GOODS North catalogue are mainly the lowest-mass galaxies for which I have no major detection in *Herschel* (see Chapt. 4).

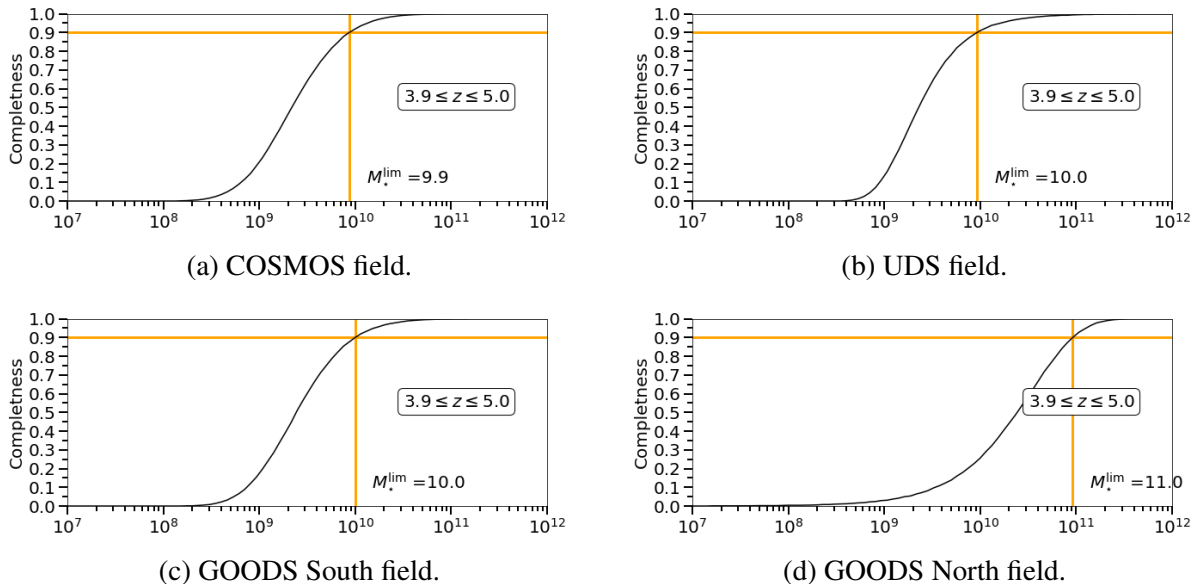


Figure 2.2: Completeness of catalogues over the four fields for $3.1 \leq z \leq 5$.

I also checked that stacking with this GOODS North catalogue selected in the K_s band has no major impact on the stacked output photometry. To this end, I stacked only the other three fields (i.e. GOODS South, COSMOS and UDS) and compared the output flux with those from the stacks of the four fields; the results are given in Table 2.3. The main conclusion from Table 2.3 is that the differences are almost insignificant for all fluxes except at $24\mu\text{m}$. The measurements at $24\mu\text{m}$ are located on the polycyclic aromatic hydrocarbon (PAH) emission, for $1 \leq z \leq 5$, which varies strongly within a population of similar redshift and M_\star . However, this does not imply major differences in key properties such as the infrared luminosity (L_{IR}), T_{dust} or M_{dust} . The only difference I observe is in the highest bin of redshift and M_\star (i.e., $3.1 \leq z \leq 5$ and $\log_{10}(M_\star/M_\odot) \geq 11$), which has a L_{IR} 40% higher with the GOODS North catalogue than without, but shows no major differences on T_{dust} and M_{dust} . I conclude that, in this bin, the GOODS North field only adds galaxies with high star formation (i.e., high L_{IR}) to the stack, leading to an increase in L_{IR} . This point alone will have no impact on the conclusions drawn in this study. The main difference in photometry results in a larger error in the flux measurements due to the stacking of fewer galaxies. For these reasons and because the inclusion of GOODS-North improves the flux density measurements, I decide to include it in the stacks.

Table 2.3: Differences in output flux with (wGN) and without (woGN) the GOODS North catalogue. ALMA does not appear in this Table because I do not have access to a GOODS-North map at 1.13 mm to begin with.

Wavelength (μm)	$(S_\nu^{\text{woGN}} - S_\nu^{\text{wGN}})/S_\nu^{\text{wGN}}$
24	$21\%^{+70\%}_{-18\%}$
100	$1\%^{+12\%}_{-14\%}$
160	$-2\%^{+10\%}_{-9\%}$
250	$-2\%^{+5\%}_{-7\%}$
350	$-1\%^{+8\%}_{-6\%}$
500	$-4\%^{+6\%}_{-9\%}$

I plan to replace the GOODS-North catalogue from S15 with the catalogue selected in the H -band of Barro et al. (2019) for the publication of the paper corresponding to this study. The catalogue should improve the completeness of the study and provide better S/N measurements for the lowest masses in each redshift bin. I will also take this opportunity to add the UDS field to the $24\mu\text{m}$ stack using the SpUDS *Spitzer* Legacy program (PI: J. Dunlop)¹. I do not expect it to change anything important in this study, but it will make it more coherent overall.

2.2 Observation maps

To obtain the mid-IR to submillimeter properties of these galaxies (i.e., their SFR_{IR} , T_{dust} and M_{dust}), we complement these catalogues with observations maps from various telescopes: *Spitzer*, *Herschel* and ALMA.

Observations with *Spitzer*-MIPS at $24\mu\text{m}$ include maps of the COSMOS field, (PI: D. Sander;

¹<https://irsa.ipac.caltech.edu/data/SPITZER/SpUDS/>

(LeFloc'h et al. 2009), the GOODS-South and GOODS-North fields (GOODS Legacy program; PI: M. Dickinson, Magnelli et al. 2011).

The *Herschel* PACS (at 100 and 160 μm) and SPIRE (at 250, 350 and 500 μm) maps of the four fields come mainly from the CANDELS-*Herschel* program, with the exception of the PACS GOODS-North and GOODS-South maps that are the combined *Herschel*-PACS data from the PEP (Lutz et al. 2011) and GOODS-*Herschel* (Elbaz et al. 2011) programs, as described in Magnelli et al. (2013). For the PACS maps, I used the truncated point spread function (PSF) derived from Vesta, while for *Herschel*-SPIRE the PSF is assumed to be Gaussian with a full width half maximum (FWHM) of 18''.15, 25''.15 and 36''.3 respectively at 250, 350 and 500 μm according to Griffin et al. (2010) (see also Shirley et al. 2021).

For ALMA, I used the 1.13 mm low-resolution GOODS-ALMA map (Gómez-Guijarro et al. 2022a), within the GOODS-South field with the 1''.1 circularised PSF FWHM. I note that there is a global and local offset between the position of sources in the ALMA and *HST* images (Franco et al. 2018, 2020). I corrected them using the offsets provided by Franco et al. (2020).

A representation of the four 100 μm fields is shown in Fig. 2.3. Figure 2.3, shows that the COSMOS and UDS fields are wider (388 and 412 arcmin², respectively), compared to the GOODS-South and GOODS-North fields (134 and 142 arcmin², respectively).

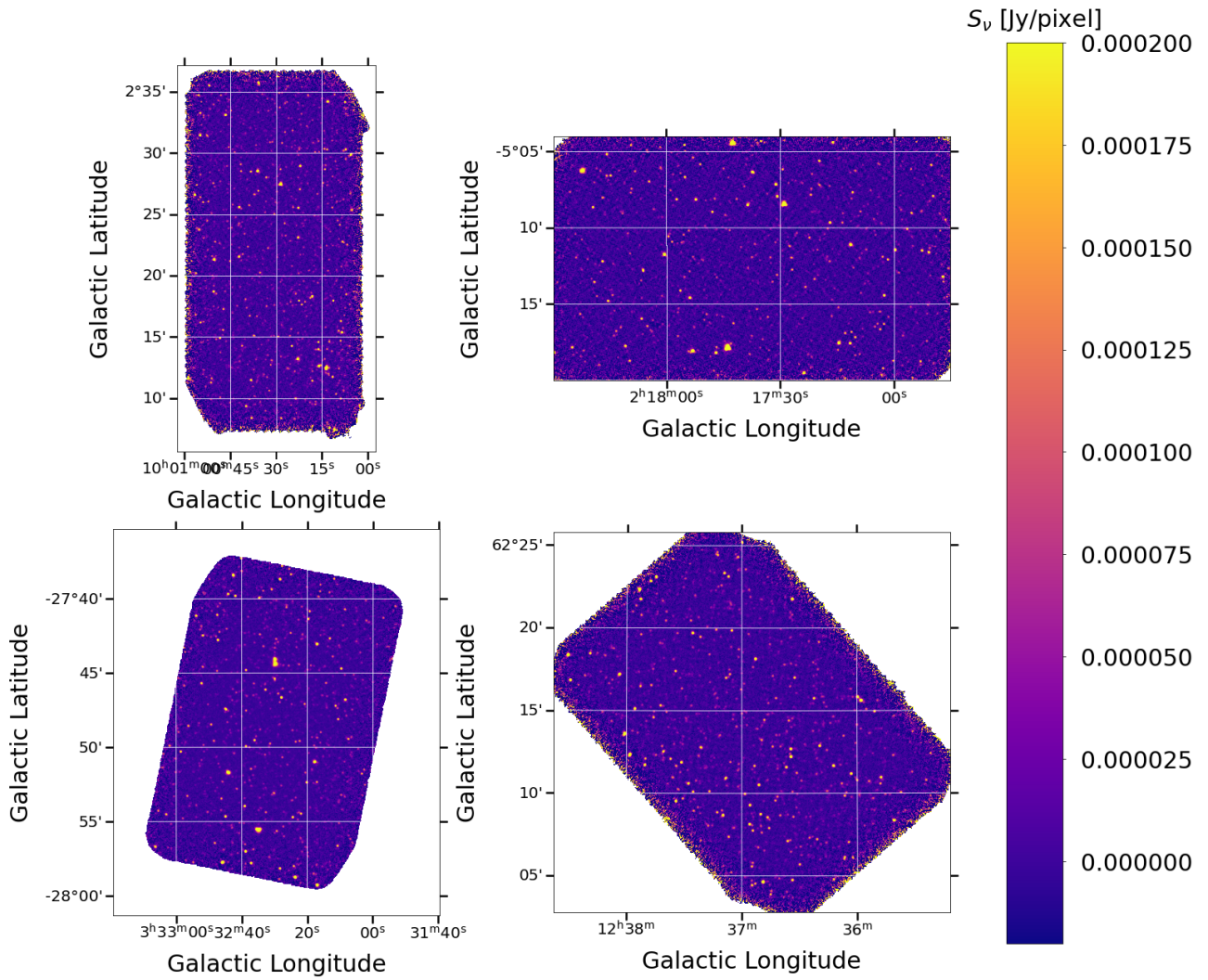


Figure 2.3: CANDELS fields maps at $100\mu\text{m}$. Top left: COSMOS field. Top right: UDS field. Bottom left: GOODS South field. Bottom right: GOODS North field.

CHAPTER 3

GALAXY STACKING

3.1	The stacking method in theory	26
3.2	Mean or median stacking?	26
3.3	The mean stacking method in practice	27
3.3.1	How to group galaxies into bins?	27
3.3.2	How to deal with detected/undetected sources?	30
3.3.3	How to deal with a possible gradient in maps?	30
3.4	How to measure flux densities?	31
3.4.1	<i>Herschel</i> : Clustering bias and PSF fitting method	31
3.4.2	How to deal with clustering bias in <i>Herschel</i> bands	32
3.4.3	<i>Spitzer</i> and ALMA: the aperture photometry method	37
3.4.4	How to measure the signal-to-noise ratio?	39
3.5	The mean stacking developed programs	39

In this chapter, I will describe the method I used to go from the raw data (i.e., the galaxy catalogues and photometry maps) to the photometry flux densities which, once fitted (see chapter 4), make it possible to deduce the properties of the galaxies (see chapter 5). I will present the stacking method and how I applied it to my dataset.

3.1 The stacking method in theory

The stacking method consists in adding the photometric images, of a single band, of several galaxies in order to increase the S/N over this population. The main goal of this method is to deduce the characteristic flux density of a population of galaxies that could not be detected individually. One way of demonstrating how stacking can be used to study galaxies with low S/N is to model each galaxy image as follows:

$$S_i(x, y) = \varphi_i \times PSF(x, y) + \omega_i(x, y), \quad (3.1)$$

where S_i is the stamp corresponding to the i^{th} galaxy, PSF the point spread function associated with the maps considered (for example, the $100\mu\text{m}$ map of the GOODS-South field), φ_i is the flux density emitted by the i^{th} galaxy and $\omega_i \sim \mathcal{N}(\mu, \sigma^2)$ the i^{th} realisation of a Gaussian noise of mean μ and standard deviation σ . One could always go back to the case where $\mu = 0$ by simply applying an offset, so I will assume that $\mu = 0$ from now on. Each of these galaxies has $S/N_i = \varphi_i/\sigma$. By stacking the images of N of these galaxies, one obtains the following:

$$\sum_{i=1}^N S_i(x, y) = \sum_{i=1}^N \varphi_i \times PSF(x, y) + \sum_{i=1}^N \omega_i(x, y). \quad (3.2)$$

In the case that galaxies stacked are similar we can reasonably assume that $\varphi_i \sim \varphi_0$ for all i , and therefore that the total part of the flux density can be approximated to $\sum_{i=1}^N \varphi_i \sim N \times \varphi_0$. Now taking X and Y following $X, Y \sim \mathcal{N}(0, \sigma^2)$, $Z = X + Y$ naturally follow $Z \sim \mathcal{N}(0, 2\sigma^2)$. From this, one can easily deduce that $\sum_{i=1}^N \omega_i(x, y) \sim \mathcal{N}(0, N\sigma^2)$ (i.e., $\sigma_{\text{stacked}} \sim \sqrt{N}\sigma$). Thus, $S/N_{\text{stacked}} = N \times \varphi_0 / (\sqrt{N}\sigma) = S/N_i \times \sqrt{N}$: the S/N has been improved by a factor \sqrt{N} .

This is a simple way to present how the stacking method can help to recover reliable flux density measurements for populations of galaxies whose S/N is too low when studied individually. This simplistic demonstration shows to the first order how stacking work. However it does not take into account some specifics of the stacking method (i.e., it can be a mean, as presented here, or a median stacking), or of the data that can represent a non uniform sample of galaxies (i.e., $\varphi_i \neq \varphi_0$ for all i) or that can include correlated noise and a non negligible signal from clustered neighbouring sources.

3.2 Mean or median stacking?

Although it may seem obvious, mean stacking consists of doing the mean of the images stacked (i.e., $\frac{1}{N} \sum_{i=1}^N S_i(x, y)$), while median stacking the median (i.e., $\langle S_i(x, y) \rangle_{i \in \{1, N\}}$, where $\langle \cdot \rangle$ is the median operation).

Median stacking has the advantage of suppressing secondary sources in the stacked stamp better than mean stacking. Figure 3.1 gives a visual example of this property. In this example, we can see that bright secondary sources still appear in the mean stacked stamp, whereas they are mostly absent from the median stacking one. The secondary sources on the stacked image can make it much more difficult to recover the stacked flux density because they can bring contamination to the central source. This effect is most noticeable when a small number of sources are stacked together, as bright neighbouring galaxies can dominate. Median stacking could allow to recover reliable flux densities from a fainter population where mean stacking would not (because of large secondary sources in the stacked image, for example).

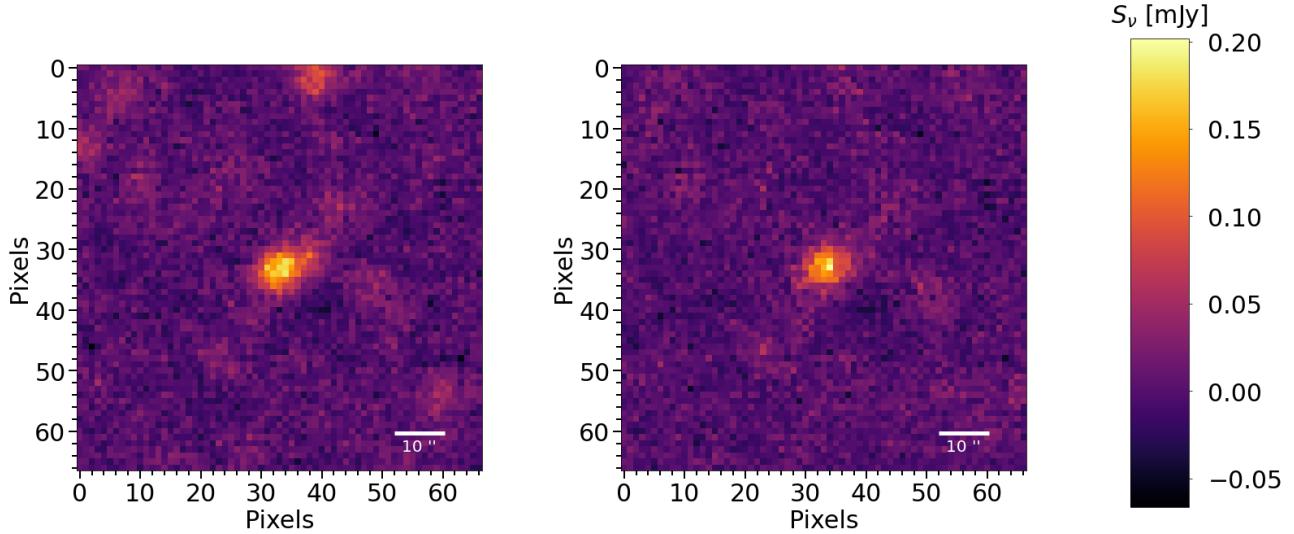


Figure 3.1: Stacking galaxies with $0.1 \leq z \leq 0.4$ and $\log_{10}(M_\star/M_\odot) \geq 11$ in the $100\mu\text{m}$ band of *Herschel*. Left: mean stacking. Right: median stacking.

However, it has been shown that median stacking also leads to systematically biased measurements at low S/N or in the presence of a flux density distribution biased towards low or high values (White et al. 2007; S15). It comes from the fact that the median is not a linear operation: $\langle a + b \rangle \neq \langle a \rangle + \langle b \rangle$. S15 shows, using a Monte Carlo analysis, the extent of this bias (see Fig. 3.2). These simulations basically generate a median stacking while assuming a given input flux distribution. As shown in S15, correcting for these systematic biases involves making strong assumptions about the actual flux density distribution (which is unknown by definition) of the stacked sources, which is non-trivial and highly uncertain. In contrast, mean stacking has no such biases because averaging is a linear operation.

Finally, the mean stack gives us access to the total flux density in the stack, which I currently miss to infer properties such as ρ_{SFR}^{IR} and then ρ_{SFR} . For these reasons, mean stacking is the preferred method for our analysis.

3.3 The mean stacking method in practice

In this section, I will review the steps I took to stack galaxies for this study. I will emphasise several points that should be borne in mind during this process, such as: how to construct the bins (i.e., how to regroup galaxies), how to deal with detected/undetected sources, how to deal with a possible background gradient in the maps, how to measure the flux densities, and finally, how to deal with the clustering bias.

3.3.1 How to group galaxies into bins?

As mentioned earlier, an effective way to take advantage of the stacking method is to group galaxies into sub-populations with similar properties. In this way, the flux densities deduced from stacking

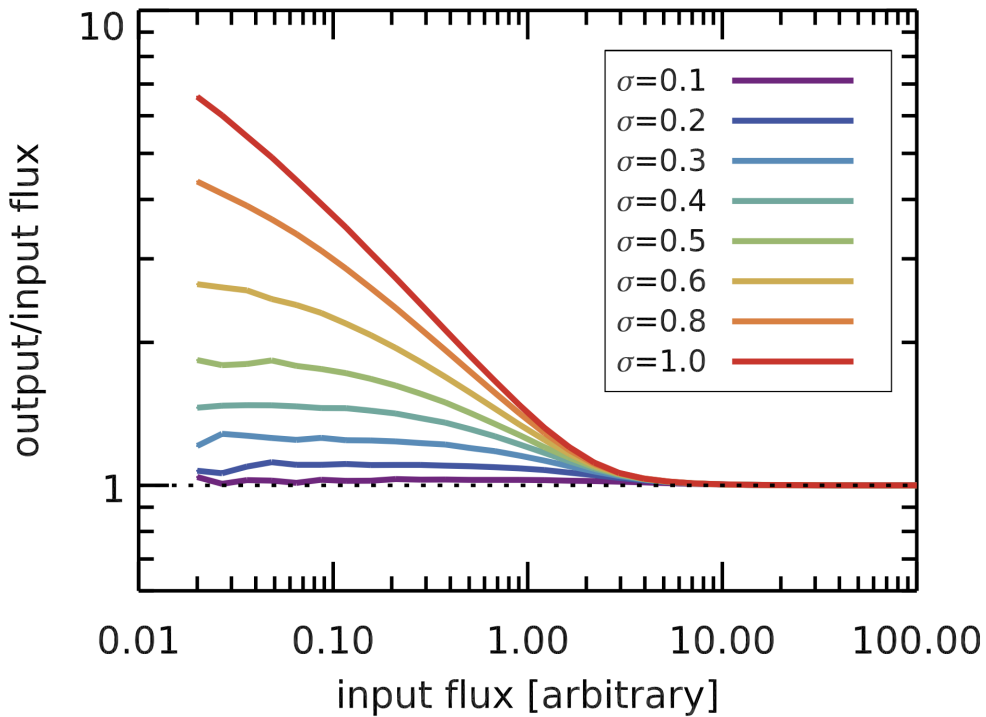


Figure 3.2: Monte Carlo analysis showing evidence for a systematic bias in median stacking. Coloured lines represent the results obtained by computing the medians of log-normally distributed flux in the presence of different Gaussian noise of fixed amplitude σ . Credit: [Schreiber et al. \(2015\)](#).

should be a close approximation to the whole stacked population. The aim of my analysis is to deduce the evolution of galaxy properties over time (i.e. the evolution with redshift) and M_\star . The mean stacking will therefore help me to measure the properties of galaxies with a lower M_\star and a higher redshift than what individual detection would allow. To this end, in this study, I stacked my sample of galaxies over different redshift and M_\star bins. The total number of galaxies per bin is displayed in the Table 3.1.

A good way to build these bins is to follow a few guidelines:

- The galaxies stacked together must be similar in some way (i.e. a similar redshift and M_\star in our case), so that the stacked output flux density makes sense to be associated with the stacked population of galaxies.
- The ideal would be to have as many bins as possible. However, a bin provides little information if one is unable to detect the stacked flux density reliably (i.e. only an upper limit). A compromise must therefore be found between the number and size of bins.
- When creating redshift bins, it is important to bear in mind that redshift is already a logarithmic measure of time: my first redshift bin ($0.1 \leq z \leq 0.4$) already accounts for ~ 3 Gyr, whereas the last one ($3.9 \leq z \leq 5.0$) accounts for ~ 0.4 Gyr only. In the best of cases, it would be desirable to have short redshift bins at low redshift to limit the time span corresponding to each bins. This can be difficult to manage while trying to have a large enough sample of galaxies to

Table 3.1: Number of galaxies in each bin of M_{\star} and redshift for the stacking in the *Herschel* 100 μm , 160 μm , 250 μm , 350 μm and 500 μm bands, and for the stacking in the ALMA band are displayed in the top and bottom row of each cell, respectively. The two axes represent the boundaries of the bins in redshift and M_{\star} . Bins with a FIR, and a submillimeter stack detection are highlighted in shaded blue and red, respectively. Bins that are mass complete are noted with a black bar.

	$\log_{10}(M_{\star}/M_{\odot})$					
	8.5	9.5	10	10.5	11	12
Redshift	0.1	0.4	0.7	1.0	1.3	1.8
0.1	999 86	197 10	109 13	49 3	5 1	
0.4	3,178 298	703 67	445 56	191 21	38 7	
0.7	5,019 403	1,567 98	837 71	388 21	80 5	
1.0	5,090 382	1,595 115	788 70	359 44	96 10	
1.3	9,929 905	2,767 188	1,392 86	605 47	167 10	
1.8	3,565 410	1,908 145	1,112 83	569 47	257 17	
2.3	3,469 475	2,324 187	1,254 125	516 55	171 16	
3.1	1,457 352	1,087 115	691 55	181 7	57 3	
3.9	611 131	423 69	362 35	131 10	29 2	
5.0						

obtain a stacked detection. In any case, this should always be borne in mind when interpreting the results: the corresponding population extends over a much longer period at low redshift.

- Finally, although it is not the most important factor and can sometimes be overlooked, it is worth trying to find out which bins have been chosen in the literature, as this will make it much easier to compare results. For example, comparing the evolution of one property of galaxies, between $1.0 \leq z \leq 1.2$, whereas the literature displays it between $0.9 \leq z \leq 1.1$ and $1.1 \leq z \leq 1.3$ is tricky, because the interpolation is probably not trivial.

3.3.2 How to deal with detected/undetected sources?

During the stacking procedure, it is possible to treat detected and undetected galaxies separately. The main way to do this is to stack only the undetected sources on the residual map (i.e., the original map from which the contribution of the detections has been removed), and then add them to the flux densities of the detected galaxies using a weighted mean (e.g., Magnelli et al. 2009). Although this method reduces the confusion noise from faint sources and removes most of the contamination from bright neighbours, it can also introduce some bias (S15). One of the problems can be the creation of artefacts on the residual map when the flux of detected sources is not correctly subtracted. These artefacts can then contaminate the stack of undetected sources. Following S15, I have therefore chosen to treat detected and undetected sources in the same way for consistency reasons (i.e. directly from the image and not from the residual).

For *Herschel*-PACS, it was shown that the high-pass filter data reduction technique that was used to remove low-frequency noise in the maps could induce an underestimation of the photometric measurements of the unmasked faint sources (Popesso et al. 2012; Magnelli et al. 2013). A correction factor of 17%, and 10% should be taken into account when stacking undetected, and detected sources in the PACS maps ($100\,\mu\text{m}$ and $160\,\mu\text{m}$), respectively.

3.3.3 How to deal with a possible gradient in maps?

Throughout my study, I noticed the presence of a global background gradient in most *Herschel* images. The effect is most noticeable in images of the COSMOS and GOODS-North fields (see left panel of Fig. 3.3). In general, I have observed that the gradient also becomes larger with increasing wavelength. Even when stacking on four fields, the effect can still dominate and prevent stacked flux densities from being detected correctly: as shown in Fig. 3.3 this particular bin looks very different when the gradient is removed. The bin shown in Fig. 3.3 would not yield a 3σ detection when stacking in all four fields if the gradient were not taken into account, but would if it is.

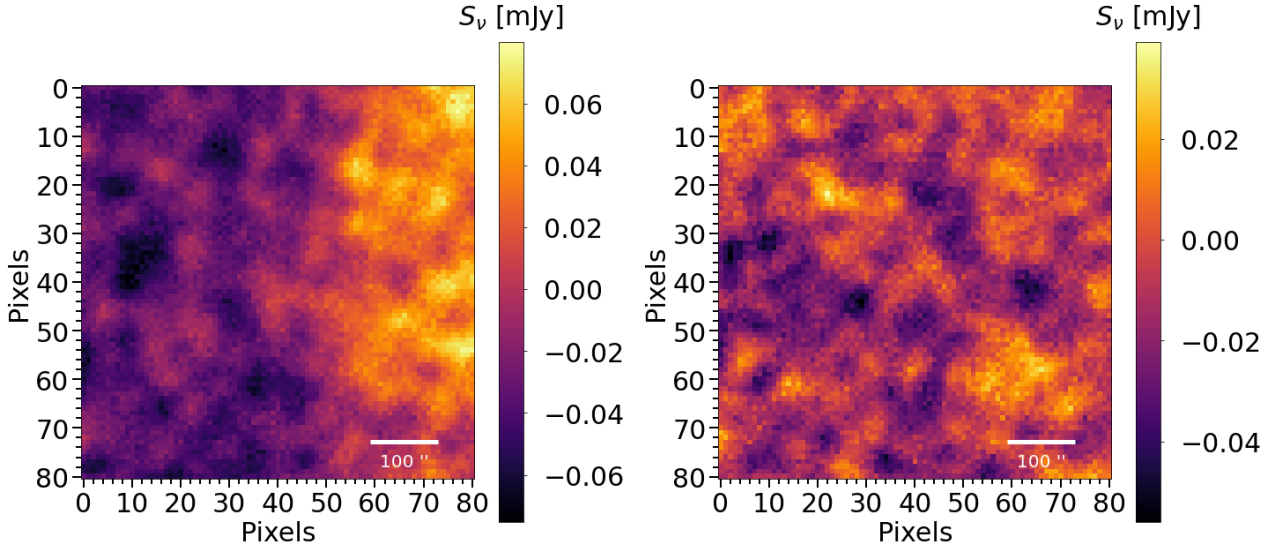


Figure 3.3: Left panel: Example of gradient in a stack in the COSMOS field at $500\mu\text{m}$ of galaxies with $2.3 \leq z \leq 3.1$ and $10.0 \leq \log_{10}(M_\star/M_\odot) \leq 10.5$. Right panel: stack but after having dealt with the gradient in the map.

In order to deal with it, I have decided to rotate the stacked postage stamp images successively by 90° . Of course, the gradient will be completely eliminated if only a multiple of four images is stacked. However, this possible residual gradient is negligible when many galaxies are stacked (i.e., several hundred or thousand), which is precisely when the gradient starts to have an impact on the stack and needs to be removed.

3.4 How to measure flux densities?

In this section, I will review the different methods available, and explain my preferred method, in each band, for measuring flux density from the stacked image. I will also discuss an important bias that can arise when stacking galaxies: the clustering bias. Then, I will present how to deduce the S/N .

3.4.1 *Herschel*: Clustering bias and PSF fitting method

When stacking galaxies, a "clustering bias" can occur due to the galaxies physically associated with the main stacking targets. Such contamination from these true neighbouring sources (as opposed to random projection alignment) can become significant when the size of the PSF becomes comparable to the typical cluster length of SFGs. It has been shown that the clustering bias has a non-negligible impact when stacking galaxies in the *Herschel* bands (e.g., [Bavouzet et al. 2008](#); [Béthermin et al. 2010b](#); [Kurczynski & Gawiser 2010](#); [Bourne et al. 2012](#); [Béthermin et al. 2012](#); [Viero et al. 2013](#); [Béthermin et al. 2014](#); [Magnelli et al. 2014](#); [S15](#); [Béthermin et al. 2015](#), hereafter B15; [Delvecchio et al. 2021](#)) due to the large PSF of *Herschel*. We can see in Fig. 3.4 that correcting for this bias is crucial to accurately measuring the SED peak of SFGs, as this bias tends to cause an overestimation of *Herschel* flux densities with increasing wavelength (as the size of the PSF increases with wavelength).

In this study, I have an ALMA measurement that lies on the low frequency tail of the dust emission, which reduces the chances of overlooking this bias: not correcting for it will probably lead to a poor SED fit with a best fit that struggles to reconcile both *Herschel* and ALMA flux density measurements. However, in the absence of ALMA measurements, such a bias could go unnoticed, giving rise to reasonable χ^2 associated with SED with a dust temperature biased towards cold values.

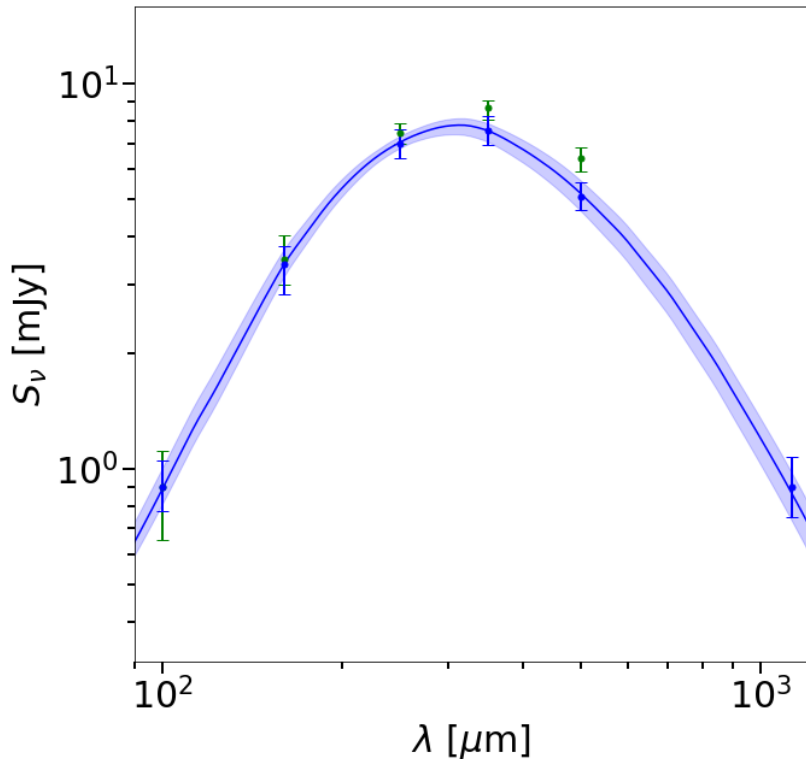


Figure 3.4: Flux density measurements for galaxies with $2.3 \leq z \leq 3.1$ and $11 \leq \log_{10}(M_\star/M_\odot) \leq 12$. Green dots correspond to the *Herschel* flux density measurements with no clustering bias correction. Blue dots correspond to the flux density measurements from this work corrected from the clustering bias. Blue line is the best fit SED, the blue shaded area shows the 68% uncertainty of the fit.

3.4.2 How to deal with clustering bias in *Herschel* bands

In this section, I will examine two different methods, both using PSF fitting, that can correct for the clustering bias and recover a reliable flux density measurement when stacking the *Herschel* bands. After briefly introducing the PSFs used and the high-pass filtering problem, I will first present the method I used throughout my study, then the alternative method, and finally I will compare the two and argue my choice.

How I dealt with the clustering bias in this study

To mitigate the contamination of the clustering signal, I choose to follow the method presented in [S15](#). It consists in fitting the stacked image with a PSF and a local background:

$$S(x, y) = \varphi \times PSF(x, y) + \varepsilon, \quad (3.3)$$

where φ and ε are the normalisation of the source flux density and background, respectively. The fit is performed considering all pixels within a fixed aperture of radius $r_{AP} = 0.9 \times \text{FWHM}$, as this was found to minimise the clustering contamination to φ ([S15](#)). The clustering bias signal is in this case largely included in the background term. Nevertheless, even with this radius, the contamination of φ is not null and I still need to apply a correction for what remains of the clustering signal in the mean flux density term (φ). These additional correction factors were calculated, in [S15](#), by simulating the stacking procedure on mock images (see [S15](#) for more details). The correction factors of [S15](#) are listed in Table [3.2](#).

Table 3.2: Clustering bias correction factor from [S15](#)

Wavelength (μm)	Correction
100	$0\%^{+7\%}_{-7\%}$
160	$3\%^{+9\%}_{-8\%}$
250	$8\%^{+12\%}_{-8\%}$
350	$13\%^{+12\%}_{-10\%}$
500	$25\%^{+19\%}_{-18\%}$

It should be noted that the additional correction factors listed in the Table [3.2](#) are median values, and variations around these values should be expected in any given of our stacked bins. However, when a large number of galaxies are stacked, they should accurately mitigate the clustering signal.

In the following sections of this chapter, I will refer to this method to correct the clustering bias as the method from [S15](#).

An alternative method to deal with clustering bias

Alternatively, one can model the stacked image as a central point source with the mean flux density of the underlying population of interest, a clustering component convolved with the PSF, and a local background term. Following [B15](#), we can attempt at separating these components via a simultaneous fit in the stacked images ([Béthermin et al. 2012; Heinis et al. 2013, 2014; Welikala et al. 2016; Delvecchio et al. 2021](#)):

$$S(x, y) = \varphi \times PSF(x, y) + \psi \times (PSF \otimes w)(x, y) + \varepsilon, \quad (3.4)$$

where $S(x, y)$ is the stacked image, PSF the point spread function, w the auto-correlation function, the symbol \otimes represents the convolution, and the parameters φ , ψ , and ε are the free normalisation

of the source flux density, clustering signal and background term, respectively. The form of the auto-correlation function is chosen following Béthermin et al. (2010a,b):

$$w(\theta) = \left(\frac{\theta}{\text{deg}} \right)^{-0.8}, \quad (3.5)$$

where θ is the distance from the centre of the image. $w(\theta)$ represents the expected average probability position distribution of neighbouring sources due to clustering. The fit is performed considering all pixels within a fixed aperture.

In the following sections of this chapter, I will refer to this method to correct the clustering bias as the method from B15.

Why I chose the method from S15

It may come as a surprise that I have chosen the method from S15 which relies primarily on simulations and median coefficient to remove the clustering bias. As I said above, this method may struggle to remove the right amount of clustering signals occasionally, but on average it should perform just right. In contrast, the method from B15 fits directly the clustering bias and should have no problem removing the correct amount of clustering. So why that choice?

When I first tried to correct for clustering bias, I considered the method from B15: including clustering as a separate term in the fit seemed to be the best way to get rid of it. However, I came across a few issues that made me reconsider the preferred method of dealing with clustering bias.

First of all, I realised that while the method from B15 can give excellent results when many galaxies are stacked, this is not the case when only a few are stacked. This is because the term used in Eq. 3.4 to fit the clustering bias (i.e., $(PSF \otimes w)(x, y)$) is an idealised mathematical version of the clustering signal that becomes true when the number of stacked galaxies goes to infinity. It is easy to imagine that when 5 galaxies are stacked (I am taking an extreme case here to illustrate my point, but it is also true when a few dozen galaxies are stacked), the clustering signal could just be a few scattered secondary sources close to the main source of the stack. As a result, the clustering signal looks nothing like $(PSF \otimes w)(x, y)$, which results in a rather poor fit when using Eq. 3.4. In such a situation, the method from (S15), on average, does a better job.

Secondly, I realised that for my sample, although the flux density component (i.e., $\varphi \times PSF(x, y)$) was robustly constrained by the method from B15, this was not the case for the clustering bias (i.e., $(PSF \otimes w)(x, y)$) and background (i.e., ε) components. In Fig. 3.5, it can be seen that the flux density component is well constrained and in fact agrees within the uncertainties with that obtained with the method from (S15) in this case. However, the clustering and background bias components vary considerably. This is because these two components are difficult to distinguish in small apertures. The distinction is easier in large apertures, because $PSF \otimes w$ goes to zero as we move away from the centre of the stack, and only the background remains. So why not just fit in large aperture? A larger aperture means that more noise is allowed in the fit while very few signal (i.e., information) is added at large radii, resulting in a lower S/N . This would not be a problem if the stack had a very high S/N to begin with; in that case, it would be sufficient to opt for a large aperture. Nevertheless, this high S/N scenario is rarely encountered.

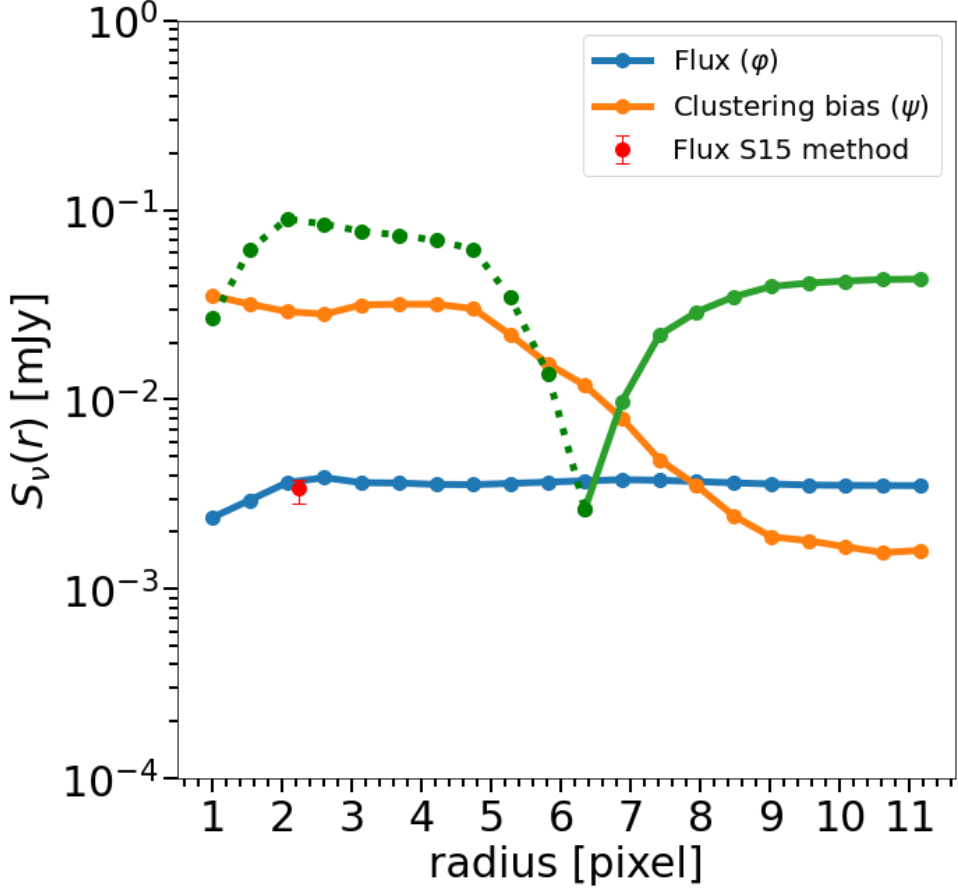


Figure 3.5: Blue, orange and green dots represent the flux density, clustering bias and background components, respectively (see Eq. 3.4) for the bin of galaxies with $2.3 \leq z \leq 3.1$ and $11 \leq \log_{10}(M_*/M_\odot) \leq 12$ at $350\mu\text{m}$, as a function of the aperture radius within which the fit was performed. Dotted and solid green lines represent a negative and positive background, respectively. Red points represent the flux density computed through the method from (S15) and used later on in my study.

Finally, the method from B15 occasionally tends to confuse the component (i.e., $\varphi \times PSF(x, y)$) with the clustering signal (i.e., $\psi \times (PSF \otimes w)(x, y)$). In Fig. 3.6, we can see that the method from B15 removed much more signal from the flux density component than the method from (S15), even at $100\mu\text{m}$ and $160\mu\text{m}$ where the clustering should have only a minor effect due to the size of the PSF. This problem occurs when stacking a medium amount of galaxies (i.e., $\sim 40 - 100$), and could be due to the fact that, again, the clustering signal does not exactly match the form of $(PSF \otimes w)(x, y)$. In these scenarios, the resulting stacked galaxy appears cooler.

Let us summarise:

- When very few galaxies are stacked, the two methods struggle. However, the method from (S15) should provide, on average, the correct flux density.
- Although the method from B15 can disentangle clustering signal and background in theory, it does not translate into practice at least for my sample. I ultimately have little interest in knowing

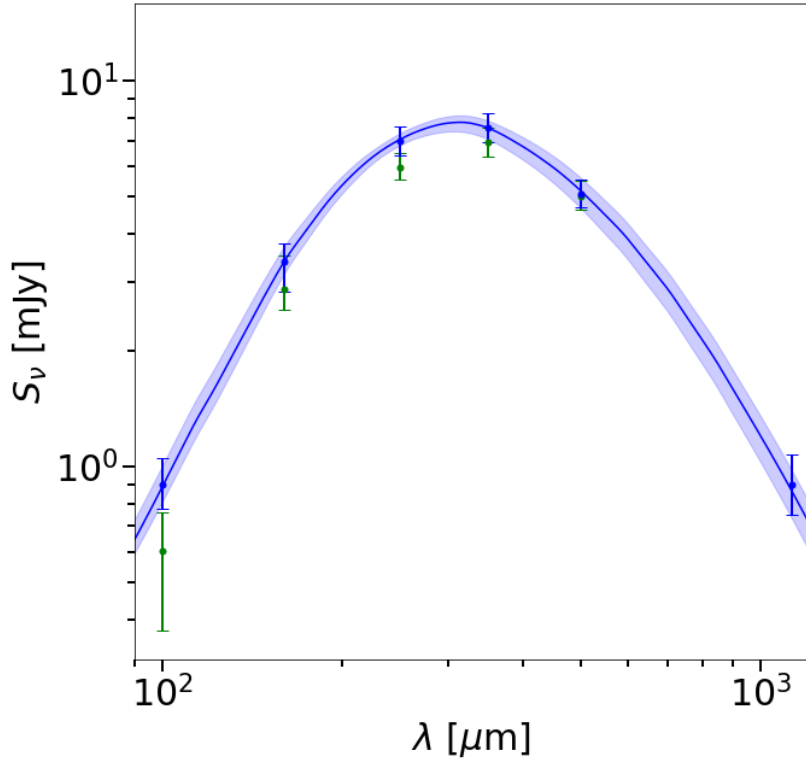


Figure 3.6: Flux density measurements for galaxies with $2.3 \leq z \leq 3.1$ and $11 \leq \log_{10}(M_\star/M_\odot) \leq 12$. Green dots correspond to the *Herschel* flux density measurements using the method of B15 to correct for the clustering bias. Blue dots correspond to the flux density measurements from the method of (S15) to correct for the clustering bias. Blue line is the best fit SED, the blue shaded area shows the 68% uncertainty of the fit.

the relative strength of the clustering signal and background, as long as I get the correct flux density of the stacked sources. There is, therefore, little need to fit them.

- There is, occasionally, some confusion between the flux density component (i.e., $\varphi \times PSF(x, y)$) and the clustering signal (i.e., $\psi \times (PSF \otimes w)(x, y)$) when using the method from B15

For all these reasons, I have chosen to deal with the clustering bias by using the method from (S15), which seems more reliable on average and in practice for my study. It should be noted, however, that when stacking several thousand galaxies and obtaining a very high S/N stacked signal, the method from B15 should be favoured over the method from (S15).

I still consider the clustering bias correction to be the main source of uncertainty and potential error in the main study I conducted during my PhD. This could be the cause of some discrepant results with the literature, as those did not necessarily use the same method to deal with clustering biases. However, I am confident that the method I have chosen to correct the clustering bias is the most appropriate to this study and that conclusions resulting from the stacking analysis can be trusted.

3.4.3 *Spitzer* and ALMA: the aperture photometry method

The ALMA 1.1mm map has a much better resolution ($\sim 1''.1$ PSF FWHM) than *Herschel*-PACS ($\sim 7''$ and $\sim 11''.3$ PSF FWHM at $100\mu\text{m}$ and $160\mu\text{m}$, respectively). The $24\mu\text{m}$ MIPS-*Spitzer* map ($\sim 5''.8$ PSF FWHM) has a better resolution than *Herschel*-PACS ($\sim 7''$ and $\sim 11''.3$ PSF FWHM at $100\mu\text{m}$, and $160\mu\text{m}$, respectively). Thus, I do not expect the clustering bias to be a dominant effect on the stacked stamp for either MIPS and ALMA.

The aperture photometry method simply consists in measuring the flux density within an aperture (i.e., summing all the pixels inside the aperture after having eventually removed a constant background). The simplest way to define the aperture is to take it to be circular with a radius r_{AP} . This method is particularly suitable when considering unresolved or barely resolved sources, which is the case in all the bands considered here, as we do not have to worry about the morphology of the sources. MIPS is unresolved and ALMA is at the limit of source resolution.

At this point, a reasonable question arises: how to choose the radius r_{AP} ? Let us consider the case of my ALMA stacking sample. There are several aspects to consider when varying r_{AP} . Firstly, the greater the r_{AP} , the greater the incoming flux density from the source inside the aperture. We therefore want r_{AP} to be as large as possible, because it increasingly reduces the correction needed to account for this missing flux. Secondly, due to the shape of the PSF, as we can see in Fig. 3.7, the growth curve flattens out at a certain point: here, the inflection point is $\sim 0''.7$. This means that as r_{AP} increases, you will get less and less additional flux density from the source. As a result, you may even reach a point where you are adding more noise than source flux density to your aperture. To illustrate this effect, I picked my ALMA stacked bins with a high S/N (i.e., $S/N \geq 10$), and tracked the evolution of the $S/N / S/N_{\text{max}}$ with r_{AP} . Figure 3.7 shows that up to $r_{\text{AP}} \sim 1''$ the $S/N / S/N_{\text{max}}$ was fairly constant, but then started to decrease due to the addition of more noise than source flux density in the aperture. According to this type of study, a good way of optimising r_{AP} is to choose it as large as possible but before it leads to a significant drop in S/N . In this case, $r_{\text{AP}} = 1''$ seems to be a good compromise.

Now that the radius r_{AP} has been chosen, it should be borne in mind that the flux density in this radius (S_{AP}) represents only a fraction of the total flux density (S_{Tot}). The two can be linked by a relationship of the type $S_{\text{AP}} = \alpha \times S_{\text{Tot}}$. In the case where the source is unresolved, we will simply observe a point source convolved with the PSF. This is precisely why the aperture photometry method is simple and effective in this case, as we can deduce α from the PSF itself, as $\alpha_{\text{AP}} = S_{\text{AP}}^{\text{PSF}} / S_{\text{Tot}}^{\text{PSF}}$.

One of the advantages of this method is its simplicity. On the other hand, as we are simply adding up all the pixels within an aperture, it is difficult to disentangle the multiple components that can contribute to the signal within that aperture, such as: source flux density, background, clustering bias. The background can be estimated at the outer edges of the stacked image because it is supposed to dominate there. On the other hand, the clustering bias has a more complex shape, and is therefore much more difficult to estimate or correct when using the aperture photometry method.

Application to ALMA

In this study, I decided to work in the image plane when dealing with ALMA. Another option would have been to work in the uv plane (i.e., in Fourier space), as ALMA measurements are made in the uv plane. Although this may give more robust results, since I would not need to go through the conversion

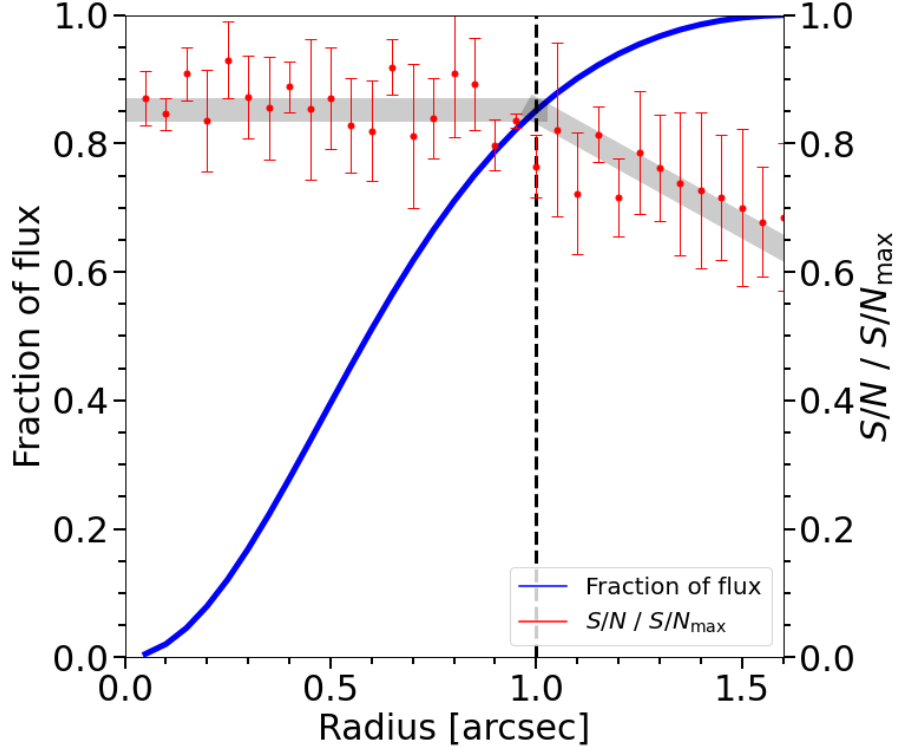


Figure 3.7: The blue curve represents the curve of growth (i.e., the fraction of flux density within a radius) of the ALMA PSF used in this work. Red points represent $S/N / S/N_{\max}$ as a function of the radius within which the aperture photometry method is performed. This example is taken from high S/N bins (i.e., $S/N \geq 10$).

between the uv plane and the image plane first, it is very computationally intensive. Furthermore, on few test bins I only observed a 10% difference between flux densities calculated from stacks in the uv and image planes. I decided not to stack directly in the uv plane but in the image plane in order to save computing time as this should not impact the results of this study.

Due to the high angular resolution of the ALMA data ($\sim 1''.1$ PSF FWHM; which is comparable to the typical sizes of individual SFGs; [Suess et al. 2019](#); [Wang et al. 2022](#)), and to possible small offsets between the optical centroids (on which our stack positions are based) and millimeter centroids, the stacked images are extended on scales larger than that of the ALMA PSF. However, this has no significant impact on the measured flux densities via the aperture photometry method. To measure ALMA flux densities, I applied an aperture photometry within a radius of $1''$, containing 85% of the total flux density (i.e., $S_{AP}^{PSF}/S_{Tot}^{PSF} = 0.85$).

Application to *Spitzer*

The flux densities are calculated using a classical aperture photometry method. The aperture is chosen to be $4''.8$ in radius, which contains about $\sim 50\%$ of the total flux density for a point source.

3.4.4 How to measure the signal-to-noise ratio?

As we saw already, for my study all flux densities are measured by aperture photometry (MIPS and ALMA) or PSF fitting (*Herschel*) over a circular aperture of radius r_{AP} . Depending on the method used to calculate the flux density, r_{AP} corresponds either to the radius used for the aperture measurement method, or to the radius in which the PSF fitting method was performed. To this radius, I can always associate a flux density S_{AP} corresponding to the flux density from the stacked sources inside this aperture (i.e., directly S_{AP} for the aperture photometry method and S_{Tot}/α_{AP} for the PSF fitting method). The S/N corresponding to these stacked sources is then calculated using a simple Monte Carlo approach, i.e., $S/N = S_{AP}/\sigma_{MC}$, where σ_{MC} is the standard deviation of the signal in 100 apertures of the same radius r_{AP} , randomly positioned on the outer edges of the stacked stamp, in a way to avoid contamination from the central stacked source.

In addition to this photometric noise, there is an uncertainty in the recovered flux density due to the intrinsic dispersion of the underlying stacked population (i.e., all galaxies in the stack do not have the exact same flux density). This flux dispersion can be quantified using a bootstrap analysis (e.g., S15). The method consists in repeating several times the full stacking and flux density measurement process, picking, for each realisation, the galaxies from the origin sample, with replacement, until the number of galaxies in the original sample is reached. In this study, we compute a 100 runs. The error is then deduced from the standard deviation of the computed flux densities for this bin. This bootstrap analysis has the advantage of taking account of the flux dispersion and photometric noise, and thus yields the total error for the stack.

3.5 The mean stacking developed programs

The code I developed in Python to perform the stacking of my sources relies on standard libraries and packages such as **numpy**, **astropy**, **photutils**, **scipy** and **emcee**. The program input are the maps and PSF for the chosen wavelength and the galaxies catalogues which are first spilt into the desired bins. Then the mean (or median) stacking is performed using a routine I developed using **numpy** package. The flux measurement part relies on the **photutils** package by using the **photutils.aperture** tools to perform aperture photometry measurements. The PSF fitting method is carried out by a sub program that uses a fitting procedure using the **emcee** library to perform fits of the PSF through a MCMC sampler to navigate the parameter space. The S/N are computed using a Monte Carlo method I developped using mostly **numpy** and **photutils.aperture** tools. I ran the stacking program on the laboratory cluster. The program runs in parallel for each bin (over 10 cores) using the **pool** Python library in a slurm environment. This main program performs the split into the desired bins and the mean stacking of my full sample from about 20 minutes to 1 hour and 30 minutes depending on the wavelength, and returns the bin information (galaxies, redshift and M_* bin boundaries) and the results of the stacking (fluxes, list of individual images, stacked images, best fit parameters, S/N).

A second code computes the error of the fluxes by bootstrapping. It is built in a similar way as the main one by following the same method as for the stacking of sources but resampling according to a bootstrap method. This second program runs in parallel for each bin (over 10 cores) using the **pool** Python library in a slurm environment. This second code can perform 100 bootstrapping on flux measurement from about 2 to 8 hours depending on the wavelength and returns the error on the flux.

CHAPTER 3

CHAPTER 4

FROM FLUX DENSITY MEASUREMENTS TO GALAXY PROPERTIES

4.1	The SED fitting procedure	42
4.2	The M_{dust} debate	45
4.3	Adding ALMA to <i>Herschel</i>	48
4.4	Looking for biases in the SED fitting procedure	50
4.4.1	Simulations to correct for averaging biases	50
4.4.2	Active galactic nuclei bias	51

In this chapter, I will describe the method I used to fit the flux measurements inferred from the stacking analysis described Chap. 3. I will compare two model libraries that can be used to fit SEDs, and introduce a conversion method between the two. I will also present the analysis of the fitting procedure in order to evaluate all possible biases that could have an impact on the galaxy properties that will be presented in Chap. 5.

4.1 The SED fitting procedure

One of the objectives of my study is to retrieve several properties such as SFR, T_{dust} , M_{dust} and M_{gas} from my FIR to submillimetre stacking analysis, and compare them to the literature. To this end, I performed an SED fit from the measured fluxes for each bin of redshift and M_{\star} . Because I do not have many points on the FIR at low M_{\star} and high redshifts, I used the library from Schreiber et al. 2018, hereafter S18, which is well suited for my study given its small number of free parameters. Choosing a model with more parameters, such as Draine & Li (2007) and Draine et al. (2014), would imply using a large set of free parameters that my limited data set would not permit to fit. In this case, we would have to correct some of them, which would lead to a situation similar to that of the direct use of models S18 with its limited number of parameters. I will compare in Sect. 4.2 that the two methods (i.e., S18 and Draine & Li 2007) are consistent.

The templates from the library of S18 are determined by five parameters: the redshift, $T_{\text{dust}}^{\text{M}}$, $\text{IR8} = L_{\text{IR}}/L_8$ where L_8 is the luminosity at $8 \mu\text{m}$, the fraction of PAH (f_{PAH}), and M_{dust} as all templates are normalised to $M_{\text{dust}} = 1 M_{\odot}$. The impact of the free parameters are displayed in Fig. 4.1, and an example of such template is given in Fig. 4.2. In addition, S18 provides a parametrisation of the IR8 parameter for the main sequence as a function of redshift,

$$\text{IR8}^{\text{MS}} = 4.08 + 3.29 \times \begin{cases} 0 & \text{if } z < 1, \\ (z - 1) & \text{if } 1 \leq z \leq 2, \\ 1 & \text{if } z > 2, \end{cases} \quad (4.1)$$

$$\text{IR8} = \text{IR8}^{\text{MS}} \times R_{\text{SB}}^{0.66}, \quad (4.2)$$

where IR8^{MS} is the IR8 for main sequence galaxies (i.e., $R_{\text{SB}} = 1$). The template are all normalised to a $M_{\text{dust}} = 1 \times M_{\odot}$. Since, I expect to recover main sequence galaxies (i.e., I can assume $R_{\text{SB}} = 1$), therefore I will use the IR8^{MS} parameterisation of S18 and be left with three free parameters: $T_{\text{dust}}^{\text{M}}$, f_{PAH} and M_{dust} .

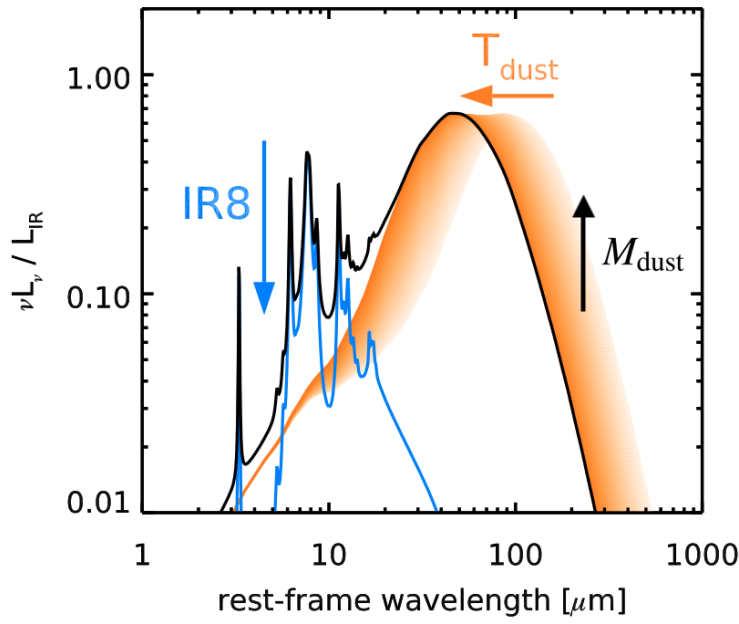


Figure 4.1: Example of templates from the S18 library. The impact of $T_{\text{dust}}^{\text{M}}$, IR8 and M_{dust} are displayed through arrows. The f_{PAH} will determine the strength of the PAH peaks. Credit S18.

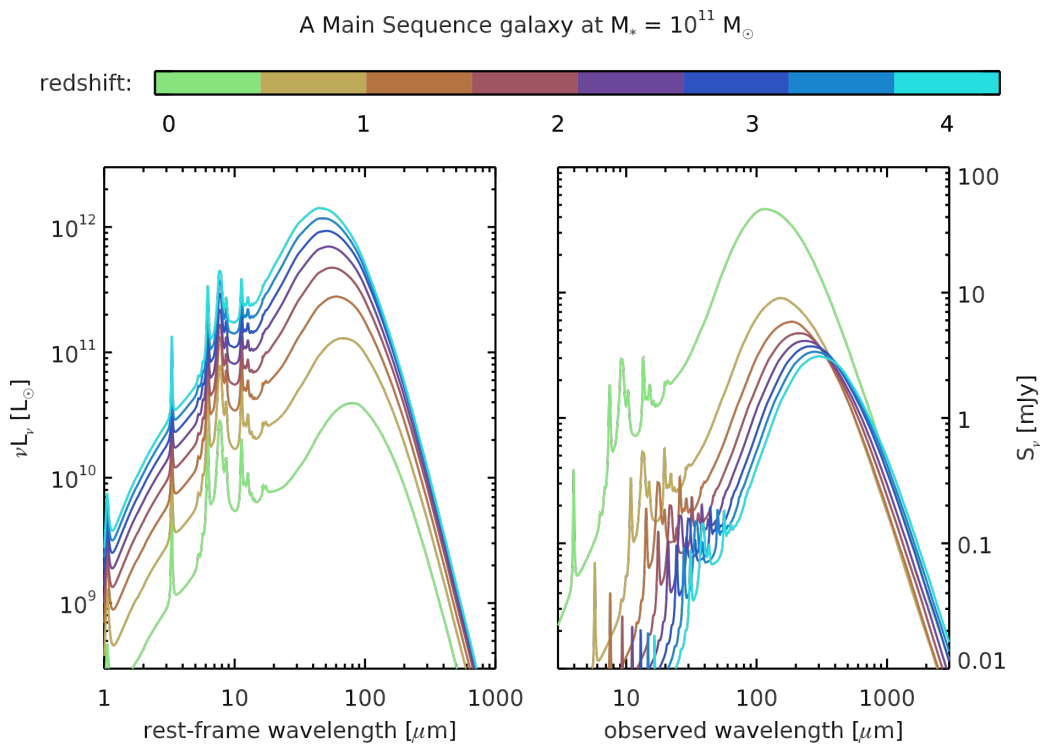


Figure 4.2: Example of a template from the S18 library for a main sequence galaxy with $M_{\star} = 10^{11} M_{\odot}$. Template are colour coded by redshift. Left: νL_{ν} as a function of the rest-frame wavelength. Right: νL_{ν} as a function of the observed wavelength. Credit S18.

The library of S18 was calibrated on galaxies, from $z = 0.5$ up to $z = 4$, which allows to have a realistic SED while reducing the number of free parameters. Note that here I have assumed no active galactic nucleus (AGN) contribution to the stacked SED. I check in Sect. 4.4.2 that this assumption is indeed correct.

To fit the SED, I only considered fluxes with $S/N \geq 3$. Stacked flux measurements with $S/N < 3$ are replaced by conservative 5σ upper limits. At $z > 4$, MIPS-24 stacked fluxes, if available, have been transformed to upper limits as they are no longer dominated by dust and PAH emissions, but rather by stellar emission. From these SED fits (see Fig. 4.4), I measured the corresponding L_{IR} by integrating the best fit SED in the range 8-1000 μm rest frame. The error on L_{IR} was obtained by varying their stacked photometry randomly within their uncertainties and repeating their SED fit.

The T_{dust} can be defined in different ways, i.e., weighted by mass or luminosity. The luminosity weighted T_{dust}^L , associated to each template of the (S18) library was calculated from a grey body of effective emissivity $\beta = 1.5$ (S18). This means that T_{dust}^L follows Wien's law:

$$T_{\text{dust}}^L [\text{K}] = 2.897 \times 10^3 / (\lambda_{\text{max}} [\mu\text{m}]), \quad (4.3)$$

where λ_{max} is the wavelength corresponding to the peak of $\lambda^\beta L_\lambda$. A mass weighted T_{dust}^M , was also calculated for each template by mass weighted averaging each individual template of Galliano et al. (2011) constituting the corresponding template of S18, i.e., T_{dust}^M is the mass weighted mean of the T_{dust}^L of each individual template template of Galliano et al. (2011). T_{dust}^L and T_{dust}^M are simply read from the best SED fit, and their corresponding uncertainties come again from varying the stacked photometry randomly within their uncertainties and repeating their SED fit. For the rest of the manuscript, I chose to work with mass-weighted dust temperatures, and we will refer to T_{dust}^M simply as T_{dust} .

In the cases where I only had one or two points to perform our fit (i.e., the SED peak was not well defined in this case), I chose to restrict the T_{dust}^M during the fit to ± 10 K from the T_{dust}^M evolution for main sequence galaxies from S18. This is a reasonable way to reduce the uncertainties on the deduced L_{IR} by slightly restricting T_{dust}^M to reasonable values.

Before fitting a flux density by the template library from S18, I took into account the transmission window of the corresponding passbands of each telescope. A flux density measurement is not a simple measurement at a fixed wavelength, but rather an integration over a wider range.

Consequently, if one wants to recover an SED more accurately from flux density measurements, the transmission windows must be taken into account. I give an example of this in Fig. 4.3. In Fig. 4.3, one can see that for the *Herschel* bands, this would have no major impact because the SED is fairly smooth at these wavelengths. On the other hand, the MIPS measurement is right in the middle of the PAH for the redshift range covered by my study. In the particular example shown in Fig. 4.3, the MIPS measurement falls right in the middle of two PAH peaks which, when viewed through the MIPS transmission window, contribute to the flux density measurement. This is why, in this case, the flux density measurement at 24 μm stands above the best fit SED. Not taking the transmission window into account would have led to a poorer fit. My best fits of SEDs for all bins stacked in this study are displayed in Fig. 4.4.

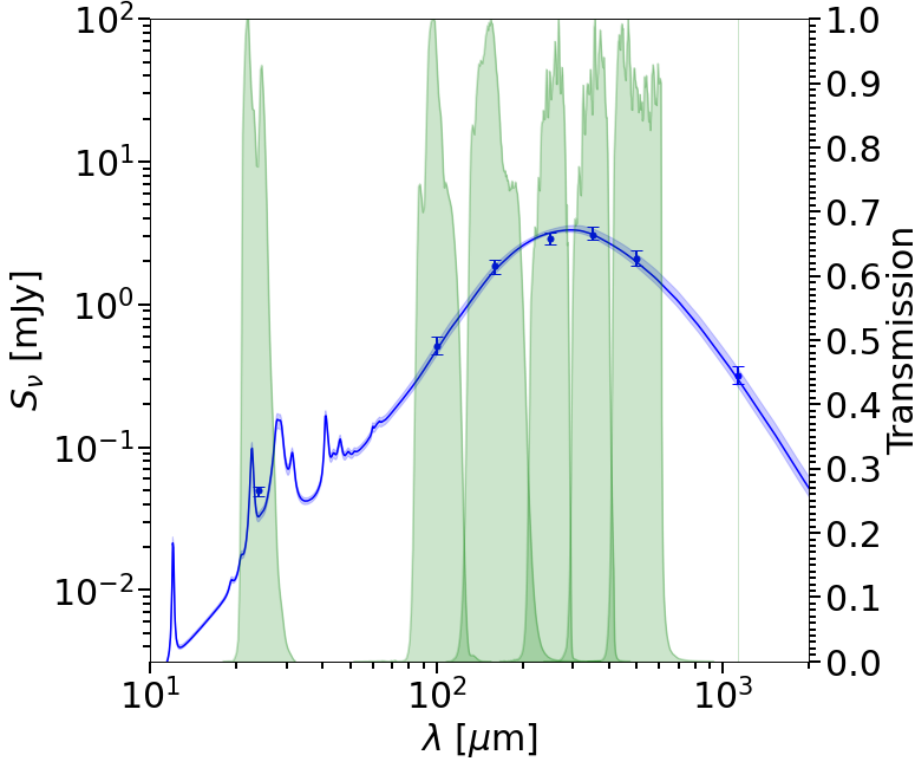


Figure 4.3: Blue dot are the stacked flux for galaxies with $2.3 \leq z \leq 3.1$ and $10.5 \leq \log_{10}(M_\star/M_\odot) \leq 11$. The blue line represents the best fit SED with the template library from S18. The blue shaded area shows the 68% uncertainty of the fit. The green areas represent the transmission window for each wavelength considered.

The Python program I developed to perform the SED fitting relies on a fit of the flux deduced from the stacking analysis by the S18 template library using the `emcee` library to perform fits through a MCMC sampler to navigate parameters space. The program returns the best fit SED, the corresponding properties (i.e., T_{dust} , M_{dust} , $L_{\text{IR}}\dots$) and their error for each bin of galaxies. The program runs on the laboratory cluster takes about 7 hours to run.

4.2 The M_{dust} debate

The templates from the library of S18 are built using the amorphous carbon model for dust from Galliano et al. (2011). This differs from the model from Draine & Li (2007) which takes into account amorphous silicate and graphite grains. This change of model was shown in Galliano et al. (2011) to lower the tension, in the Large Magellanic Cloud and the Milky Way, between the observed dust-to-gas ratio and the stellar abundances. The differences between the two models are mainly reflected in the different emissivities. The choice of a different emissivity does not affect the dust temperature or the L_{IR} , as these properties correspond to the peak and the area under the SED, respectively. The M_{dust} deduced from Galliano et al. (2011) is, in contrast, about a factor of 2 lower than the one deduced from Draine & Li (2007). However, this does not affect the value of the M_{gas} as the factor cancels out when converting M_{dust} to M_{gas} using the appropriate dust-to-gas mass ratio value.

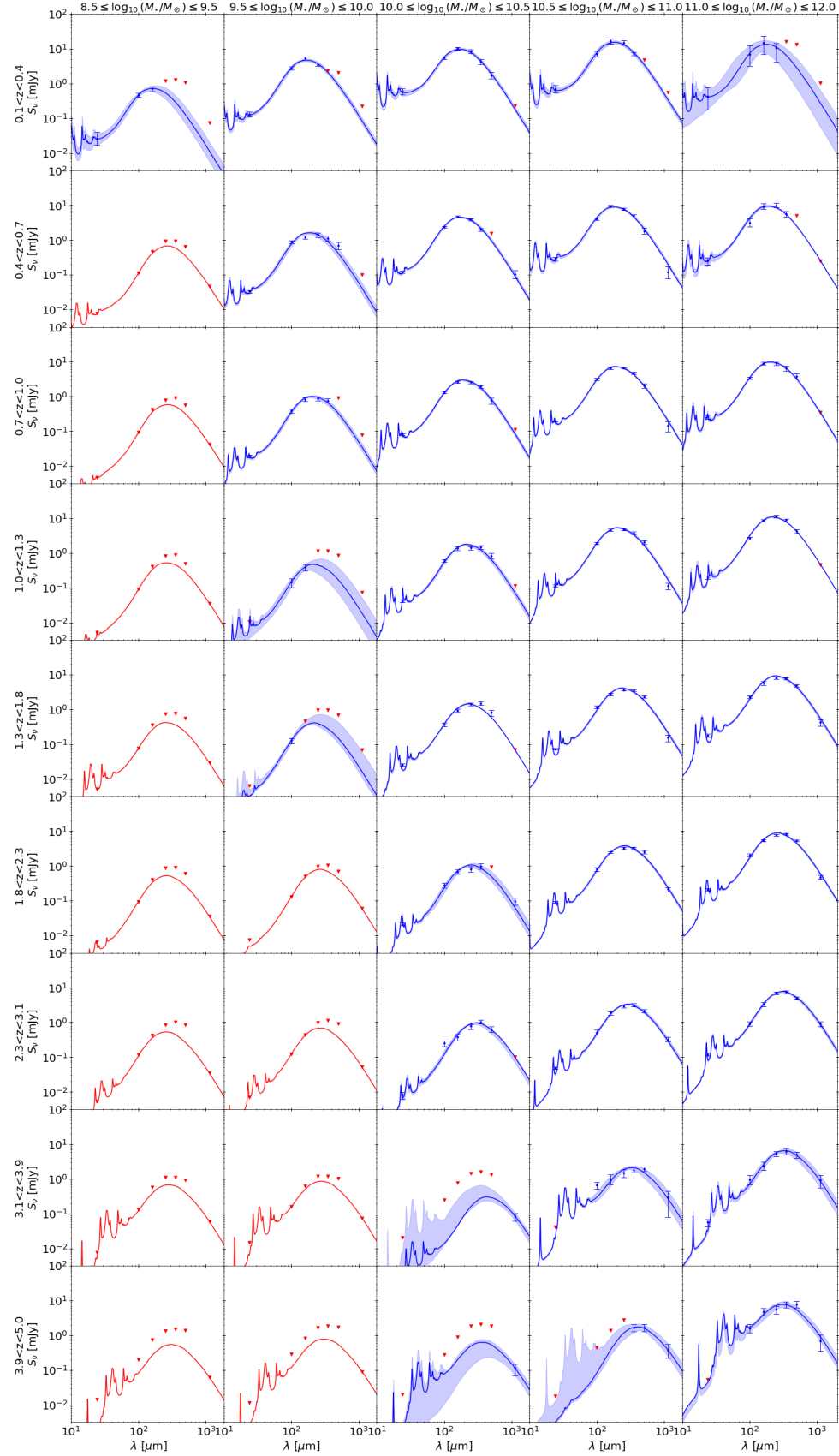


Figure 4.4: Best fit SED for each bin of redshift and stellar mass. Blue dots correspond to the flux measurements, red triangles represent the 5σ upper limits. Blue line is the best fit SED, the blue shaded area shows the 68% uncertainty of the fit. Red line is the SED maximising L_{IR} in case only upper limits are available.

I chose to work with M_{dust} derived from the [Draine & Li \(2007\)](#) model, as it will ease comparison with the literature, which is widely based on the latter model.

In practice, I have re-fitted each template of the library of [S18](#) with a [Draine & Li \(2007\)](#) model, using the code CIGALE ([Boquien et al. 2019](#)), to associate the M_{dust} . I therefore created a conversion table, which I made available, that associates each template of the [S18](#) library for main sequence galaxies (i.e., following the $\text{IR8} - z$ relation of Eq. 4.1). This is a very useful tool for people who want to use the [S18](#) library because many measurements of M_{dust} from the literature were made using the [Draine & Li \(2007\)](#) model. This facilitates comparison with the literature.

In Fig. 4.5, I present just a few values of this table. A conversion factor is given for $0 \leq z \leq 5$ (due to the redshift dependence of IR8^{MS} introduced by Eq. 4.1), $0.001 \leq f_{\text{PAH}} \leq 0.5$, and $15 \text{ K} \leq T_{\text{dust}}^M \leq 60 \text{ K}$. It can be seen that the values actually used in this study are approximately around a conversion factor of ~ 2 .

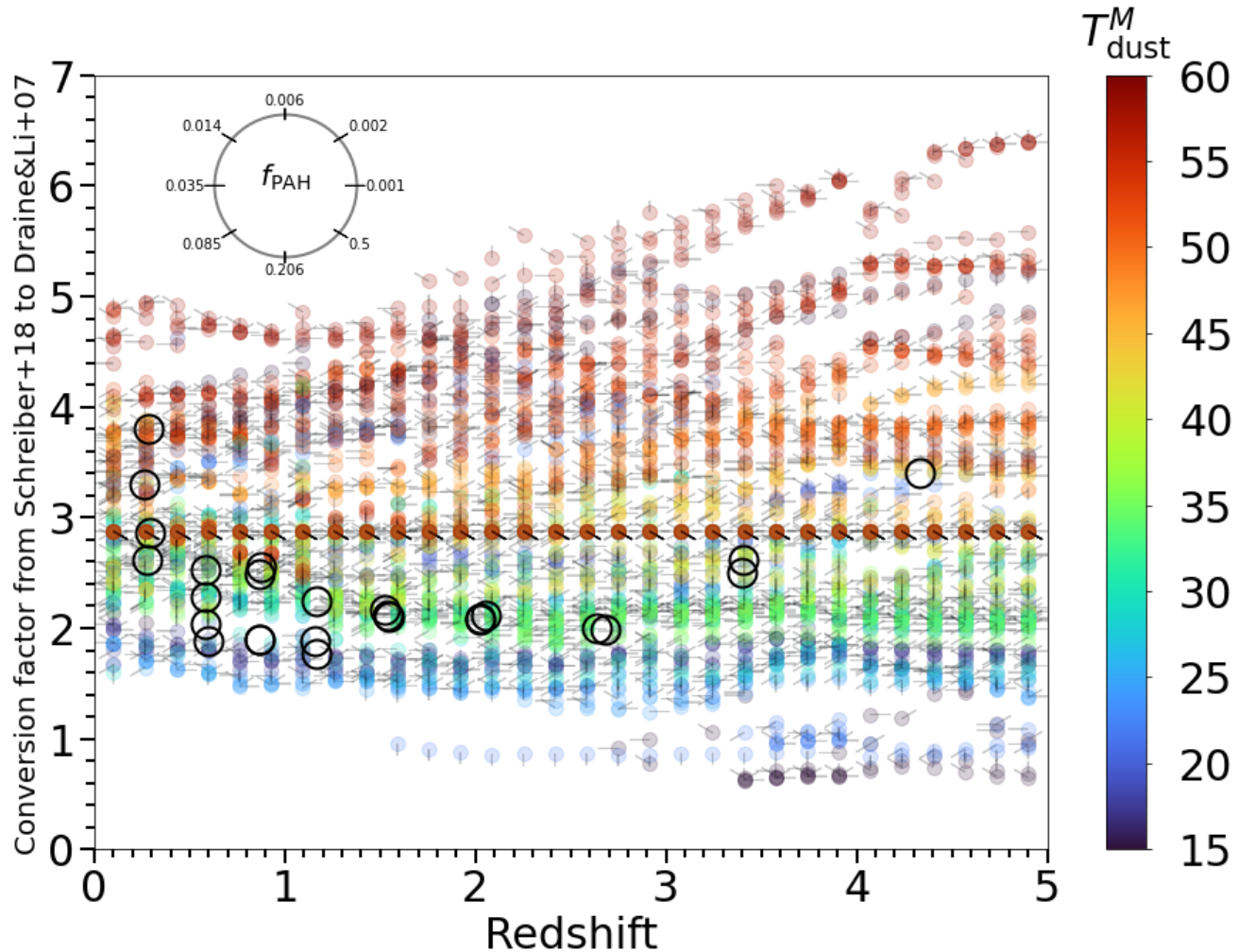


Figure 4.5: [S18](#) to [Draine & Li \(2007\)](#) conversion factor for M_{dust} as a function of redshift. The T_{dust}^M is colour coded. The f_{PAH} is indicated by a vector referring to angle from the upper left circular axis. Values used in this study are marked by a black circle.

Finally, I verified that fitting our stacked flux with the S18 or Draine & Li (2007) libraries has little to no impact on my results. Figure 4.6, shows an example comparison of the two best fits. Figure 4.6 shows no major differences between the two fits, but at the ALMA measurement (i.e., at $1130\mu\text{m}$) where the Draine & Li (2007) model tends to be slightly below the measurement. To assess the importance of this feature, I checked whether it was at the origin of certain differences in the properties of the galaxies that could be deduced from these SED. However, the differences in key properties such as L_{IR} , M_{dust} (once corrected for the emissivity chosen in S18) and $T_{\text{dust}}^{\text{L}}$ are quite small (see Fig. 4.7): $-6\%^{+6\%}$ for L_{IR} , $1\%^{+10\%}$ for $T_{\text{dust}}^{\text{L}}$, and $1\%^{+11\%}$ for M_{dust} . An essential consequence of these findings is that despite the simplicity of the S18 model compared to the Draine & Li (2007) model, it captures the essential properties (L_{IR} , M_{dust} and $T_{\text{dust}}^{\text{L}}$) of our stacked galaxies. This reinforces the choice I made to use the S18 templates instead of Draine & Li (2007) for this study.

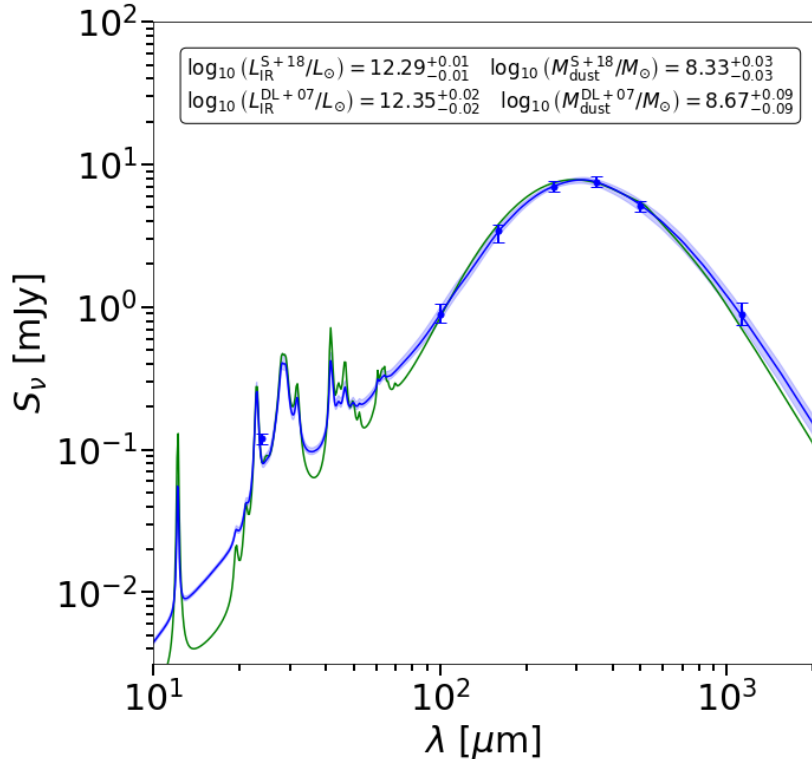
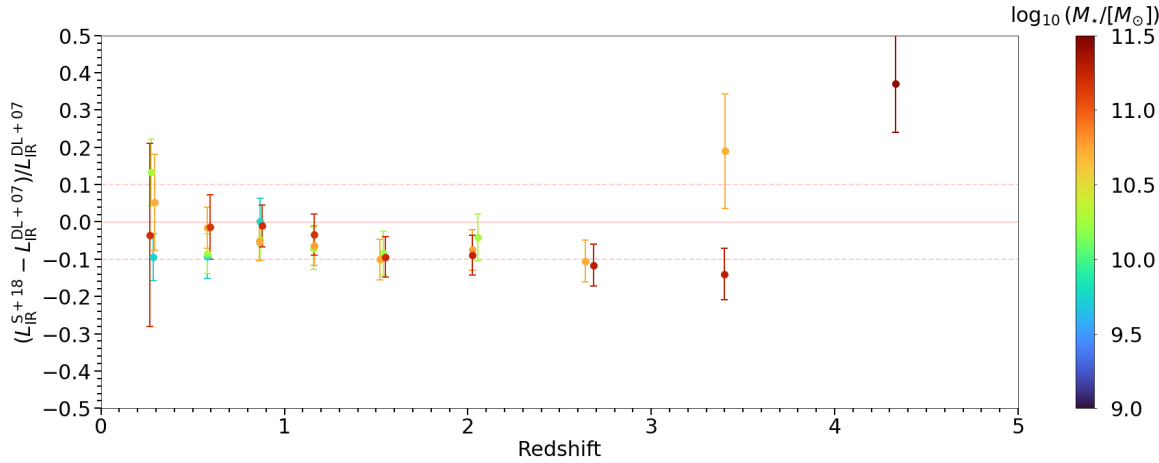


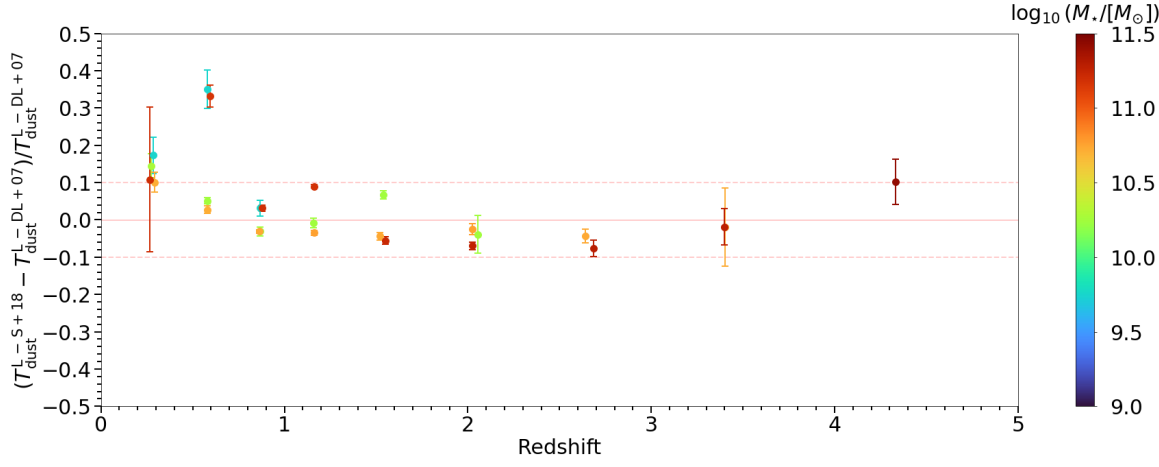
Figure 4.6: Blue dots are the stacked flux densities for galaxies with $2.3 \leq z \leq 3.1$ and $11 \leq \log_{10}(M_{\star}/M_{\odot}) \leq 12$. The blue and green lines represent the best fit SEDs with the template libraries from S18 and Draine & Li (2007), respectively. The blue and green shaded area shows the 68% uncertainty of each fit.

4.3 Adding ALMA to *Herschel*

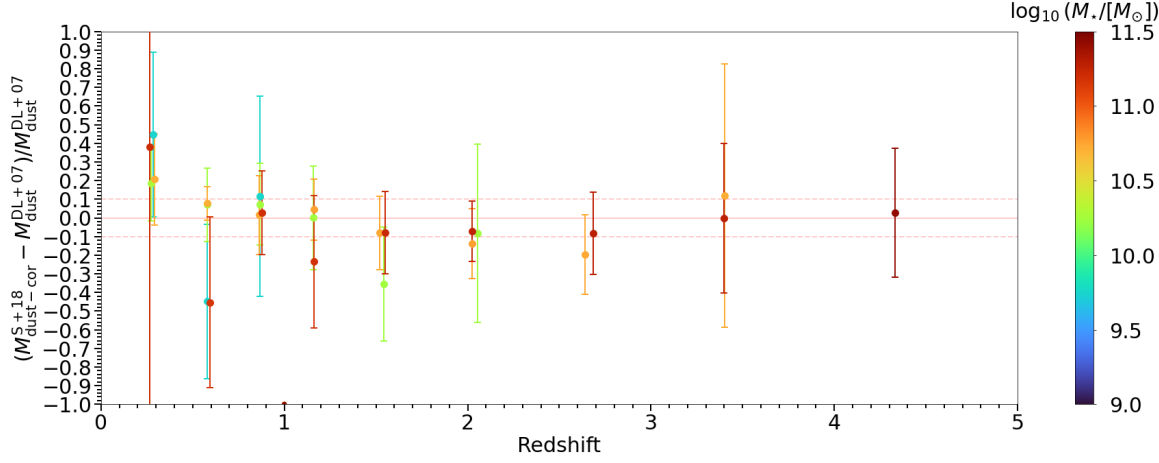
The addition of ALMA to this study results in an improvement of the SED at high redshift (i.e., at $3.1 \leq z \leq 5.0$). More specifically, it allows to get a rest-frame FIR measurement at $10.0 \leq \log_{10}(M_{\star}) \leq 10.5$ for $3.1 \leq z \leq 3.9$ and $3.9 \leq z \leq 5$ that provides information on some of the



(a) Relative comparison of the L_{IR} inferred using the [S18](#) (L_{IR}^{S+18}) and [Draine & Li \(2007\)](#) ($L_{\text{IR}}^{\text{DL}+07}$) libraries as a function of redshift and colour coded by M_* .



(b) Relative comparison of the $T_{\text{dust}}^{\text{L}}$ inferred using the [S18](#) (T_{dust}^{S+18}) and [Draine & Li \(2007\)](#) ($T_{\text{dust}}^{\text{DL}+07}$) libraries as a function of redshift and colour coded by M_* .



(c) Relative comparison of the M_{dust} inferred using the [S18](#) ($M_{\text{dust}-\text{cor}}^{S+18}$) and [Draine & Li \(2007\)](#) ($M_{\text{dust}}^{\text{DL}+07}$) libraries as a function of redshift and colour coded by M_* . $M_{\text{dust}-\text{cor}}^{S+18}$ is the M_{dust} from a fit with [S18](#) template library and corrected to correspond to a [Draine & Li \(2007\)](#) model.

Figure 4.7: Comparison of properties of stacked galaxies deduced from the best fit SED with [Draine & Li \(2007\)](#) model and [S18](#) template library.

properties of galaxies (i.e., L_{IR} and M_{gas}) at these redshifts and M_{\star} instead of what would have just been an upper limit on these properties. At $10.5 \leq \log_{10}(M_{\star}) \leq 11.0$ for $3.1 \leq z \leq 3.9$ and $3.9 \leq z \leq 5$, and $11.0 \leq \log_{10}(M_{\star}) \leq 12.0$ for $3.9 \leq z \leq 5$, this also allows the SED peak to be constrained more effectively, as it is only weakly constrained, if at all, by the *Herschel* data alone. The SED peak is crucial for determining properties such as $T_{\text{dust}}^{\text{M}}$ and M_{gas} . Elsewhere it also provides an extra point or upper limit that significantly reduces the uncertainty in the properties inferred from the SED fit. These extra ALMA points are also not affected by clustering bias. As results, they push the SED towards "the real one", and are therefore decisive for this study.

4.4 Looking for biases in the SED fitting procedure

In this section, I will examine whether the stacking analysis performed in Chap. 3 leads to biases once the SED fitting procedure is performed to infer galaxy properties. I will also check that the assumption made earlier that there is no contribution from AGN is justified.

4.4.1 Simulations to correct for averaging biases

Because a mean stacking procedure is luminosity weighted, it can have non-linear effects on the shape of the resulting SED (e.g., Elbaz et al. 2011; S15; S18). These effects include the widening of the FIR bump and a bias of the peak towards warmer $T_{\text{dust}}^{\text{L}}$. It is mainly a result of mixing galaxies of different redshifts and $T_{\text{dust}}^{\text{L}}$ (e.g., Elbaz et al. 2011; S15; S18). The broadening of the SED increases the difficulty of determining precisely $T_{\text{dust}}^{\text{L}}$ (S18). To ensure that my conclusions are not biased by these effects, I performed simulations to identify any systematic bias due to my stacking procedure.

To this end, for each bin of M_{\star} and redshift, I simulated the averaging biases starting from the distribution of the galaxies in the bin. For each set of galaxies, I created a mock counterpart in order to compare the properties resulting from the stacking with those expected.

To each galaxy of mass M_{\star} and redshift z , I assigned the SFR starting from M_{\star} and following $SFR = R_{\text{SB}} \times SFR_{\text{MS}}$. The SFR_{MS} was calculated from the main sequence trend found in this work (See Eq. 5.11 and parameters Table 5.2) as a function of redshift and M_{\star} . R_{SB} represents the starburstiness and is defined by $R_{\text{SB}} = SFR/SFR_{\text{MS}}$. I want to generate both mock main sequence galaxies and starburst galaxies. It was shown in S15 that both the main sequence width (~ 0.3 dex, see S15) and the starburst fraction do not evolve with redshift and M_{\star} . I can therefore reasonably assume that the distribution function of R_{SB} does not vary (S15). This assumption still allows the luminosity functions to be reconstructed properly (e.g., Sargent et al. 2012; S15). Following Sargent et al. (2012), I have modelled the probability density function of R_{SB} by a double log-normal distribution (see Eq. 4.4).

$$\Phi_{R_{\text{SB}}}(x) = \frac{1 - f_{\text{SB}} - f_{\text{miss}}}{\sqrt{2\pi}\sigma_{\text{MS}}} \exp\left(\frac{-\log_{10}(x/x_0)^2}{2\sigma_{\text{MS}}}\right) + \frac{f_{\text{SB}}}{\sqrt{2\pi}\sigma_{\text{SB}}} \exp\left(\frac{-\log_{10}(x/B_{\text{SB}})^2}{2\sigma_{\text{SB}}}\right), \quad (4.4)$$

where f_{SB} is the fraction of starbursts, f_{miss} is the fraction of galaxies missed by such distribution (neither starburst nor main sequence galaxies), σ_{MS} and σ_{SB} are the widths of the main sequence and

starburst distributions, B_{SB} is the median multiplicative boost of star formation that can be expected for a starburst compared to a main sequence galaxy (i.e., the median of starburst galaxies), and x_0 is the median R_{SB} of main sequence galaxies. I note that with this parametrisation, we expect f_{miss} and x_0 to be close to 0 and 1 respectively, by construction. I have chosen here to use the parametrisation of S15: $\sigma_{\text{MS}} = \sigma_{\text{SB}} = 0.31$ dex, $f_{\text{SB}} = 3.3\%$, $B_{\text{SB}} = 5.3$, $f_{\text{miss}} = 0\%$, and $x_0 = 0.87$.

To each galaxy I assign L_{IR} , deduced from the SFR by subtracting the SFR_{UV} assuming the UV dust attenuation (A_{UV}) derived from M_{\star} as in Pannella et al. (2015) (see Eq. 4.5 and 4.6) and Kennicutt (1998a) (see Eq. 4.7).

$$A_{\text{UV}} = 1.6 \times \log_{10}(M_{\star}) - 13.5, \quad (4.5)$$

$$\begin{aligned} SFR_{\text{IR}} &= SFR - SFR_{\text{UV}} \\ \text{where } SFR_{\text{UV}} &= SFR \times 10^{-0.4 \times A_{\text{UV}}}, \end{aligned} \quad (4.6)$$

$$L_{\text{IR}}[L_{\odot}] = 5.8 \times 10^9 \times SFR_{\text{IR}}[M_{\odot}\text{yr}^{-1}]. \quad (4.7)$$

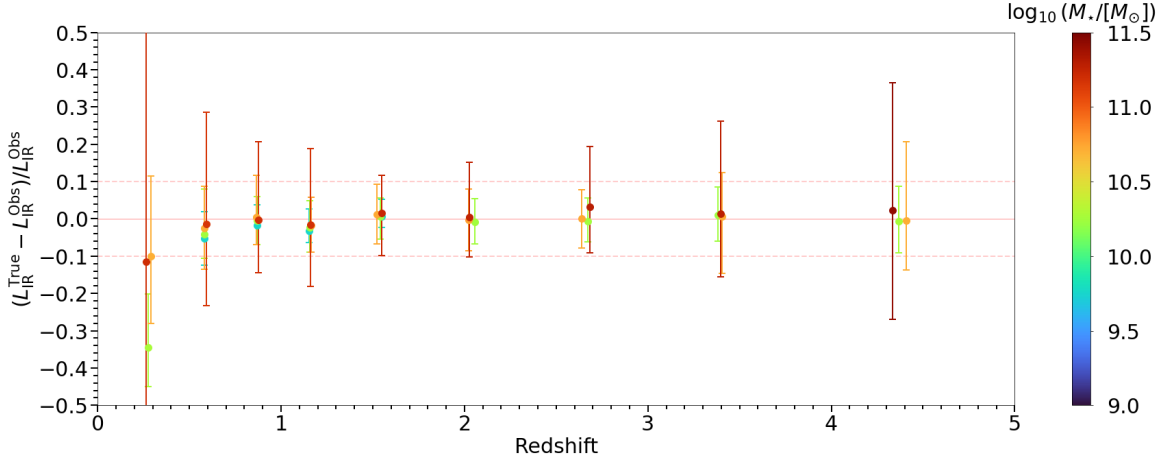
Then T_{dust} was calculated using the best fit of our work (see Eq. 5.2) for the main sequence trend, and we followed Magnelli et al. (2014) (see their Eq. 9) to take into account the impact on T_{dust} of the distance of the mock galaxy from the main sequence (i.e., R_{SB}). The SED, for each mock galaxy, was then calculated using T_{dust} , L_{IR} and redshift with the template library from S18 assuming a contribution of PAH molecules $f_{\text{PAH}} \equiv M_{\text{dust}}^{\text{PAH}} / M_{\text{dust}}$. The value of f_{PAH} was set to follow a Gaussian distribution with a mean of 0.039 and a scatter 2.5/100 (S18, roughly for main sequence galaxies). Next, the M_{dust} were obtained from the selected SED template and the M_{gas} were calculated according to the different methods presented in Sect. 5.4. The individual SEDs were then stacked using a mean stacking method (see Chap. 3). Stacked fluxes at 24, 100, 160, 250, 350, 500 and 1130 μm were deduced from the stacked SED. The stacked fluxes were then fitted with the template library from S18 (see Sect. 4.1). The properties of the best fit SED were deduced using the method presented in the corresponding section of this paper: see Sect. 5.1 for T_{dust} , Sect. 5.3 for L_{IR} and Sect. 5.4 for M_{gas} . Potential biases were then investigated by comparing the true average properties (labelled 'True') with those deduced from my stacking analysis (labelled 'Obs').

The results of this analysis are presented in Fig. 4.8 for L_{IR} , T_{dust} , and M_{dust} . Figure 4.8a, 4.8b and 4.8c do not show any major bias as the mean values are: $-1\%^{+2\%}_{-4\%}$ for L_{IR} , $-6\%^{+1\%}_{-2\%}$ for T_{dust} , and $7\%^{+2\%}_{-4\%}$ for M_{dust} . As a result, I find no clear evidence of significant averaging bias when examining T_{dust} , L_{IR} , and M_{dust} ; and thus decided not to apply any correction.

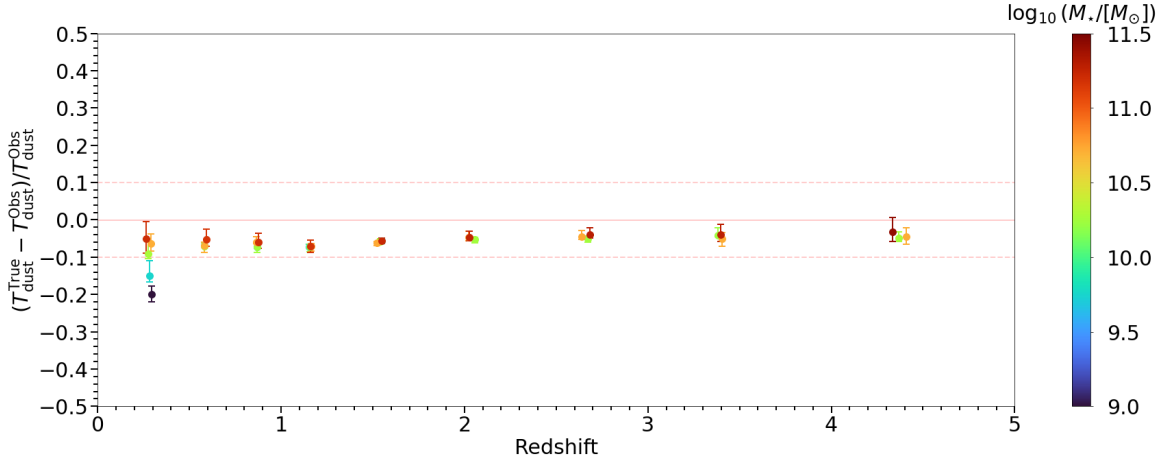
The simulations were performed using a program I coded in Python. First, mock galaxies were generated following the method presented previously and then the program perform a mean stack of the generated fluxes. Resulting stacked fluxes are then fit with the SED fitting program described earlier. The whole simulation runs in about 10 hours on the laboratory cluster over 10 cores.

4.4.2 Active galactic nuclei bias

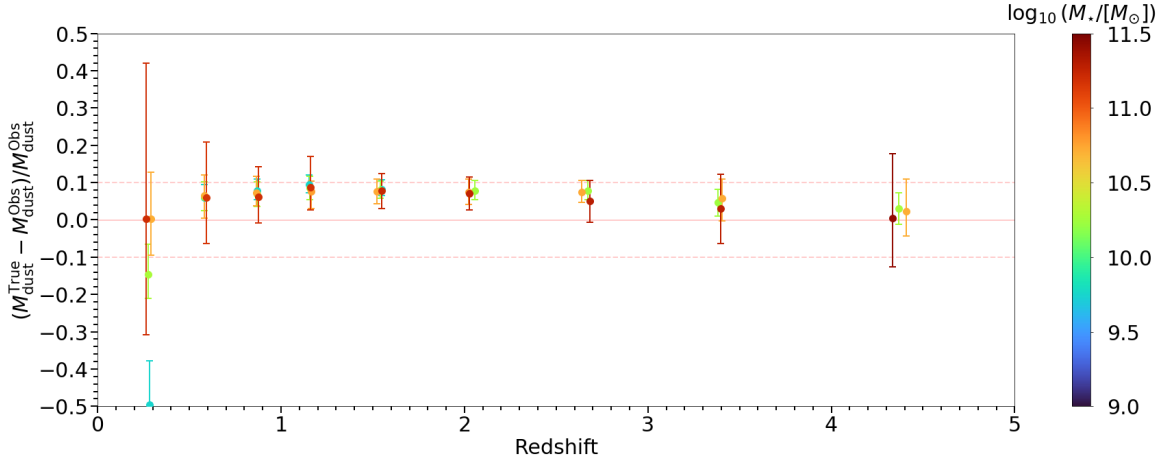
It has been reported that AGN can have a major contribution to the total outgoing light of a galaxy (e.g., Hao et al. 2005; Richards et al. 2006). However, most of this emission is radiated at wavelengths shorter than 24 μm and thus will not affect our FIR measurement. Most extreme and dust-obscured AGN may still have an impact on the mid-to-far infrared ratio (in particular 24 μm in our case), but should not affect the FIR colour compared to normal star-forming galaxies (Hatziminaoglou et al.



(a) Relative difference of the "True" and "Obs" L_{IR} as a function of redshift and colour coded by M_{\star} .



(b) Relative difference of the "True" and "Obs" T_{dust} as a function of redshift and colour coded by M_{\star} .



(c) Relative difference of the "True" and "Obs" M_{dust} as a function of redshift and colour coded by M_{\star} .

Figure 4.8: Comparison between the "True", i.e., the mean property value (L_{IR} , T_{dust} and M_{dust}) of the simulated galaxies, and "Obs", i.e., the observed value retrieved after simulating our stacking and SED fitting procedures on these simulated galaxies.

2010). I checked for any AGN contribution by fitting my stacked fluxes with a combination of [Draine & Li \(2007\)](#) dust model, and [Fritz et al. \(2006\)](#) AGN model, using the SED fitting tool CIGALE ([Boquien et al. 2019](#)). No conclusive evidence for a major contribution from AGNs to the rest-frame FIR (i.e., $L_{\text{IR}}^{\text{AGN}}/L_{\text{IR}}^{\text{TOT}} \geq 10\%$) was found in any of our M_{\star} and redshift bins.

CHAPTER 4

CHAPTER

5

REDSHIFT EVOLUTION THE DUST-OBSCURED STAR-FORMING PROPERTIES OF GALAXIES

5.1	Deducing the T_{dust} of SFGs	57
5.1.1	Influence of the CMB on T_{dust}	57
5.1.2	The T_{dust} of main sequence SFGs	57
5.1.3	The evolution of λ_{peak} as a function of L_{IR}	59
5.1.4	Influence of H -dropout galaxies on T_{dust}	61
5.2	Deducing the dust attenuation of SFGs	62
5.2.1	Deducing SFR for SFGs	63
5.2.2	The evolution of A_{UV}	63
5.2.3	The contribution of H -dropout galaxies to A_{UV}	66
5.3	Deducing the main sequence of SFGs	67
5.3.1	Fitting the shape of the main sequence of SFGs	67
5.3.2	The contribution of H -dropouts galaxies to SFR	72
5.4	Deducing the gas mass of SFGs	72
5.4.1	From M_{dust} to M_{gas} and how to derive the metallicity	72
5.4.2	The contribution of H -dropout galaxies	75
5.4.3	Fitting the M_{gas} evolution of SFGs	75
5.4.4	Impact on M_{gas} of the dust grain model	76
5.5	Deducing the cosmic star formation history	77
5.6	Deducing the cosmic evolution of the gas mass density	79
5.7	Discussion	81
5.7.1	SFR, M_{gas} and SFE	81
5.7.2	ρ_{SFR} and ρ_{gas}	84
5.7.3	The Kennicutt-Schmidt relation	85
5.8	Retrospective: the impact of the clustering bias correction method on properties of galaxies	88
5.8.1	The T_{dust} evolution deduced from the method from B15	88
5.8.2	The $SFR - M_{\star}$ evolution deduced from the method from B15	90
5.8.3	The M_{gas} dependences deduced from the method from B15	90

In this chapter, I will review the redshift evolution of the galaxy properties that I have been able to deduce from the stacking analysis presented in Chap. 3 and the SED fitting procedure presented in Chap. 4. The aim of this chapter is to give an overview of the evolution of the properties of main sequence galaxies, focusing on their dependence on redshift and M_{\star} . In particular, I will present the redshift evolution of T_{dust} , the A_{UV} , the SFR, and M_{gas} for SFGs. I will then deduce the comic star formation history, and the cosmic gas mass density. Finally, I will discuss what we can learn by putting all these properties together.

5.1 Deducing the T_{dust} of SFGs

In this section, I examine the evolution of T_{dust} . T_{dust} could be an indicator of the activity of a galaxy. For example, starbursts, which form more stars than main sequence galaxies, are generally hotter (i.e., the peak of the SED is at a shorter wavelength) compared to main sequence SFGs (S18). However, the link between T_{dust} and the star formation efficiency ($SFE = SFR/M_{\text{gas}}$) of SFGs is not as straightforward because the metallicity Z has an impact on the amount of dust per unit gas mass: at high metallicity more dust is created per unit of M_{gas} which leads to lower dust temperature.

The T_{dust} of stacked SFGs are given by the best fit of the SEDs presented in Chapter 4. Before interpreting the results one must check for a potential bias to our results, namely the influence of the cosmic microwave background (CMB).

5.1.1 Influence of the CMB on T_{dust}

The temperature of the CMB ranges from 2.73 K at $z = 0$, up to 16.4 K at $z = 5$, and, thus, it could become a significant source of heating at high redshift. Before drawing any conclusion on the evolution of T_{dust} , I must check that the CMB does not have a major contribution.

To estimate the contribution of the CMB, I compared my T_{dust} with the equivalent dust temperature at $z = 0$ ($T_{\text{dust}}^{z=0}$), i.e., for a CMB of 2.73 K, following da Cunha et al. (2013):

$$T_{\text{dust}}^{z=0}[\text{K}] = \left((T_{\text{dust}}^{\text{meas}}[\text{K}])^{4+\beta} - (T_{\text{CMB}}^{z=0}[\text{K}])^{4+\beta} \times [(1+z)^{4+\beta} - 1] \right)^{1/(4+\beta)}, \quad (5.1)$$

where $T_{\text{dust}}^{\text{meas}}$ is my measured T_{dust} , and $\beta = 1.5$ is the emissivity of the templates in the library from Schreiber et al. (2018). The contribution of the CMB $C_{\text{CMB}} = (T_{\text{dust}}^{\text{meas}} - T_{\text{dust}}^{z=0}) / T_{\text{dust}}^{z=0}$ never exceeds 7×10^{-4} and is thus negligible for $0.1 \leq z \leq 5.0$.

This conclusion is not affected by the choice of $\beta = 1.5$: the same conclusion has already been drawn by B15 for $\beta = 1.8$. For example, for $\beta = 1.8$, C_{CMB} does not exceed 5×10^{-4} in our case. C_{CMB} on the T_{dust} being negligible, it means that any evolution observed is solely due to the properties of the galaxies, independently of the CMB.

There is a second effect coming from the CMB, that can impact the L_{IR} and M_{dust} of galaxies, coming from the fact that the CMB is a non-negligible background against which the continuum emission is measured (da Cunha et al. 2013). However, this effect mainly affect low temperature galaxies (i.e., $T_{\text{dust}}^{z=0} \leq 20$ K) at $z \sim 5$ (da Cunha et al. 2013). At the highest redshift considered here, i.e., $z \sim 4.3$, galaxies have a $T_{\text{dust}}^{z=0} \geq 40$ K. Thus, I do not expect this second effect coming from the CMB to impact the L_{IR} and M_{dust} deduced in this study.

5.1.2 The T_{dust} of main sequence SFGs

I have checked that the CMB does not have a significant impact on the conclusions I could draw from the evolution of T_{dust} as a function of redshift and M_{\star} (see Fig. 5.1). In Fig. 5.1, my results seem to be globally consistent with the trend of S18. In Fig. 5.1, I do not see a significant dependence of

T_{dust} as a function of M_{\star} . It seems that the T_{dust} of a main sequence galaxy is mainly determined by its redshift, independently of its M_{\star} (see also Magdis et al. 2012; Magnelli et al. 2014). This result is very interesting in itself: low-mass and high-mass galaxies can have SFRs that are two orders of magnitude different but have similar T_{dust} . The impression is that massive galaxies are the sum of star-forming regions that are relatively similar to those in a lower-mass galaxy. This means that galaxies of different masses have, to the first order, the same SFE (i.e., the same number of heating photons per mass of gas). I observe only slight evidence that the highest M_{\star} bin ($11 \leq \log_{10}(M_{\star}) \leq 12$) could be cooler than lower-mass galaxies at a fixed redshift. This effect can be observed for $z \leq 2.5$. This could simply show that high-mass galaxies are actually starting to slowly reduce their SFE on their way to become quiescent. This is particularly apparent in our first redshift bin ($0.1 \leq z \leq 0.4$) in which the bending of the main sequence is also the strongest (see Sect. 5.3; S15).

The highest stellar mass bin of our highest redshift bin (i.e., $11 \leq \log_{10}(M_{\star}) \leq 12$ and $3.9 \leq z \leq 5.0$) seems a bit at odd compared to the general trend. This might come from a small number statistical effect and that some starbursts might be dominating this bin, hence the higher T_{dust} .

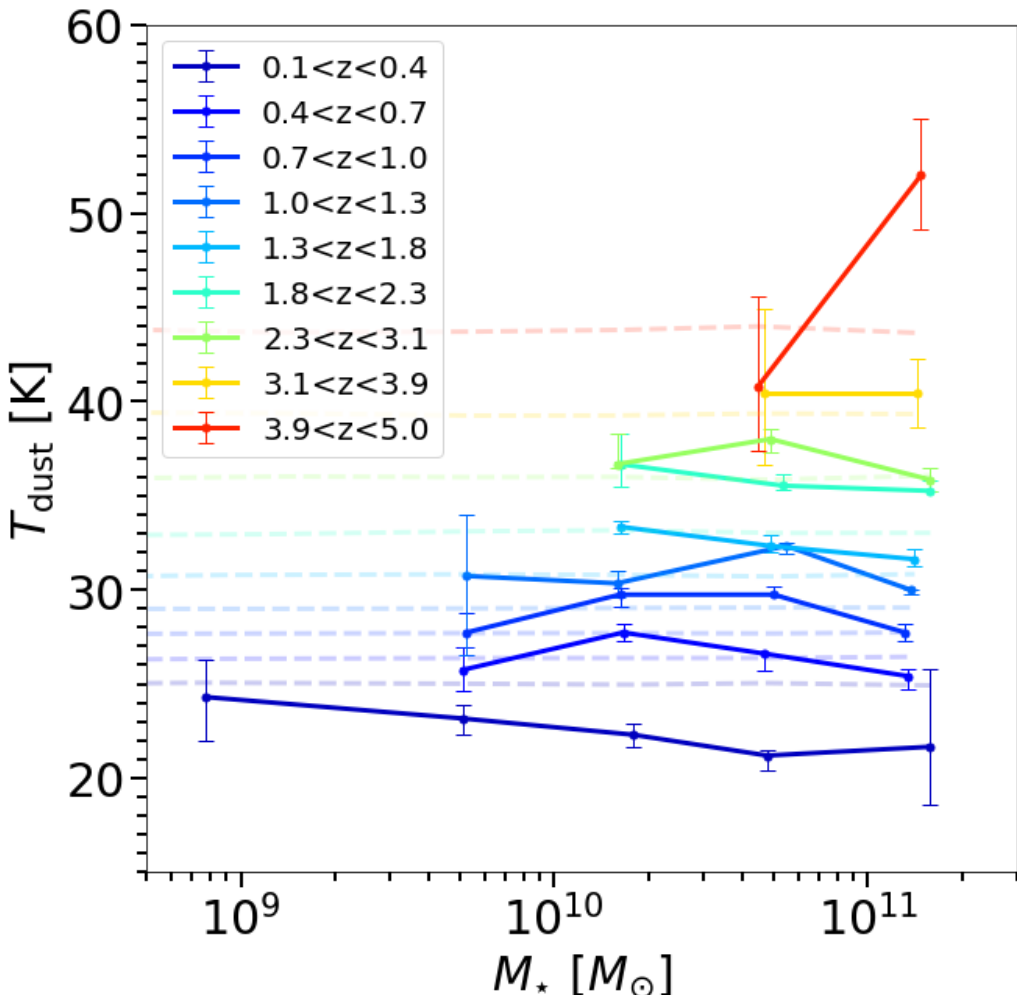


Figure 5.1: T_{dust} as a function of M_{\star} colour-coded by redshift bin. Average trend of T_{dust} as a function redshift from S18, is shown as a reference in faded coloured dashed line.

In Fig. 5.2, I display the mean T_{dust} over each redshift bin, weighted by the number of galaxies in each bin of M_\star . My analysis suggests a linear evolution of T_{dust} as a function of redshift. My best linear fit, for $0.1 \leq z \leq 5$, follows:

$$T_{\text{dust}} [\text{K}] = 33.84^{+0.14}_{-0.14} + 4.66^{+0.03}_{-0.03}(z - 2). \quad (5.2)$$

The fit was performed using the `emcee` library using an MCMC approach to navigate the parameter space and runs in about 30 minutes on my work laptop.

I compared my results with those in the literature: S18, Magnelli et al. (2014), Bouwens et al. (2020), Magdis et al. (2012) and B15. I also re-fitted the two stacks of Béthermin et al. (2020) using the template library from S18. For consistency, I converted all $T_{\text{dust}}^{\text{L}}$ to $T_{\text{dust}}^{\text{M}}$ when comparing my results with the literature (i.e., for Magnelli et al. 2014; Bouwens et al. 2020). To do this, I adopt the conversion factor, between mass and light weighted dust temperature, given by S18:

$$T_{\text{dust}}^{\text{M}} [\text{K}] = 0.91 \times T_{\text{dust}}^{\text{L}} [\text{K}]. \quad (5.3)$$

This conversion factor (i.e., "0.91" in Eq. 5.3) represents the average conversion factor between $T_{\text{dust}}^{\text{M}}$ and $T_{\text{dust}}^{\text{L}}$ for all templates in the library of S18. Some studies (i.e., Magdis et al. 2012; B15) consider the mean starlight heating rate ($\langle U \rangle$) (Draine & Li 2007; Draine et al. 2014) instead of T_{dust} as defined here. To compare my results with those, I have chosen to use the $\langle U \rangle$ -to- T_{dust} conversion formula of S18 (see Eq. 5.4).

$$T_{\text{dust}} [\text{K}] = \left(\frac{\langle U \rangle}{U_\odot} \right)^{1/5.57} \times 18.2 [\text{K}]. \quad (5.4)$$

As $\langle U \rangle$ is only a proxy of T_{dust} , any comparison between the two quantities should be essentially qualitative.

My T_{dust} as a function of redshift is consistent within the uncertainties with S18, extended to $z = 5$. I find no clear evidence for the softening of the T_{dust} as the redshift increases reported by Magnelli et al. (2014); Magdis et al. (2012). This could stem from the lack of clustering bias correction in their study, as previously reported in S18. Clustering bias correction is a quite important step when stacking in *Herschel* passbands. Especially in the SPIRE wavelengths, as this effect can account for up to 50% of the total signal, on average at 500 μm (e.g., S15; B15; Delvecchio et al. 2021). Ignoring this could result in a cooler SED and a lower T_{dust} (see Sect. 3.4 for more details). Comparing my trend to B15; Béthermin et al. (2020); Bouwens et al. (2020), all agree on a linear trend but slightly flatter than mine. The differences with my trend may again stem from the way the correction for clustering bias is handled in the two works.

5.1.3 The evolution of λ_{peak} as a function of L_{IR}

Drew & Casey (2022) presented an evolution of the peak wavelength of the SED (λ_{peak}) as a function of L_{IR} . I, thus, looked at the $\lambda_{\text{peak}} - L_{\text{IR}}$ plane (see Fig. 5.3). In this case, I only measured λ_{peak} when the SED peak was well defined by my flux density measurements. I observe no dependence of λ_{peak} as a function of L_{IR} at fixed redshift, up to $z \simeq 4$. Only my last redshift bin ($3.9 \leq z \leq 5.0$) shows some evolution. However, for the same reason as above, this could result from a bias due to selection effects, as well as the fact that I only have two points in this redshift interval. I conclude that

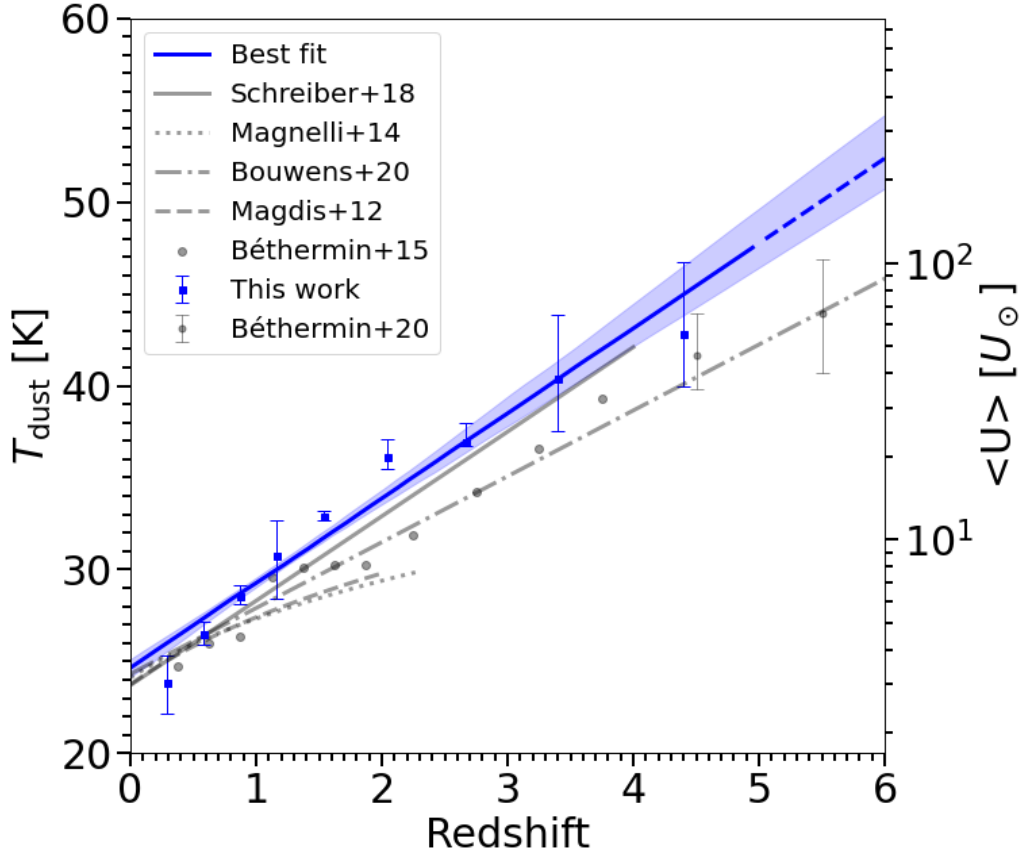


Figure 5.2: T_{dust} and $\langle U \rangle$ as a function of redshift. The blue dots represent the T_{dust} of this work, the blue line is the best fit (up to $z = 5$), the dashed blue line is the best fit extrapolation (for $z \geq 5$), and the blue shaded area represents the 68% uncertainty of the fit. From the literature: S18 (grey solid line), Magnelli et al. (2014) (grey dotted line) and Bouwens et al. (2020) (grey dash-dotted line) converted using Eq. 5.3, Magdis et al. (2012) (grey, dashed line) and B15 (grey dots) converted using Eq. 5.4. We also re-fitted the two stacks from Béthermin et al. (2020) (grey dots with error bars) using the template library from S18.

λ_{peak} of main sequence galaxies does not depend significantly on L_{IR} at a given redshift. However, the normalisation seems to evolve with redshift, reflecting the smooth increase of T_{dust} with redshift presented in the previous section.

Thus my results differ from those of Drew & Casey (2022) who claimed to have found an evolution of T_{dust} , as probed by λ_{peak} , with L_{IR} (i.e., a decreasing λ_{peak} with increasing L_{IR}). This discrepancy comes from the probable incompleteness of their sample. I stack galaxies to recover the main sequence, so I look at a mass complete sample, where non-detections are accounted for thanks to the stacking technique. On the other hand, Drew & Casey (2022) worked with individually detected galaxies, and thus might be biased toward the brightest galaxies at all redshifts (i.e., starbursts). In addition, their flux-limited sample suffer from selection effect: at low L_{IR} , their λ_{peak} comes from low redshift galaxies, while at high L_{IR} , their values are coming from distant galaxies. What Drew & Casey (2022) find is an effect of redshift not an effect of L_{IR} .

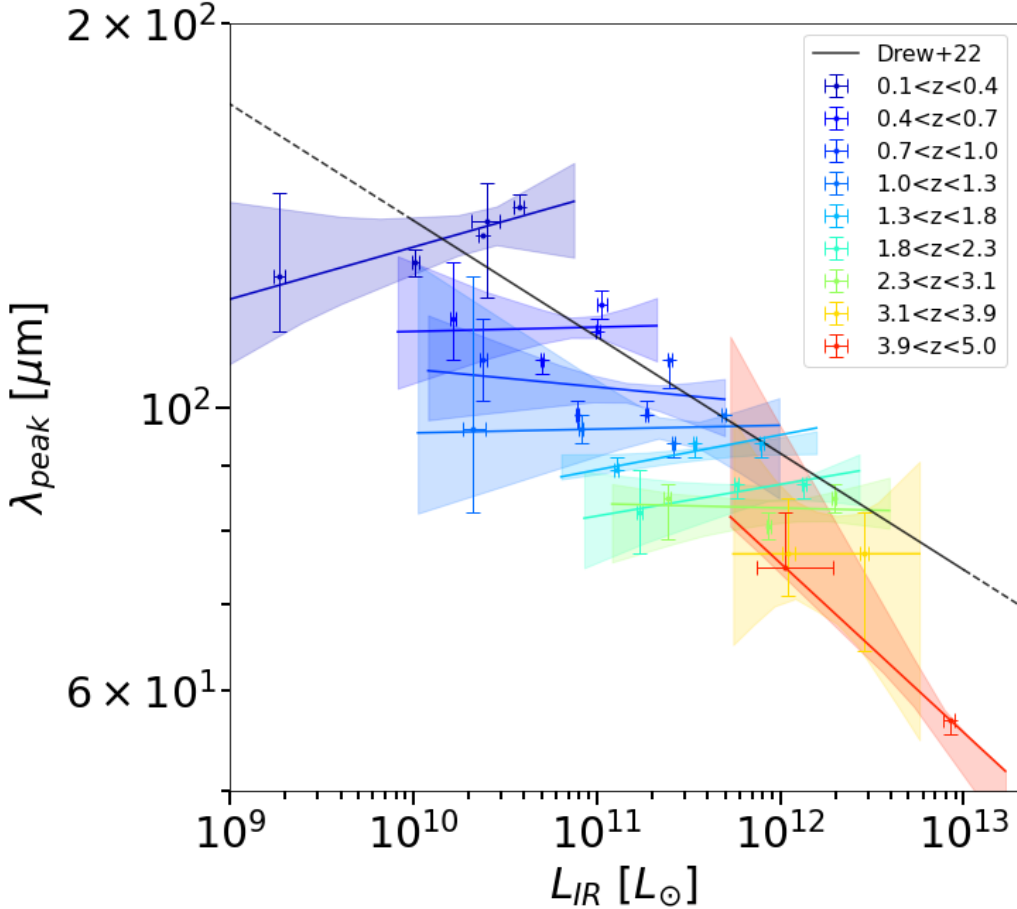


Figure 5.3: λ_{peak} as a function of L_{IR} . The colour-coded dots (per redshift bins) represent the results of this work, coloured lines represent the best fit and shaded area the 68% uncertainty of the fit. The solid black line corresponds to the trend of [Drew & Casey \(2022\)](#), while the dotted black line is an extrapolation of their relation.

The fits were performed using the `emcee` library using an MCMC approach to navigate the parameter space and runs in about 1 hour on my work laptop.

5.1.4 Influence of H -dropout galaxies on T_{dust}

My results come from H -band selected galaxies and thus do not take into account the H -dropout galaxies ([Wang et al. 2019](#)). Here I study the sample of H -dropout galaxies from [Wang et al. \(2019\)](#), and assess the impact of this sample on the redshift evolution of T_{dust} for all SFGs (i.e., galaxies selected by the H -band and H -dropout galaxies).

There are 63 H -dropout galaxies that have been detected in [Wang et al. \(2019\)](#) over $\sim 600 \text{ arcmin}^2$. The H -dropout sample from [Wang et al. \(2019\)](#) is constituted of galaxies with $\geq 10^{10} M_{\odot}$ and $z \geq 3$. In my work, I have 1451 galaxies with $M_{\star} \geq 10^{10} M_{\odot}$ and $z \geq 3$ over $\sim 1077 \text{ arcmin}^2$. The H -dropout would then only account for $\sim 7.4\%$ of the total sample. I re-fitted the stack of H -dropout from [Wang et al. \(2019\)](#) with S18 templates (see Fig. 5.4) assuming $z = 4$ for the sample ([Wang et al. 2019](#)),

and deduced a $T_{\text{dust}}^{H\text{-drop}} = 37.34_{-1.27}^{+1.2}$ K. Overall, with $T_{\text{dust}}^{H\text{-drop}}$ being within the error bars of my dust temperature estimates at $z \geq 3$ and $M_{\star} \geq 10^{10} M_{\odot}$ (see Sect. 5.1.2), and accounting for $\sim 7.4\%$ of the total sample, I am confident that the H -dropout galaxies would not affect my conclusions on the redshift evolution of T_{dust} for main sequence galaxies.

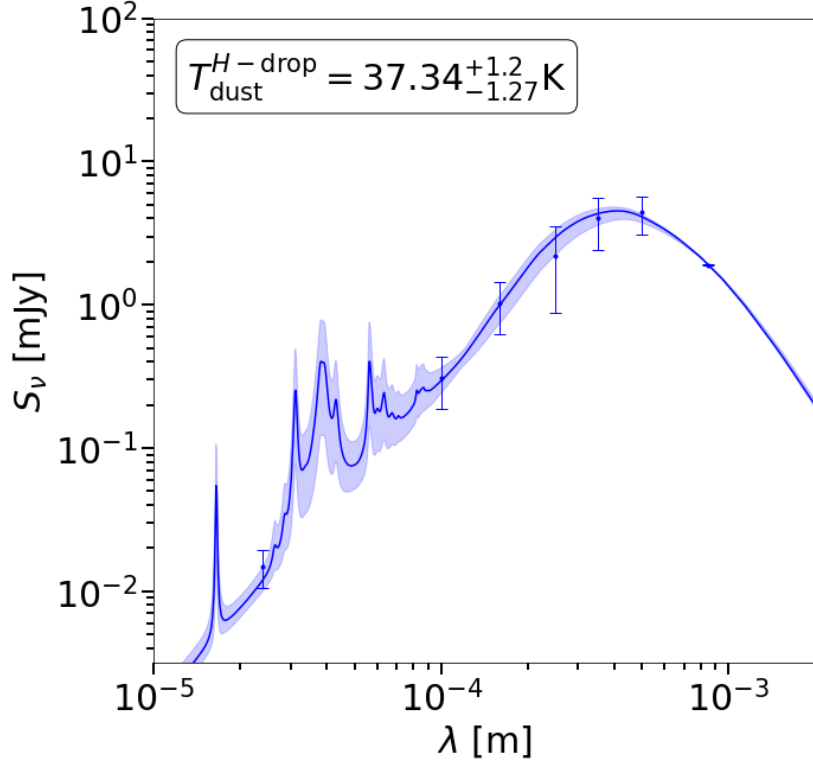


Figure 5.4: Best fit SED for the stacked sample of H -dropout galaxies from Wang et al. (2019). Blue dots correspond to the flux measurements. Blue line is the best fit SED, the blue shaded area shows the 68% uncertainty of the fit.

5.2 Deducing the dust attenuation of SFGs

In this section, I examine the dependence of A_{UV} , defined by Eq. 5.5, with redshift and M_{\star} . There are several definitions of attenuation; I have chosen one that compares the SFR observed in the UV and IR. According to this definition, a strongly attenuated galaxy has most of its light absorbed by dust and re-emitted in the IR (e.g., SFR_{IR} account for 99% of the total SFR for $A_{\text{UV}} \sim 5$).

$$A_{\text{UV}} = 2.5 \times \log_{10} \left(\frac{\text{SFR}_{\text{IR}} + \text{SFR}_{\text{UV}}}{\text{SFR}_{\text{UV}}} \right). \quad (5.5)$$

5.2.1 Deducing SFR for SFGs

The preferred method for estimating the SFR of a galaxy is to study the light from OB stars, because of the close link between their short lifetimes and the instantaneous SFR of galaxies. Although most of their light is emitted in the UV, it can be largely absorbed by dust and then re-emitted as thermal radiation in the IR. To obtain the total SFR associated with a galaxy, or in my case the stack of several galaxies, it is necessary to combine the SFRs deduced from both the UV and the IR as:

$$SFR_{\text{Tot}} = SFR_{\text{UV}} + SFR_{\text{IR}}. \quad (5.6)$$

For the rest of the manuscript I will refer to SFR_{Tot} simply as SFR. The SFR_{UV} , uncorrected for dust attenuation, is computed from L_{UV} (rest-frame 1500 Å UV luminosity) following [Daddi et al. \(2004\)](#):

$$SFR_{\text{UV}}[M_{\odot}\text{yr}^{-1}] = 2.17 \times 10^{-10} L_{\text{UV}}[\text{L}_{\odot}]. \quad (5.7)$$

For my catalogues, the L_{UV} were calculated for all individual galaxies from *EAZY* ([Pannella et al. 2015](#)). In this study, the SFR_{UV} was derived for each redshift and M_{\star} bin by averaging the SFR_{UV} of all individual galaxies in the bin. I deduced the SFR_{IR} following [Kennicutt \(1998a\)](#) (see Eq. 4.7), while L_{IR} was obtained from the SED fit of my stacks, by integrating the best-fit SED in the range 8–1000 μm rest-frame.

5.2.2 The evolution of A_{UV}

From SFR_{IR} and SFR_{UV} , I deduce A_{UV} using Eq. 4.5. Results are displayed in Fig. 5.5. I observe a general increase of A_{UV} with M_{\star} at fixed redshift. At $z \leq 0.4$, results might be harder to interpret as the optical data are in this case not probing the rest-frame UV. The A_{UV} of galaxies with $\log_{10}(M_{\star}/M_{\odot}) \leq 11$ show no major evolution with redshift for $z \gtrsim 0.4$ –0.7. On the contrary, the A_{UV} of the higher mass bin (i.e., $11 \leq \log_{10}(M_{\star}/M_{\odot}) \leq 12$) increases rapidly with redshift: from $A_{\text{UV}} = 2$ for $0.1 \leq z \leq 0.4$ to $A_{\text{UV}} = 6$ for $3.9 \leq z \leq 5$.

In Fig. 5.5, I compared to A_{UV} from [Pannella et al. \(2015\)](#). [Pannella et al. \(2015\)](#) observes a linear dependence of A_{UV} with M_{\star} and no evolution with redshift (see their Eq. 7). When considering the redshift and M_{\star} covered by both studies, my results are consistent with the data points from [Pannella et al. \(2015\)](#). The discrepancies are mainly due to the fact that [Pannella et al. \(2015\)](#) probed a smaller area with a shallower depth, resulting in a larger error on the data points. Even though, it was chosen in [Pannella et al. \(2015\)](#) to not fit any evolution with redshift, it was observed that the slope was evolving marginally for $1.2 \leq z \leq 4.0$ by ~ 0.3 mag. When looking at individual measurements, [Pannella et al. \(2015\)](#) also observed that the highest M_{\star} bin increases rapidly with redshift: from $A_{\text{UV}} = 3$ for $z \sim 0.7$ to $A_{\text{UV}} = 5$ for $z \sim 3.3$. This reflects what is observed in my results.

It seems clear from my results that A_{UV} evolves with the redshift and M_{\star} , at least for the most massive galaxies (i.e., $11 \leq \log_{10}(M_{\star}/M_{\odot}) \leq 12$). Thus, I fitted the dependence of A_{UV} by allowing the linear slope to change with redshift:

$$A_{\text{UV}}[\text{mag}] = a_0 + a_1 \times \log_{10}(1+z) + \log_{10}(M_{\star}/M_{\odot}) \times (n_0 + n_1 \times \log_{10}(1+z)). \quad (5.8)$$

This is a simplistic way of fitting the evolution of A_{UV} as a function of redshift and should represent, to first order, the evolution of A_{UV} better than the model from [Pannella et al. \(2015\)](#) which only allows a linear dependence on M_{\star} . The best-fit parameters are presented in Table 5.1.

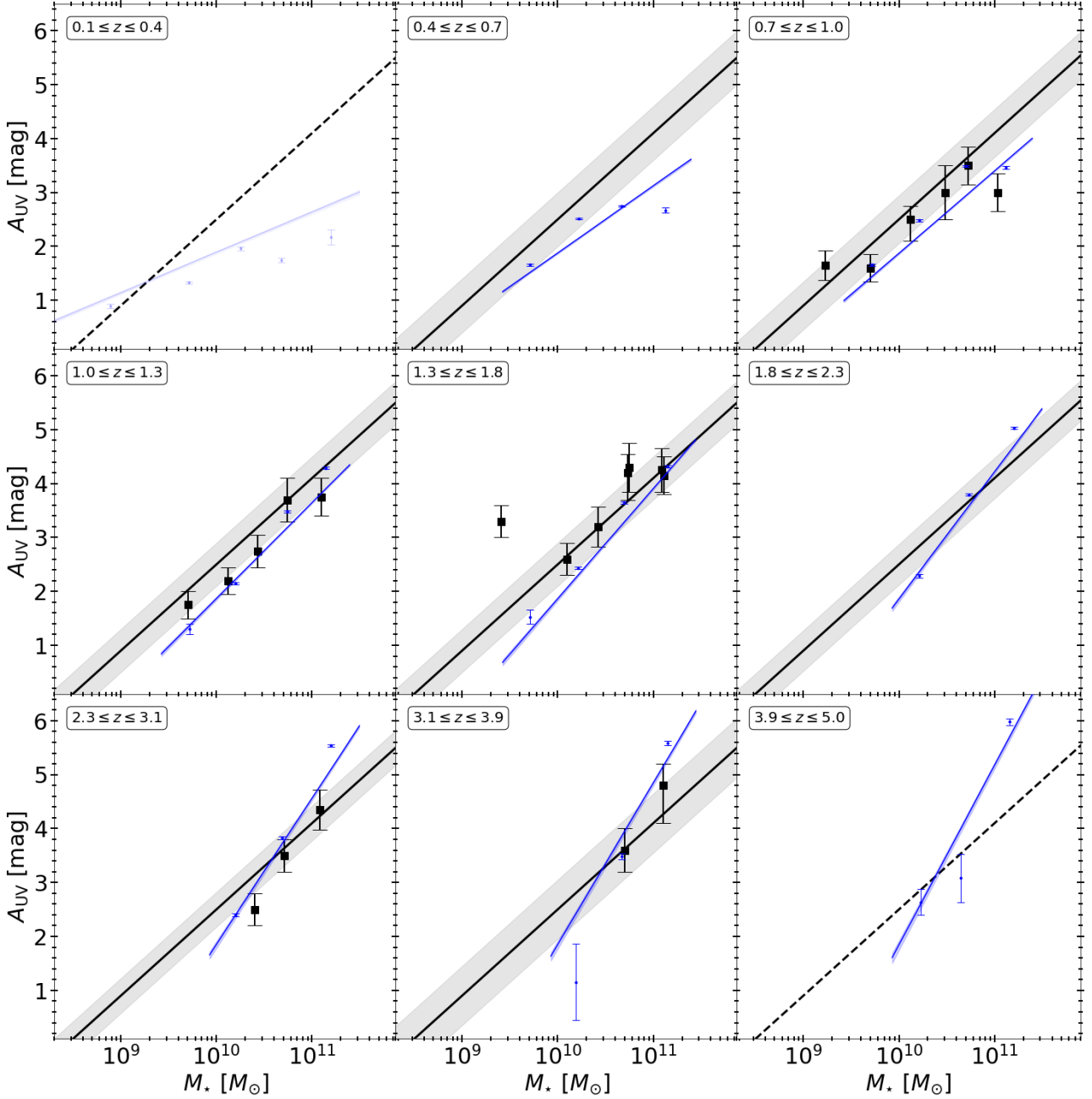


Figure 5.5: A_{UV} as a function of M_{\star} in different redshift bins. The blue points represent data deduced from this work. The blue line represents the best fit according to Eq. 5.8, the shaded blue area the 68% uncertainty of the fit. At $z \leq 0.4$, data points from this work are faded as the optical data are in this case not probing the rest-frame UV. The black squares are the A_{UV} measurements from Pannella et al. (2015) put in the closest corresponding bin from this work. The black lines represent the redshift-independant $A_{\text{UV}} - M_{\star}$ relation of Pannella et al. (2015), dashed lines an extrapolation of it. The grey area is a representation of the error on the fit from Pannella et al. (2015) (~ 0.4 mag on average).

Table 5.1: Best fit parameters of the A_{UV} of star-forming galaxies using Eq. 5.8

a_0	a_1	n_0	n_1
$-3.05^{+0.41}_{-0.50}$	$-40.47^{+1.59}_{-1.34}$	$0.497^{+0.05}_{-0.04}$	$4.07^{+0.13}_{-0.15}$

To investigate my hypothesis that A_{UV} of the most massive galaxies (i.e., $11 \leq \log_{10}(M_{\star}/M_{\odot}) \leq 12$) increases more rapidly, I also examined the evolution of A_{UV} with redshift for different M_{\star} bins (see Fig. 5.6). For $z \gtrsim 1$, A_{UV} is fairly constant for all but the most massive M_{\star} (i.e., $11 \leq \log_{10}(M_{\star}/M_{\odot}) \leq 12$). The A_{UV} of the most massive galaxies (i.e., $11 \leq \log_{10}(M_{\star}/M_{\odot}) \leq 12$) increases by a factor 2 from $z \sim 1$ ($A_{\text{UV}} \sim 3$) to $z \sim 4.5$ ($A_{\text{UV}} \sim 6$), and crosses, at $z \sim 2$, the limit where only 1% of the total SFR comes from the UV. At this stage, galaxies can be considered to be heavily obscured. Next, looking at low redshift (i.e., $0.4 \leq z \lesssim 1$), the A_{UV} of two bins of the most massive galaxies (i.e., $10.5 \leq \log_{10}(M_{\star}/M_{\odot}) \leq 11$ and $11 \leq \log_{10}(M_{\star}/M_{\odot}) \leq 12$) falls rapidly as the redshift goes to 0.4 (by a factor ~ 1.35). On the other end, the A_{UV} of galaxies with $10 \leq \log_{10}(M_{\star}/M_{\odot}) \leq 10.5$ and $9.5 \leq \log_{10}(M_{\star}/M_{\odot}) \leq 10$, decreases only marginally and remains fairly constant.

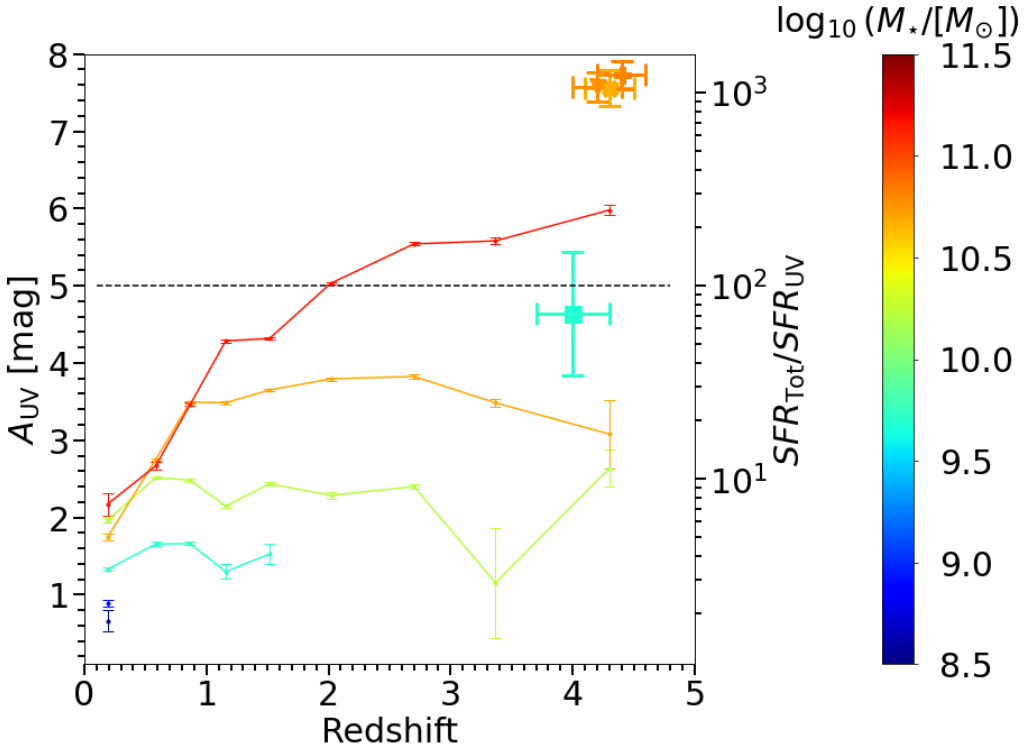


Figure 5.6: A_{UV} as a function of redshift, colour coded in different M_{\star} bin. The black dashed line represents the limit where SFR_{UV} account for 1% of the total SFR. The square, cross, plus and triangle represent optically faint galaxies (OFGs) that are Lyman-break galaxies (LBGs), OFGs that are not LBGs, massive OFGs that are not LBGs and ALMA-detected OFGs, respectively; colour coded by M_{\star} , from Xiao et al. (2023).

The fits were performed using the `emcee` library using an MCMC approach to navigate the pa-

rameter space and runs in about 30 minutes on my work laptop.

5.2.3 The contribution of H -dropout galaxies to A_{UV}

An important point to consider is that this sample does not take into account H -dropout galaxies, which are by definition massive and highly obscured galaxies (Wang et al. 2019; Xiao et al. 2023). However, it is difficult to estimate the degree of attenuation of H -dropout galaxies compared to normal H -band galaxies. One way of studying this would be to stack a sufficiently large number of H -dropout galaxies to obtain a UV detection in order to deduce their SFR_{UV} . However, this would require a separate study.

To give an idea of the degree of attenuation of H -dropouts, I have added to Fig. 5.6 a few groups of optically faint galaxies (OFGs) from Xiao et al. (2023). I deduced their A_{UV} with the SFR_{IR} and SFR_{UV} given in Xiao et al. (2023). OFGs are defined by slightly less restrictive rules than H -dropout galaxies. The criteria are based on the H band and the magnitude of $4.5 \mu\text{m}$. The H -dropout and OFGs are defined by:

$$H\text{-dropout} = \begin{cases} \text{undetected in the } H\text{-band} \\ [4.5] < 24 \text{ mag} \end{cases}, \quad (5.9)$$

$$\text{OFGs} = \begin{cases} H > 26.5 \text{ mag} \\ [4.5] < 25 \text{ mag} \end{cases}, \quad (5.10)$$

where H and $[4.5]$ are the H -band and $4.5 \mu\text{m}$ magnitude, respectively (see Fig. 5.7 for a representation in the $H - [4.5] - [4.5]$ plane). However, Fig. 5.6 clearly shows that this type of galaxy is already much more attenuated than the galaxies detected in the H -band. Thus, the mean evolution of A_{UV} observed here for galaxies with $\log_{10}(M_{\star}/M_{\odot}) \gtrsim 10$ and $z \geq 3$ might be an underestimate.

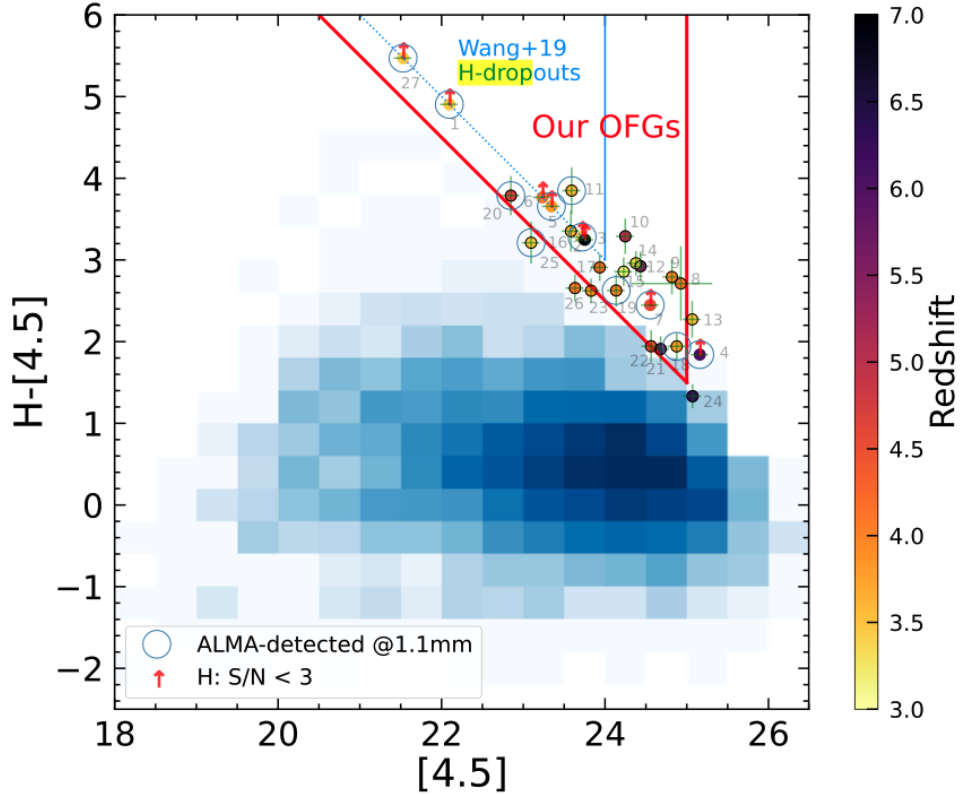


Figure 5.7: Colour-magnitude diagram of the sample from [Xiao et al. \(2023\)](#) colour-coded by photometric redshift. The red lines represent the criteria for the OFGs selection of [Xiao et al. \(2023\)](#). The blue lines represent the criteria for the H -dropout galaxies selection of [Wang et al. \(2019\)](#). See [Xiao et al. \(2023\)](#) for more details. Credit: [Xiao et al. \(2023\)](#).

5.3 Deducing the main sequence of SFGs

In this section, I constrain the $SFR - M_\star$ correlation, also called the "main sequence" of star-forming galaxies ([Noeske et al. 2007](#)).

5.3.1 Fitting the shape of the main sequence of SFGs

In this section, I will fit the main sequence. The Fig. 5.8 displays our SFR for each bin of redshift and M_\star . The SFR follows a monotonic dependence with increasing M_\star , at fixed redshift; and with increasing redshift, at fixed M_\star . The high mass end presents a bending of the main sequence slope, which is more prominent as the redshift decreases.

The $SFR - M_\star$ correlation was then fitted using the formula introduced in [S15](#) as it is able to capture the bending of the main sequence at the high-mass end.

$$\log_{10}(SFR_{\text{MS}}[M_\odot \text{yr}^{-1}]) = m - m_0 + a_0 r - a_1 [\max(0, m - m_1 - a_2 r)]^2, \quad (5.11)$$

where $r \equiv \log_{10}(1+z)$ and $m \equiv \log_{10}(M_\star/10^9 M_\odot)$. In Eq. 5.11, m_1 represents the stellar mass at which the bending of the main sequence starts at $z \sim 0$.

It was shown in S15 that the main sequence has a dispersion in logarithmic space of a Gaussian distribution with a homogeneous scatter of $\sigma \simeq 0.3$ dex. Because I stacked my galaxies, via mean stacking, I actually recover the mean SFR ($\langle SFR \rangle$) of our sample which is different from the mean of a Gaussian distribution in logarithmic space with a dispersion σ_{dist} , with, $\langle 10^X \rangle = \exp((\sigma_X \times \ln(10))^2/2) \times 10^{\langle X \rangle}$, $X = \log_{10}(SFR)$ following a Gaussian distribution. Assuming that the dispersion of this Gaussian distribution in logarithmic space is $\sigma_{\text{dist}} = 0.3$ dex (S15), I can therefore correct this effect analytically. My best-fit parameters are given in Table 5.2, and displayed in Fig. 5.8.

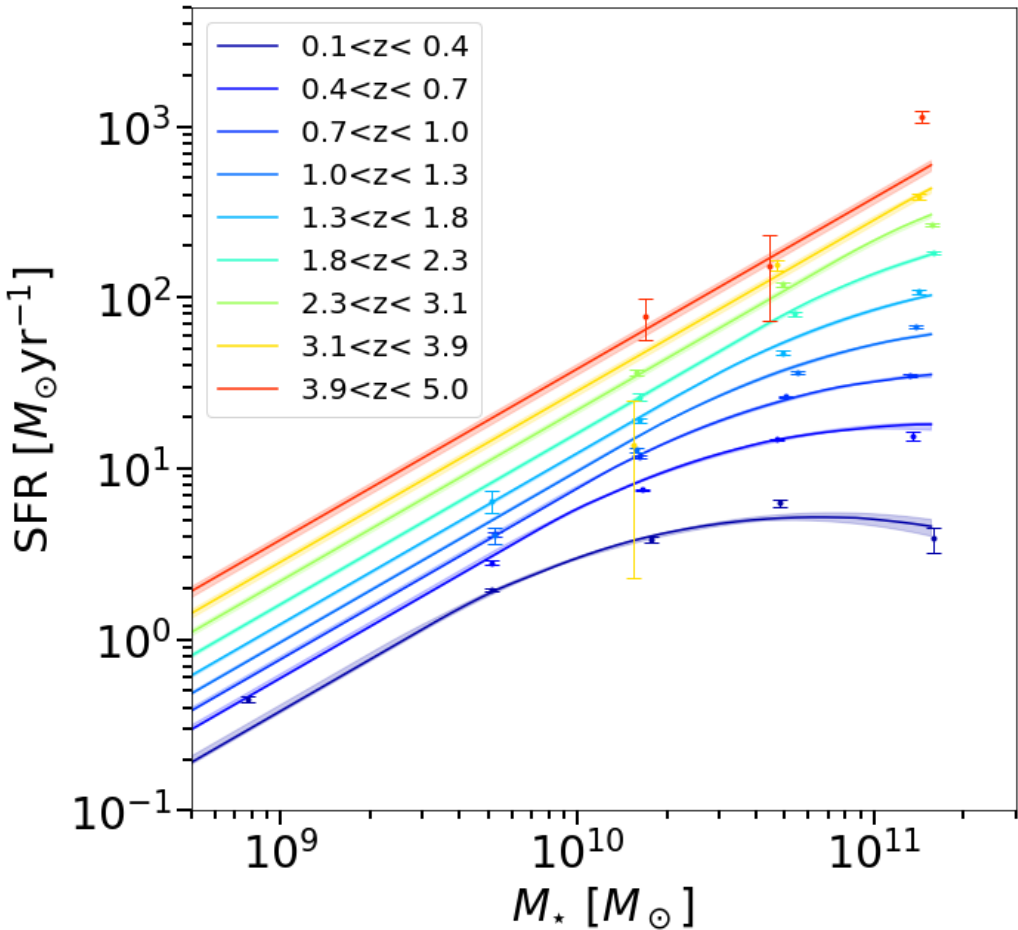


Figure 5.8: SFR as a function of M_\star over different redshift bins. The dots represent data from this work. The upper limits of the SFR for a given redshift and a M_\star bin were used to perform the fit but are not shown here for clarity. Data are fitted using Eq. 5.11, the coloured shaded areas represents the 68% uncertainty of the fit.

Table 5.2: Best fit parameters of the main sequence of star-forming galaxies using Eq. 5.11

m_0	m_1	a_0	a_1	a_2
$9.54^{+0.02}_{-0.02}$	$9.13^{+0.11}_{-0.09}$	$1.53^{+0.07}_{-0.04}$	$0.292^{+0.04}_{-0.02}$	$2.85^{+0.14}_{-0.15}$

The fit was performed using the **emcee** library using an MCMC approach to navigate the parameter space and runs in about 30 minutes on the Feynman laboratory cluster.

The shape chosen for the fit has two regimes: a slope of one at low M_\star and a bending after the transition mass (i.e., $m_1 - a_2 r$). These two regimes are observed in my data points. The normalisation of the main sequence increases significantly with redshift, e.g., at $M_\star = 10^{10} M_\odot$ the SFR increases by a factor 13 from $z \sim 0.2$ to $z \sim 4.3$. As I have already pointed out in the study of T_{dust} , the highest redshift and M_\star bin (i.e., $3.9 \leq z \leq 5.0$ and $11 \leq \log_{10}(M_\star) \leq 12$), appears to be highly star-forming and lies above my main sequence by a factor of two. This suggests that this bin includes a significant fraction of galaxies with high SFR relative to the main sequence (i.e., high R_{SB}).

I compare my results with several versions of the main sequence from the literature in Figure 5.9. Compared to [Speagle et al. \(2014\)](#), my best fit is consistent with the general trend and evolution of the normalisation, but [Speagle et al. \(2014\)](#) did not report any bending. However, my work suggests that the bending is real and becomes stronger at low redshift. Overall, my best-fit remains close to what was found by [S15](#) at $z \geq 0.7$. The main sequence from [S15](#) was recovered by [Delvecchio et al. \(2021\)](#) who studied mainly FIR data. Nevertheless, I find a stronger curvature of the main sequence at $z \leq 0.7$ compared to what we could extrapolate from [S15](#). This is probably due in part to the fact that they did not probe the main sequence for $z \leq 0.3$ where the bending becomes even stronger. The version of the main sequence by [Leslie et al. \(2020\)](#) was derived from a study of the radio continuum at 3 GHz, which may explain the differences in slope, normalisation and bending. But both roughly agree on the same evolutionary trend and on a bending of the main sequence. The bending of the main sequence being at the high mass end, it suggests that it is triggered by some mass driven physical processes. The bending of the main sequence can also be linked to the lower T_{dust} observed in higher mass galaxies for $z \leq 2.5$ which suggests a drop in their SFE.

The evolution of the stellar mass knee (i.e., the M_\star at which the bending appears on the main sequence) is a parameter of great importance in the global shape of the main sequence. Thus, I follow the evolution of the stellar mass knee by following [Daddi et al. \(2022\)](#) (see Eq. 5.12).

$$\frac{\text{SFR}}{\text{SFR}_0} = \frac{1}{1 + (M_0/M_\star)^\gamma}, \quad (5.12)$$

where M_0 represents the stellar mass knee (i.e., the bending point of the main sequence). Following recommendations from [Daddi et al. \(2022\)](#), I set $\gamma = 1.1$, which should help to reduce the errors and should not affect the result much. If γ was defined as a free parameter in the fit, the $\langle \gamma \rangle$ would be close to 1.1 anyway. My best fit parameters are given in Table 5.3, and displayed in Fig. 5.10.

The fit was performed using the **emcee** library using an MCMC approach to navigate the parameter space and runs in about 30 minutes on the laboratory cluster.

Overall, my results are quite comparable to the evolution of the bending found by [Lee et al. \(2015\)](#) and [Daddi et al. \(2022\)](#) (i.e., a decrease in M_0 as one moves to a lower redshift). I see little or no evidence of a bending for $z > 3.1$. I suggest that this may be because the physical processes that trigger the main sequence bending have not had enough time to impact the main sequence trend at the high mass end at $z > 3.1$. Another possibility is that the bending still occurs at high redshifts, but only for very high mass galaxies ($M_\star > 2 - 3 \times 10^{11} M_\odot$), which I could not probe with this study because they are extremely rare.

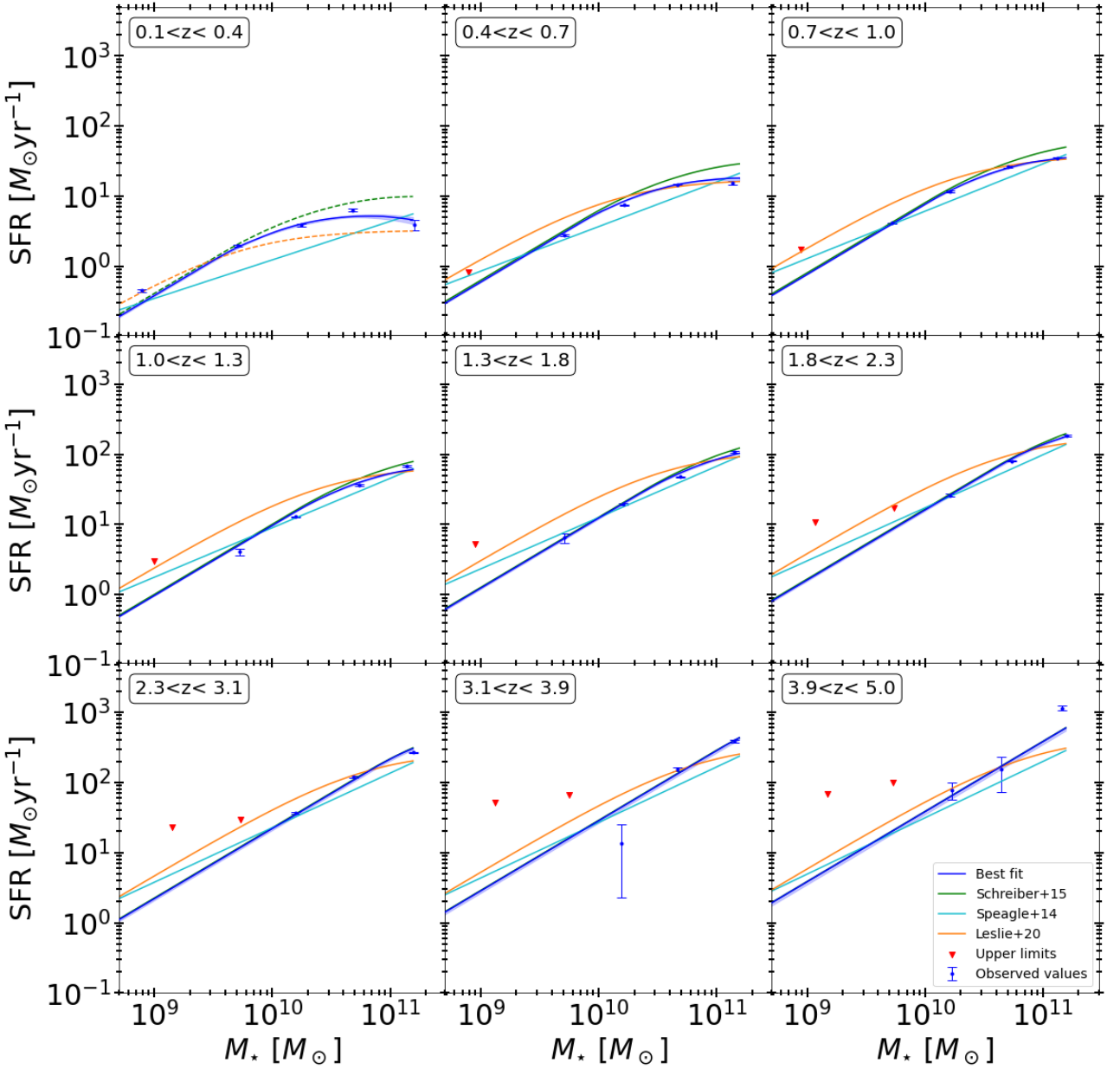


Figure 5.9: SFR as a function of M_* . The red triangles represent upper limits, the blue dots are the observed values from this work. The blue lines represent the best fit from this work, and the shaded area the 68% uncertainty of the fit. The green, cyan and orange lines represent the main sequence from S15, Speagle et al. (2014) and Leslie et al. (2020), respectively. The dashed lines represent extrapolation to redshifts that were not investigated in their respective studies.

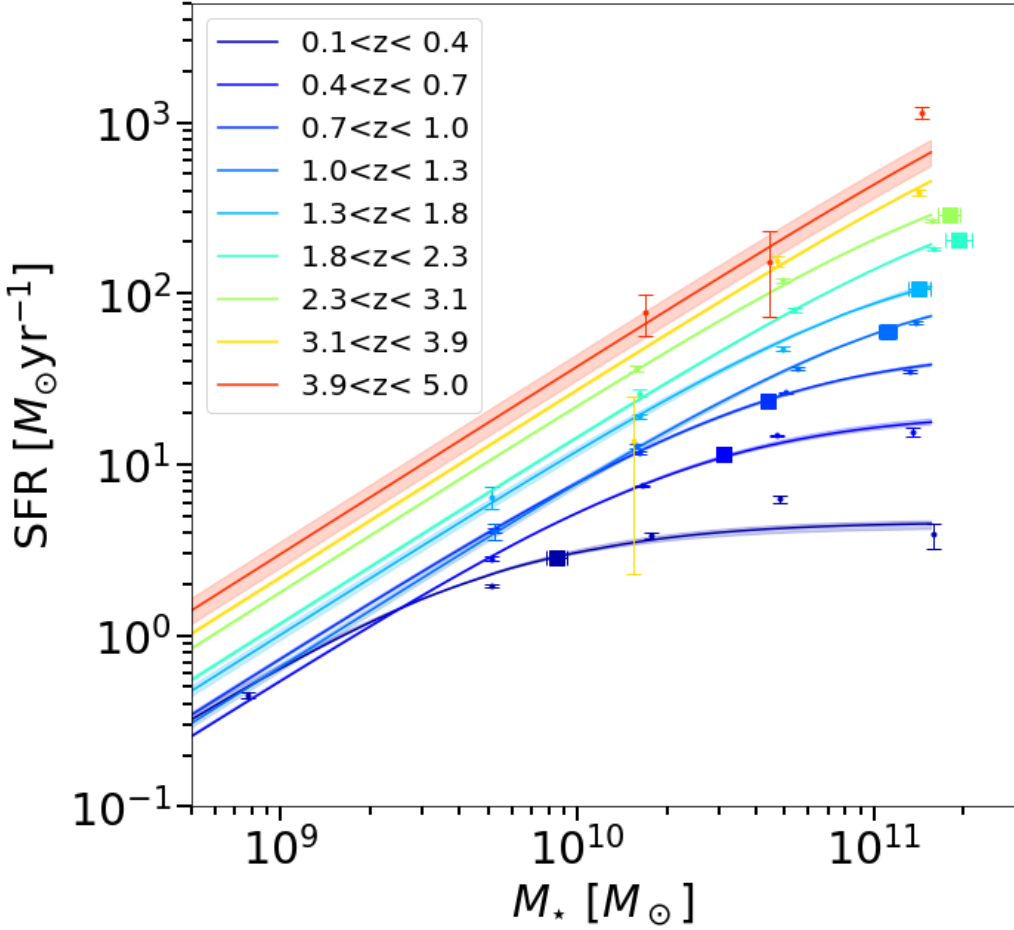


Figure 5.10: SFR as a function of M_{\star} over different redshift bins. The dots represent data from this work. The upper limits were used to perform the fit but are not shown here for clarity. Data are fitted by the Eq. 5.12, the shaded area represents the 68% uncertainty of the fit. The squares represent the best fit parameter M_0 . No bending was detected for $z > 3.1$ and therefore no square error bars are displayed.

Table 5.3: Best fit parameters of the main sequence of star-forming galaxies using Eq. 5.12.

Redshift bin	$\langle z \rangle$	$\log_{10}(M_0/M_{\odot})$	$\log_{10}(SFR_0/M_{\odot}\text{yr}^{-1})$
$0.1 \leq z \leq 0.4$	0.19	$9.93^{+0.04}_{-0.03}$	$0.76^{+0.02}_{-0.02}$
$0.4 \leq z \leq 0.7$	0.59	$10.49^{+0.02}_{-0.03}$	$1.37^{+0.02}_{-0.01}$
$0.7 \leq z \leq 1.0$	0.87	$10.64^{+0.02}_{-0.02}$	$1.68^{+0.02}_{-0.01}$
$1.0 \leq z \leq 1.3$	1.16	$11.05^{+0.03}_{-0.03}$	$2.08^{+0.02}_{-0.02}$
$1.3 \leq z \leq 1.8$	1.52	$11.15^{+0.04}_{-0.03}$	$2.33^{+0.03}_{-0.03}$
$1.8 \leq z \leq 2.3$	2.02	$11.28^{+0.05}_{-0.04}$	$2.61^{+0.04}_{-0.03}$
$2.3 \leq z \leq 3.1$	2.70	$11.25^{+0.04}_{-0.04}$	$2.76^{+0.03}_{-0.03}$
$3.1 \leq z \leq 3.9$	3.37	$11.56^{+0.34}_{-0.16}$	$3.18^{+0.30}_{-0.14}$
$3.9 \leq z \leq 5.0$	4.30	$11.92^{+0.06}_{-0.09}$	$3.90^{+0.07}_{-0.09}$

5.3.2 The contribution of H -dropouts galaxies to SFR

Again, I look at the contribution of H -dropouts to my main sequence estimate. [Wang et al. \(2019\)](#) reported that ALMA-detected H -dropouts mostly fall within the main sequence at $z \sim 4$ (the version from [S15](#) which coincides with that of this work for $2 \leq z \leq 5$). Moreover, as they would increase our sample of galaxies at $M_\star \geq 10^{10} M_\odot$ and $z \geq 3$ by $\sim 7.4\%$, their omission should not alter the overall shape of the main sequence.

5.4 Deducing the gas mass of SFGs

In this section, I look at the evolution of M_{gas} of SFGs, with redshift and M_\star . The M_{gas} of a galaxy is an important property as it represents the fuel available to form stars.

5.4.1 From M_{dust} to M_{gas} and how to derive the metallicity

I chose to calculate M_{gas} from M_{dust} deduced from our stacked SEDs. I can link M_{gas} to M_{dust} by a gas-to-dust mass ratio (δ_{GDR}) that depends only on the metallicity Z ($\log Z = 12 + \log_{10}(O/H)$) of the galaxy,

$$M_{\text{gas}} = \delta_{\text{GDR}}(Z)M_{\text{dust}}. \quad (5.13)$$

Multiple studies (e.g., [Leroy et al. 2011](#); [Magdis et al. 2012](#); [Rémy-Ruyer et al. 2014](#); [Genzel et al. 2015](#)) show consistent $\delta_{\text{GDR}} - Z$ relations that hold at both low and high redshift. We chose here to use the relation from [Magdis et al. \(2012\)](#),

$$\log \delta_{\text{GDR}} = 10.54 - 0.99 \times (12 + \log_{10}(O/H)). \quad (5.14)$$

As for most galaxies we do not have UV or optical spectra, I do not have a direct measurement of their metallicity. To go around this problem, I use the mass-metallicity relation (MZR; [Erb et al. 2006](#)) and follow its redshift dependent version from [Genzel et al. \(2015\)](#),

$$12 + \log_{10}(O/H) = a - 0.087 \times (\log_{10}(M_\star/1.7) - b)^2, \quad (5.15)$$

where $a = 8.74$ and $b = 10.4 + 4.46 \log_{10}(1+z) - 1.78(\log_{10}(1+z))^2$. I note that [Genzel et al. \(2015\)](#) use a [Chabrier \(2003\)](#) IMF to define the MZR. In order to use it correctly, my M_\star must first be divided by a factor of 1.7. We chose to adopt an uncertainty of 0.2 dex for my metallicity following the recommendation from [Magdis et al. \(2012\)](#). These latter metallicities are calibrated in the PP04 N2 scale ($N_2 = [N_{\text{H}}] \lambda 6583/H_\alpha$; [Pettini & Pagel 2004](#)). I note that using the δ_{GDR} relation of [Leroy et al. \(2011\)](#), instead of [Magdis et al. \(2012\)](#), would not change our conclusions because for my sample, the relative median difference in linear scale between the two estimates is $(M_{\text{gas}}^{\text{MZR-Leroy11}} - M_{\text{gas}}^{\text{MZR-Magdis12}})/M_{\text{gas}}^{\text{MZR-Magdis12}} = 0.15^{+0.06}_{-0.08}$.

Another way to calculate the metallicity is the fundamental metallicity relation (FMR; [Mannucci et al. 2010](#), see Eq. 5.16). It differs from the MZR by adding some dependence on the SFR but removing the dependence on the redshift.

$$12 + \log_{10}(O/H) = 8.90 + 0.37m - 0.14s - 0.19^2 + 0.12ms - 0.054s^2, \quad (5.16)$$

where $m = \log_{10}(M_\star/1.7) - 10$ and $s = \log_{10}(SFR/1.7)$. These metallicities are calibrated for the KD02 photoionization models (Kewley & Dopita 2002). I used the recipe from Kewley & Ellison (2008) to convert it into a PP04 N2 scale. But once again the differences in metallicities between the MZR and FMR method do not impact our conclusions, as for our sample, the relative median is $(M_{\text{gas}}^{\text{FMR-Magdis12}} - M_{\text{gas}}^{\text{MZR-Magdis12}})/M_{\text{gas}}^{\text{MZR-Magdis12}} = 0.19^{+0.36}_{-0.22}$.

The previous methods are only reliable when the SED peak is well defined (i.e., T_{dust} and M_{dust}), which is not the case when I only have a single ALMA measurement. The only two bins concerned are $10.0 \leq \log_{10}(M_\star) \leq 10.5$ for $3.1 \leq z \leq 3.9$ and $3.9 \leq z \leq 5.0$. In this situation, I can also estimate M_{gas} from a single band measurement located in the Rayleigh-Jeans part of the SED (e.g., Scoville et al. 2014; Groves et al. 2015; Schinnerer et al. 2016). The main limitation is that it does not take into account the evolution with redshift of the M_{gas} metallicity and T_{dust} (e.g., Genzel et al. 2015; Berta et al. 2016; Schinnerer et al. 2016; Magdis et al. 2017; Harrington et al. 2021). However, this is a reliable way of estimating M_{gas} at low cost (25% uncertainties; Scoville et al. 2016) and especially when there is only one band measured in the Rayleigh-Jeans tail. For these reasons, while I favoured $\delta_{\text{GDR}} - \text{MRZ}$ methods to deduce M_{gas} as long as the T_{dust} was well defined, when only an ALMA measurement is available, we calculated M_{gas} by the method described in Scoville et al. (2016), i.e.,

$$M_{\text{gas}} = 1.78S_{\nu_{\text{obs}}}[\text{mJy}](1+z)^{-4.8} \left(\frac{\nu_{850\mu\text{m}}}{\nu_{\text{obs}}} \right)^{3.8} (d_{\text{L}}[\text{Gpc}])^2 \times \frac{6.7 \times 10^{19}}{\alpha_{850}} \frac{\Gamma_0}{\Gamma_{\text{RJ}}} 10^{10} M_\odot \quad \text{for } \lambda_{\text{rest}} > 250\mu\text{m}, \quad (5.17)$$

$$\Gamma(z) = \frac{h\nu_{\text{obs}}(1+z)}{k_B T_d} \frac{1}{\left(\exp(\frac{h\nu_{\text{obs}}(1+z)}{k_B T_d}) - 1 \right)}, \quad (5.18)$$

where d_{L} is the luminosity distance, $\alpha_{850} = 6.2 \times 10^{19} \text{ erg sec}^{-1} \text{ Hz}^{-1} \text{ M}_\odot^{-1}$, $\Gamma_0 = \Gamma(z=0)$ and $\Gamma_{\text{RJ}} = \Gamma(z)$, h is Planck constant, k_B is Boltzmann constant, $T_d = 25\text{K}$ and $\nu_\lambda = \frac{c}{\lambda}$. I note that this technique provides, for our sample, consistent results with those of the MZR method, with a relative median $(M_{\text{gas}}^{\text{Scoville16}} - M_{\text{gas}}^{\text{MZR-Magdis12}})/M_{\text{gas}}^{\text{MZR-Magdis12}} = 0.20^{+0.37}_{-0.30}$ when both the $\delta_{\text{GDR}} - \text{MRZ}$ and Scoville et al. (2016) could be performed.

In summary, I chose to calculate our M_{gas} using Magdis et al. (2012) for $\delta_{\text{GDR}}(Z)$ (Eq. 5.14) and Genzel et al. (2015) MZR for the metallicities (Eq. 5.15). When the peak of the SED is poorly constrained and an ALMA flux is available, I chose to calculate M_{gas} from Scoville et al. (2016) method. For the rest of the paper, I will refer to $M_{\text{gas}}^{\text{MZR-Magdis12}}$, or $M_{\text{gas}}^{\text{Scoville16}}$ simply as M_{gas} . My M_{gas} measurements are displayed in Fig. 5.11.

Here M_{gas} represents the total gas budget of a galaxy including both the molecular gas mass (M_{H_2}) and the atomic gas mass (M_{HI}), i.e., $M_{\text{gas}} = M_{\text{H}_2} + M_{\text{HI}}$. The HI content of galaxies is still poorly known outside the local universe because the 21cm emission line is difficult to detect with current facilities. However, Bauermeister et al. (2010) showed that it is unlikely that the HI content of galaxies varies strongly with redshift. In contrast, the H_2 content evolves strongly with redshift (e.g., Daddi et al. 2010; Tacconi et al. 2010, 2013; Lagos et al. 2015; Genzel et al. 2015; Tacconi et al. 2018). In Tacconi et al. (2018), it was concluded that the assumption $M_{\text{gas}} \sim M_{\text{H}_2}$ should hold for $z > 0.4$. Therefore, I decided not to consider my M_{gas} for $z < 0.4$ (i.e., my first redshift bin), as I could not probe and thus remove the HI contribution to M_{gas} at these redshifts. In order to add some reliable measurements of M_{H_2} to my study at $z < 0.4$, I used data points from Saintonge et al. (2017) that come from very local measurements ($0.01 \leq z \leq 0.05$).

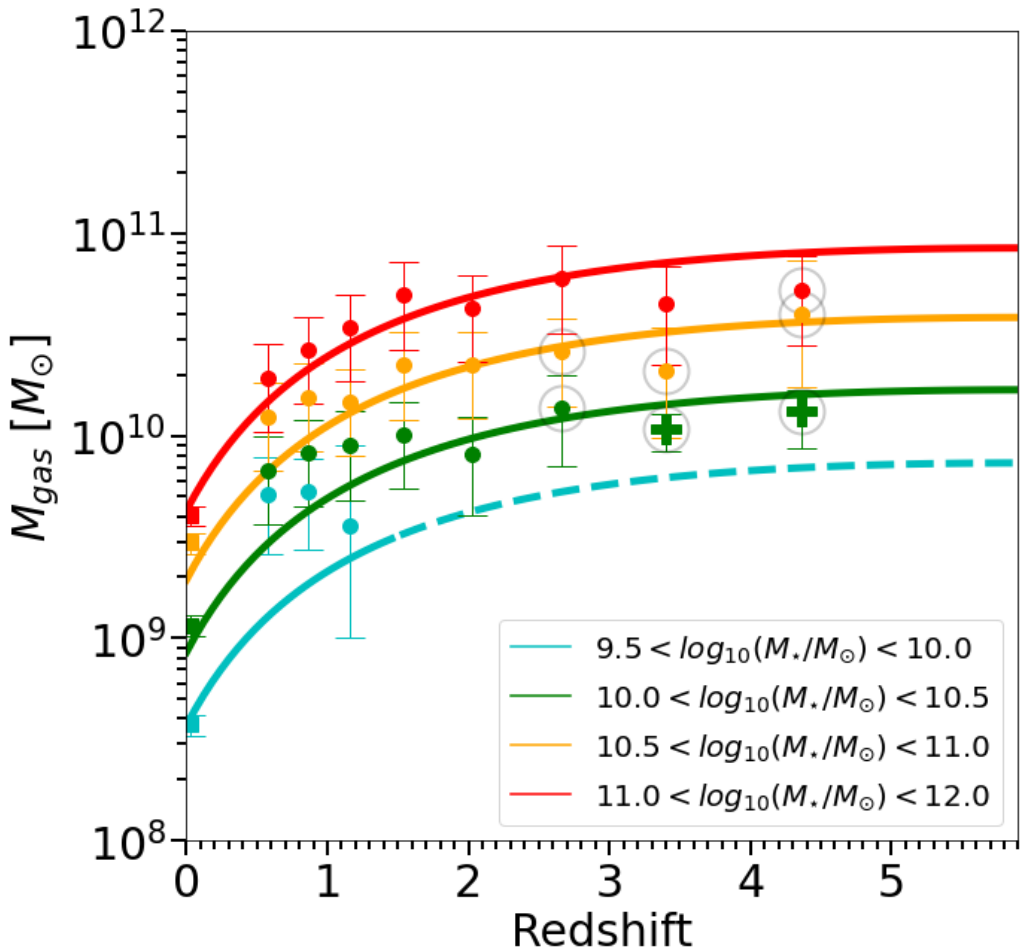


Figure 5.11: M_{gas} as a function of redshift for different M_{\star} . The dots represent M_{gas} estimates from this work using the $\delta_{\text{GDR}}-\text{MRZ}$ method. The crosses represent M_{gas} estimates from this work following the method from Scoville et al. (2016). The squares are measurements from Saintonge et al. (2017). The bins that have been corrected for the H -dropout contribution are circled. The solid colour lines represent the best fit from this work, the dashed lines are the best fit extrapolation.

Table 5.4: Best fit parameters of M_{gas} evolution of the main sequence using Eq. 5.19. * indicates that this parameter was fixed during the fit.

A	B	F	D	β^*
$0.0572^{+0.176}_{-0.044}$	$-1.81^{+0.82}_{-1.86}$	$0.843^{+0.253}_{-0.366}$	$-0.264^{+0.073}_{-0.068}$	2

5.4.2 The contribution of H -dropout galaxies

I examined the contribution of the H -dropouts to M_{gas} in order to have the most unbiased view possible. Here, I have simply calculated the M_{gas} , associated with each H -dropout in the sample of [Wang et al. \(2019\)](#), using their ALMA measurement at $870\mu\text{m}$ and following the [Scoville et al. \(2016\)](#) method.

The final contribution of the H -dropout to the total M_{gas} within each bin is $M_{\text{gas}}^{H-\text{dropout}} \times \frac{N_{\text{gal}}^{H-\text{dropout}}}{\text{Area}^{H-\text{dropout}}} / (M_{\text{gas}}^{H-\text{dropout}} \times \frac{N_{\text{gal}}^{H-\text{dropout}}}{\text{Area}^{H-\text{dropout}}} + M_{\text{gas}} \times \frac{N_{\text{gal}}}{\text{Area}}) = 12\%^{+11\%}_{-4\%}$ on average (only the bins with at least one H -dropout are taken into account). The contribution of H -dropouts can represent up to $\sim 20\%$ for some bins, hence I chose to add it to our data. The seven bins that have been corrected for the H -dropout contribution are circled Fig. 5.11.

5.4.3 Fitting the M_{gas} evolution of SFGs

In Fig. 5.11, I observe a rapid rise with redshift from [Saintonge et al. \(2017\)](#) data at low redshift, to my first data points at $z \sim 0.6$. Then, at fixed M_{\star} , M_{gas} reach a maximum at $z \sim 1 - 2$ and remains relatively constant as the redshift increases. At fixed redshift, M_{gas} gradually increase with M_{\star} .

I chose to fit our data using the formula of [Tacconi et al. \(2018\)](#):

$$\log_{10}(M_{\text{gas}}) = A + B(\log_{10}(1 + z) - F)^{\beta} + D(\log_{10}(M_{\star}/1.7) - 10.7) + \log_{10}(M_{\star}/1.7), \quad (5.19)$$

where the factor 1.7 represents the conversion of M_{\star} from a [Salpeter \(1955\)](#) to [Chabrier \(2003\)](#) IMF. As my data points represent main sequence galaxies, I cannot probe the C_{μ} term in [Tacconi et al. \(2018\)](#), that represents the evolution with respect to the distance to the main sequence, i.e., R_{SB} . I do not explore the morphology of galaxies in my study, which makes it impossible to probe the term E_{μ} , which compares the effective radius of galaxies (R_{e}) to the mean effective radius of the star forming population R_{e_0} . The results are displayed in Fig. 5.11, and our best fit parameters are given in Table 5.4.

The fit was performed using the `emcee` library using an MCMC approach to navigate the parameter space and runs in about 20 minutes on my work laptop.

Looking at Fig. 5.11, I notice that M_{gas} observed at low redshift ($0.4 \leq z \leq 1$) tends to be higher than the best fit trend (even though it is in most cases within the error bars). A similar effect has been observed by [Tacconi et al. \(2018\)](#) who measured higher depletion times ($\tau_{\text{dep}} = M_{\text{gas}}/\text{SFR} = 1/\text{SFE}$) deduced from dust observations compared to the ones deduced from CO line fluxes. The

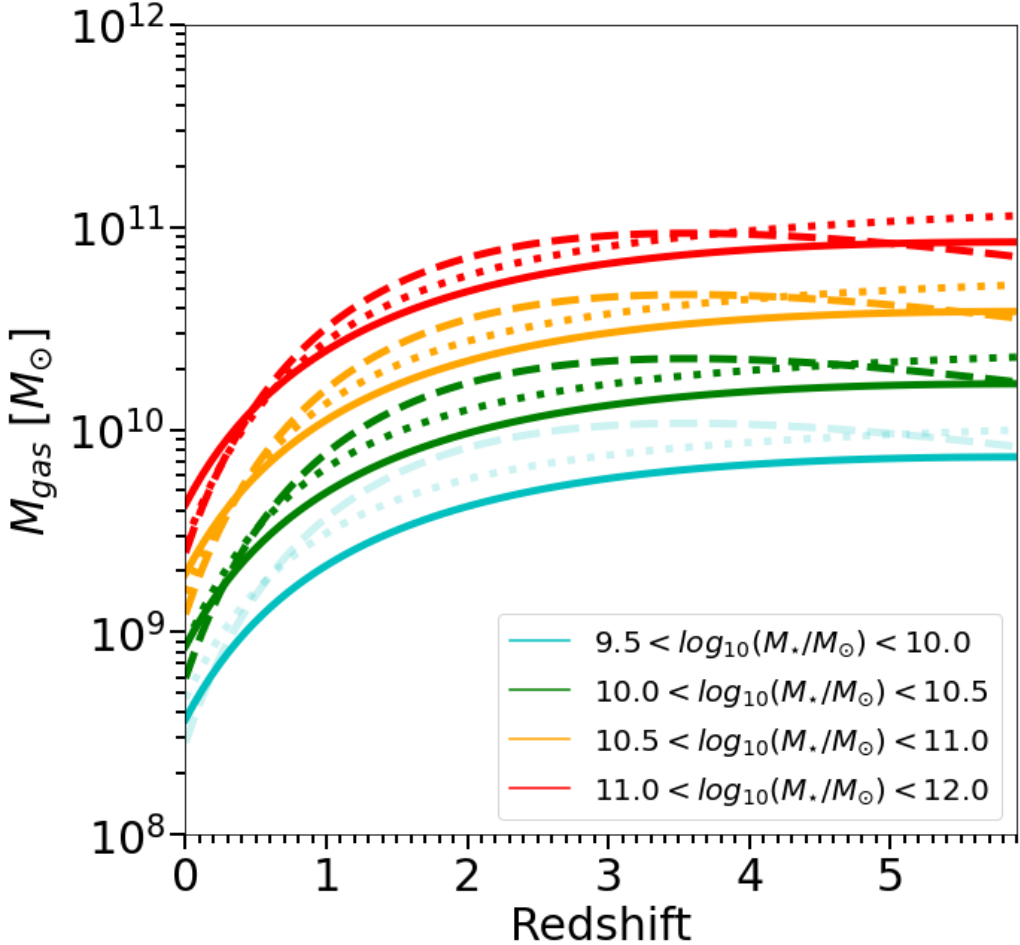


Figure 5.12: M_{gas} as a function of redshift and M_{\star} . The solid lines represent the best fit from this work colour-coded by M_{\star} , the dashed lines represent the trend from Tacconi et al. (2018), the dotted lines are from Wang et al. (2022). The faded lines represent an extrapolation from their respective laws.

effect observed in Tacconi et al. (2018) decreases slowly with redshift (about 0.3 dex at $z \sim 0.4$ to 0 at $z \sim 1.5$) and roughly matches the effect observed here. As in Tacconi et al. (2018), I conclude that this effect arises when deducing M_{gas} from dust observations.

I compare my results to the trends observed by Tacconi et al. (2018) and Wang et al. (2022) in Fig. 5.12. The trend observed by Wang et al. (2022) M_{gas} comes from millimetre fluxes used to deduce M_{gas} using the method from Scoville et al. (2016). Overall, my trend is much more similar to that found in Wang et al. (2022) than Tacconi et al. (2018), but tends to yield slightly lower M_{gas} at high redshift compared to what is reported by Wang et al. (2022).

5.4.4 Impact on M_{gas} of the dust grain model

As mentioned in Chapter 4, I chose to work with M_{dust} from amorphous silicate and graphitic grains (Draine & Li 2007) instead of amorphous carbon (Galliano et al. 2011; S18). I investigated what

the impact would have been on M_{gas} if I had chosen a model based on amorphous carbon such as [Galliano et al. \(2021\)](#), i.e., reading M_{dust} directly from the [S18](#) library template and converting it into M_{gas} following [Galliano et al. \(2021\)](#). Although the results are quite comparable, using the model from [Galliano et al. \(2021\)](#), would translate into slightly lower M_{gas} ($\sim -10\%$ at $z = 4$). These differences would not have changed the conclusions drawn in this work.

5.5 Deducing the cosmic star formation history

To calculate the ρ_{SFR} , I start from the stellar mass function of SFGs of [Davidzon et al. \(2017\)](#), that is given for different redshift bins. For each redshift bin, I generated galaxies with uniform redshift distribution within the bin, and a M_{\star} distribution following these stellar mass functions. From the redshift and M_{\star} , I then assigned a SFR using the same method as in Sect. 4.4.1. In summary, $SFR = R_{\text{SB}} \times SFR_{\text{MS}}$, where SFR_{MS} is calculated from the main sequence evolution found in this work (See Eq. 5.11 and parameters Table 5.2). And a R_{SB} is randomly drawn from a double lognormal distribution representing the position of normal and starbursting galaxies relative to the main sequence (Eq. 4.4). Then ρ_{SFR} is calculated by summing the SFR of galaxies down to $M_{\star}^{\text{lim}} = 3 \times 10^9 M_{\odot}$ (i.e., integrating the stellar mass function down to roughly $0.03 \times M_{\star}$, where M_{\star} corresponds to the M_{\star} of the knee of the stellar mass function). Errors were generated by varying the SFR_{MS} trend of Eq. 5.11 within the errors of the fit, a 100 times.

The program runs on the laboratory cluster and mostly take advantage of the **numpy** and **astropy** libraries. It takes about 13 hours to generate the galaxies catalogues following the previous method, and an extra 40 minutes to compute a corresponding ρ_{SFR} (ρ_{gas} is computed at the same time).

The study of [Wang et al. \(2019\)](#) presents the contribution to ρ_{SFR} of H -dropout galaxies, which can reach up to 10% at $z \sim 4 - 5$. I have therefore added the contribution of H -dropout galaxies of [Wang et al. \(2019\)](#) to my ρ_{SFR} considering the sample of H -dropout galaxies have a median stellar mass of $M_{\star} \sim 10^{10.6} M_{\odot}$ ([Wang et al. 2019](#)).

I compare the ρ_{SFR} evolution with that of [Madau & Dickinson \(2014\)](#) who integrate UV and IR luminosity functions down to $L_{\min} = 0.03L_{\star}$. Deducing ρ_{SFR} by integrating luminosity functions down to $0.03L_{\star}$, or the mass function down to $3 \times 10^9 M_{\odot}$ should yield, to the first order, similar results ([Schreiber et al. 2015](#)). Thus, all conclusions on the evolution of the ρ_{SFR} in this thesis should be understood in this framework, as integrating the luminosity function down to lower luminosities, or the mass function down to lower masses, must yield a higher total ρ_{SFR} .

The total ρ_{SFR} is displayed in Fig. 5.13 along with some examples from the literature, and the data points from this work are summarised in Table 5.5. I observe a gradual rise of ρ_{SFR} from $z \sim 5$ to $z \sim 2$, and then it decreases down to $z \sim 0.35$. The high masses (i.e., $\log_{10}(M_{\star}/M_{\odot}) > 10$) account for most of the ρ_{SFR} until $z \sim 4$. On the other hand the ρ_{SFR} associated to low mass galaxies (i.e., $\log_{10}(M_{\star}/M_{\odot}) \leq 10$) is roughly constant over $0 \leq z \leq 5$.

I can see that our estimate of the total ρ_{SFR} is close to what has been observed by [Leslie et al. \(2020\)](#) and to the evolution of [Madau & Dickinson \(2014\)](#). On the other hand, the measurements from [Gruppioni et al. \(2020\)](#) are mostly in disagreement with my results at high redshift (i.e., $z \geq 2$). The ρ_{SFR} from [Gruppioni et al. \(2020\)](#) is deduced from the integration of the IR-luminosity function (which makes it ρ_{SFR}^{IR}) down to $10^8 L_{\odot}$.

Table 5.5: ρ_{SFR} as a function of redshift. Here, ρ_{SFR} values include the H -dropout contribution from Wang et al. (2019).

Redshift	0.35	0.65	0.95	1.3	1.76	2.26	2.76	3.25	3.75	5.06
$\log_{10} \left(\frac{\rho_{\text{SFR}}}{M_{\odot} \text{yr}^{-1} \text{Mpc}^{-3}} \right)$	$-1.34^{+0.01}_{-0.01}$	$-1.18^{+0.01}_{-0.01}$	$-1.00^{+0.01}_{-0.01}$	$-0.91^{+0.01}_{-0.01}$	$-0.87^{+0.01}_{-0.01}$	$-0.95^{+0.01}_{-0.01}$	$-1.01^{+0.02}_{-0.01}$	$-1.15^{+0.02}_{-0.02}$	$-1.29^{+0.03}_{-0.02}$	$-1.41^{+0.03}_{-0.03}$
$\log_{10} \left(\frac{\rho_{\text{SFR}}^{M_{\star} > 10^{10} M_{\odot}}}{M_{\odot} \text{yr}^{-1} \text{Mpc}^{-3}} \right)$	$-1.48^{+0.01}_{-0.01}$	$-1.30^{+0.01}_{-0.01}$	$-1.09^{+0.01}_{-0.01}$	$-0.99^{+0.01}_{-0.01}$	$-0.93^{+0.01}_{-0.01}$	$-1.03^{+0.01}_{-0.01}$	$-1.12^{+0.02}_{-0.01}$	$-1.30^{+0.02}_{-0.02}$	$-1.45^{+0.03}_{-0.02}$	$-1.57^{+0.04}_{-0.03}$
$\log_{10} \left(\frac{\rho_{\text{SFR}}^{M_{\star} < 10^{10} M_{\odot}}}{M_{\odot} \text{yr}^{-1} \text{Mpc}^{-3}} \right)$	$-1.90^{+0.02}_{-0.01}$	$-1.81^{+0.01}_{-0.01}$	$-1.72^{+0.01}_{-0.01}$	$-1.70^{+0.01}_{-0.01}$	$-1.69^{+0.01}_{-0.01}$	$-1.75^{+0.01}_{-0.01}$	$-1.67^{+0.02}_{-0.02}$	$-1.70^{+0.03}_{-0.02}$	$-1.81^{+0.04}_{-0.02}$	$-1.93^{+0.05}_{-0.02}$

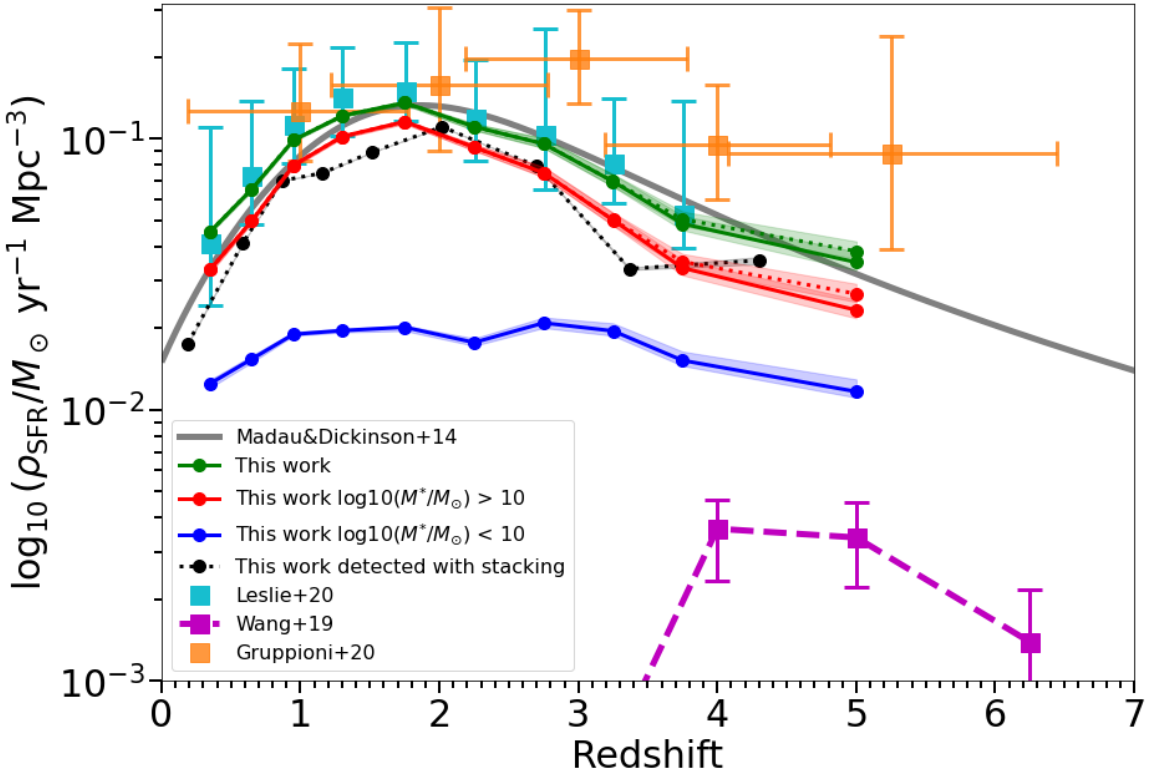


Figure 5.13: Cosmic star formation rate density as a function of redshift. The green line represents the total ρ_{SFR} trend from this work (i.e., integrating the stellar mass function down to $3 \times 10^9 M_{\odot}$). The red and blue lines represent the contribution of galaxies with $\log_{10}(M_{\star}/M_{\odot}) > 10$ and $\log_{10}(M_{\star}/M_{\odot}) < 10$, respectively. The black dotted line represents the ρ_{SFR} detected with stacking. The purple squares show the contribution of H -dropout from Wang et al. (2019). The dotted green and red lines show the trend once H -dropout contribution from Wang et al. (2019) has been added to the respective coloured solid lines. The grey line represents the trend from Madau & Dickinson (2014). The cyan and orange squares represent ρ_{SFR} estimate from Leslie et al. (2020) and Gruppioni et al. (2020), respectively.

In Fig. 5.14, I show the contribution to the total ρ_{SFR} of the full range of stellar masses. I observe that the increase in the total ρ_{SFR} , from $z \sim 5$ to $z \sim 2$, comes from the growing number of massive

galaxies (i.e., $\log_{10}(M_\star/M_\odot) > 10$), which can be seen in the evolution of the stellar mass function at these redshifts (Davidzon et al. 2017). Downsizing and the bending of the main sequence explain the fall of the contribution of massive galaxies from $z \sim 2$ to $z \sim 0$. I again observe that massive galaxies (i.e., $\log_{10}(M_\star/M_\odot) > 10$) dominate the total ρ_{SFR} at all redshifts (i.e., they account for more than 70%). In particular, it appears that galaxies with $10.5 \leq \log_{10}(M_\star/M_\odot) \leq 11.25$ account for more than $\sim 55\%$ of the total ρ_{SFR} at $z = 2$, making them the main driver of the peak in the observed cosmic star formation history at this redshift.

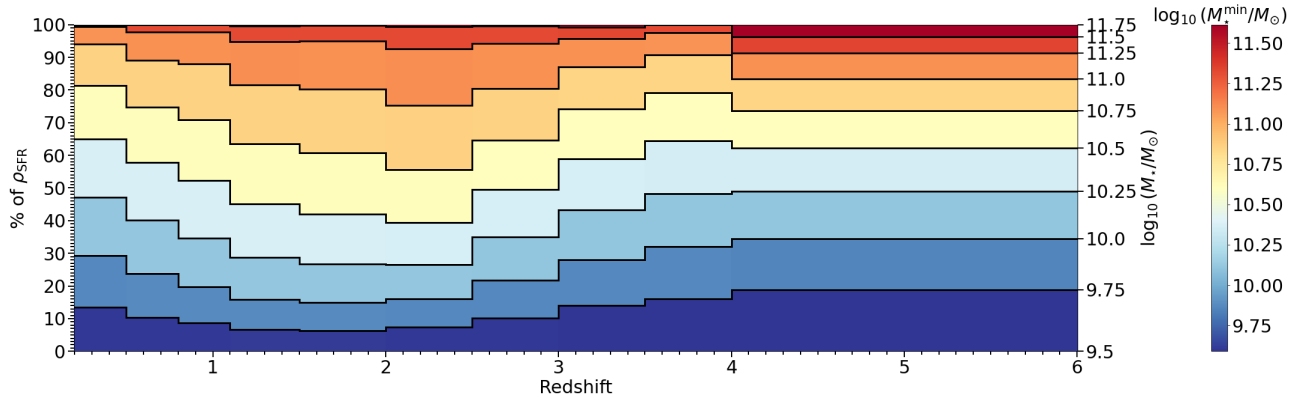


Figure 5.14: Contributions over the whole range of stellar masses to the total ρ_{SFR} as a function of redshift for SFGs.

The program used to generate Fig. 5.14 (and other figures of this type, i.e. Fig. 5.18) runs on the laboratory cluster and takes about 40 minutes to be completed.

5.6 Deducing the cosmic evolution of the gas mass density

In Sect. 5.5, I have simulated a catalogue of galaxies where for each of them, I calculated M_\star and R_{SB} . From these properties, I now infer M_{gas} by expanding Eq. 5.19 as:

$$\begin{aligned} \log_{10}(M_{\text{gas}}) = & A + B(\log_{10}(1+z) - F^\beta) + D(\log_{10}(M_\star/1.7) - 10.7) \\ & + \log_{10}(M_\star/1.7) + C \times \log_{10}(R_{\text{SB}}(z, M_\star)). \end{aligned} \quad (5.20)$$

Here A, B, D, F and β are taken from this work (see Table 5.4), and $C = 0.53$ is taken from Tacconi et al. (2018). Next, the cosmic evolution of gas mass density (ρ_{gas}) is calculated by summing the M_{gas} of galaxies down to $M_\star^{lim} = 3 \times 10^9 M_\odot$. Errors were generated by varying our best-fit of $M_{\text{gas}}^{\text{MS}}$ within its errors, one hundred times. Defined this way, ρ_{gas} directly represents the gas content of galaxies contributing to the ρ_{SFR} presented in Fig. 5.13. I display the evolution of ρ_{gas} as a function of redshift in Fig. 5.15. I can see the same kind of features as for the evolution of ρ_{SFR} : a rise and fall with redshift with a maximum around $z \sim 2$; a dominance across all redshifts of the high mass galaxies (i.e., $\log_{10}(M_\star/M_\odot) > 10$) contribution; and a relatively flat evolution of the low mass galaxies (i.e., $\log_{10}(M_\star/M_\odot) < 10$). This shows that the SFE of both high and low mass galaxies are not drastically changing with time, and thus that the gas content of galaxies (i.e., the accretion) is the primary driver of their SFRs: high mass galaxies have higher SFR at fixed redshift because they have more gas. However, comparing the relative evolution of ρ_{gas} (see Fig. 5.15) and ρ_{SFR} (see Fig. 5.13) shows that

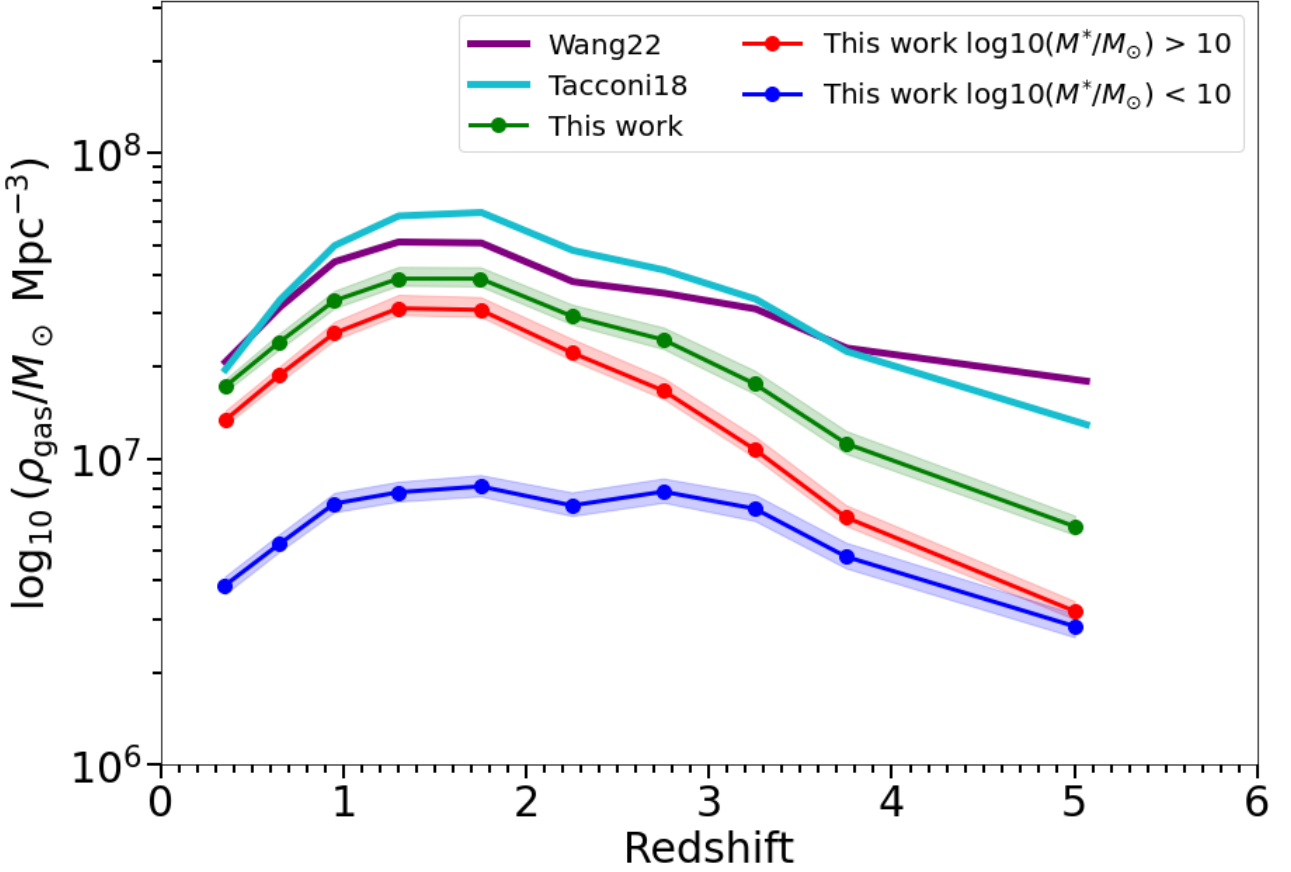


Figure 5.15: The cosmic gas mass density as a function of redshift. The green line represents the total ρ_{gas} inferred from this work (i.e., integrating the stellar mass function down to $0.03M_{\star}$). The red and blue lines represent the contribution to the total ρ_{gas} of galaxies with $\log_{10}(M_{\star}) > 10$ and $\log_{10}(M_{\star}) < 10$, respectively. The purple and cyan lines represent ρ_{gas} deduced from the M_{gas} definition of [Wang et al. \(2022\)](#) and [Tacconi et al. \(2018\)](#), respectively

$\rho_{\text{gas}}^{z=5}/\rho_{\text{gas}}^{z=0}$ (and in particular the high mass contribution) is lower by a factor $\sim 3 - 4$ compared to $\rho_{\text{SFR}}^{z=5}/\rho_{\text{SFR}}^{z=0}$. This hints that one unit of gas leads to more stars being formed at $z \sim 5$ compared to $z \sim 0$ (i.e., a higher SFE at $z \sim 5$ compared to $z \sim 0$).

I substituted, in the later method to estimate ρ_{gas} , M_{gas} from this work, for best-fit of M_{gas} from the literature and compared it to my estimate of ρ_{gas} . I can see in Fig. 5.15, that the redshift evolution of ρ_{gas} from [Tacconi et al. \(2018\)](#) or [Wang et al. \(2022\)](#) are higher compared to the one from this work. These are simply resulting from discrepancies already observed in the respective M_{gas} trends they were built from. As already pointed out in [Liu et al. \(2019\)](#), the form of the formula chosen to fit M_{gas} can have a significant impact on the resulting ρ_{gas} trend, and could be the cause of what is observed here.

I also computed ρ_{gas} by summing M_{gas} of all galaxies down to several different M_{lim}^* ($M_{\text{lim}}^* = 1.7 \times 10^8$, 1.7×10^9 and $1.7 \times 10^{10} M_{\odot}$). I compare it to [Magnelli et al. \(2020\)](#) where a ρ_{gas} was computed for the same M_{lim}^* from the stacking in ALMA of H -band selected galaxies and through the method from [Scoville et al. \(2016\)](#). Results are displayed in Fig. 5.16. Here, my work agrees quite

well with that of [Magnelli et al. \(2020\)](#) for the total ρ_{gas} (i.e., $M_{\star}^{\text{lim}} = 1.7 \times 10^8$). However the mass distribution is not similar: massive galaxies (i.e., $M_{\star}^{\text{lim}} = 1.7 \times 10^{10}$) contribute more at low redshift (i.e., $z \leq 0.7$) in my work in comparison to [Magnelli et al. \(2020\)](#); conversely, their contribution is lesser at higher redshift (lower by a factor ~ 2.7 at $z \sim 2.8$) compared to [Magnelli et al. 2020](#).

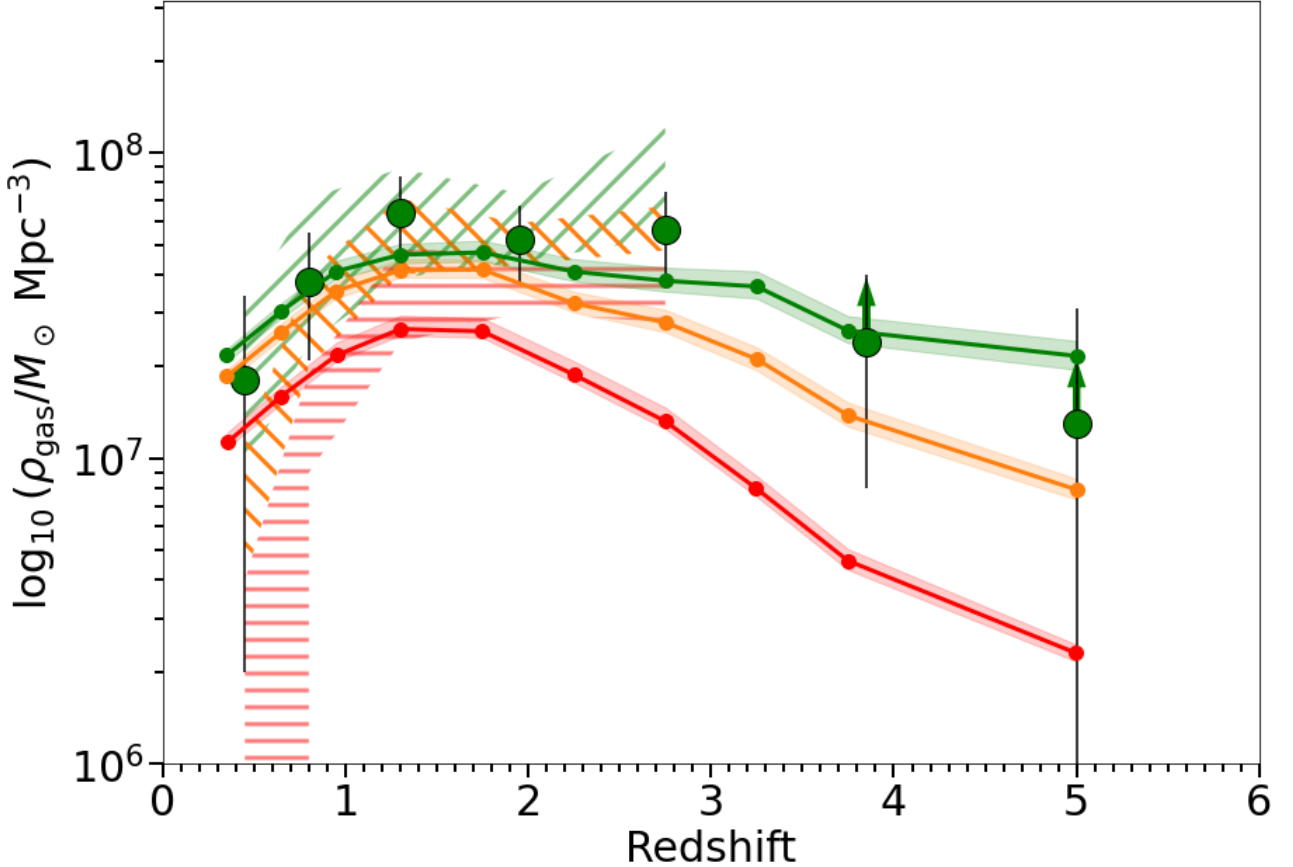


Figure 5.16: The cosmic gas mass density as a function of redshift. The green, orange and red lines represent ρ_{gas} derived from this work with M_{\star}^{lim} of 1.7×10^8 , 1.7×10^9 and $1.7 \times 10^{10} M_{\odot}$, respectively. The green, orange and red hatches represent estimates of ρ_{gas} from [Magnelli et al. \(2020\)](#) with M_{\star}^{lim} of 1.7×10^8 , 1.7×10^9 and $1.7 \times 10^{10} M_{\odot}$, respectively. The green dots with black circles depict the estimate of ρ_{gas} from [Magnelli et al. \(2020\)](#) for $M_{\star} > M_{\text{limit}}$, M_{limit} being the stellar mass completeness limit from [Magnelli et al. \(2020\)](#). The green dots with a green arrow represent lower limits.

5.7 Discussion

In this section, I will attempt to put together all galaxy properties deduced earlier into a global view.

5.7.1 SFR, M_{gas} and SFE

Here, when I discuss the evolution of galaxies, it should be understood that I am discussing the evolution of main sequence galaxies, as the scaling relations of SFR and M_{gas} with M_{\star} and redshift

have been deduced for main sequence galaxies.

One can get a better picture of the evolution of main sequence galaxies by combining evolutionary properties such as SFR (see Fig. 5.8) and M_{gas} (see Fig. 5.11). In Fig. 5.17, I display the $SFE = SFR/M_{\text{gas}}$ as a function of M_{\star} at different redshifts. I fitted the SFE using Eq. 5.12; in this case the parameter γ was not fixed. In Fig. 5.17, we can observe two regimes depending on the redshift: at $z \leq 2$ and $z > 2$.

The fit was performed using the **emcee** library using an MCMC approach to navigate the parameter space and runs in about 40 minutes on my work laptop.

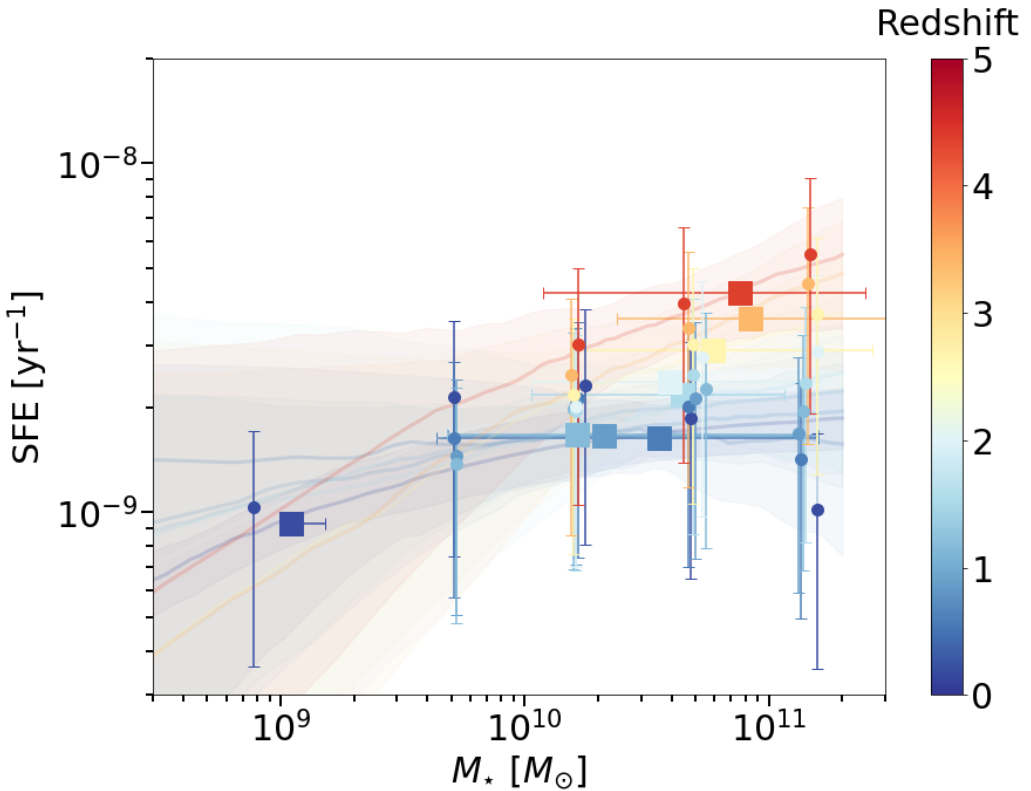


Figure 5.17: SFE as a function of M_{\star} , colour coded by redshift. Dots are measurements from this work. Data are fitted by the Eq. 5.12, the shaded area represents the 68% uncertainty of the fit. The squares represent the best fit parameter M_0 .

At $z \leq 2$, in Fig. 5.17, the SFE does not evolve much with redshift and is roughly the same for all stellar masses (except for the highest bin, i.e., $M_{\star} \geq 10^{11} M_{\odot}$): $SFE \sim 2 \text{ Gyr}^{-1}$. At $z \leq 2$, the fit gives γ close to 0 (M_0 is not relevant in that case), which means that the SFE is constant. On the other hand, in Fig. 5.11, M_{gas} increases with redshift and M_{\star} at $z \leq 2$. This means that an increase in SFR as a function of redshift or stellar mass, at $z \leq 2$, is mainly due to the variation of M_{gas} .

At $z > 2$, in Fig. 5.17, the SFE increases with redshift at fixed stellar mass: by a factor ~ 1.7 between $z \sim 2$ and $z \sim 4.3$. On the other hand, in Fig. 5.11, M_{gas} remains roughly constant for $z > 2$. This means that SFE plays a non-negligible role in increasing the normalisation of the main sequence SFR between $2 \leq z \leq 4.3$. We can try to quantify how much of the increase in the normalisation of the

main sequence is due to SFE. Between $2 \leq z \leq 4, 3$, the normalisation of the main sequence increases by a factor $\alpha_{\text{SFR}} \sim 2, 5$ of which $\alpha_{\text{SFE}} \sim 1.7$ comes from the increase in SFE, and $\alpha_{M_{\text{gas}}} = \alpha_{\text{SFR}}/\alpha_{\text{SFE}} \sim 1.5$ comes from M_{gas} , which correspond approximately to the increase observed in Fig. 5.11. At $z > 2$, the increase in SFE and M_{gas} has a comparable impact on the increase in SFR at fixed stellar mass (i.e., the normalisation of the main sequence).

Next, if one believe the evolution with stellar mass of the SFE in Fig. 5.17 (a constant fit within the error bars of the data points is possible at all redshifts), the contribution of SFE and M_{gas} to an increase in SFR can be also seen as a function of stellar mass. For example, at $z \sim 4.3$, where there is no bending of the main sequence, we can observe in Fig. 5.8 an increase of SFR by a factor 10 between $10^{10} M_{\odot} \leq M_{\star} \leq 10^{11} M_{\odot}$ (i.e., a slope of 1). This same range results in an increase by a factor of ~ 5 in M_{gas} (see Fig. 5.11), and ~ 2 in SFE (see Fig. 5.17). Thus, at $z \sim 4.3$, although the increase in SFR along M_{\star} is mainly due to M_{gas} , SFE also plays an important role. However, if we consider lower redshifts (i.e. $z \leq 2$), SFE now remains constant with stellar mass (SFE is arguably decreasing, in particular for the highest stellar mass range, i.e., $M_{\star} \geq 10^{11} M_{\odot}$ but let us consider $M_{\star} \leq 10^{11} M_{\odot}$ for now). Consequently, an increase in SFR with stellar mass is entirely due to an increase in M_{gas} . For example, at $z \sim 1.15$, between $10^{10} M_{\odot} \leq M_{\star} \leq 10^{11} M_{\odot}$, SFR and M_{gas} both increase by a factor of ~ 5 , while SFE remains constant. As a result, the slope of the main sequence at $z \sim 1.15$ (and for $10^{10} M_{\odot} \leq M_{\star} \leq 10^{11} M_{\odot}$) is no longer 1 but $\log_{10}(5) = 0.7$, which results in the appearance of the bending of the main sequence. To take this further, we can now look at the apparent decrease in SFE with redshift for the highest stellar mass bin (i.e., $M_{\star} \geq 10^{11} M_{\odot}$) to explain the bending of the main sequence. Again, if we consider the data points between the two mass bins $10^{10} M_{\odot} \leq M_{\star} \leq 10^{10.5} M_{\odot}$ and $M_{\star} \geq 10^{11} M_{\odot}$ at $z \sim 0.2$, the bending of the main sequence can be explained: SFR remains roughly constant, M_{gas} increases by a factor ~ 2.5 and SFE actually decreases by a factor ~ 2.5 . This specific case, at $z \sim 0.2$, can however be discussed as it is strongly influenced by the point at $M_{\star} \geq 10^{11} M_{\odot}$ for which I only have 5 galaxies to stack and, therefore, might not exactly represent the true main sequence at $z \sim 0.2$.

My conclusion is that the gradual appearance of the bending of the the main sequence with redshift is due to the gradual disappearance of this extra factor of 1.7 due to SFE (observed at $z \sim 4.3$ and absent at $z \sim 2$). Then, at a fixed lower redshift (i.e. $z < 2$), the bending of the main sequence (as M_{\star} increases) is mainly due to a decrease in M_{gas} with stellar mass, and to second order, to a decrease in SFE with stellar mass. This characteristic is also observed in the local universe (i.e., for $0.01 < z < 0.05$) in [Saintonge et al. \(2016\)](#): when the stellar mass increase by a factor 10, SFR increase by a factor ~ 1.4 , which is due to an increase of M_{gas} by a factor ~ 1.8 and a decrease in SFE by a factor ~ 1.25 . [Saintonge et al. \(2016\)](#) reaches the same conclusion in the local universe: at a fixed redshift, M_{gas} is the main reason for the bending of the main sequence. The slow downfall of star formation efficiency in the most massive galaxies (i.e., $M_{\star} \geq 10^{11} M_{\odot}$) observed in Fig. 5.17 between $0.1 \leq z \leq 4.3$, was also observed in [Schreiber et al. \(2016\)](#). It seems that a discontinuation of gas accretion cannot be the only reason for the bending of the SFR main sequence ([Daddi et al. 2022](#)). It must be coupled with other effects that prevent the gas in high M_{\star} galaxies from cooling and collapsing into stars (i.e., an evolution of the SFE). The main driver of the bending could be the quenching of galaxies due to environmental effects, as massive galaxies populate denser environments where they suffer from ram pressure stripping, galaxy harassment (e.g., [Kalita et al. 2022](#)).

5.7.2 ρ_{SFR} and ρ_{gas}

One of the first results of this study is to be able to estimate the contribution of H -dropout galaxies to the ρ_{SFR} of galaxies detected in the H band with similar M_{\star} . The H -dropout galaxies of Wang et al. (2019) are galaxies with $M_{\star} \geq 10^{10.3} M_{\odot}$. We estimate that at $z \sim 5$, H -dropout galaxies account for $\sim 23\%$ of the stars formed in massive galaxies (i.e., $M_{\star} \geq 10^{10.3} M_{\odot}$). Wang et al. 2019 estimate a contribution of $\sim 11\%$ to the total ρ_{SFR} for H -dropout galaxies, which is consistent with my measurement of $\sim 13\%$ for the contribution of H -dropout galaxies to the total ρ_{SFR} .

An interesting feature of Fig. 5.13 is the fact that the contribution to ρ_{SFR} of galaxies with $M_{\star} \leq 10^{10} M_{\odot}$ appears to be constant over $1 \leq z \leq 5$. This means that the balance of the number of these galaxies and the number of stars they produce remains constant with cosmic time. This feature can also be seen in Fig. 5.15, where the contribution to ρ_{gas} is also quite stable for galaxies with $M_{\star} \leq 10^{10} M_{\odot}$. On the other hand, galaxies with $M_{\star} \geq 10^{10} M_{\odot}$ account for most stars formed up to $z \sim 5$. This shows that it is galaxies with $M_{\star} \geq 10^{10} M_{\odot}$ that are responsible for the observable shape on the ρ_{SFR} , especially at the cosmic noon (i.e., at $z \sim 2$). In Fig. 5.18a, we display the contribution to ρ_{SFR} , for SFGs, as a function of redshift, where each bin includes 10% of the galaxies in number, picking from the lowest M_{\star} onwards. The previous feature can also be seen in Fig. 5.18a as the contribution of galaxies with $M_{\star} \sim 10^{11} M_{\odot}$ appears relatively constant over $0 \leq z \leq 5$ (i.e., it follows the shape of the global ρ_{SFR}).

In Fig. 5.18a, one can see that the 10% (of the total number of galaxies contributing to ρ_{SFR}) most massive galaxies contribute to a large fraction of the ρ_{SFR} at all redshift. This contribution goes from $\sim 24\%$ at $z \sim 0$ to $\sim 48\%$ at $z \sim 5$. In particular, this means that by studying in details the physical properties (morphology, dynamic, content) of only 10% (in number) of the most massive galaxies, one can understand the mechanisms that trigger most of the star formation of the universe at these redshifts. From these numbers, I also recognise some hierarchical growth effect, as bins gradually rise in M_{\star} over time.

I see in Fig. 5.18a the gradual quenching of most massive galaxies, at $z < 2$, as the global contribution to ρ_{SFR} falls. The global change in the efficiency with which massive galaxies form stars is best seen in Fig. 5.18c. Here, one can clearly see massive galaxies, at high redshift, with $\tau_{\text{dep}} \lesssim 200 \text{ Myr}$; and then slowly being quenched, with $\tau_{\text{dep}} \gtrsim 600 \text{ Myr}$, at low redshift.

In Fig. 5.18d, bins represent 10% of the total L_{IR} contributing to ρ_{SFR} . The first thing that I note is that the contribution of each bin is stable over time and equal to $\sim 10\%$. However, it was shown in Pannella et al. (2015), and also in Sect. 5.2, that A_{UV} evolves with M_{\star} . This means that the L_{IR} (compared to the L_{UV}) is the main contributor to the SFR. This shows the importance to consider the dust emission to derive reliable SFR. Here again, one can see the decreasing efficiency of galaxies (with high L_{IR} this time) to produce stars.

In Fig. 5.18b, I show, at fixed redshift, bins of ascending M_{\star} including each time 10% of the total M_{\star} of galaxies contributing to ρ_{SFR} . I thus determine how efficient galaxies are at forming stars depending on the M_{\star} of their host galaxies. By considering two groups of bins: the most massive galaxies (50 – 100% of M_{\star}) and the least massive galaxies (0 – 50% of M_{\star}); one can see that even at high redshift the most massive group only accounts for $\sim 44\%$ of the ρ_{SFR} , meaning that it is slightly less likely that a star forms in the 50% more massive galaxies than in the 50% of the least massive galaxies. This shows some early evidence of the bending of the main sequence at $z \sim 5$. This effect

increases over time to go from $\sim 44\%$ at $z \sim 5$ to $\sim 25\%$ at $z \sim 0$. This can be interpreted as a consequence of a slow quenching and reduced efficiency of massive galaxies to form stars. This also supports the scenario that a massive galaxy does not necessarily form stars uniformly, but is rather composed of star-forming regions of different intensities.

5.7.3 The Kennicutt-Schmidt relation

Through this work, I have obtained measurement of both SFR and M_{gas} of main sequence galaxies over various redshift and M_{\star} bins. I can thus deduce the corresponding Kennicutt-Schmidt relation ([Kennicutt 1998b](#)), which studies similar properties by examining SFR and M_{gas} surface density (i.e., Σ_{SFR} and Σ_{gas} respectively):

$$\Sigma_{\text{SFR}} = \text{SFR}/(2\pi R_{\text{e}}^2), \quad (5.21)$$

$$\Sigma_{\text{gas}} = M_{\text{gas}}/(2\pi R_{\text{e}}^2), \quad (5.22)$$

where R_{e} is the half-light radius. The Kennicutt-Schmidt relation links Eq. 5.21 and 5.22 by:

$$\log_{10}(\Sigma_{\text{SFR}}) = A + N \times \log_{10}(\Sigma_{\text{gas}}). \quad (5.23)$$

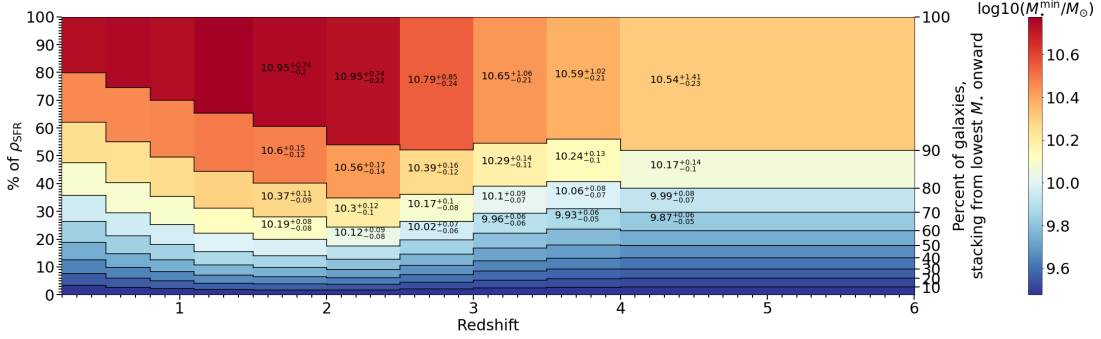
I do not probe R_{e} in this study, thus, I chose to use $R_{\text{e}}(z, M_{\star})$, for galaxies with $M_{\star} \geq 10^{10}$, from [Wang et al. \(2022\)](#). Therefore, I used the values of SFR and M_{gas} from my galaxy bins with $0 \leq z \leq 5$ and, restricted to $10 \leq \log_{10}(M_{\star}) \leq 12$. When fitting all bins, I added the sample with low redshift and low M_{\star} from [Kennicutt \(1998b\)](#). Then, I fitted the evolution of the normalisation at fixed redshift (i.e., by fixing the slope to the value of the best fit of all bins : $N = 1.21^{+0.01}_{-0.01}$). I decided to fix the slopes because I have only three data points to fit for each bin of redshift and two free parameters. Fixing one of these parameters (i.e., N) allows to reduce the uncertainty on the other (i.e., A). When I tried to fit both parameters A and N , for each bin of redshift, the average value, over all bin of redshift, of N was close to ~ 1.2 anyway, so fixing it seems reasonable. The errors on the fits were generated by randomly varying the bin values within the uncertainties of the corresponding bin. I display the Kennicutt-Schmidt relation deduced from this work in Fig. 5.19.

The fit was performed using the **emcee** library using an MCMC approach to navigate the parameter space and runs in about 1 hour on my work laptop.

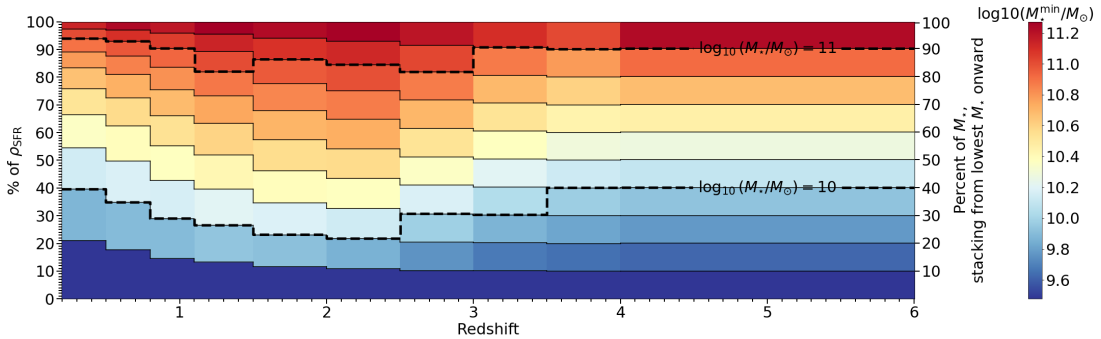
All studies agree on a linear evolution of $\log_{10}(\Sigma_{\text{SFR}})$ as a function of $\log_{10}(\Sigma_{\text{gas}})$ with an overall slope ranging from 1 to 2 (e.g., [Kennicutt 1998b](#); [Bigiel et al. 2008](#); [Liu et al. 2011](#); [Bigiel et al. 2014](#); [Morokuma-Matsui & Muraoka 2017](#); [de los Reyes & Kennicutt 2019](#); [Wang et al. 2022](#)), with no evolution of the slope or normalisation with redshift or M_{\star} . My best fit, over all redshifts and M_{\star} bins, also suggests a linear evolution with a slope of $N = 1.21^{+0.01}_{-0.01}$. However, I observe an increase of the normalisation when we examine the evolution at a fixed redshift. The normalisation increases when fitting individual redshift bins.

The evolution of the normalisation observed in Fig. 5.19 reflects my conclusions from Sect. 5.7.1: we can also see the two regimes I presented for $z \leq 2$ and $z > 2$. At $z \leq 2$ the normalisation barely evolves (i.e., the SFE does not evolves with redshift), and at $z > 2$ the normalisation greatly evolves (i.e., SFE increase with redshift).

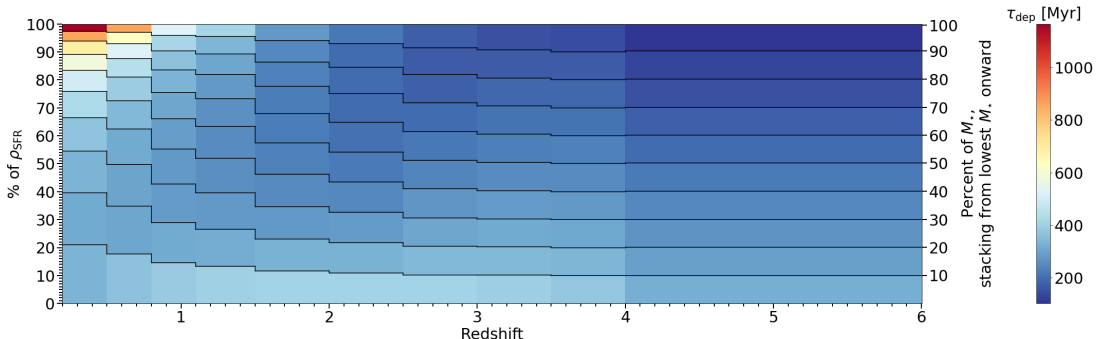
I note that the effect observed in Fig. 5.19 is not inherent to my specific data points deduced from my stacks, or even to my best fit evolution laws of SFR and M_{gas} (if I was to generate catalogues from



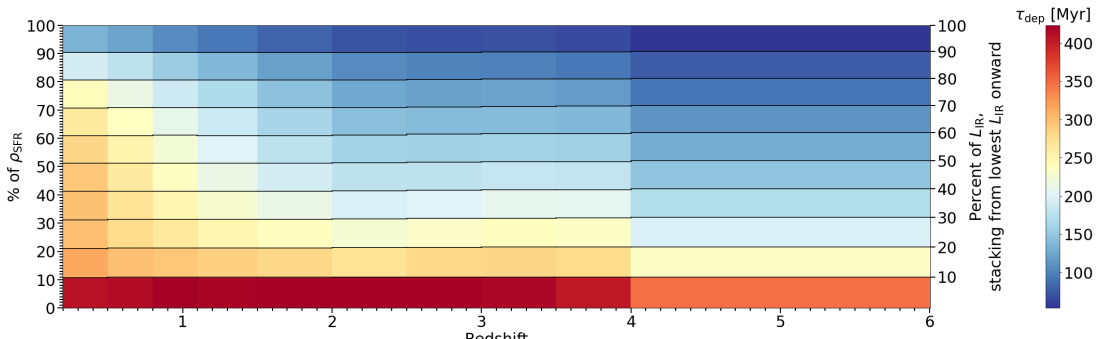
(a) Each bin includes 10% of the galaxies in number, picking from the lowest M_\star onwards. The minimum M_\star in the bin defines the colour. The numbers give the median M_\star within the bin along with the lower and maximum extension of the bin.



(b) Each bin includes 10% of the total M_\star of all galaxies, picking from the lowest M_\star onwards. The minimum M_\star in the bin defines the colour. Contours of $\log_{10}(M_\star/M_\odot) = 10$ and $\log_{10}(M_\star/M_\odot) = 11$ are added as black dashed lines.



(c) Each bin includes 10% of the total M_\star of all galaxies, picking from the lowest M_\star onwards. The median τ_{dep} in the bin defines colour.



(d) Each bin includes 10% of the total L_{IR} of all galaxies, picking from the lowest L_{IR} onwards. The median τ_{dep} in the bin defines colour.

Figure 5.18: Contribution to ρ_{SFR} , for SFGs, as a function of redshift. Catalogues were binned through different methods and a specific property is displayed through colours: see each sub-figure for specifics.

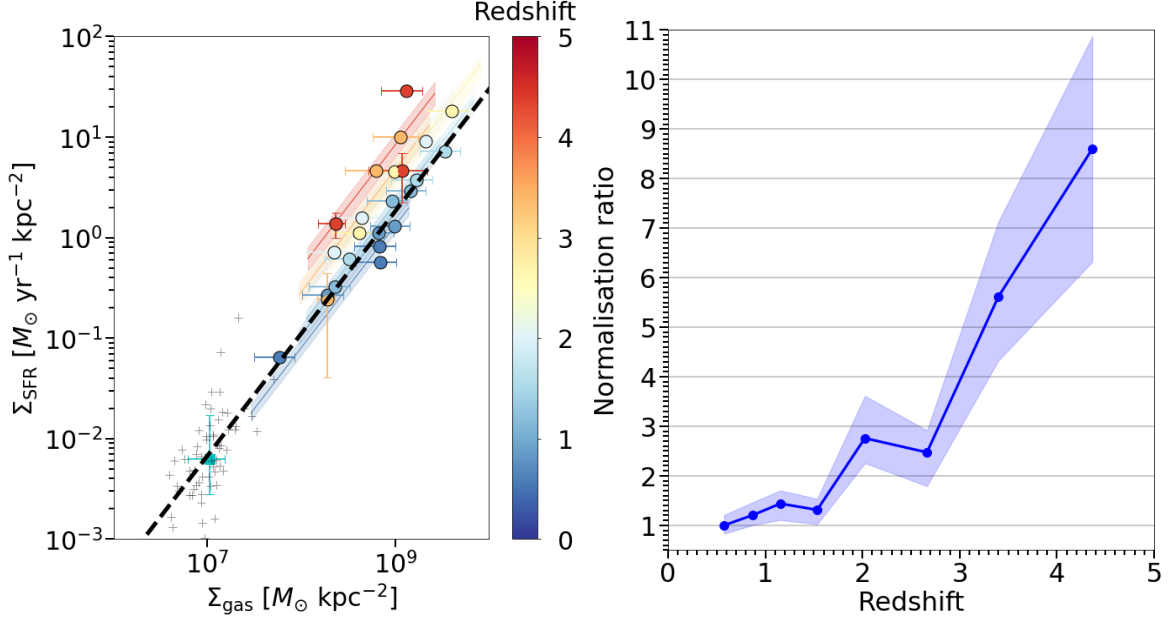


Figure 5.19: Left panel: the Kennicutt-Schmidt relation: Σ_{SFR} as a function of Σ_{gas} . The dots represent the data from this work, and are colour coded by redshift. The cyan squared error bar represents the median of the sample distribution from Kennicutt (1998b), with individual galaxies displayed as grey crosses. The dashed black line represents the best fit of all points. Coloured lines represent the best fit, at fixed redshift, by fixing the slope to the all points best fit value (i.e., $N = 1.21^{+0.01}_{-0.01}$). Right panel: redshift evolution of the normalisation when fitting at fixed slope for each redshift bin.

the laws deduced in this work following the method used to generate ρ_{SFR} and ρ_{gas} see Sect. 5.5 and 5.6). In fact, a similar evolution could be observed if I was to generate catalogues from the laws of S15 for SFR, and Wang et al. (2022) or Tacconi et al. 2018 for M_{gas} . If I was to choose laws from Speagle et al. 2014 for SFR and Tacconi et al. (2018) for M_{gas} , this effect disappears completely, and we end up with a linear non-evolving normalisation depending on redshift or M_{\star} . I conclude, in this case, that the correct normalisation and the presence of the bending of the main sequence, which are lacking from Speagle et al. (2014) SFR evolution, are essential to observe this effect. One could advocate that the observation of an increase in efficiency with redshift, in the case we are generating catalogues, for example, from S15 for SFR, and Tacconi et al. 2018 for M_{gas} , comes from the fact that the M_{gas} fitting form from Tacconi et al. (2018) does not allow a bending or an evolution of it. However, I found no evidence of a bending or its evolution at high-mass when I tried to fit my data using various forms allowing them. Overall, it suggests that some physical processes limit star formation in low-redshift galaxies, compared to high-redshift galaxies, beyond the simple fact that they have less available gas.

I found that $\Sigma_{\text{SFR}} = A \times (\Sigma_{\text{SFR}})^N$ with $N \sim 1.2$ which means that an increase in M_{gas} induces some increase in SFE (i.e., $\text{SFE} \sim (M_{\text{gas}})^{0.2}$). It would not be the case if the slope of the Kennicutt-Schmidt relation was $N = 1$ as in Tacconi et al. (2013). In our case, it means that, in the discussion of Sect. 5.7.1, we need to differentiate two effects: an increase of SFE due to the increase of M_{gas} , and an intrinsic increase in SFE. We can apply it to the example of the difference of SFE between $z \sim 2$ and $z \sim 4.3$ at fixed stellar mass (i.e., SFR increase by a factor $\alpha_{\text{SFR}} \sim 2.5$, SFE by $\alpha_{\text{SFE}} \sim 1.7$ and M_{gas} by $\alpha_{M_{\text{gas}}} \sim 1.5$). The first effect is an increase of SFE due to the increase of M_{gas} (i.e., resulting from

the Kennicutt-Schmidt relation of slope $N \sim 1.2$): $\alpha_{\text{SFE}}^{\text{due to } M_{\text{gas}}} \sim \alpha_{M_{\text{gas}}}^{N_1} = (1.5)^{0.2} = 1.08$. The second effect is an intrinsic increasing in SFE between the two redshifts (i.e., independent of the increase of M_{gas}): $\alpha_{\text{SFE}}^{\text{intrinsic}} \sim \alpha_{\text{SFE}} / \alpha_{\text{SFE}}^{\text{due to } M_{\text{gas}}} \sim 1.6$. Finally, we could conclude by saying that a factor ~ 1.6 is solely due to an increase of SFE, and a factor $\sim \alpha_{M_{\text{gas}}} \times \alpha_{\text{SFE}}^{\text{due to } M_{\text{gas}}} = 1.62$ is due to the increase of M_{gas} . Because N is close to one, this does not affect much our results and all the conclusions of Sect. 5.7.1 are unchanged.

Overall, even though the evolution of the normalisation is not well contained, this study suggests that galaxies at high-redshift form stars more efficiently at a fixed gas surface density. This excess cannot be explained by a universal Kennicutt-Schmidt relation over all redshifts. This may partly explain the early results of *JWST*: a higher ρ_{UV} at $z \geq 8$ (Finkelstein et al. 2023; Donnan et al. 2023; Mason et al. 2023) compared to pre-*JWST* extrapolation Oesch et al. (2018); more massive galaxies at $z \geq 7$ (Labbe et al. 2022). This observation could also coincide with the study of Dekel et al. (2023) which showed that the environment of the most massive dark-matter haloes at $z \geq 10$ would be favourable to high star-formation efficiencies.

5.8 Retrospective: the impact of the clustering bias correction method on properties of galaxies

In this section, I will talk one last time about the methods used to correct the clustering bias in Chap. 3. Here, I will compare the properties of galaxies that I would have if I chose to correct the clustering bias using the method from B15 instead of the method from S15. I will examine the properties of galaxies such as T_{dust} , SFR (i.e., from L_{IR}) and M_{gas} .

Before I start looking at the properties, I think it is important to stress that the results I am going to present here are preliminary and are intended to give depth and weight to the method I have chosen to deal with clustering bias and to the results and conclusions presented earlier in this chapter, while acknowledging the potential impact of the method choice. Consequently, this small study should not be seen as mature and aimed at highlighting the effectiveness or shortcomings of either method. I have already pointed out, in chap. 3, that I argued that the method of S15 was better suited to my specific study, mainly because the results were more robust and reliable when it came to inferring flux densities.

For this section, I have chosen to ignore the bins that resulted in an unrealistic SED fit due to the problems outlined in Chap. 3 when trying to fit the clustering component (which can end up being confused with the flux component at times). Having said that, I am going to use the remaining "good SED fit" to try and highlight the overall impact of the two methods on the properties of SFGs.

5.8.1 The T_{dust} evolution deduced from the method from B15

I present in Fig. 5.20 the T_{dust} obtained when correcting for the clustering bias using the method from B15. In Fig. 5.20, we can see that, as I predicted in Chap. 3, the galaxies appear cooler on average. The evolution of T_{dust} as a function of redshift is in this case closer to that of Magnelli et al. (2014);B15; Béthermin et al. (2020); Bouwens et al. (2020). This confirm the hypothesis I

made in the section dedicated to T_{dust} in this chapter earlier: the differences between S18 and B15; Béthermin et al. (2020); Bouwens et al. (2020) are mainly coming from the method used to correct for the clustering bias.

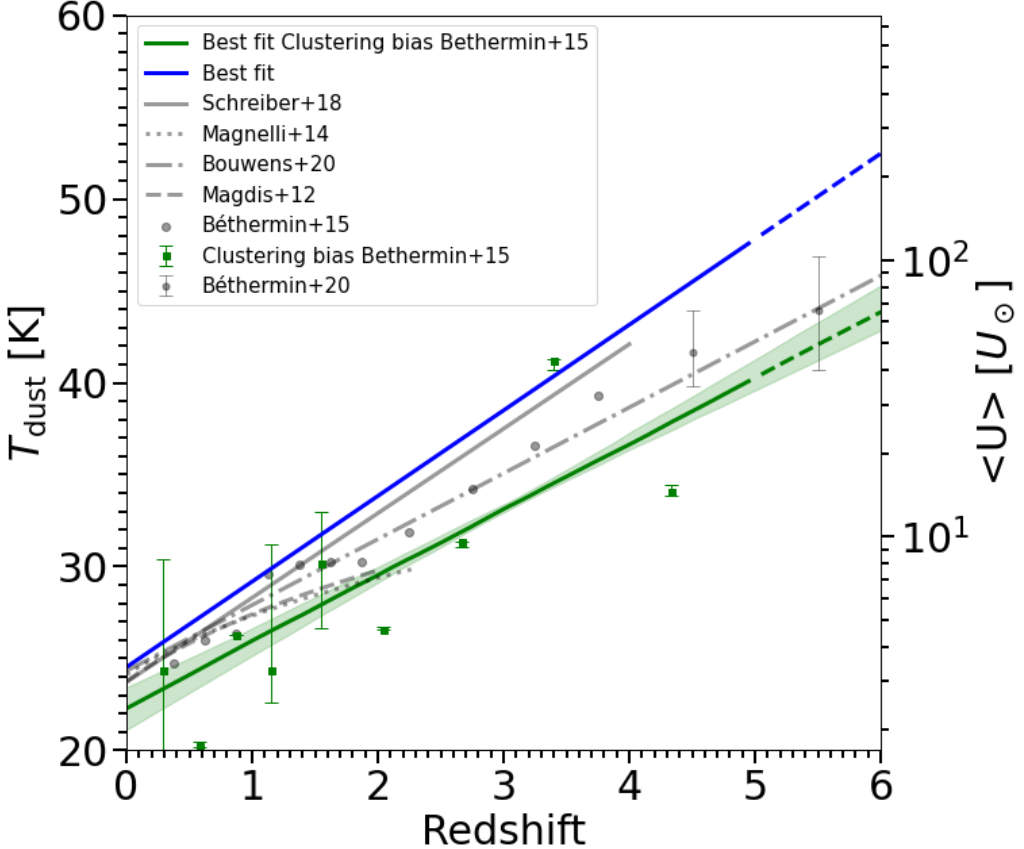


Figure 5.20: T_{dust} and $\langle U \rangle$ as a function of redshift. The green dots represent the T_{dust} deduced from the method from B15, the green line is the best fit (up to $z = 5$), the dashed green line is the best fit extrapolation (for $z \geq 5$), and the green shaded area represents the 68% uncertainty of the fit. The blue line is the best fit from this work (i.e., using the method from S15), up to $z = 5$; the dashed blue line is the best fit extrapolation (for $z \geq 5$). From the literature: S18 (grey solid line), Magnelli et al. (2014) (grey dotted line) and Bouwens et al. (2020) (grey dash-dotted line) converted using Eq. 5.3. Magdis et al. (2012) (grey, dashed line) and B15 (grey dots) converted using Eq. 5.4. We also re-fitted the two stacks from Béthermin et al. (2020) (grey dotted error bars) using template library from S18.

The remaining differences in T_{dust} between the evolution deduced here using the method of B15, and that of Béthermin et al. (2020); Bouwens et al. (2020) could come down to a few details in the method I used, such as the radius chosen to perform the PSF fitting, or the fact that I have fewer bins available here. In this case, I chose the same radius as in my main study (i.e. $0.9 \times FWHM$). I think that a proper study on the choice of the optimal radius to maximise the efficiency of this method and to reduce flux density fitting mistakes (i.e. when part of the flux density ends up being misidentified as a clustering signal), would make the inferred evolution closer to what was found in B15.

5.8.2 The $SFR - M_\star$ evolution deduced from the method from B15

I present in Fig. 5.21, the main sequence that would be inferred by correcting the clustering bias using the method of B15. In Fig. 5.21, we can see that the differences between the best fits from the two methods are small. As a result, it seems that the method used to correct for clustering bias has little or no effect on the L_{IR} (and therefore SFR) deduced. Indeed, the correction due to the clustering bias tends to shift the SED a little towards a colder temperature but does not change the area under the curve much (which is L_{IR}).

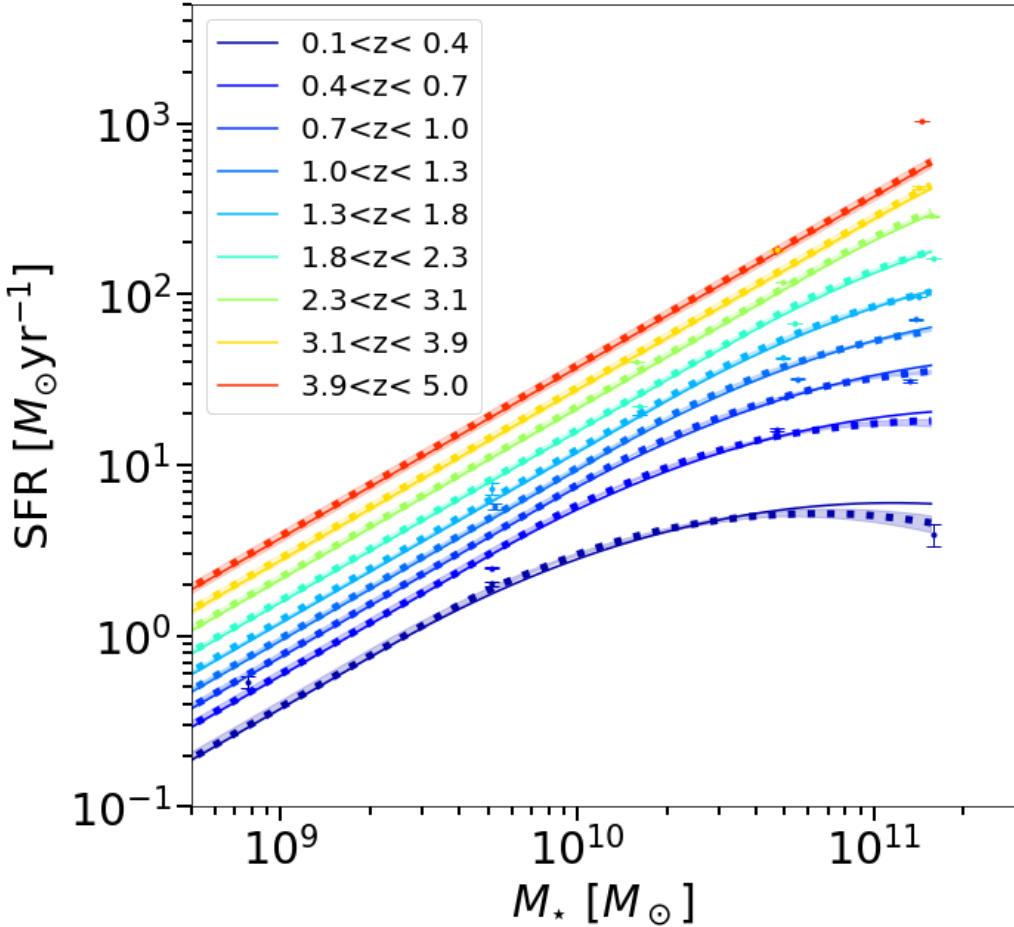


Figure 5.21: SFR_{MS} as a function of M_\star over different redshift bins. The dots represent SFR deduced from the method from B15. The upper limits were used to perform the fit but are not shown here to avoid overloading the figure. The solid line represents the best fit from this work (i.e., using the method from S15). The dotted line is the best fit when the data are fitted by the Eq. 5.11, the shaded area the 68% uncertainty of the fit.

5.8.3 The M_{gas} dependences deduced from the method from B15

In Fig. 5.22, I present measurements of M_{gas} correcting for clustering bias using the method of B15. With the exception of the highest mass bin (i.e., $11 \leq \log_{10}(M_\star/M_\odot) \leq 12$) and part of the mass bin

where $10.5 \leq \log_{10}(M_*/M_\odot) \leq 11$, most data points are largely at odds with the evolution of Tacconi et al. (2018) and Wang et al. (2022).

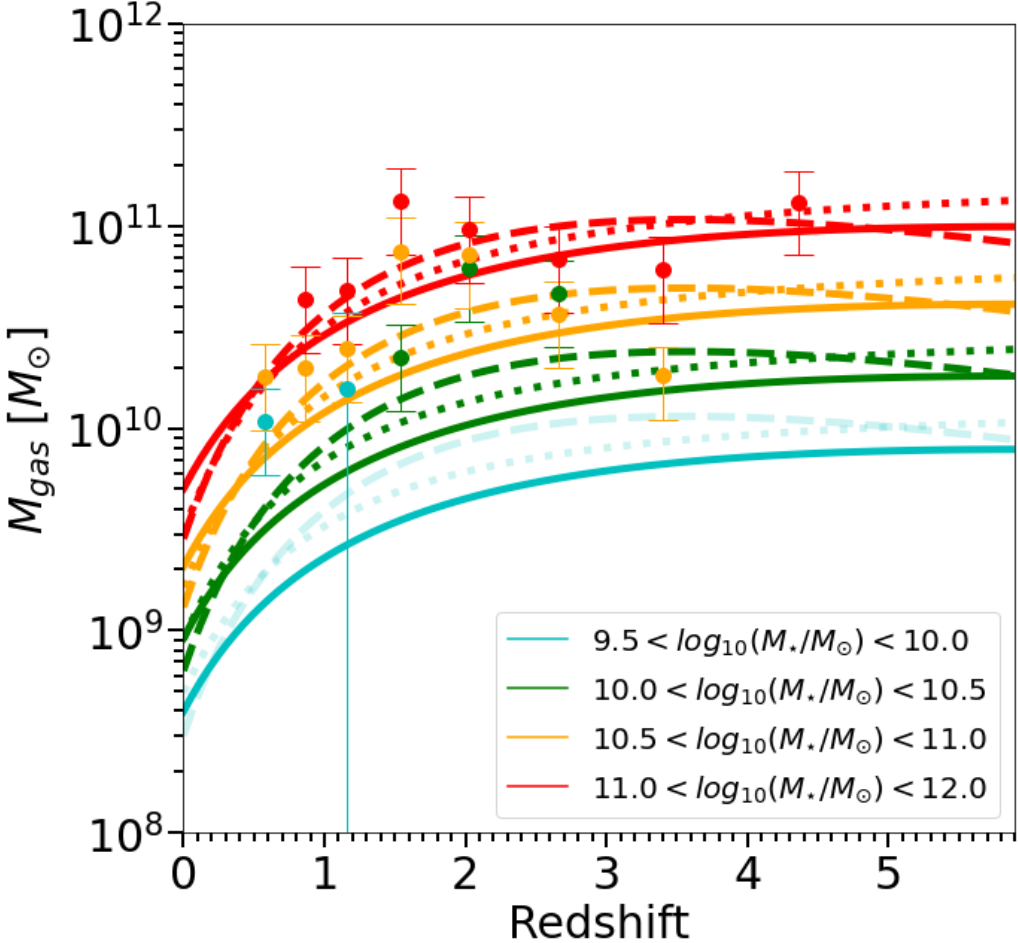


Figure 5.22: M_{gas} as a function of redshift and M_* . The dots represent M_{gas} measurements while correcting from the clustering bias using the method from B15. The solid lines represent the best fit from this work (i.e., using the method from S15) colour-coded by M_* , the dashed lines represent the trend from Tacconi et al. (2018), the dotted lines are from Wang et al. (2022). The faded lines represent an extrapolation from their respective laws.

These differences are somewhat difficult to interpret from Fig. 5.22 alone and would require further study to understand. Nevertheless, it appears that the high masses are broadly close to what is found in the literature or to the results of this work (i.e. using the S15 method).

To conclude on the choice of the clustering bias method, it seems that the properties most impacted are T_{dust} and M_{gas} ; SFR being largely unchanged. This confirms that the method used to correct the clustering bias is of great importance and should not be taken lightly. The main impact is on the SED peak (towards colder T_{dust} on average), which translates into different M_{dust} , and then M_{gas} .

CHAPTER 5

CHAPTER 6

COMPARAISON WITH THE TNG100 COSMOLOGICAL SIMULATION

6.1	The IllustrisTNG project	94
6.2	How to work with the TNG100 output data, and what to choose?	95
6.3	Galaxy properties of the TNG100 simulation	96
6.3.1	Deducing the stellar mass function of TNG100	96
6.3.2	SFR and f_{gas} in TNG100	97
6.3.3	The cosmic star formation history in TNG100	99
6.4	Discussion and conclusions on the TNG100 simulation	100

Simulations and observations usually go hand in hand to assess our current understanding of the physics behind the evolution of galaxies. Therefore, throughout this chapter, I compare my results to one of the state-of-the-art cosmological simulation: TNG100 (Nelson et al. 2019, 2018; Springel et al. 2018; Marinacci et al. 2018; Naiman et al. 2018; Pillepich et al. 2018b,a; Weinberger et al. 2017) from the IllustrisTNG project. The aim is to check whether large-scale hydro-dynamical simulations are able to correctly recover the properties of main sequence galaxies. This exercise will test our current physical understanding of galaxy evolution and should highlight some areas for improvement.

6.1 The IllustrisTNG project

The IllustrisTNG project represents the latest generation of simulations based on the Illustris simulations. The three TNG simulations (TNG50, TNG100 and TNG300) have made major improvements to the physics of galaxy formation, compared to the Illustris project, for example (but not limited to, see [Weinberger et al. 2017](#); [Pillepich et al. 2018b](#) for more details):

- Microphysical gas radiative mechanisms,
- Tracking of chemical enrichment and elements (H, He, C, N, O, Ne, Mg, Si, and Fe),
- Stellar feedback driven galactic-scale outflows,
- Formation and evolution of blackholes,
- A multi-mode blackhole feedback model.

One of the key steps in the simulations is the quenching of galaxies, as this will largely determine whether the simulation is able to reproduce the observable universe. In the IllustrisTNG project, the quenching of galaxies is mainly handled by the multi-mode black hole feedback model, which quenches the galaxy once the central black hole reaches a critical mass. In this framework, an accreting black hole has two mode: at low-accretion rates the black hole is in a "kinetic wind" mode, and at high-accretion rates it enters a "quasar" mode.

A summary of the specifics of the three TNG simulations is given in Table 6.1. TNG50 has the best spatial resolution but only covers a small volume (i.e., $L_{\text{box}}^{\text{TNG50}} = 35\text{Mpc}/h$, where L_{box} is the edge of a comoving cube box). Conversely, the TNG300 trades some of its spatial resolution for a larger box size (i.e., $L_{\text{box}}^{\text{TNG300}} = 205\text{Mpc}/h$). The TNG100 offers a good balance between a large box size (i.e., $L_{\text{box}}^{\text{TNG100}} = 75\text{Mpc}/h$), and an acceptable spatial resolution (i.e., a maximum softening length of dark matter and star particles of $\epsilon_{\text{DM},\star} \sim 0.74\text{kpc}$ at $z = 1$). For the comparisons with our results to be relevant, the size of the box must be large enough, so that we have enough statistics to construct the evolution of the properties, which exclude TNG50. On the other hand, some processes may have a major impact on the evolution of galaxies (e.g., stellar and AGN feedback, inflow and outflow of gas, and chemical enrichment), and may need to be resolved to be reproduced effectively. Therefore, the higher the spatial resolution, the better, which exclude TNG300. TNG100 is the most appropriate choice for comparing galaxy properties such as evolution with redshift and M_{\star} of SFR, M_{gas} and ρ_{SFR} . In the following I will focus on the TNG100 simulation ([Nelson et al. 2019, 2018](#); [Springel et al. 2018](#); [Marinacci et al. 2018](#); [Naiman et al. 2018](#); [Pillepich et al. 2018b,a](#); [Weinberger et al. 2017](#)) of the IllustrisTNG project.

Table 6.1: Specifics of the three TNG simulations. L_{box} is the edge of the comoving cube box of the simulation corresponding to the Volume assuming $h = 0.6774$. N_{GAS} , N_{DM} and N_{TR} represent the initial number of gas cells, dark matter particles, and Monte Carlo tracer particles, respectively. m_{baryon} and m_{DM} represent the target baryon mass and the dark matter particle mass respectively. $\epsilon_{\text{gas,min}}$ and $\epsilon_{\text{DM},\star}$ represent the minimum comoving value of the adaptive gas gravitational softenings, and the Plummer equivalent gravitational softening of the collision less component in comoving units, respectively. Credit: IllustrisTNG project

		TNG50	TNG100	TNG300
Volume	[Mpc ³]	51.7 ³	110.7 ³	302.6 ³
L_{box}	[Mpc/h]	35	75	205
N_{GAS}	-	2160 ³	1820 ³	2500 ³
N_{DM}	-	2160 ³	1820 ³	2500 ³
N_{TR}	-	2160 ³	2×1820^3	2500 ³
m_{baryon}	[M_{\odot}]	8.5×10^4	1.4×10^6	1.1×10^7
m_{DM}	[M_{\odot}]	4.5×10^5	7.5×10^6	5.9×10^7
$\epsilon_{\text{gas,min}}$	[pc]	74	185	370
$\epsilon_{\text{DM},\star}$	[pc]	288	740	1480

6.2 How to work with the TNG100 output data, and what to choose?

The results of the simulations can indeed be somewhat misleading to an observer, as they do not necessarily represent observable quantities. The TNG100 simulates the evolution of dark matter, gas and stellar particles from predefined initial conditions. The simulation results range from $z \sim 20$ to $z = 0$. Throughout the simulation, 100 snapshots are taken to evaluate the state of the simulation over time. The TNG100 simulation gives access to three types of output data: the snapshots themselves, the catalogue of FoF (Friends-of-Friends; a standard FoF algorithm is run on the dark matter particles, with linking length $b = 0.2$) and subhalo groups at each snapshot, and some additional catalogues of various properties. Here I want to compare this simulation to my own work which probes $0 \lesssim z \lesssim 5$ and properties such as SFR, M_{gas} and the stellar mass function (so I need the M_{\star} of galaxies). One would think that additional catalogues dedicated to SFR, masses of HI and H_2 , and aperture stellar masses is the way to go. Unfortunately, most of these catalogues are only available for a few snapshots between $z = 0$ and $z = 2$, and are therefore incomplete for the comparison we seek. The snapshots themselves are far too large a dataset and are a bit difficult to navigate. The best option is the FoF and the subhalo group catalogues as subhalos actually represent galaxies. The subhalos are derived with the Subfind algorithm ([Springel et al. 2001](#)). The TNG100 simulation has two types of snapshots: "full" and "mini". Both encompass the entire volume, but the "mini" snapshots contain only a subset of the particle fields. In my case, I am interested in comparing the overall evolution of properties, so restricting my analysis to a subset of the particle fields is not possible, and I thus use the "full" snapshots. I end up with 14 snapshots ranging from $z = 0$ to $z = 6$.

In each subhalo catalogue, there is no intrinsic value for properties such as SFR, M_{gas} and M_{\star} .

They are all defined in different radii, namely the half-maximum radius of the galaxy, twice the half-maximum radius of the galaxy, and a value that captures all particles bound to the galaxy. As mentioned earlier, I had to be careful with the value chosen for each property, as they do not necessarily represent the corresponding properties of my observation. The right question is therefore: "what do the properties of my observations represent in the TNG100 framework?". To answer this question, we need to go back to our flux measurements on the dust continuum. With the exception of the ALMA measurement which barely resolved galaxies, MIPS, *Herschel*-PACS and *Herschel*-SPIRE measurements do not resolve galaxies. Thus, my best bet would be to consider the properties deduced within a radius of twice the radius of the half-maximum because all particles within this radius should have an impact on the properties according to my observation. After some tests, it appears that these properties are the closest to my observable. In addition, certain observables (e.g., the stellar mass function and SFR) that I was able to deduce this way from the TNG100 simulation, correspond to those found in the literature. I therefore choose to draw the properties of the TNG100 simulation from a radius of twice the half maximum radius.

As a disclaimer, it is fair to say that I have no certainty that these properties represent exactly what I observe, as such a conclusion would require a dedicated study. Therefore, some observed differences between the TNG100 properties and my measurements may still be due to the fact that they do not represent exactly the same thing. This being said, the properties deduced within a radius of twice the half maximum radius, are the closest I can get to my observable without going directly into each snapshot output and trying to simulate an observation from particle data.

All the programs I developed for the TNG100 analysis are mostly based on **numpy** and **astropy** Python libraries and are rather fast to run (i.e., less than 5 minutes). However the data extraction can be a bit longer and runs in about 20 minutes on my work laptop.

6.3 Galaxy properties of the TNG100 simulation

In this section, I will present the evolution of the SFR, M_{gas} and the stellar mass function from the TNG100 simulation and compare them to the evolution I deduced.

All the property I deduced before are for SFGs. The SFGs have been UVJ selected for my work (see Sect. 2). Unfortunately, I do not have access to UVJ colours directly from the TNG100 simulation. I therefore decided to distinguish SFGs from quiescent galaxies by a threshold on the SFR. Following [Pillepich et al. \(2019\)](#), I defined SFGs such that $SFR \geq SFR_{\text{MS}}/10^{0.5}$, where $SFR_{\text{MS}}(z, M_{\star})$ is given by the evolution deduced from this work (see Sect. 5.3.1).

6.3.1 Deducing the stellar mass function of TNG100

For the stellar mass function, I will compare it to the stellar mass function of [Davidzon et al. \(2017\)](#). The stellar mass function of [Davidzon et al. \(2017\)](#) is given for 10 bins of redshift from $z = 0$ to $z = 5$. The redshift of the TNG100 simulation snapshots does not match the redshift of [Davidzon et al. \(2017\)](#), so the stellar mass function will be interpolated to the redshift of the snapshot when it lies between $z = 0$ and $z = 5$. I present this comparison in Fig 6.1. The stellar mass function is quite well reproduced in the TNG100 simulation and the differences with that of [Davidzon et al. \(2017\)](#)

are limited and no particular trend can be found. This means that the next properties of the TNG100 simulation should be comparable to our measurements since they concern a similar population of galaxies.

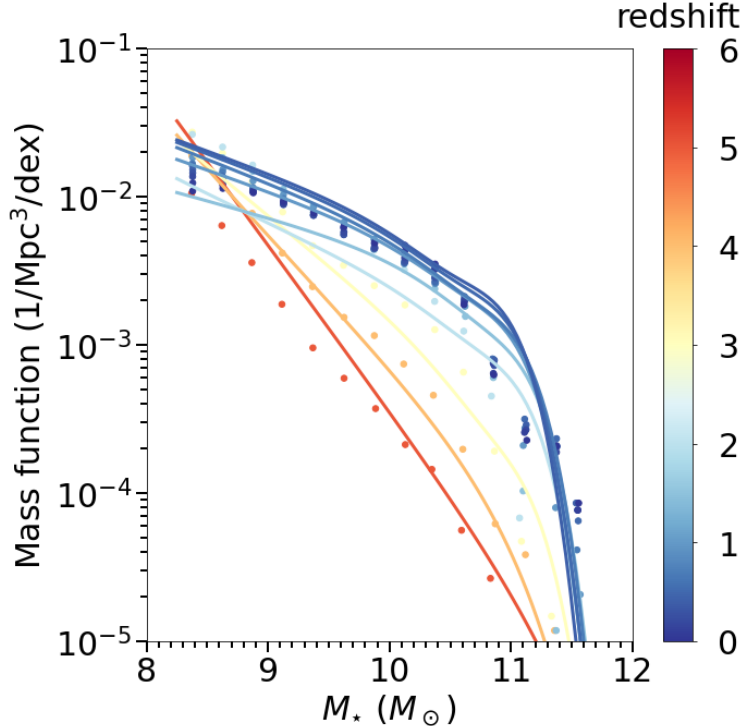


Figure 6.1: The stellar mass function for different redshifts. Coloured points represent the stellar mass function deduced from the TNG100 simulation. Coloured lines represent an interpolation of the stellar mass function from [Davidzon et al. \(2017\)](#) to the redshift of each snapshot of TNG100.

6.3.2 SFR and f_{gas} in TNG100

Next, I compared the SFR (see Fig. 6.2) and the gas fraction ($f_{\text{gas}} = M_{\text{gas}}/(M_{\text{gas}} + M_{\star})$; see Fig. 6.3) of the simulations to those of the observed SFGs in this work. The TNG100 simulation tends to predict, for massive SFGs (i.e., $M_{\star} > 10^{10} M_{\odot}$), lower SFR and gas fractions compared to observations. In TNG100, $f_{\text{gas}} < 15\%$ for $M_{\star} > 10^{10} M_{\odot}$ for $z \geq 4$ (Fig. 6.3), as found in [Pillepich et al. \(2019\)](#). Moreover, TNG100 lacks stars formation in massive galaxies already in the early history of the universe (i.e., $z > 4$, see Fig. 6.2). [Lewis et al. \(2023\)](#) show a lack of metal content in IllustrisTNG simulations at $z = 1$ (see Fig. 6.4), that might be due to AGN feedback that removes large quantities of metal-rich gas from the centres of massive galaxies. The lower metallicities observed by [Lewis et al. \(2023\)](#) in IllustrisTNG simulations at $z = 1$ could be a residual memory of how AGN affected star-formation at higher redshift, which matches the lack of star formation we observe in Fig. 6.2.

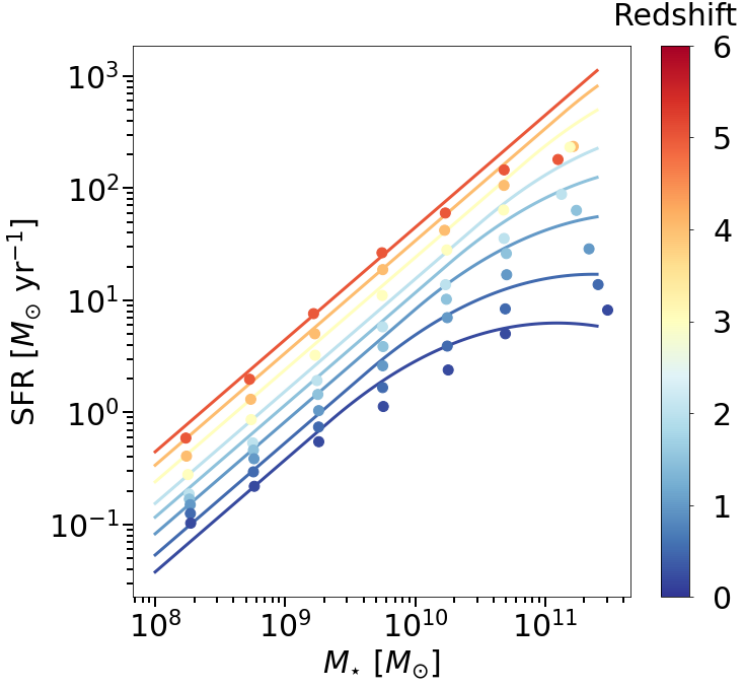


Figure 6.2: SFR as a function of M_{\star} for SFGs in TNG100. Dots represent the SFR predicted by the TNG100 simulation, colour coded by redshift. Coloured lines represent the best fit from this work (see Table 5.2).

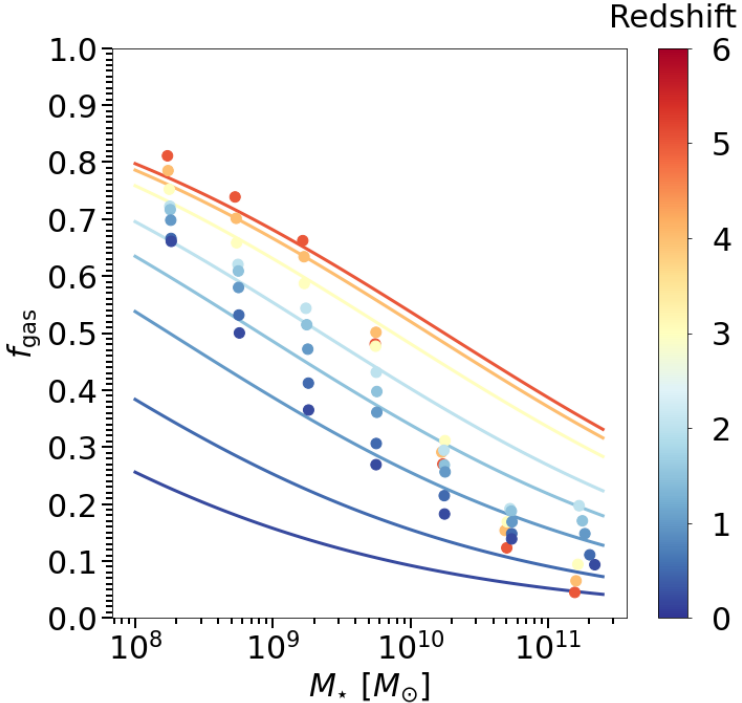


Figure 6.3: The gas fraction as a function of M_{\star} for SFGs in TNG100. Dots represent the gas fraction predicted by the TNG100 simulation, colour coded by redshift. Coloured lines represent the evolution deduced from the best fit of M_{gas} from this work (see Table 5.4).

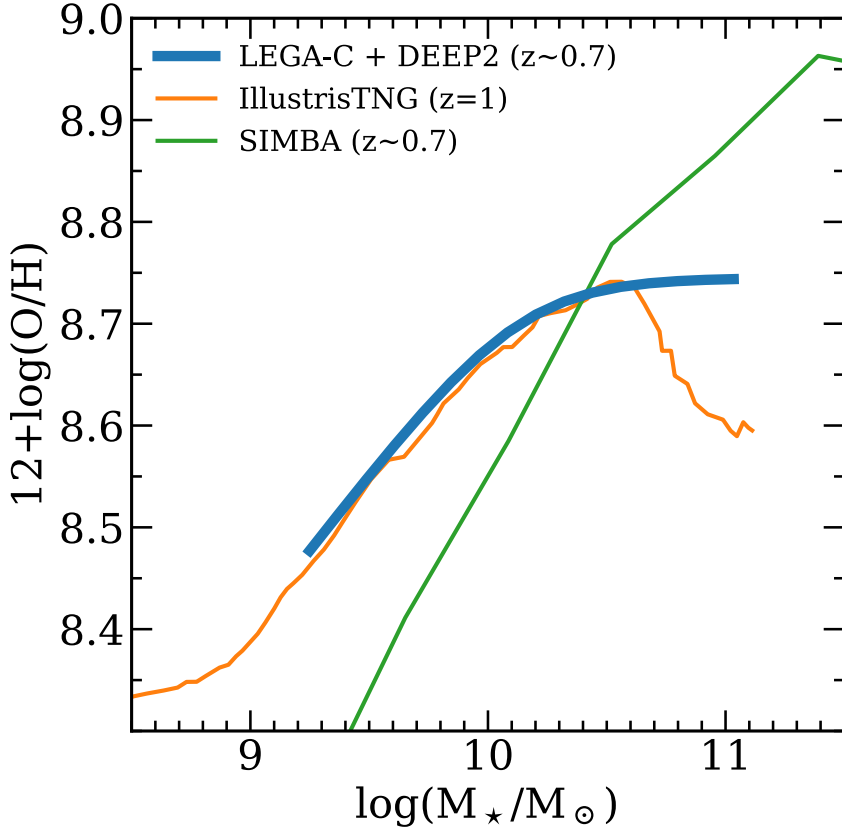


Figure 6.4: Metallicity (i.e., $12 + \log(\text{O/H})$) as a function of M_\star . The blue, orange and green lines represent the observed LEGA-C+DEEP2 MZR from [Lewis et al. \(2023\)](#), the MZRs from the IllustrisTNG simulation ([Torrey et al. 2019](#)) and the SIMBA simulation ([Davé et al. 2019](#)), respectively. Credit: [Lewis et al. \(2023\)](#).

6.3.3 The cosmic star formation history in TNG100

In addition to SFR and M_{gas} , I also retrieved the ρ_{SFR} of TNG100 using the same method as the one from which we calculate the ρ_{SFR} in this work, i.e., by integrating down to a stellar mass of $3 \times 10^9 M_\odot$. In order to compare the trends with my work, this was also done by integrating only galaxies with $\log_{10}(M_\star/M_\odot) > 10$ and $\log_{10}(M_\star/M_\odot) < 10$. I display the evolution of ρ_{SFR} over redshift retrieved from the TNG100 simulation in Fig. 6.5. By comparing the trends of the TNG100 simulation with my results, one can see clear discrepancies. The ρ_{SFR} of the low masses in TNG100 (i.e., $\log_{10}(M_\star/M_\odot) < 10$) is not nearly as flat as observed (especially at $z \leq 2$). On the other hand, the ρ_{SFR} of the high masses in TNG100 (i.e., $\log_{10}(M_\star/M_\odot) > 10$) does not account for as large a part of the total ρ_{SFR} for $z < 3$. The high masses account for less than half of the total ρ_{SFR} at $z \sim 1.7$ in the simulation compared to the observations. As a result, the ρ_{SFR} peak is reached too early (i.e., at $z \sim 3$ instead of the observed at $z \sim 1.7$) in the simulation. The disparities between the two total ρ_{SFR} trends can be almost exclusively associated with the contribution of massive galaxies being off in the TNG100 simulation.

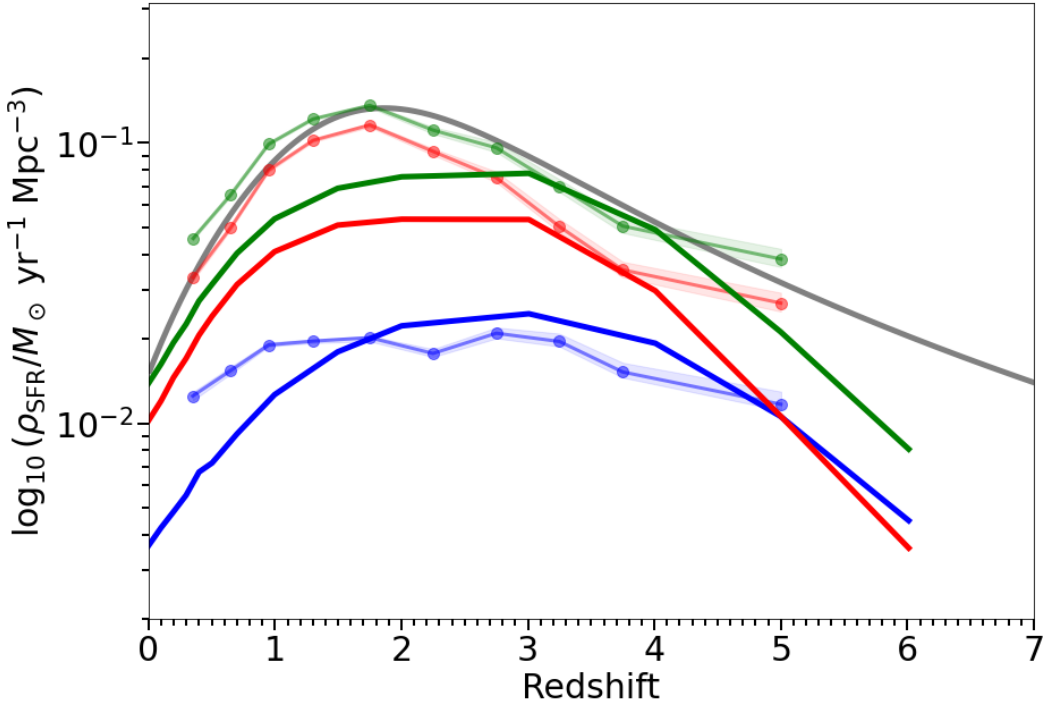


Figure 6.5: Cosmic star formation rate density as a function of redshift. The green, red and blue lines represent ρ_{SFR} deduced from the TNG100 simulation integrated from $3 \times 10^9 M_\odot$, including all galaxies, galaxies with $\log_{10}(M_\star/M_\odot) > 10$, and galaxies with $\log_{10}(M_\star/M_\odot) < 10$, respectively. The green, red and green faded dots represent the total ρ_{SFR} trend, ρ_{SFR} of galaxies with $\log_{10}(M_\star/M_\odot) > 10$, and galaxies with $\log_{10}(M_\star/M_\odot) < 10$, respectively (including H -dropout contribution from Wang et al. (2019)), from this work. The grey line represents the trend from Madau & Dickinson (2014) for reference.

Another way to show the difference in behaviour between the TNG100 simulation and my observations for the two mass bins, is to look at the evolution over redshift of $\rho_{\text{SFR}}^{M_\star > 10^{10}} / \rho_{\text{SFR}}^{M_\star < 10^{10}}$ (see Fig. 6.6). We can see that the ratio decreases continuously with increasing redshift in the simulation, while observations show a clear peak in the ratio around $z \sim 1.7$ (i.e., the cosmic noon) where the amount of stars formed in high-mass galaxies (i.e., $\log_{10}(M_\star/M_\odot) > 10$) exceeds by a factor up to ~ 5.6 the one from low mass galaxies (i.e., $\log_{10}(M_\star/M_\odot) < 10$).

6.4 Discussion and conclusions on the TNG100 simulation

Overall, everything that I presented and is at odds with observations for massive galaxies and the way the TNG100 simulation handles their evolution through time. This could indicate flaws in the way gas accretion, the efficiency of galaxies to form stars from their gas content, or the ejection of gas through galactic winds is treated in the simulations. This shows that the problems encountered in the simulations may be due to the feedback processes used to regulate star formation and the gas reservoir of galaxies. In particular, the impact of AGN feedback may be overestimated to regulate star formation and kill massive galaxies.

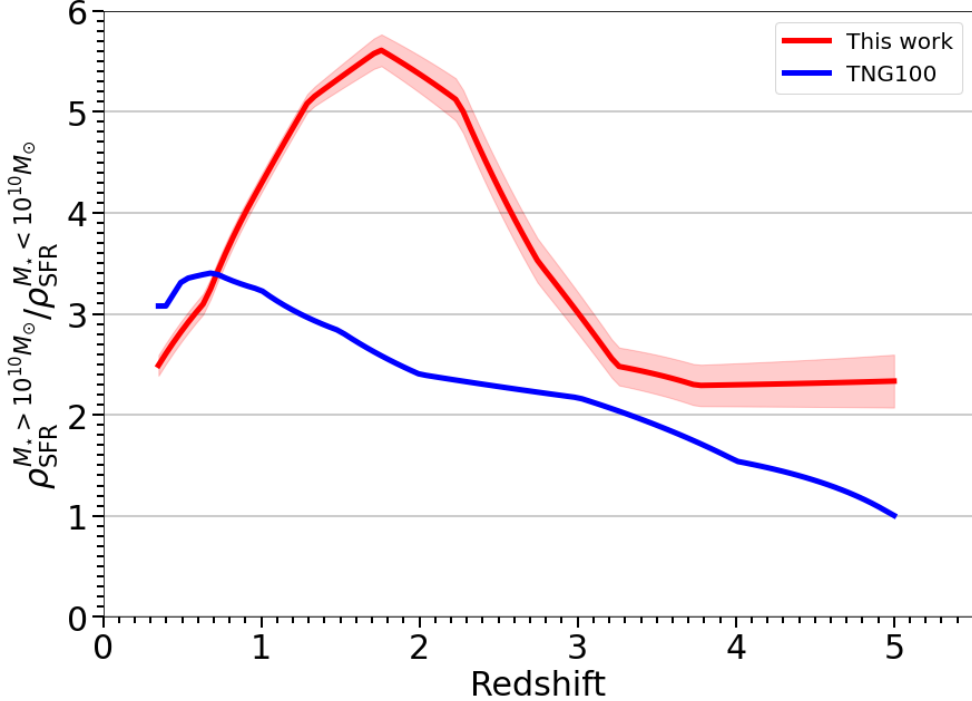


Figure 6.6: Ratio of the ρ_{SFR} of high mass ($M_\star > 10^{10} M_\odot$) over low mass ($M_\star < 10^{10} M_\odot$) galaxies, as a function of redshift. The red line represents the ratio deduced from this work (i.e., from observations). The blue line represents the ratio deduced from the TNG100 simulation.

Several high-resolution simulations have shown that AGN feedback does not have much impact on quenching galaxies (Gabor & Bournaud 2014; DeGraf et al. 2017; Biernacki & Teyssier 2018). High-resolution simulations (i.e., with maximum spatial resolution $\sim 100 - 5\text{pc}$) show that the AGN feedback tends to have little or no effect on the dense gas inside the galactic disc, because most of the out flowing winds escape perpendicular to the galactic disc (Gabor & Bournaud 2014). AGN-driven outflows (i.e., ejective feedback), if sustained, could only quench a galaxy after a long time scale, i.e., more than one Gyr (Gabor & Bournaud 2014; Biernacki & Teyssier 2018). These high-resolution simulations favour preemptive feedback (i.e., cutting out inflows of gas into the disc), via AGN-driven winds, to quench a galaxy (Gabor & Bournaud 2014; DeGraf et al. 2017; Biernacki & Teyssier 2018). However, even strong AGN-driven winds (i.e., $\sim 2500\text{km/s}$) would only reduce star formation in the galaxy by a factor of 2 (DeGraf et al. 2017).

The TNG100 simulation has a much lower spatial resolution (i.e., a softening length of $\sim 0.74\text{kpc}$ at $z = 1$), and is therefore not able to resolve the AGN-feedback interactions correctly. The sub-grid model of AGN feedback used in the *IllustrisTNG* has already been advocated to be responsible for a lower submillimetre galaxies (SMGs) number counts compared to observations (Hayward et al. 2021). The first *JWST* results interestingly go in the same direction: the number of bright, possibly massive, galaxies is found to exceed predictions at high z (Finkelstein et al. 2023; Donnan et al. 2023; Mason et al. 2023).

To summarise on the TNG100 simulation and the comparison with my work: First, and importantly, the TNG100 simulation reproduces well the global evolution of some properties of SFGs galaxies (i.e., SFR, stellar mass function and ρ_{SFR}), especially for low mass galaxies (i.e., $\log_{10}(M_\star/M_\odot) <$

10). However, if I start to look more closely, I find discrepancies with the properties I have deduced. Everything from the low f_{gas} , low SFR and low ρ_{SFR} at high mass (i.e., $\log_{10}(M_{\star}/M_{\odot}) > 10$) point to a problem with the way the SFR in high mass galaxies is artificially reduced in the TNG100 simulation: the sub-grid AGN feedback model. Comparisons with high-resolution simulations show that this AGN feedback does not have as much impact on quenching galaxies as observed in the TNG100 simulation. Achieving better spatial resolution is an easy way to improve large cosmological simulations, although it involves a higher computational cost that may not be feasible. Fortunately, the revision of the AGN sub-grid feedback model could already bring major improvements. Discrepancies with observations, such as ρ_{SFR} , are a starting point for improving large cosmological simulations, and may already give insight into the underestimation of global ρ_{SFR} in TNG100 for ($1 \leq z \leq 2$) reported by [Donnari et al. \(2019\)](#) or the non-trivial problems in simulated galaxy and halo populations found in the Illustris simulation ([Nelson et al. 2015](#)).

CHAPTER 7

CONCLUSION

My PhD can be divided into two main parts: the study of the stacking and SED fitting methods, and their potential biases; the study of the evolution of galaxy properties and comparison with the TNG100 simulation.

The stacking analysis

In the first part of this manuscript, I explained how I transformed the initial sample of galaxies (from the catalogues of the CANDELS-*HST* team) and the CANDELS field maps into exploitable properties of galaxies at a redshift and M_\star never reached on a mass complete sample (i.e. down to $M_\star \sim 10^{10} M_\odot$ at $z \sim 5$).

During my PhD, I gathered catalogues of H -band (GOODS-South, COSMOS, UDS) and K_s -band (GOODS-North) selected SFGs over four fields. I stacked this sample over 7 wavelengths ($24\mu\text{m}$, $100\mu\text{m}$, $160\mu\text{m}$, $250\mu\text{m}$, $350\mu\text{m}$, $500\mu\text{m}$ and 1.13 mm). The main addition to this work, compared to previous studies, is the use of the GOODS-ALMA survey (Gómez-Guijarro et al. 2022b), which helps to reach lower M_\star and higher redshifts, when combined with *Herschel*. I analysed the stacking method and presented a roadmap on how to put it into practice on different bands. In particular, I presented a strategy to build up bins of galaxies when stacking, how to deal with a gradient when stacking.

I also looked at the clustering bias, a signal contamination by neighbouring sources, that can occur during stacking. This bias becomes significant when the PSF size becomes comparable to the typical SFG clustering length, which is particularly true in the *Herschel* bands: the clustering bias represents about 50%, on average, of the measured flux when stacking at $500\mu\text{m}$. I compared two methods, from Schreiber et al. (2015) (hereafter S15), and from Béthermin et al. (2015) (hereafter B15), which can be used to deal with the clustering bias when stacking galaxies. The method from S15 relies on a simple PSF fitting method (i.e., fitting only a signal and background term) and on simulation to infer the remaining contamination from the clustering. The method from B15 uses a PSF fitting method that account for a signal, a clustering bias and a background term. I argued that the method from S15 was the most suitable for my study, mainly due to its robustness and the fact that I do not need a

measure of clustering bias, but rather to remove it along with the background.

The clustering bias being an important part of my study, I also investigated the impact of the method chosen on the evolution of galaxy properties. I found that the differences in the evolution with redshift of T_{dust} between those deduced by Schreiber et al. (2018) (hereafter S18), and B15; Béthermin et al. (2020); Bouwens et al. (2020) are mainly due to the method used to correct the clustering bias. T_{dust} deduced with the method from S15 are between 10% and 15% higher in comparison to the ones deduced with the method from B15. I have also shown that the method can have a significant impact on M_{gas} (up to 40% at some redshift of the higher stellar mass bin for example). I have shown that the method chosen has no effect on the evolution of the SFR depending on the method used as the same SFR- M_{\star} relation is retrieved with both methods (consistent within the 68% uncertainty of the fits).

I then presented the SED fitting procedure I used to go from flux density measurements to galaxy properties. I compared two models (i.e., from S18 and from Draine & Li 2007), and showed that the impact of choosing one over the other on the inferred galaxy properties is small ($-6\%^{+6\%}_{-4\%}$ for L_{IR} , $1\%^{+10\%}_{-5\%}$ for $T_{\text{dust}}^{\text{L}}$, and $1\%^{+11\%}_{-21\%}$ for M_{dust}). In particular, I examined the impact of the different dust models and created a conversion table between the M_{dust} of the two models.

Finally, I examined the potential biases arising from the SED fitting procedure. I found no significant bias from either the averaging throughout the stacking and SED fitting procedure, or from an AGN contribution.

Galaxy properties

In the second part of this manuscript, I presented the study of galaxy properties that could be deduced from the stacking analysis. I combined the stacking of H -band selected galaxies with H -dropout galaxy properties to obtain a complete view of the cosmic history of galaxies. I studied the properties of galaxies such as T_{dust} , A_{UV} , SFR, M_{dust} , and the $\Sigma_{\text{SFR}}-\Sigma_{\text{gas}}$ plane; and properties of the universe such as: ρ_{SFR} , ρ_{gas} ; and deduced their dependence on redshift and M_{\star} through a consistent analysis. I have also taken into account the contribution of H -dropout galaxies for each property in order to obtain a complete and unbiased view over the cosmic time. I generated a detailed view of the cosmic star formation rate density and cosmic gas mass density and their dependence with key galaxy properties such as M_{\star} , L_{IR} and τ_{dep} .

In the course of this analysis, I confirmed some of the characteristics of the main sequence galaxies. First, the dust temperature increases linearly with redshift (e.g., S18; B15; Béthermin et al. (2020); Bouwens et al. (2020)). My work extends the dust temperature evolution from S18 to $z \sim 5$. I confirm that there is no clear evidence for a dependence of T_{dust} on M_{\star} at a fixed redshift when considering main sequence galaxies (e.g., Magdis et al. 2012; Magnelli et al. 2014) at least up to $z \sim 4$. The SFR- M_{\star} relation has a slope close to unity at low mass (i.e. $M_{\star} \lesssim 10^{10} - 10^{11} M_{\odot}$), with a bending appearing below $z \sim 2$ on the high mass end (e.g., S15; Leslie et al. 2020; Delvecchio et al. 2021). My work extends the SFR- M_{\star} evolution from S15 to $0.1 \leq z \leq 5$. The bending of the main sequence corresponds to the gradual quenching or slow downfall of star-formation of massive galaxies (e.g., Schinnerer et al. (2016)). It is mainly due to the progressive decrease in gas mass (e.g., Saintonge et al. 2016) with stellar mass, but also, to second order, to a progressive decrease in the SFE with stellar mass: for example, at $z \sim 0.9$, between the two mass bins $10^{10} M_{\odot} \leq M_{\star} \leq 10^{10.5} M_{\odot}$ and

$M_\star \geq 10^{11} M_\odot$, SFR increase by a factor ~ 3 , M_{gas} by a factor ~ 3.4 , and SFE increase by a factor of ~ 0.9 . Next, we find that the total ρ_{SFR} follows a form close to the one presented in [Madau & Dickinson \(2014\)](#), at least up to $z = 5$. The contribution of H -dropout galaxies to the total ρ_{SFR} is $\sim 13\%$ at $z \sim 5$ (e.g., [Wang et al. 2019](#)).

I have confirmed that the T_{dust} and SFR of H -dropout galaxies are similar to those of normal main-sequence galaxies of similar stellar mass (e.g., [Wang et al. 2019](#)). However, they have on average a larger M_{gas} compared to main sequence galaxies of similar M_\star . I estimate, for the first time, that the H -dropout sample of galaxies from [Wang et al. \(2019\)](#) contributes to $\sim 23\%$ of the ρ_{SFR} of galaxies with $M_\star \geq 10^{10.3} M_\odot$ at $z = 5$. Consequently, it appears that H -dropout galaxies contribute significantly to the total number of stars formed in galaxies with $M_\star \geq 10^{10.3} M_\odot$ at $z = 5$.

I was able to measure the contribution of galaxies of different M_\star to the total cosmic SFR density over cosmic time. I found that massive galaxies (i.e. $M_\star \geq 10^{10} M_\odot$) account for most of the ρ_{SFR} up to $z \sim 5$. On the other hand, the ρ_{SFR} of low mass galaxies (i.e. $M_\star \leq 10^{10} M_\odot$), is roughly constant between $0.4 \leq z \leq 5$. Moreover, the cosmic noon (i.e., at $z \sim 2$) appears to be formed by the increase of the number of massive galaxies from $z = 4$ to $z = 2$; and its fall, from $z = 2$ to $z = 0$, is primarily due to the gradual decrease in gas content within galaxies and the quenching of massive galaxies.

I have found that the TNG100 simulation ([Nelson et al. 2019, 2018; Springel et al. 2018; Marinacci et al. 2018; Naiman et al. 2018; Pillepich et al. 2018b,a; Weinberger et al. 2017](#)) fails to reproduce the contributions of the different M_\star slices to the total ρ_{SFR} . In particular, in the TNG100 simulation, massive galaxies do not form enough stars over the cosmic time. I conclude that the mechanisms used to regulate star formation, in particular through AGN feedback, are misused in this simulation (e.g., [Hayward et al. 2021](#)).

I found hints that high-redshift galaxies may be intrinsically more efficient at forming stars compared to low-redshift galaxies by examining the SFE and $\Sigma_{\text{SFR}}-\Sigma_{\text{gas}}$ plane. While the SFR, at a fixed M_\star , is mostly correlated with M_{gas} . Small variations in the SFE seem to play a role in the evolution of the SFR of galaxies over time. Overall, it appears that, at fixed stellar mass, high-redshift galaxies produce more stars per unit of time, than low-redshift galaxies, due to the larger amount of gas available in the galaxy, and a slightly higher efficiency in star production, at second order. The fact that the slope of the Kennicutt-Schmidt relation was found to be $N \sim 1.2$, instead of $N = 1$ in [Tacconi et al. \(2013\)](#), means that an increase in M_{gas} translate into an increase in SFE. Therefore an increase in SFE can be separated between two effects: an increase of SFE due to the increase of M_{gas} , and an intrinsic increasing in SFE. I estimated that at $z \sim 4.3$, galaxies produce more stars than at $z \sim 2$ due to an increase by a factor ~ 1.7 of their SFE and a factor ~ 1.5 of their gas mass. Due to the Kennicutt-Schmidt relation found in this work (i.e., $N = 1.2$), the relative contributions to the increase of SFR become a factor ~ 1.6 , which is solely due to an increase of SFE, and a factor ~ 1.62 due to the increase of M_{gas} . Because the slope of the Kennicutt-Schmidt relation is close to one the effect is small, but still there. Overall, I found that high-redshift galaxies may be intrinsically more efficient at forming stars compared to low-redshift galaxies. The greater efficiency of galaxies in forming stars at high redshift could explain why massive galaxies were observed with *JWST* at such an early stage in the universe (i.e., at $z \geq 7$, e.g., [Labbe et al. 2022](#)).

CHAPTER 8

PERSPECTIVES

The work presented in this manuscript opens up many new perspectives. This is mainly due to the fact that the understanding of the evolution of galaxies is far from being mastered. Obviously, every aspect that I have presented in this manuscript on the evolution and inter-dependence of galaxy properties could always be further investigated at a higher redshift and at lower M_\star . However, there are also very interesting aspects of galaxy evolution that can be studied with existing datasets.

The work I carried out during my PhD was mainly based on observations by *HST*, *Spitzer*, *Herschel* and ALMA. Although there is still a lot to be done with these tools, I will focus on the many possibilities offered by *JWST*, and what it can help us to understand about the evolution of galaxies; and will also discuss how it already has contributed since it became operational a year ago.

The study of faint galaxies with *JWST*

JWST is the successor of *Spitzer* as the main space telescope probing the mid-infrared (MIR). In figure 8.1, we can see the difference in quality between an image taken by *Spitzer*-IRAC at $8\,\mu\text{m}$ and *JWST*-MIRI at $7.7\,\mu\text{m}$. Part of *JWST* work will involve confirming and refining the flux densities previously measured in the MIR by *Spitzer*, which has a much lower angular resolution. In particular, it will be possible to further study galaxies whose flux density measurements have been, sometimes heavily, contaminated by bright neighbours due to the large PSF of some *Spitzer* instruments (e.g., [González et al. 2010](#); [Wang et al. 2019](#)).

One major prospect for the coming years with *JWST* is to extend the *HST* vision towards less massive (e.g., [Barrufet et al. 2023](#); [Bisigello et al. 2023](#)) and higher redshift (e.g. [Castellano et al. 2022](#); [Harikane et al. 2022](#); [Finkelstein et al. 2023](#); [Donnan et al. 2023](#); [Curtis-Lake et al. 2023](#)) galaxies. This could have an impact on several levels. The first is perhaps the most obvious and the most widely publicised: the detection of galaxies at very high redshift (i.e. with $z \geq 10$, e.g. [Curtis-Lake et al. 2023](#)). The strength of *JWST* is that it has both instruments for detecting galaxies (NIRCam, MIRI and NIRISS) and for spectroscopically confirming the redshift of galaxies (primarily NIRSpec, but also NIRCam, MIRI and NIRISS). In [Curtis-Lake et al. \(2023\)](#), four galaxies, selected with NIRCam, are now spectroscopically confirmed at redshift $10.3 \leq z \leq 13.2$. However, *JWST*

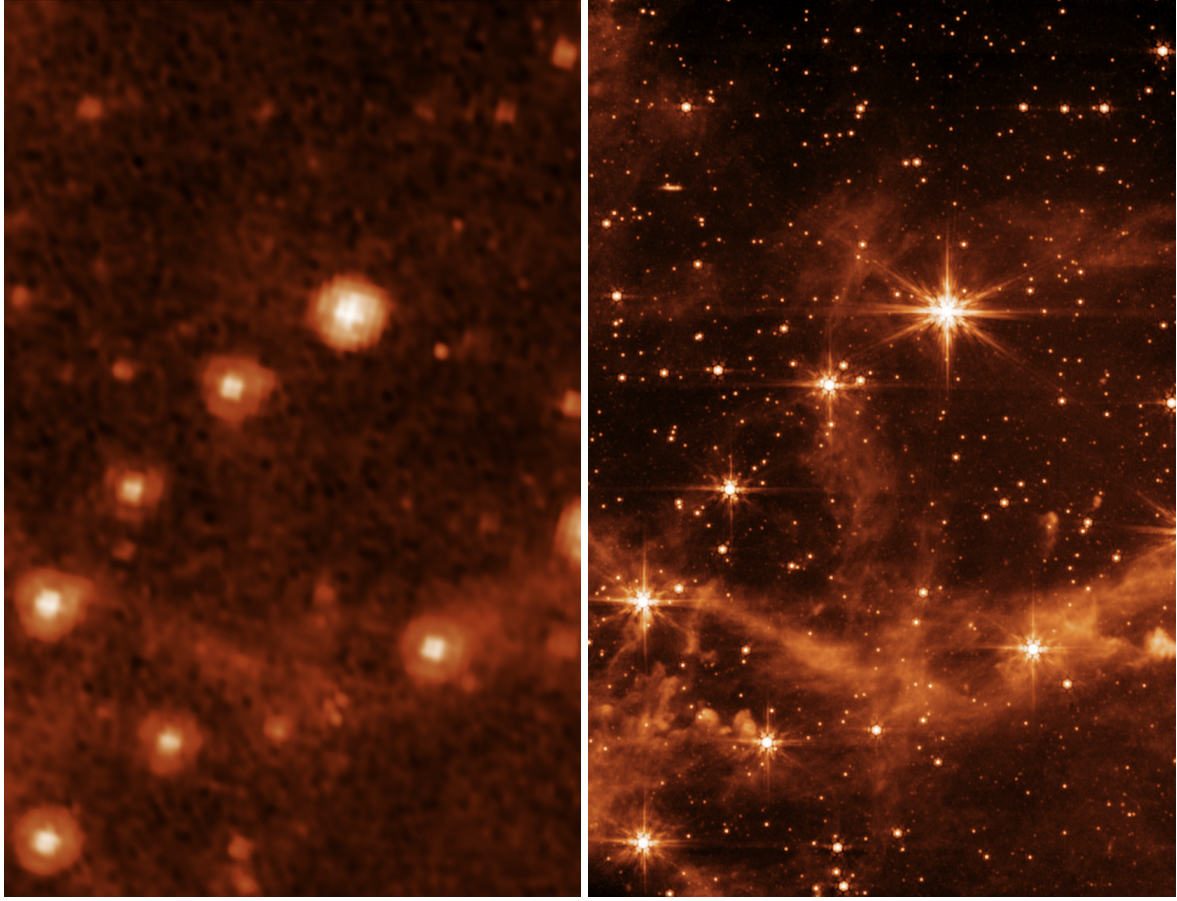


Figure 8.1: Left: Image from *Spitzer*-IRAC at $8\text{ }\mu\text{m}$. Right: Same image taken by *JWST*-MIRI at $7.7\text{ }\mu\text{m}$. Credit: Spitzer: NASA/JPL-Caltech; MIRI: NASA/ESA/CSA/STScI.

can offer the scientific community much more than just the most distant galaxies in the universe. *JWST* will be able to: detect new galaxies at every redshift, reach lower M_\star (e.g., [Barrufet et al. 2023](#); [Bisigello et al. 2023](#)); unveil the morphology of galaxies thanks to its high sensitivity to low surface brightness (e.g., [Kartaltepe et al. 2023](#); [Jacobs et al. 2023](#)); detect more emission lines (e.g., [Trump et al. 2023](#); [Tacchella et al. 2023](#)) which will result in a better diagnosis of the metallicity, the age of the stellar population and AGNs. Overall, this will allow the community to greatly extend its knowledge on galaxy evolution.

JWST sees the universe in the MIR, and is therefore able to probe the stellar emission of galaxies at $z \geq 5$ that was inaccessible to *HST*. Consequently, *JWST* is a powerful tool for measuring and confirming stellar mass of galaxies, and furthermore reducing the error attached to it. The prospect of reducing the errors on stellar masses would be a great improvement in our knowledge of galaxies as a whole.

But why it is important to get to lower stellar mass and higher redshift? Following what I presented in this manuscript one can wonder what happens at high redshift where we start to see large discrepancies with simulation and some increase of SFE with redshift? To start to answer this question we need a mass complete sample of galaxies at $z \geq 5$, which was inaccessible to *HST* but in reach of *JWST*. Another question is what happens at low stellar mass (i.e., $M_\star \leq 10^{9.5} M_\odot$)? What is the

gas content of these galaxies? How does the slope and scatter of the main sequence evolve? What are the peculiar physical mechanisms in place? Again, getting a hand on a mass complete sample down to lower stellar mass with *JWST* would allow to investigate these questions. For these reasons, one great prospect for *JWST* is to further improve our current studies and catalogues of galaxies, either by measuring properties such as redshift and M_\star , or by detecting new galaxies at lower M_\star and higher redshift.

A better characterisation of the population of *HST*-dark galaxies

Another great perspective for *JWST* is to help us better understand *HST*-dark galaxies. As we said earlier, *JWST* is the successor of *Spitzer* as the main space telescope probing the MIR, and it will be able to refine flux densities measurements, and detect new galaxies in the MIR. For example, the *H*-dropout sample of Wang et al. (2019) was selected with *Spitzer*/IRAC at $4.5\mu\text{m}$ and could be re-studied with *JWST* to refine the flux density measurements. *JWST* is also capable of detecting galaxies deeper than *Spitzer* and can discover *HST*-dark galaxies missed by *Spitzer* (e.g., Barrufet et al. (2023)).

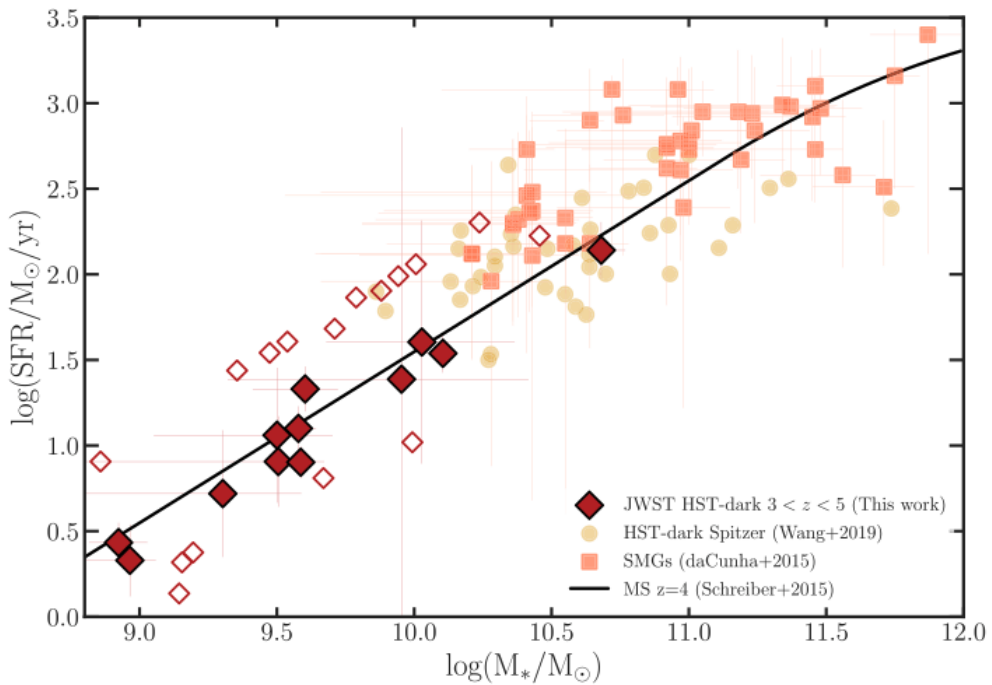


Figure 8.2: SFR as a function M_\star . The black line is the main sequence at $z = 4$ from S15. The red and empty diamonds represent the sample within $3 < z < 5$ and the total sample (the SFR of these galaxies is not rescaled to the main sequence at $3 < z < 5$), respectively, of *HST*-dark galaxies from Barrufet et al. (2023). The yellow dots represent the *H*-dropout sample from Wang et al. (2019). The orange squares represent the SMGs from da Cunha et al. (2015). Credit: Barrufet et al. (2023).

One application, directly related to the work presented in this manuscript, is to update the contribution to ρ_{SFR} of *H*-dropout galaxies. About a year after the first *JWST* observation, we already have an idea of the number of galaxies missed by pre-*JWST* studies. In Fig. 8.2, I display the recent sample

of new *HST*-dark sources selected by *JWST* in Barrufet et al. (2023). In Fig. 8.2, this new sample of Barrufet et al. (2023) is mainly composed of low M_\star galaxies (i.e., most of them have $M_\star \leq 10^{10} M_\odot$) compared to the sample from Wang et al. (2019) (i.e., most of them have $M_\star \geq 10^{10} M_\odot$). It therefore seems that most of the *H*-dropout populations with high M_\star was already identified before *JWST*. The main impact on the work I have presented here is that my estimate of the contribution of *H*-dropouts to the ρ_{SFR} massive galaxies (i.e., $M_\star \geq 10^{10.3} M_\odot$) and the total ρ_{SFR} should stay relevant. It is very unlikely that my estimates are wrong by a large factor due to a wrong estimate of the pre-*JWST* *H*-dropout galaxy population at $z \leq 5$.

However, there is still much to learn from the *HST*-dark galaxies. The cosmic SFR density I deduced in this manuscript depends on the cosmic SFR density of *H*-dropout galaxies from Wang et al. (2019) which is constituted of almost exclusively massive galaxies (i.e., $M_\star \geq 10^{10} M_\odot$). Therefore, my estimate of the cosmic SFR density lacks the contribution of lower mass *H*-dropouts (i.e., $3 \times 10^9 M_\odot \leq M_\star \leq 10^{10} M_\odot$) to be complete. Moreover, further work on these galaxies is needed so that we can better understand what differentiates them from normal main sequence galaxies. For example, one can compare their morphology and attenuation to the ones of normal main sequence galaxies. Overall, there is no doubt that *JWST*, combined with other telescopes and interferometers (to measure their properties such as SFR_{IR} and M_{gas}), will be crucial to our understanding of the *HST*-dark galaxies.

The low mass scatter of the main sequence

In this manuscript, I have measured the main sequence at high stellar masses (see also Whitaker et al. 2014; Magnelli et al. 2014; S15; Delvecchio et al. 2021; Leslie et al. 2020). However it is still unclear whether it translates to lower M_\star . Is the same shape maintained when M_\star is lower? Does the dispersion increase? Therefore, another perspective brought by *JWST* is the study now possible of the low-mass part (i.e. $M_\star \leq 10^9 M_\odot$) of the main sequence at low redshifts (i.e. $z \leq 2$).

Here again, *JWST* can contribute to a better understanding of the main sequence at a lower M_\star . During the last part of my PhD, I began to study this subject. My aim was to measure the dispersion of the main sequence at low redshift (i.e. $z < 1$) and low M_\star (i.e. $\log(M_\star/M_\odot) \leq 8$). I used the first CEERS observations in the EGS field. I first examined the galaxies newly detected by MIRI (259 sources). I fitted flux density measurements of these sources with the library of S18 by fixing the IR8 following Eq. 4.1; a few examples of the best fit SED are displayed in Fig. 8.3. But, as it was expected, almost none of them are detected in the *Herschel* bands and especially for $\log(M_\star/M_\odot) \leq 8$. This makes it impossible to derive individual SFR_{IR} without using a MIR/FIR ratio. The MIR/FIR ratio is still uncertain at low M_\star , due to the limited sensibility of *Herschel*, which makes the SFR_{IR} derived in such way not that robust, compared to studying directly the peak of the dust emission. However, it is important to note that *JWST*'s MIRI instrument is able to track the individual PAH peaks of galaxies.

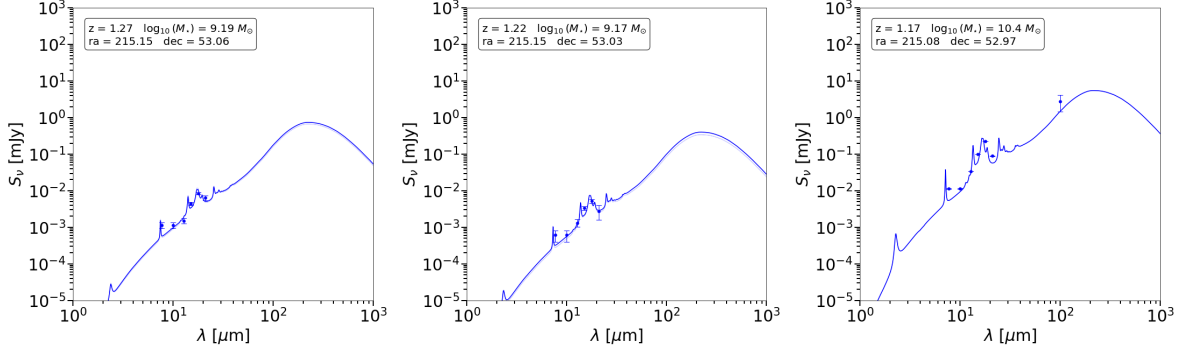


Figure 8.3: Examples of SED fitting on galaxies detected with *JWST*-MIRI.

I have therefore tried to stack with MIRI all known galaxies, using the super deblended FIR catalog of the EGS field (Le Bail et al., in preparation), in the area covered by these first observations. I present the results of the SED fit in Fig. 8.4 for the galaxy stack with $0 \leq z \leq 0.5$ and $6 \leq \log_{10}(M_*/M_\odot) \leq 8$. Even with only two MIRI pointings, I was able to get a stacking detection down to such low M_* . Unfortunately, there were too few galaxies, only 103, to detect anything in the *Herschel* bands. However, during the study presented in this manuscript, I was able to get a 3σ detection by stacking in *Herschel*-PACS 100 and $160\mu\text{m}$, over the GOODS-South, GOODS-North, COSMOS and UDS fields, galaxies at $0 \leq z \leq 0.4$ with $M_* \leq 10^{8.5} M_\odot$ and $10^{8.5} M_\odot \leq M_* \leq 10^{9.5} M_\odot$. By bringing together some of the wider and deeper fields covered by *Herschel*, we might be able to detect something as such low M_* . However, this is already very promising for *JWST*: studying the end of the low-mass main sequence seems very feasible with the help of *JWST*. The problem with studying the main sequence dispersion in *JWST*-MIRI bands is that they lie right in the middle of PAHs at low redshift that can vary considerably (which is why the main sequence dispersion was deduced near the dust emission peak of the SED by S15). Moreover, deducing the SFR with MIR observations alone is uncertain because the MIR/FIR ratio is not well constrained at low M_* . While it is difficult to obtain a well constrained SFR by measuring a flux density in the *Herschel* bands, one could realistically hope to at least put an upper or lower limit on the measure of the scatter of the main sequence at low M_* by trying to apply the method from S15 to one of the MIRI bands.

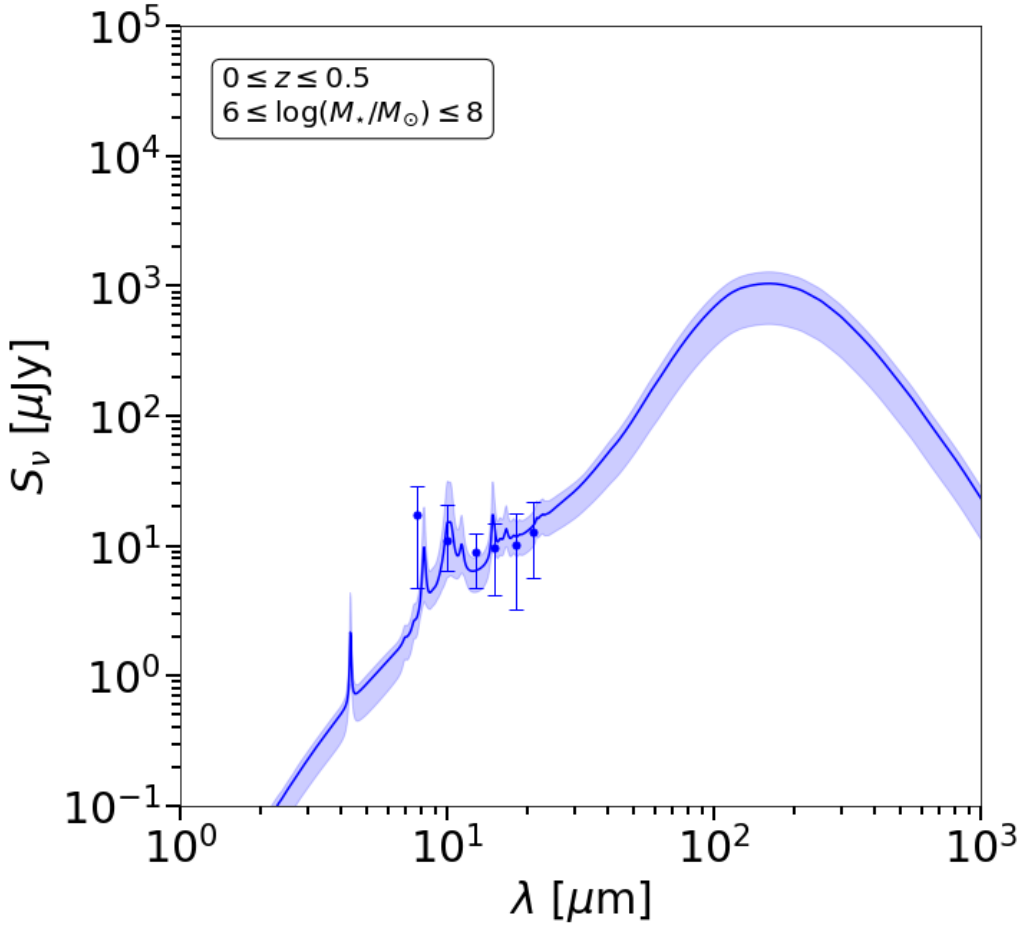


Figure 8.4: Example of SED fitting on the stack of 103 galaxies on the first two MIRI pointings of CEERS observations in the EGS fields.

One problem can come from galaxies detectable with *JWST* but not with *Herschel*, typically at low stellar masses. This could lead to studies correcting the SFR_{UV} for dust attenuation, or using some MIR/FIR ratio to deduce the SFR for the faintest galaxies detected by *JWST*. Both of these methods have their own uncertainties and appear, today, to be much less robust than a correct FIR measurement of the SFR_{IR} (by studying the dust emission peak as it was done in this manuscript). This shows that the community may need a successor to *Herschel* in the FIR to meet the potential of *JWST*.

The study of the morphology of galaxies

Throughout this manuscript, I demonstrate the presence of the bending of the main sequence at the high mass end. However, there is still much unanswered as why a bending appears. A way to look at the problem would be to study the evolution of the morphology of galaxies in the bent part of the main sequence. How much a bulge or disk component of a galaxy correlate with its loss of efficiency?

This study is mainly possible with the NIRCam instrument. There is a lot to discuss and study while looking at the morphology of galaxies with *JWST*. For example, *JWST* has already discovered

that disc galaxies are more common than we thought, and has made it possible to study the diversity of galaxy morphology (e.g., [Kartaltepe et al. 2023](#); [Jacobs et al. 2023](#)).

Another study by [Gómez-Guijarro et al. \(2023\)](#) shows that morphology can have an impact on attenuation. The results of [Gómez-Guijarro et al. \(2023\)](#) are shown in Fig. 8.5. In Fig. 8.5, the strongly attenuated SFGs (i.e. $A_V > 1$, where A_V is the dust attenuation in the V -band defined in [Gómez-Guijarro et al. 2023](#)) appear more compact (i.e., 30% smaller effective radius compared to the average SFGs at the same M_\star and redshift; [Gómez-Guijarro et al. 2023](#)). This shows the peculiarity of strongly attenuated galaxies and how *JWST* will help to better understand this population.

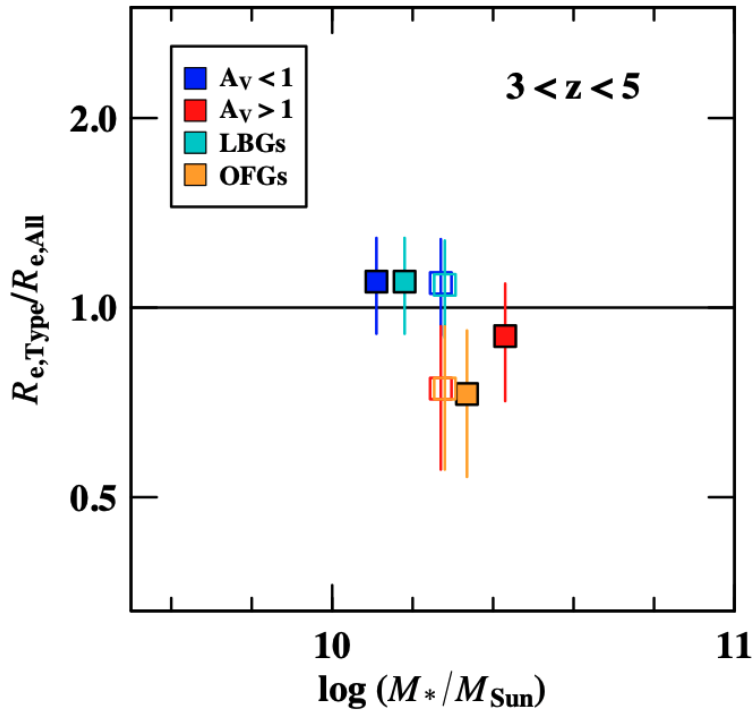


Figure 8.5: "Ratio of the effective radius for different galaxy types over those of the parent SFGs sample. Galaxies are in the redshift bin $3 < z < 5$ and massive ($\log_{10}(M_\star/M_\odot) > 10$). In the case of the effective radius, ratios after applying a correction to a common redshift and stellar mass are displayed with open squares. The ratios are obtained by dividing the median values of a given galaxy type over the median values of the parent SFGs sample, with the error bars representing the uncertainty of the ratio of the medians." [Gómez-Guijarro et al. 2023](#). Credit: [Gómez-Guijarro et al. \(2023\)](#).

Then, [Magnelli et al. \(2023\)](#) shows that the ratio of $R_{e,\text{opt.}}/R_{e,\text{MIR}}$ varies with the distance of the SFGs from the main sequence. In Fig. 8.6, galaxies with $\Delta MS > 0.5$ appear on average ~ 2 times smaller in the MIR ($R_{e,\text{MIR}}$) compared to their rest optical sizes ($R_{e,\text{Opt.}}$). This study highlights that starburst galaxies have a different morphology compared to normal main sequence galaxies.

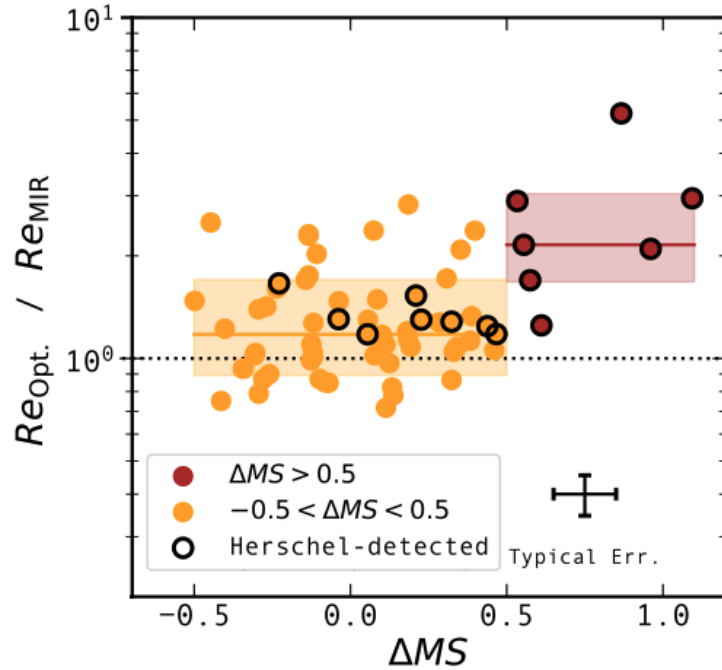


Figure 8.6: "Rest-optical to rest-MIR size ratios for 69 galaxies with $S/N > 10$ and above our mass completeness limits ($M_\star = 10^{9.5}, 10^{9.5}$, and $10^{10} M_\odot$ at $z \sim 0.3, 1.0$, and 2.0 , respectively) as a function of their distances to the MS. Circles are color-coded by the distance of each galaxy to the main sequence (MS), i.e., $-0.5 < \Delta MS < 0.5$ (orange), and $\Delta MS > 0.5$ (brown). Circles outlined by black edges are detected in the far-infrared by *Herschel*. Brown line and shaded region shows the median and 16th and 84th percentiles of starbursts ($\Delta MS > 0.5$) in bins of distance to the MS. Orange regions display the same quantities but for MS galaxies. These rest-MIR sizes were inferred by setting $n_{\text{MIR}} = 1$ (where n_{MIR} is the Sérsic index in the MIR) during our partial structural parameter analysis. Typical 1σ error bars for individual objects are shown. The discretized values along the dust attenuation axis correspond to the sampling of this parameter used for our CIGALE fits." See [Magnelli et al. \(2023\)](#) for more detail. Credit: [Magnelli et al. \(2023\)](#).

These examples show how much we can learn about the evolution of galaxies by studying their morphology. Studying the morphology of galaxies is something that I was not able to do during my PhD. An interesting study that I wanted to pursue was to relate the morphology of galaxies, probed by *JWST*-NIRCam, to the study presented in this manuscript. My aim would be to examine the dependence of morphological parameters, such as R_e and the Sérsic index, on the properties I have deduced here (i.e., T_{dust} , A_{UV} , SFR, M_{gas} and the $\Sigma_{\text{SFR}}-\Sigma_{\text{gas}}$ plane).

The impact of the environment on galaxy evolution

Finally, the last perspective I will address in this manuscript is the study of the impact of the environment on the evolution of galaxies. Throughout this manuscript, I presented a redshift evolution in the $\Sigma_{\text{SFR}}-\Sigma_{\text{gas}}$ plane. This evolution with redshift still needs to be confirmed and if so, to be explained and one possibility that I would like to consider is the impact of the environment on the SFE and SFR as

a whole. The study of Chiang et al. (2017) (see Fig. 8.7) shows, using a set of N -body simulations and semi-analytical models, that galaxies in protoclusters should contribute significantly to ρ_{SFR} as the redshift increases. In Fig. 8.7, the contribution of galaxies in protoclusters is expected to increase from 1% at $z = 0$, to 50% at $z = 10$. In addition, *JWST* will be able to study this question by enabling the observation of galaxies at high redshift. In the coming years, we might obtain the ρ_{SFR} contribution of protocluster galaxies at high redshift (i.e., $z > 6$) from *JWST* observations. However, the field of view of *JWST* being limited, this question might need to wait for the EUCLID telescope to be answered.

JWST will also enable us to study the impact of the environment on the evolution of galaxies. In particular, this could help us to better understand the role of the environment in the growth and death of galaxies, as well as its impact on galaxy morphology.

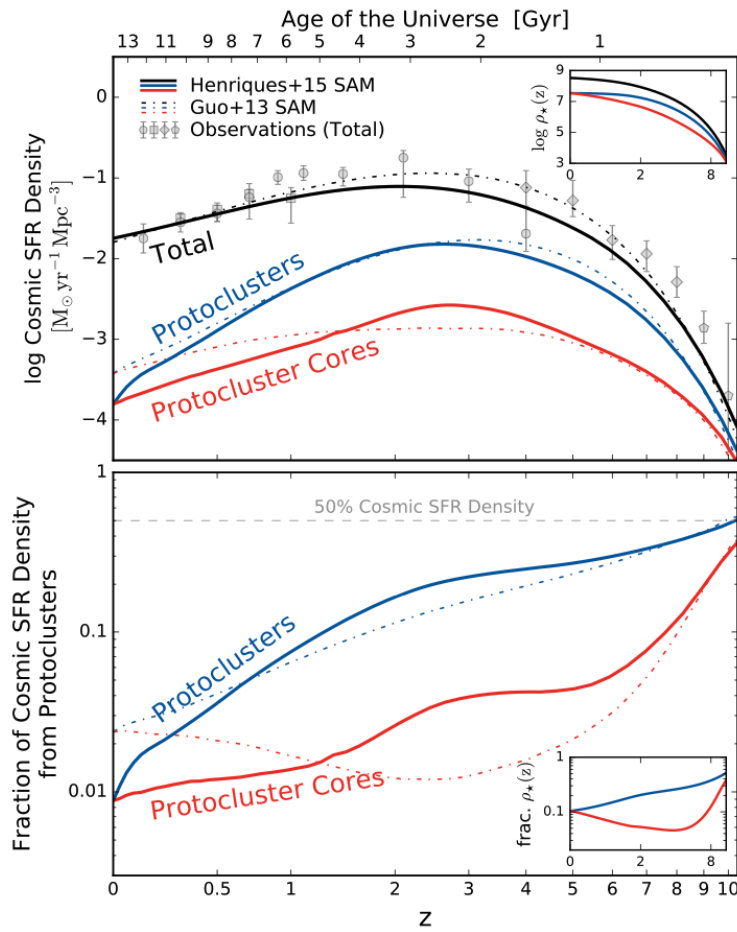


Figure 8.7: "Upper panel: SFR density for all galaxies (black), protoclusters (blue), and cores (red). The associated stellar mass densities are shown in the inset. Data points show a set of observationally derived cosmic SFR density for comparison (circles: Cucciati et al. 2012; squares: Schiminovich et al. 2005; diamonds: Finkelstein et al. 2015, and pentagons: Oesch et al. 2013). Lower panel: Fractional contributions to the total cosmic SFR density of protoclusters (blue) and protocluster cores (red). The associated stellar mass density fractions are shown in the inset." Credit: Chiang et al. (2017).

LIST OF PUBLICATIONS

First author publication

L. Leroy, D. Elbaz, B. Magnelli, C. Gómez-Guijarro, E. Daddi, M. Xiao, and M. Dickinson: "The role of stellar mass in the cosmic history of star-formation as seen by *Herschel* and ALMA". Submitted.

Other publications

C. Gómez-Guijarro, [...], **L. Leroy** et al. : "GOODS-ALMA 2.0: Starbursts in the main sequence reveal compact star formation regulating galaxy evolution prequenching", A&A 659, A196 (2022).

<https://doi.org/10.1051/0004-6361/202142352>

M. Xiao, D. Elbaz, C. Gómez-Guijarro, **L. Leroy** et al. : "The hidden side of cosmic star formation at $z > 3$ Bridging optically dark and Lyman-break galaxies with GOODS-ALMA", A&A 672, A18 (2023).

<https://doi.org/10.1051/0004-6361/202245100>

M. Xiao, [...], **L. Leroy** et al. : "Massive Optically Dark Galaxies Unveiled by JWST Challenge Galaxy Formation Models". Submitted.

<https://doi.org/10.48550/arXiv.2309.02492>

R. Mérida, [...], **L. Leroy** et al. : "Measuring the gas reservoirs in $10^9 < M_\star < 10^{11} M_\odot$ galaxies at $1 \leq z \leq 3$ ". To be submitted.

The role of stellar mass in the cosmic history of star-formation as seen by *Herschel* and ALMA

L. Leroy¹*, D. Elbaz¹, B. Magnelli¹, C. Gómez-Guijarro¹, E. Daddi¹, M. Xiao^{1,2}, and M. Dickinson³

¹ Université Paris Cité, Université Paris-Saclay, CEA, CNRS, AIM, F-91191, Gif-sur-Yvette, France

² Department of Astronomy, University of Geneva, Chemin Pegasi 51, 1290 Versoix, Switzerland

³ NSF's National Optical-Infrared Astronomy Research Laboratory, 950 N. Cherry Ave., Tucson, AZ 85719, USA

ABSTRACT

Aims. We explore the contribution of galaxies, as a function of their stellar mass, to the cosmic star formation history (CSFH). In order to avoid uncertain extrapolations of the infrared luminosity function, which is often polluted by the contribution of starbursts, we base our analysis on stellar mass. Attenuation by dust is accounted for thanks to the combination of deep surveys by *Herschel* and the Atacama Large Millimeter/submillimeter array (ALMA).

Methods. We combine for the first time the deepest *Herschel* (GOODS-South, GOODS-North, COSMOS and USD) and ALMA (GOODS-South) surveys. We constrain the star formation rate (SFR), dust mass (M_{dust}), dust temperature (T_{dust}) and gas mass (M_{gas}) of galaxies as a function of their stellar mass (M_{\star}) from $z \sim 5$ to $z \sim 0$ by performing a stacking analysis of over 128,000 *Hubble* Space Telescope (*HST*) *H*-band selected galaxies. We study the evolution of galaxies in the $\Sigma_{\text{SFR}}-\Sigma_{\text{gas}}$ plane as a function of redshift and M_{\star} .

Results. We show that the addition of ALMA to *Herschel* allows us to reach lower M_{\star} and higher redshifts. We confirm that the SFR- M_{\star} star-formation main sequence (MS) follows a linear evolution with a slope close to unity with a bending at the high mass end at $z < 2$. The mean T_{dust} of MS galaxies evolves linearly with redshift, with no apparent correlation with M_{\star} . We show that, up to $z \sim 5$, massive galaxies (i.e., $M_{\star} \geq 10^{10} M_{\odot}$) account for most of the total SFR density (ρ_{SFR}), while the contribution of lower mass galaxies (i.e., $M_{\star} \leq 10^{10} M_{\odot}$) is rather constant. We compare the evolution of star-forming galaxy (SFGs) to the cosmological simulation TNG100. We find that TNG100 exhibits a noticeable difference in the evolution of the CSFH, i.e., the marked evolution of massive galaxies found in the observations appears to be smoothed in the simulation, possibly due to too efficient feedback. In this mass complete analysis, *H*-dropout (also called HST-dark) galaxies account for $\sim 23\%$ of the CSFH in massive galaxies at $z > 3$. Finally, we find hints that the star-formation efficiency of distant galaxies ($z=3-5$) is stronger (shorter depletion time) as compared to low-redshift galaxies, i.e., a possible evolution of the local Kennicutt-Schmidt relation.

Key words. galaxies:evolution – galaxies:high-redshift – galaxies:photometry – galaxies:star formation – submillimeter: galaxies – infrared:galaxies

1. Introduction

The evolution of the SFR density (ρ_{SFR}) over time follows a gradual growth from the big bang to the cosmic noon (i.e., $z \sim 2$), followed by a continuous decline by a factor ~ 10 up to our time (e.g. Madau & Dickinson 2014; Bouwens et al. 2015b; Liu et al. 2018; Leslie et al. 2020 and Schreiber et al. 2015, hereafter S15). This evolution alone raises many questions about the growth and death of galaxies. For example, the contribution to the ρ_{SFR} of galaxies of different M_{\star} , or the ρ_{SFR} at high redshift (i.e., $z \geq 4$) are still largely uncertain. Our understanding of the high-redshift part (i.e., $z \geq 4$) is mainly built from the ultraviolet (UV), and then deduced by correcting these UV measurements from dust attenuation (e.g. Bouwens et al. 2012b,a; Schenker et al. 2013; Bouwens et al. 2015a,b; Oesch et al. 2018). However, it has recently been claimed, through studies using dust-unbiased measurements (i.e., radio or far-infrared emission), that ρ_{SFR} is actually higher at high redshift (e.g. Novak et al. 2017; Lagache 2018; Gruppioni et al. 2020).

In order to deduce the cosmic star formation history, it is necessary to correctly infer the star formation rate (SFR) of galaxies. It has been shown that the SFR of star-forming galaxies (SFGs)

is positively correlated with their stellar mass (M_{\star} ; e.g. Elbaz et al. 2007; Daddi et al. 2007; Whitaker et al. 2012, 2014; Speagle et al. 2014; S15; Lee et al. 2015; Delvecchio et al. 2021; Leslie et al. 2020; Popesso et al. 2023) with a small scatter of $\sim 0.2 - 0.3$ dex (e.g. Elbaz et al. 2007; Whitaker et al. 2012; Speagle et al. 2014; S15). This correlation is called the "main sequence" (Noeske et al. 2007) of SFGs. Although the specifics of this correlation remains a matter of debate, most recent studies tend to favour a linear main sequence in logarithmic space with a bending appearing at high M_{\star} and for $z \leq 2 - 3$ (e.g. Whitaker et al. 2014; Magnelli et al. 2014; S15; Delvecchio et al. 2021; Leslie et al. 2020), rather than a strictly linear correlation between SFR and M_{\star} (e.g. Whitaker et al. 2012; Speagle et al. 2014).

The fraction of star formation obscured by dust is still highly uncertain at high redshift (i.e., $z \geq 3$), as it could be higher up to a factor of 10 above unobscured formation (Casey et al. 2018). As the correction factors for dust extinction are quite large (e.g. Calzetti et al. 1994; Madau et al. 1998; Steidel et al. 1999), this leads studies to combine SFR from the UV (uncorrected from dust extinction) and SFR deduced directly from the infrared (IR) (e.g. S15; Delvecchio et al. 2021) when seeking the total SFR and ρ_{SFR} . Although most of them are based on *Hubble* Space

* email: lucas.leroy@cea.fr

45 Telescope (*HST*) detected catalogues to infer the evolution of
 46 the SFR, they do not take into account the contribution of so-
 47 called *HST*-dark galaxies in the study of the ρ_{SFR} . *H*-dropout
 48 (Wang et al. 2019), *HST*-dark (Zhou et al. 2020) or optically-
 49 dark/faint (Gómez-Guijarro et al. 2022a; Xiao et al. 2022) galax-
 50 ies, represent massive and highly obscured galaxies usually de-
 51 tected with low significance or not at all in the optical. Although
 52 initially thought to be a marginal population with little effect on
 53 the ρ_{SFR} , over time it was shown that such obscured galaxies
 54 could significantly contribute to the ρ_{SFR} above $M_\star \sim 10^{10.5} M_\odot$
 55 (e.g. Wang et al. 2019; Xiao et al. 2022).

56 Since the Atacama Large Millimeter/submillimeter array
 57 (ALMA) came online in 2013 has enabled large and deep
 58 surveys, with better resolution, in the millimetre/submillimetre
 59 range (e.g. Franco et al. 2018; Gómez-Guijarro et al.
 60 2022a). Studies can now combine higher quality millime-
 61 tre/submillimetre measurements with IR measurements. ALMA
 62 has proven to be a powerful tool to probe the gas content of
 63 galaxies (e.g. Scoville et al. 2014; Groves et al. 2015; Scoville
 64 et al. 2016; Schinnerer et al. 2016; Kaasinen et al. 2019; Liu
 65 et al. 2019b; Millard et al. 2020; Magnelli et al. 2020; Wang et al.
 66 2022), and developing our global understanding of high-redshift
 67 galaxies (see Hodge & da Cunha 2020 for a review).

68 Spatially resolved studies show that the SFR mostly corre-
 69 lates with molecular gas (H_2) surface density, and very little
 70 with atomic gas (HI) surface density (e.g. Bigiel et al. 2008;
 71 Leroy et al. 2008). The gas content of galaxies is usually probed
 72 through CO emission lines because of the difficulty of directly
 73 observing the H_2 content (see Bolatto et al. 2013 for a review).
 74 However, other techniques have been developed to infer the gas
 75 content of galaxies through the study of multi-wavelength dust
 76 spectral energy distribution (SED) fits, and by applying gas-to-
 77 dust ratio to infer M_{gas} from M_{dust} (e.g. Leroy et al. 2011; Magdis
 78 et al. 2011, 2012; Magnelli et al. 2012; Rémy-Ruyer et al. 2014;
 79 Genzel et al. 2015).

80 By combining the SFR and the gas content of galaxies, we
 81 can infer the star formation efficiency ($SFE \equiv SFR/M_{\text{gas}}$) of
 82 galaxies, which gives a more complete picture of how galaxies
 83 form stars at a different moment in cosmic time. One way of
 84 looking at this is to use the Kennicutt-Schmidt relation (Ken-
 85 nicutt 1998b). This relation has been shown to give a universal
 86 power law correlation between SFR and gas surface density with
 87 a slope of $\sim 1.0 - 1.5$ (e.g. Kennicutt 1998b; de los Reyes & Ken-
 88 nicutt 2019; Wang et al. 2022).

89 In this paper, combining *Spitzer*, *Herschel* and ALMA, we
 90 study the evolution of galaxy properties from $z \sim 0$ to 5 through
 91 stacking on four fields: COSMOS, UDS, GOODS-South and
 92 GOODS-North. We try to answer few open questions about the
 93 evolution and global history of galaxies. In particular, we seek to
 94 constrain the main sequence, ρ_{SFR} at high redshift (i.e., $z \geq 4$),
 95 the different contributions to ρ_{SFR} as a function of M_\star , and the
 96 impact of the *H*-dropout galaxy population on the properties of
 97 galaxies as a whole. A similar study using *Spitzer* and *Herschel*
 98 measurements has been carried out by S15. However, the addition
 99 of ALMA measurements to *Herschel* using stacking has not
 100 yet been carried out. The reason is that this requires access to an
 101 extensive study programme on ALMA. This has only recently
 102 been possible thanks to blind surveys like the GOODS-ALMA
 103 survey (Franco et al. 2018, 2020; Gómez-Guijarro et al. 2022a).
 104 A summary of the data used in this study is given in Sect. 2. The
 105 stacking method is described in Sect. 3. Sect. 4 is devoted to the
 106 SED fitting procedure. Sect. 5 reviews the properties of galax-
 107 ies that can be deduced from this analysis. Sect. 6 and 7 present
 108 the cosmic star formation history and the cosmic evolution of

Table 1: Number of galaxies in the final sample from each field.

Field	Number of galaxies	Area (arcmin 2)
GOODS South	26,811	134
GOODS North	35,322	142
COSMOS	34,124	388
UDS	32,695	412
Total	128,952	1,077

the gas mass density deduced from this work, respectively. We
 109 interpret and discuss our results in a global cosmological con-
 110 text in Sect. 8, and in Sect. 9 we summarise the main results and
 111 conclusions.
 112

In this work, we adopt a Salpeter (1955) initial mass
 113 function (IMF) and the cosmological parameters (Ω_M , Ω_Λ ,
 114 h)=[0.30,0.70,0.70]. Throughout the paper, we will use a fac-
 115 tor of 1.7 to convert M_\star and SFR from a Chabrier (2003) to
 116 a Salpeter (1955) IMF whenever necessary (e.g. Reddy et al.
 117 2006; Santini et al. 2012; Elbaz et al. 2018; Gómez-Guijarro
 118 et al. 2022b). When mentioned, magnitudes are in the AB sys-
 119 tem, such that $M_{\text{AB}} = 23.9 - 2.5 \log_{10}(S_v [\mu\text{Jy}])$.
 120

2. Sample and observations

2.1. Sample

In this study, we worked from catalogues of *H*-band selected
 123 SFGs on four fields: GOODS-South, GOODS North, COSMOS
 124 and UDS. We used the ultra-deep *H*-band catalogue of the
 125 CANDELS-*HST* team (Grogin et al. 2011; Koekemoer et al.
 126 2011) for GOODS-South (Guo et al. 2013), COSMOS (Nayy-
 127 eri et al. 2017) and UDS (Galametz et al. 2013) fields, while in
 128 GOODS-North we use the catalogue from Barro et al. (2019).
 129 The 5σ limiting magnitude range from $H \sim 27.4$ to 29.7 for
 130 GOODS-South, $H \sim 27.4$ to 28.8 for COSMOS, $H \sim 27.1$ to
 131 27.6 for UDS, and $H \sim 27.8$ to 28.7 for GOODS-North. The
 132 photometric redshifts and M_\star of the galaxies in these catalogues
 133 were derived in S15 (GOODS-South, COSMOS and UDS) and
 134 Barro et al. (2019) (GOODS-North). Photometric data were fit-
 135 ted up to IRAC 4.5 μm , with EAZY (Brammer et al. 2008), by
 136 assuming a delayed exponentially declining star formation his-
 137 tory with the Bruzual & Charlot (2003) stellar population synthe-
 138 sis model. The SFGs are UVJ selected, following the definition
 139 from Muzzin et al. (2013). The final number of SFGs in the sam-
 140 ple is given in Table 1. *H*-dropout galaxies are by definition not
 141 included in these samples, as they are not detected in *H*-band.
 142 However, we used the sample from Wang et al. (2019) to add
 143 and discuss their impact in any necessary analyses.
 144

2.2. Observations

Observations with *Spitzer*-MIPS at 24 μm include maps of the
 146 COSMOS field, (PI: D. Sanders; LeFloc'h et al. 2009), the
 147 GOODS-South and GOODS-North fields (GOODS Legacy pro-
 148 gram; PI: M. Dickinson), and the UDS field (SpUDS *Spitzer*
 149 Legacy program; PI: J. Dunlop). The *Herschel* PACS and SPIRE
 150 maps of the four fields come mainly from the CANDELS-
 151 *Herschel* program. The PACS GOODS-North and GOODS-
 152 South maps are the combined *Herschel*-PACS data from the PEP
 153 (Lutz et al. 2011) and GOODS-*Herschel* (Elbaz et al. 2011) pro-
 154 grams, as described in Magnelli et al. (2013). For ALMA, we
 155 used the 1.13mm low-resolution GOODS-ALMA map (Gómez-
 156 Guijarro et al. 2022a), within the GOODS-South, field with the
 157

Table 2: Number of galaxies in each bin of M_{\star} and redshift for the stacking in the *Herschel* 100 μm , 160 μm , 250 μm , 350 μm and 500 μm bands, and for the stacking in the ALMA band are displayed in the top and bottom row of each cell, respectively. The two axes represent the boundaries of the bins in redshift and M_{\star} . Bins with at least a FIR, and a submillimeter stack detection (i.e., with a $S/N \geq 3\sigma$ in at least one band) are highlighted in faded blue and red, respectively. Bins that are mass complete are noted with a black bar.

			$\log_{10}(M_{\star}/M_{\odot})$			
	8.5	9.5	10	10.5	11	12
Redshift	0.1	blabk10!00954 black!d0!086	blabk10!00182 black!d0!010	blabk10!00125 black!d0!013	blabk10!0056 black!d0!0103	blabk10!0011 black!d0!011
	0.4	blabk10!003,122 black!d0!0298	blabk10!00746 black!d0!067	blabk10!00497 black!d0!036	blabk10!0039 black!d0!021	$M_{\star} = C \times L_{1.6\mu\text{m}-\text{obs}}^{\alpha}$ with a scatter. The relation and dispersion are fitted from the H -band photometry of the catalogues. We derive the completeness from Monte-Carlo simulations by generating, from a uniform redshift distribution in the redshift bin and given M_{\star} , the corresponding $L_{1.6\mu\text{m}-\text{obs}}$ taking into account the dispersion, and comparing it to the corresponding H -band detection limit for each catalogue. We assume that catalogues are mass complete when their completeness is above 90% (S15). The corresponding $M_{\star}^{90\%}$, above which all catalogues are assumed mass complete, are listed in Table 3. All but two of the catalogues which yield significant detections ($S/N \geq 3\sigma$ in at least one band from 24 μm to 1.13 mm) considered in this study are mass complete: for $9.5 \leq \log_{10}(M_{\star}/M_{\odot}) \leq 10.0$ at $2.3 \leq z \leq 3.1$, and $10.0 \leq \log_{10}(M_{\star}/M_{\odot}) \leq 10.5$ at $3.1 \leq z \leq 3.9$. The latter bin is, however, almost mass complete $M_{\star}^{90\%} = 10^{10.1} M_{\odot}$.
	0.7	blabk10!005,686 black!d0!0403	blabk10!001,449 black!d0!0098	blabk10!0087 black!d0!007	blabk10!0058 black!d0!0021	black!d0!005
	1.0	blabk10!005,325 black!d0!0382	blabk10!001,425 black!d0!0115	blabk10!0078 black!d0!070	blabk10!00403 black!d0!044	black!d0!010
	1.3	blabk10!012,091 black!d0!0905	blabk10!002,742 black!d0!0188	blabk10!0010 black!d0!0016	blabk10!00182 black!d0!0055	black!d0!016
	1.8	blabk10!05,365 black!d0!0410	blabk10!001,770 black!d0!0145	blabk10!0091 black!d0!0047	blabk10!00590 black!d0!0047	black!d0!00260
	2.3	blabk10!05,656 black!d0!0475	blabk10!002,459 black!d0!0187	blabk10!001,256 black!d0!0123	blabk10!0017 black!d0!0055	black!d0!0117
	3.1	blabk10!02,352 black!d0!0352	blabk10!01,305 black!d0!0115	blabk10!0010 black!d0!0016	blabk10!00133 black!d0!00116	black!d0!0143
	3.9	blabk10!01,063 black!d0!0131	blabk10!0692 black!d0!069	blabk10!0015 black!d0!0015	blabk10!0011 black!d0!0012	black!d0!002
	5.0					

158 1''.1 circularised point spread function (PSF) full width half maximum (FWHM). We note that there is a global and local offset
159 between the position of sources in the ALMA and *HST* images
160 (Franco et al. 2018, 2020). We corrected them using the offsets
161 provided by Franco et al. (2020).

3. Stacking

164 Our method consists in stacking several images of galaxies on
165 top of each other in order to increase the overall signal to noise
166 ratio (S/N). The result of a stacking procedure is the mean or
167 median flux for all galaxies stacked together. The main advantage
168 of this method is to be able to recover reliable flux measure-
169 ments for populations of galaxies whose S/N is too low when
170 studied individually. In practice, this means being able to mea-
171 sure the properties of galaxies with lower M_{\star} and higher red-
172 shift. An effective way to take advantage of the stacking method
173 is to group galaxies into sub-populations with similar properties.
174 To this end, in this study, we stack our sample of galaxies over
175 different redshift and M_{\star} bins. The total numbers of galaxies per
176 bin are displayed in the Table 2.

177 In order to access the completeness of the catalogues that
178 we stacked in this study, we followed the method of S15. In
179 summary, we assumed, for each redshift bin, that the observed
180 luminosity at 1.6 μm ($L_{1.6\mu\text{m}}^{\text{obs}}$) can be related to M_{\star} simply by

Table 3: M_{\star} for which we obtain a completeness of 90% in the H -band catalogues used in this work.

Redshift bin	$\log_{10}(M_{\star}^{90\%}/M_{\odot})$
$0.1 \leq z \leq 0.4$	7.5
$0.4 \leq z \leq 0.7$	7.9
$0.7 \leq z \leq 1.0$	8.1
$1.0 \leq z \leq 1.3$	8.2
$1.3 \leq z \leq 1.8$	8.6
$1.8 \leq z \leq 2.3$	9.2
$2.3 \leq z \leq 3.1$	9.7
$3.1 \leq z \leq 3.9$	10.1
$3.9 \leq z \leq 5.0$	10.0

$M_{\star} = C \times L_{1.6\mu\text{m}-\text{obs}}^{\alpha}$ with a scatter. The relation and dispersion are fitted from the H -band photometry of the catalogues. We derive the completeness from Monte-Carlo simulations by generating, from a uniform redshift distribution in the redshift bin and given M_{\star} , the corresponding $L_{1.6\mu\text{m}-\text{obs}}$ taking into account the dispersion, and comparing it to the corresponding H -band detection limit for each catalogue. We assume that catalogues are mass complete when their completeness is above 90% (S15). The corresponding $M_{\star}^{90\%}$, above which all catalogues are assumed mass complete, are listed in Table 3. All but two of the catalogues which yield significant detections ($S/N \geq 3\sigma$ in at least one band from 24 μm to 1.13 mm) considered in this study are mass complete: for $9.5 \leq \log_{10}(M_{\star}/M_{\odot}) \leq 10.0$ at $2.3 \leq z \leq 3.1$, and $10.0 \leq \log_{10}(M_{\star}/M_{\odot}) \leq 10.5$ at $3.1 \leq z \leq 3.9$. The latter bin is, however, almost mass complete $M_{\star}^{90\%} = 10^{10.1} M_{\odot}$.
We choose to use mean stacking for our work, rather than median stacking, although mean stacking better suppresses secondary sources in the stacked image (i.e., bright sources which are close to the stacked target and might appear in the final stacked image), it has been shown that it also yields systematically biased measurements at low S/N or in the presence of a flux distribution skewed towards low or high values (White et al. 2007; S15). It comes from the fact that the median ($\langle \rangle$) is not a linear operation: $\langle a + b \rangle \neq \langle a \rangle + \langle b \rangle$. As shown in S15, correcting for these systematic biases involves making strong assumptions on the actual flux distribution of the stacked sources, which is non-trivial and very uncertain. On the contrary, the mean stack gives us access to the total flux in the stack, which we currently miss to infer $\rho_{\text{SFR}}^{\text{IR}}$.

During the stacking procedure, it is possible to treat detected and undetected galaxies separately. The main way to do this is to stack only the undetected sources on the residual map, and then add them to the fluxes of the detected galaxies via a weighted mean (e.g. Magnelli et al. 2009). Although this method reduces the confusion noise of faint sources and removes most of the contamination from bright neighbours, it can also introduce some biases (S15). Following S15, we have therefore chosen to treat detected and undetected sources in the same way for consistency (i.e., directly from the image and not from the residual). The contamination of bright neighbours is dealt with later in the study (see Sect. 3.2).

We noticed the presence of a global background gradient in most *Herschel* images. In order to deal with it, we have decided to rotate the stacked postage stamp images successively by 90°.

The resulting flux density in each stacked image was obtained via standard aperture measurements or point spread function (PSF) fitting method (see detail for each wavelength in Sect. 3.1, 3.2 and 3.3). The corresponding S/N was then de-

rived using a simple Monte Carlo approach, i.e., $S/N = S_\nu/\sigma_{\text{MC}}$, where S_ν is the flux density measured at the centre of the stacked image within an aperture of radius, r , while σ_{MC} is the standard deviation of the signal in 100 circles, of the same radius r , randomly positioned on the edges of the stacked stamp. Depending on the method used to compute the flux, r corresponds to either the radius used for the aperture measurement method, or the radius within which the PSF fitting method was performed.

In addition to this photometric noise, there is an uncertainty in the recovered flux density due to the intrinsic dispersion of the underlying stacked population (i.e., all galaxies in the stack do not have the exact same flux density). This flux dispersion can be quantified using a bootstrap analysis (e.g. S15). The method consists in repeating several time the full stacking and flux density measurement process, picking, for each realisation, the galaxies from the origin sample, with replacement, until the number of galaxies in the original sample is reached. In this study, we compute a 100 runs. The error is then deduced from the standard deviation of the computed flux densities for this bin.

3.1. Spitzer

As the $24\mu\text{m}$ MIPS-*Spitzer* map ($\sim 5''.8$ PSF FWHM) has a better resolution than *Herschel*-PACS ($\sim 7''$ and $\sim 11''.3$ PSF FWHM at $100\mu\text{m}$ and $160\mu\text{m}$, respectively), we do not expect the clustering bias (see Sect. 3.2) to be a dominant effect on the stacked stamp. The fluxes are calculated using a classical aperture photometry method. The aperture is chosen to be 4 pixels (i.e., $4''.8$) in radius, which contains about $\sim 50\%$ of the total flux for a point source.

3.2. Herschel

When stacking galaxies, a "clustering bias" can occur due to the neighbouring galaxies of the main stacking targets. Such contamination from neighbouring sources can become significant when the size of the PSF becomes comparable to the typical cluster length of SFGs. It has been shown that the clustering bias has a non-negligible impact on the results when stacking galaxies in the *Herschel* bands (e.g. Bavouzet et al. 2008; Béthermin et al. 2010; Kurczynski & Gawiser 2010; Bourne et al. 2012; Béthermin et al. 2012; Viero et al. 2013; Béthermin et al. 2014; S15; Béthermin et al. 2015; Delvecchio et al. 2021) due to the large PSF of *Herschel*. Correcting for this bias is crucial to accurately measure the peak of SED of SFGs, as this bias tends to cause the fluxes of *Herschel* to be increasingly overestimated with increasing wavelength (as the size of the PSF increases with the wavelength).

To mitigate this clustering signal contamination, we choose to follow the method presented in S15. It consists in fitting only a PSF and a local background term:

$$S(x, y) = \varphi \times PSF(x, y) + \varepsilon. \quad (1)$$

where φ and ε are the normalisation of the source flux and background, respectively. The fit is performed on a fixed aperture of radius of $0.9 \times \text{FWHM}$, as this was found to minimise the clustering contamination to φ (S15). The clustering bias signal is in this case largely included in the background term. Nevertheless, even with this radius the contamination of φ is not null and we still need to apply a correction for what remains of the clustering signal in the mean flux term (φ). The correction factors were calculated by simulating the stacking procedure on mock images (see S15 for more details). The correction factors of S15

Table 4: Clustering bias correction factor from S15

Wavelength (μm)	Correction
100	$0\%^{+7\%}_{-7\%}$
160	$3\%^{+9\%}_{-8\%}$
250	$8\%^{+12\%}_{-8\%}$
350	$13\%^{+12\%}_{-10\%}$
500	$25\%^{+19\%}_{-18\%}$

are listed in Table 4. For the PACS maps, we used the truncated PSF derived from Vesta, while for *Herschel*-SPIRE the PSF is assumed to be Gaussian with a FWHM of $18''.15$, $25''.15$ and $36''.3$ respectively at 250 , 350 and $500\mu\text{m}$ according to Griffin et al. (2010) (see also Shirley et al. 2021).

Finally, for *Herschel*-PACS, it was shown (Popesso et al. 2012; Magnelli et al. 2013) that the high-pass filter data reduction technique that was used to remove low-frequency noise in the maps could induce an underestimation of the photometric measurements of the unmasked faint sources. It was shown in Popesso et al. (2012) that a correction factor of 17%, and 10% should be taken into account when stacking undetected faint, and detected, sources in the PACS maps ($100\mu\text{m}$ and $160\mu\text{m}$), respectively.

3.3. ALMA

For the purpose of this study, we decided to work in the image plane when dealing with ALMA. Another option would have been to work in the *uv* plane (i.e., in Fourier space), as ALMA provides us with measurements in the *uv* space. Although this may give more robust results, since we do not need to go through the conversion between the *uv* plane and the image plane first, it is very computationally intensive. Furthermore, on few test bins we only observed a 10% difference between fluxes calculated from stacks in the *uv* and image planes. We decided not to stack directly in the *uv* plane but in the image plane in order to save computing time as this should not impact the results of this study.

As the ALMA 1.1mm map has a much better resolution ($\sim 1''.1$ PSF FWHM; which is comparable to typical sizes of individual SFGs Suess et al. 2019; Wang et al. 2022) than *Herschel*-PACS ($\sim 7''$ and $\sim 11''.3$ PSF FWHM at $100\mu\text{m}$ and $160\mu\text{m}$, respectively), the clustering bias is negligible on the stacked stamp. Due to the high angular resolution of the ALMA data, and to possible small offsets between the optical centroids (on which our stack positions are based) and millimeter centroids, the stacked images are extended on scales larger than that of the ALMA PSF. However, this has no significant impact of the measure flux density via the aperture photometry method. To measure ALMA flux densities, we applied an aperture photometry within a radius of $1''$, containing 85% of the total flux density (i.e., $S_{\text{AP}}^{\text{PSF}}/S_{\text{tot}}^{\text{PSF}} = 0.85$).

4. SED fitting

4.1. SED fitting procedure

One of the objectives of this paper is to retrieve several properties such as SFR, dust temperature (T_{dust}), dust masses (M_{dust}) and gas masses (M_{gas}) from our far-infrared (FIR) to submillimetre stacking analysis, and compare them to the literature. We performed an SED fit from the measured fluxes for each bin of redshift and M_{\star} . Because we do not have many points on the FIR at low M_{\star} and high redshifts, we used the library

from Schreiber et al. 2018, hereafter S18, which is well suited for our study given its small number of free parameters. Choosing a model with more parameters, such as Draine & Li (2007) and Draine et al. (2014), would imply fixing parameters on some bins. The library of S18 is calibrated on galaxies from $z = 0.5$ to $z = 4$, which allows to have a realistic SED while reducing the number of free parameters. We have assumed a form of SED that we would expect for the main sequence galaxies, and no active galactic nuclei (AGN) contribution to the stacked SED.

To fit the SED, we only considered fluxes with $S/N \geq 3$. Stacked flux measurements with $S/N < 3$ are replaced by conservative 5σ upper limits. At $z > 4$ MIPS-24 stacked fluxes, if available, have been transformed to 5σ upper limits as they are no longer dominated by dust and polycyclic aromatic hydrocarbon (PAH) emissions, but rather by stellar emission. From these SED fits, we measured the corresponding infrared luminosity (L_{IR}) by integrating the best-fit SED in the range 8-1000 μm rest frame. The error on L_{IR} was obtained by varying their stacked photometry randomly within their uncertainties.

The T_{dust} can be defined in different ways (i.e., weighted by mass or luminosity). The luminosity weighted $T_{\text{dust}}^{\text{L}}$, for the library from S18, is calculated from a grey body of effective emissivity $\beta = 1.5$ (S18). This means that $T_{\text{dust}}^{\text{L}}$ follows Wien's law (see Eq. 2).

$$T_{\text{dust}}^{\text{L}} [\text{K}] = 2.897 \times 10^3 / (\lambda_{\text{max}} [\mu\text{m}]), \quad (2)$$

where λ_{max} is the wavelength corresponding to the peak of $\lambda^{\beta} L_{\lambda}$. A mass weighted $T_{\text{dust}}^{\text{M}}$, was also calculated for each template by mass weighted averaging each individual template of Galliano et al. (2011) (see S18 for more details). In the cases where we only had one or two points to perform our fit (i.e., the SED peak was not well defined in this case), we chose to restrict the $T_{\text{dust}}^{\text{M}}$ during the fit to the $T_{\text{dust}}^{\text{M}}$ evolution from S18 ± 10 K. This is a reasonable way to reduce the error on the deduced L_{IR} by slightly restricting the $T_{\text{dust}}^{\text{M}}$ to reasonable values. Our best-fits of SEDs are displayed in Fig. 1.

The templates from the library of S18 are built using the amorphous carbon model from Galliano et al. (2011). This differs from the model from Draine & Li (2007) which takes into account amorphous silicate and graphite grains. This change of model was shown in Galliano et al. (2011) to lower the tension, in the Large Magellanic Cloud and the Milky Way, between the observed dust-to-gas ratio and the stellar abundances. The differences between the two models are mainly reflected in the different emissivity. The choice of a different emissivity does not affect the dust temperature or the L_{IR} , as these properties correspond to the peak and the area under the SED, respectively. However, the M_{dust} deduced from Galliano et al. (2011) is about a factor of 2 lower than those deduced from Draine & Li (2007), without affecting the M_{gas} as the factor cancels out when converting M_{dust} to M_{gas} . The debate on the composition of dust grains goes far beyond the scope of this study. We chose to work with M_{dust} derived from the Draine & Li (2007) model, as it will ease comparison with the literature, which is widely base on the later model. In practice, we have re-fitted the model library of S18 with a Draine & Li (2007) model to associate the M_{dust} . The impact on M_{gas} of choosing an amorphous carbon model instead of an amorphous silicate and graphitic grains model is briefly discussed at the end of the Sect. 5.3.

Overall we verified that fitting our stacked flux with the S18 or Draine & Li (2007) libraries has little to no impact on our results, as the differences on some key properties such as L_{IR} , T_{dust} and M_{dust} (once corrected for the emissivity chosen in S18) are

quite small: $-7\%^{+7\%}_{-4\%}$ for L_{IR} , $1\%^{+12\%}_{-6\%}$ for T_{dust} and $4\%^{+33\%}_{-17\%}$ for M_{dust} . An essential consequence of this observation is that the models of S18 reproduce well the global SED shape of stacked galaxies. This reinforces the choice we made to use the S18 templates instead of Draine & Li (2007) for this study.

4.2. Adding ALMA to Herschel

The addition of ALMA to this study results in an improvement of the SED at high redshift (i.e., at $3.1 \leq z \leq 5.0$). More specifically, it allows to get an ALMA measurement at $10.0 \leq \log_{10}(M_{\star}) \leq 10.5$ for $3.1 \leq z \leq 3.9$ and $3.9 \leq z \leq 5$ that provides information on some of the properties of galaxies (i.e., L_{IR} and M_{gas}) at these redshifts and M_{\star} instead of what would have just been an upper limit on these properties. At $10.5 \leq \log_{10}(M_{\star}) \leq 11.0$ for $3.1 \leq z \leq 3.9$ and $3.9 \leq z \leq 5$, and $11.0 \leq \log_{10}(M_{\star}) \leq 12.0$ for $3.9 \leq z \leq 5$, this also allows the SED peak to be constrained more effectively, as it is only weakly constrained, if at all, by the *Herschel* data alone. The SED peak is crucial for determining properties such as $T_{\text{dust}}^{\text{M}}$ and M_{gas} . Elsewhere it also provides an extra point or upper limit that significantly reduces the uncertainty in the properties inferred from the SED fit. These extra ALMA point are thus decisive for this study, which aims to probe the properties of galaxies over a wide dynamic range, extending up to $z \sim 5$.

4.3. Simulations to correct for averaging biases

Because a mean stacking procedure is luminosity weighted, it can have non-linear effects on the shape of the resulting SED (e.g. Elbaz et al. 2011; S15; S18). These effects include the widening of the FIR bump and a bias of the peak towards warmer $T_{\text{dust}}^{\text{L}}$. It is mainly a result of mixing galaxies of different redshifts and $T_{\text{dust}}^{\text{L}}$ (e.g. Elbaz et al. 2011; S15; S18). The broadening of the SED increases the difficulty of determining precisely $T_{\text{dust}}^{\text{L}}$ (S18). For the rest of the paper, we chose to work with mass-weighted dust temperatures, and we will refer to $T_{\text{dust}}^{\text{M}}$ simply as T_{dust} . To ensure that our conclusions are not biased by these effects, we performed simulations to identify any systematic bias due to our stacking procedure.

To this end, for each bin of M_{\star} and redshift, we simulated the biases coming from stacking starting from the distribution of the galaxies in the bin. This has the advantage of taking into account the specificity of the M_{\star} and redshift distributions within our bin. For each set of galaxies, we created a mock counterpart in order to compare the properties resulting from the stacking with those expected.

To each galaxy of mass M_{\star} , we assigned the SFR starting from M_{\star} and following $SFR = R_{\text{SB}} \times SFR_{\text{MS}}$. The SFR_{MS} was calculated from the main sequence trend found in this work (See Eq. 12 and parameters Table 5) as a function of redshift and M_{\star} . R_{SB} represents the starburstiness and is defined by $R_{\text{SB}} = SFR/SFR_{\text{MS}}$. We want to generate both mock main sequence galaxies and starburst galaxies. It was shown in S15 that both the main sequence width (~ 0.3 dex, see S15) and the starburst fraction do not evolve with redshift and M_{\star} . We can therefore reasonably assume that the distribution function of R_{SB} does not vary (S15). This assumption still allows the luminosity functions to be reconstructed properly (e.g. Sargent et al. 2012; S15). Following Sargent et al. (2012), we have modelled the probabil-

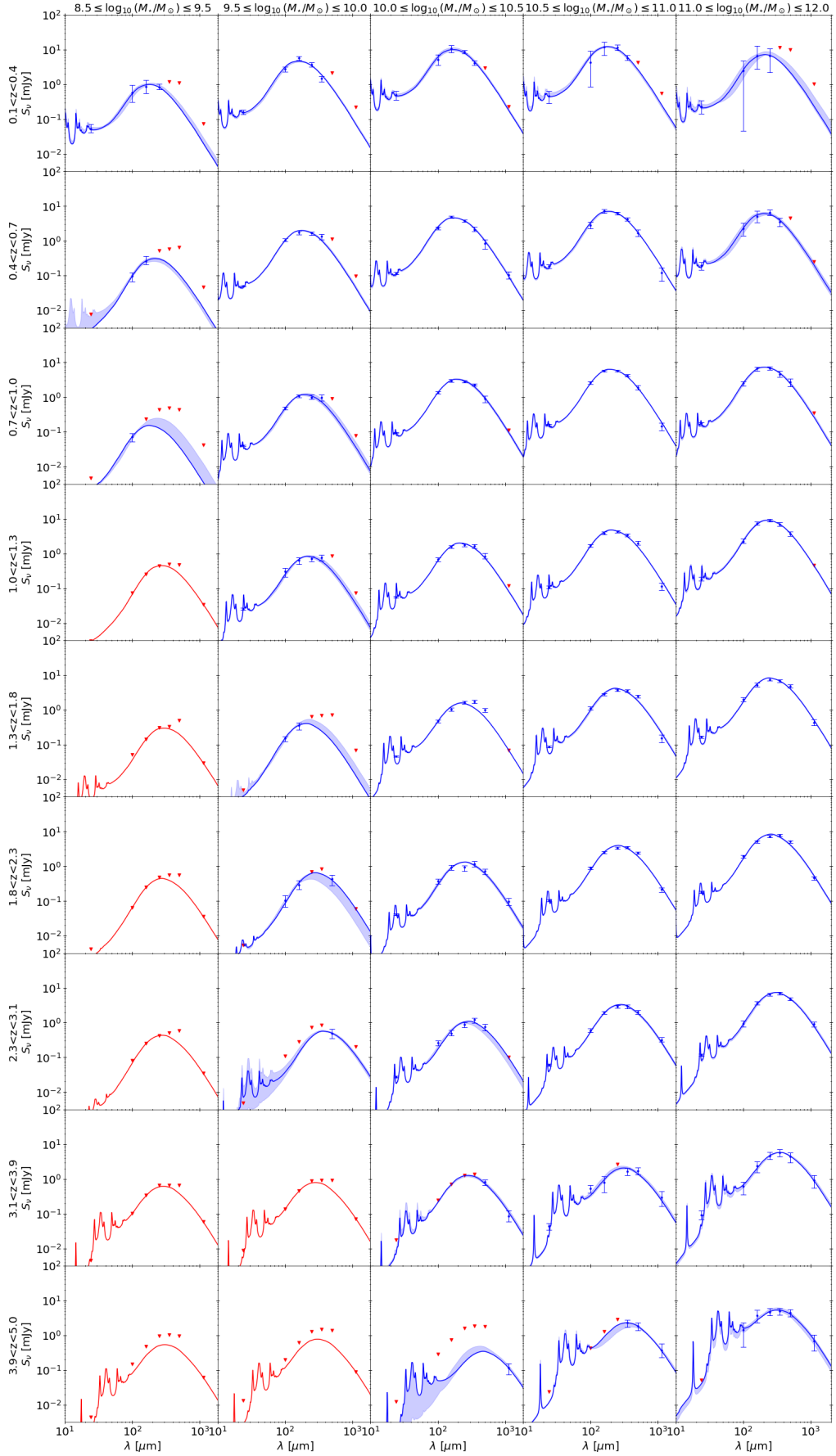


Fig. 1: best-fit SED for each bin of redshift and stellar mass. Blue dots correspond to the flux measurements, red triangles represent the 5σ upper limits. Blue line is the best-fit SED, the blue shaded area shows the 68% uncertainty of the fit. Red line is the SED maximising L_{IR} in case only upper limits are available.

453 ity density function of R_{SB} by a double log-normal distribution
 454 (see Eq. 3).

$$\Phi_{R_{\text{SB}}}(x) = \frac{1 - f_{\text{SB}} - f_{\text{miss}}}{\sqrt{2\pi}\sigma_{\text{MS}}} \exp\left(\frac{-\log_{10}(x/x_0)^2}{2\sigma_{\text{MS}}}\right) + \frac{f_{\text{SB}}}{\sqrt{2\pi}\sigma_{\text{SB}}} \exp\left(\frac{-\log_{10}(x/B_{\text{SB}})^2}{2\sigma_{\text{SB}}}\right), \quad (3)$$

where f_{SB} is the fraction of starbursts, f_{miss} is the fraction of galaxies missed by such distribution (neither starburst nor main sequence galaxies), σ_{MS} and σ_{SB} are the widths of the main sequence and starburst distributions, B_{SB} is the median multiplicative boost of star formation that can be expected for a starburst compared to a main sequence galaxy (i.e., the median of starburst galaxies), and x_0 is the median R_{SB} of main sequence galaxies. We note that with this parametrisation, we expect f_{miss} and x_0 to be close to 0 and 1 respectively, by construction. We have chosen here to use the parametrisation of S15: $\sigma_{\text{MS}} = \sigma_{\text{SB}} = 0.31 \pm 0.02$ dex, $f_{\text{SB}} = 3.3\% \pm 1.5\%$, $B_{\text{SB}} = 5.3 \pm 0.4$, $f_{\text{miss}} = 0\% \pm 2\%$, and $x_0 = 0.87 \pm 0.04$.

To each galaxy we assign L_{IR} , deduced from the SFR by subtracting the UV SFR assuming the UV dust attenuation (A_{UV}) derived from M_{\star} as in Pannella et al. (2015) (see Eq. 4 and 5) and Kennicutt (1998a) (see Eq. 6).

$$A_{\text{UV}} = 1.6 \times \log_{10}(M_\star) - 13.5, \quad (4)$$

$$SFR_{\text{IR}} = SFR - SFR_{\text{UV}} \quad (5)$$

where $SFR_{\text{UV}} = SFR \times 10^{-0.4 \times A_{\text{UV}}}$.

$$L_{\text{IR}}[L_{\odot}] = 5.8 \times 10^9 \times SFR_{\text{IR}}[M_{\odot}\text{yr}^{-1}]. \quad (6)$$

Then T_{dust} was calculated using the best-fit of our work (see Eq. 7) for the main sequence trend, and we followed Magnelli et al. (2014) (see Eq. 9) to take into account the impact on T_{dust} of the distance of the mock galaxy from the main sequence (R_{SB}). The SED, for each mock galaxy, was then calculated using T_{dust} , L_{IR} and redshift with the template library from S18 assuming a contribution of PAH molecules $f_{\text{PAH}} \equiv M_{\text{dust}}^{\text{PAH}}/M_{\text{dust}}$. The value of f_{PAH} was set to follow a Gaussian distribution with a mean of 0.039 and a scatter 2.5/100 (S18, roughly for main sequence galaxies). Next, the M_{dust} were obtained from the selected SED template and the M_{gas} were calculated according to the different methods presented in Sect. 5.3. The individual SEDs were then stacked using a mean stacking method. Fluxes at 24 μm , 100 μm , 160 μm , 250 μm , 350 μm , 500 μm and 1130 μm were deduced from the stacked SED. The fluxes were then fitted with the template library from S18. The properties of the stacked SED were deduced using the method presented in the corresponding section of this paper: see Sect. 5.1 for T_{dust} , Sect. 5.2 for L_{IR} and Sect. 5.3 for M_{gas} . Potential biases were then investigated by comparing the actual average properties with those deduced from our stacking analysis.

The relative differences between the actual average properties with those deduced from our stacking analysis are quite small: $-1\%^{+2\%}_{-4\%}$ for L_{IR} , $-6\%^{+1\%}_{-2\%}$ for T_{dust} and $7\%^{+2\%}_{-4\%}$ for M_{dust} . As a result, we find no clear evidence of significant averaging bias and thus decided not to apply any correction.

4.4. Active galactic nuclei bias

It has been reported that AGN can have a major contribution to the total outgoing light of a galaxy (e.g. Hao et al. 2005; Richards et al. 2006). However, most of this emission is radiated at wavelengths shorter than $24\mu\text{m}$ and thus will not affect our FIR measurement. Most extreme AGN may still have an impact on the mid-to-far infrared ratio (in particular $24\mu\text{m}$ in our case), but should not affect the FIR colour compared to normal star-forming galaxies (Hatziminaoglou et al. 2010). We checked for any AGN contribution by fitting our SED with a combination of Draine & Li (2007) dust model, and Fritz et al. (2006) AGN model. No conclusive evidence for a major contribution (i.e., $L_{\text{IR}}^{\text{AGN}}/L_{\text{IR}}^{\text{TOT}} \geq 10\%$) from AGNs to the rest-frame FIR was found in any of our M_{\star} and redshift bins.

5. Stacked galaxies properties

5.1. Dust temperature

In this section, we examine the evolution of T_{dust} . In Fig. 2, we display the corresponding T_{dust} for our SED as a function of redshift and M_{\star} . We do not see a significant dependence of T_{dust} on M_{\star} . It seems that, overall, the T_{dust} of a main sequence galaxy is mainly determined by its redshift, independently of its M_{\star} (see also Magdis et al. 2012; Magnelli et al. 2014).

The temperature of the cosmic microwave background (CMB) ranges from 2.73 K at $z = 0$, up to 16.4 K at $z = 5$, and, thus, it could become a significant source of heating at high redshift. We, however, verified, following da Cunha et al. (2013) that this is not the case. Indeed, the observed T_{dust} of galaxies at high redshift is significantly higher than that of the CMB.

Because our results come from H -band selected galaxies, our stacking analysis does not take into account the H -dropout galaxies (Wang et al. 2019). There are 63 H -dropout galaxies that have been detected in Wang et al. (2019) over ~ 600 arcmin 2 . In this work, we have 1464 galaxies with $M_\star \geq 10^{10} M_\odot$ and $z \geq 3$ over ~ 1077 arcmin 2 . The H -dropout would then only account for $\sim 7.2\%$ of the total sample. We re-fitted the stack of H -dropout from Wang et al. (2019) with S18 templates and deduced a $T_{\text{dust}}^{\text{H-drop}} = 37.34^{+1.2}_{-1.27}$ K. The contribution of H -dropout from Wang et al. (2019) was then added to our last bin of redshift (i.e., $3.9 \leq z \leq 5$).

In Fig. 2, our result seems to be globally consistent with the trend of S18. We see only slight evidence that the highest M_\star bin ($11 \leq \log_{10}(M_\star) \leq 12$) could be cooler than lower mass galaxies at a fixed redshift. This effect can be observed for $z \leq 2.5$. This could simply show that high-mass galaxies are actually starting to slowly reduce their SFE on their way to become quiescent. This is particularly apparent in our first redshift bin ($0.1 \leq z \leq 0.4$) in which the bending of the main sequence is also the strongest (see Sect. 5.2; S15).

In Fig. 3, we display the mean T_{dust} over each redshift bin, weighted by the number of galaxies in each bin of M_{\star} , as a function of redshift. Our analysis suggests a linear evolution of T_{dust} as a function of redshift. Our best linear fit, for $0.1 \leq z \leq 5$, follows:

$$T_{\text{dust}}[\text{K}] = 34.20_{-0.15}^{+0.14} + 5.06_{-0.03}^{+0.03}(z - 2). \quad (7)$$

We compare our results with those in the literature: S18, Magnelli et al. (2014), Bouwens et al. (2020), Magdis et al. (2012) and Béthermin et al. (2015). We also re-fitted the two stacks of Béthermin et al. (2020) using the template library from

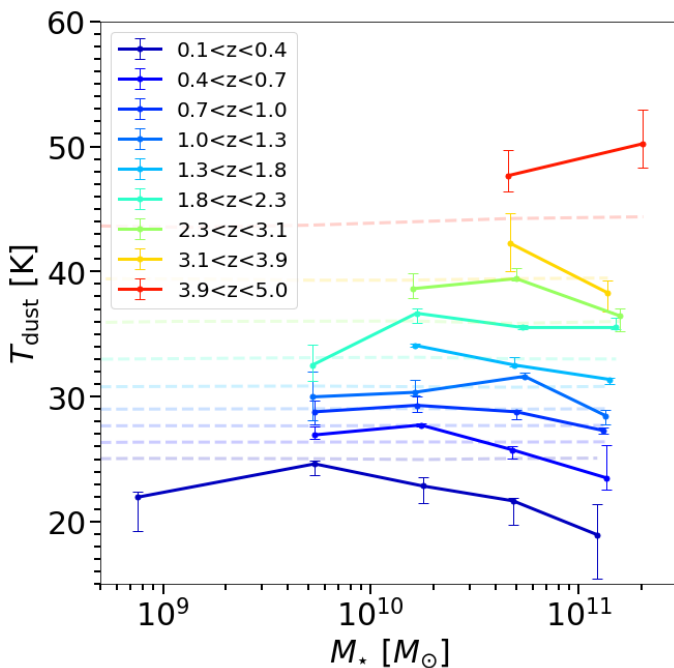


Fig. 2: T_{dust} as a function of M_{\star} , colour-coded by redshift bin. Average trend of T_{dust} as a function redshift from S18, is shown as a reference in faded coloured dashed line.

556 S18. For consistency, we converted all $T_{\text{dust}}^{\text{L}}$ to $T_{\text{dust}}^{\text{M}}$ when com-
 557 paring our results with the literature (i.e., for Magnelli et al.
 558 2014; Bouwens et al. 2020). To do this, we adopt the conver-
 559 sion factor, between mass and light weighted dust temperature,
 560 given by (S18):

$$T_{\text{dust}}^{\text{M}}[\text{K}] = 0.91 \times T_{\text{dust}}^{\text{L}}[\text{K}]. \quad (8)$$

This conversion factor represents the average conversion factor between $T_{\text{dust}}^{\text{M}}$ and $T_{\text{dust}}^{\text{L}}$ for each individual template. Some studies (i.e., Magdis et al. 2012; Béthermin et al. 2015) consider the mean starlight heating rate ($\langle U \rangle$) (Draine & Li 2007; Draine et al. 2014) instead of T_{dust} as defined here. To compare our results with those, we have chosen to use the $\langle U \rangle$ -to- T_{dust} conversion formula of S18 (see Eq.9).

$$T_{\text{dust}}[\text{K}] = \left(\frac{\langle U \rangle}{U_{\odot}} \right)^{1/5.57} \times 18.2 \text{K.} \quad (9)$$

As $\langle U \rangle$ is only a proxy of T_{dust} , any comparison between the two quantities should be essentially qualitative.

Our T_{dust} as a function of redshift is consistent within the uncertainties with S18, extended to $z = 5$. We find no clear evidence for the softening of the T_{dust} as the redshift increases reported by Magnelli et al. (2014); Magdis et al. (2012). This could stem from the lack of clustering bias correction in their study, as previously reported in S18. Clustering bias correction is a quite important step when stacking in *Herschel* passbands. Especially in the SPIRE wavelengths, as this effect can account for up to 50%, of the total signal, on average at 500 μm (e.g. S15; Béthermin et al. 2015; Delvecchio et al. 2021). Ignoring this could result in a cooler SED and a lower T_{dust} . Comparing our trend to other works by Béthermin et al. (2015, 2020); Bouwens et al. (2020), all agree on a linear trend. The differences with our trend may again stem from the way in which the correction for clustering bias is handled in the two works, as it is essential to correctly determine T_{dust} .

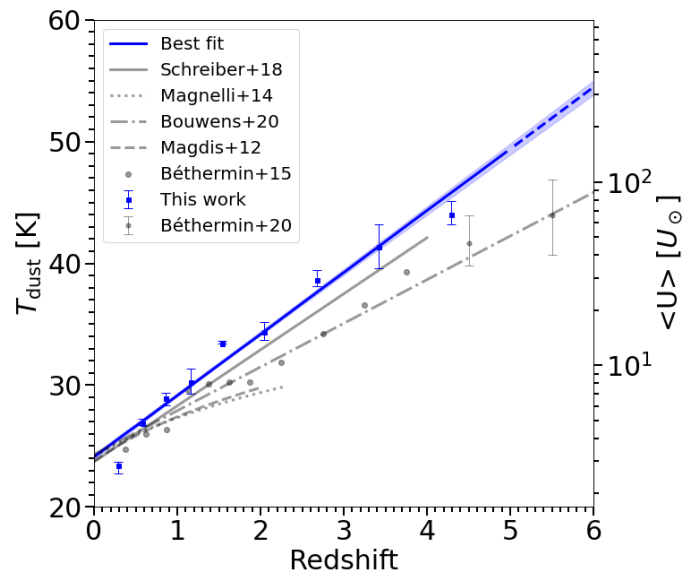


Fig. 3: T_{dust} and $\langle U \rangle$ as a function of redshift. The blue dots represent the T_{dust} of this work, the blue line is the best-fit (up to $z = 5$), the dashed blue line is the best-fit extrapolation (for $z \geq 5$), and the blue shaded area represents the 68% uncertainty of the fit. From the literature: S18 (grey solid line), Magnelli et al. (2014) (grey dotted line) and Bouwens et al. (2020) (grey dash-dotted line) converted using Eq. 8. Magdis et al. (2012) (grey, dashed line) and Béthermin et al. (2015) (grey dots) converted using Eq. 9. We also re-fitted the two stacks from Béthermin et al. (2020) (grey dotted error bars) using template library from S18.

Another way to look at the redshift evolution of the FIR SED is to consider λ_{peak} as a function of L_{IR} (see Fig. 4). We observe no dependence of λ_{peak} as a function of L_{IR} at fixed redshift, up to $z \simeq 4$. Only our last two redshift bins (i.e., $3.1 \leq z \leq 3.9$ and $3.9 \leq z \leq 5.0$) shows some evolution. However, for the same reason as above, this could result from a bias due to selection effects, as well as the fact that we only have two points in these redshift intervals. We conclude that λ_{peak} of main sequence galaxies does not depend significantly on L_{IR} at a given redshift. This property has already been observed by Magnelli et al. (2014), up to $z \simeq 2$, where no clear dependence of T_{dust} has been observed along the main sequence in the $SFR - M_{\star}$ plane. However, the normalisation seems to evolve with redshift, reflecting the smooth increase of λ_{peak} with redshift presented in Drew & Casey (2022). But our results differ from those of Drew & Casey (2022) who claimed to have found an evolution of T_{dust} , as probed by λ_{peak} , with L_{IR} . This discrepancy comes from the probable incompleteness of the sample of Drew & Casey (2022). In this paper, we stack galaxies to recover the main sequence, and we look at a mass complete sample, where non-detections are accounted for thanks to the stacking technique. On the other hand, Drew & Casey (2022) worked with individually detected galaxies, and thus might be biased toward the brightest galaxies at all redshifts (i.e., starbursts). In addition, their flux-limited sample suffer from selection effect: at low L_{IR} , their λ_{peak} comes from low redshift galaxies, while at high L_{IR} , their values are coming from distant galaxies. What Drew & Casey (2022) find is an effect of redshift not an effect of L_{IR} .

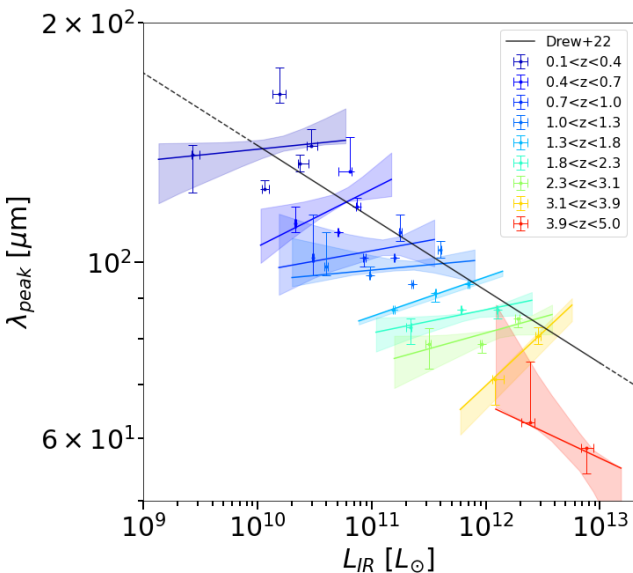


Fig. 4: λ_{peak} as a function of L_{IR} . The colour-coded error bars (per redshift bins) represent the results of this work, coloured lines represent the best-fit and shaded area the 68% uncertainty of the fit. The solid black line corresponds to the trend of Drew & Casey (2022), while the dotted black line is an extrapolation of their relation.

5.2. The main sequence of star-forming galaxies

Here we constrain the $SFR - M_{\star}$ correlation, also called the "main sequence" of star-forming galaxies (Noeske et al. 2007). The preferred method for estimating the SFR of a galaxy is to study the light from OB stars, because of the close link between their short lifetimes and the instantaneous SFR of galaxies. Although most of their light is emitted in the UV, it can be largely absorbed by dust and then re-emitted as thermal radiation in the IR. To obtain the total SFR associated with a galaxy, or in our case the stack of several galaxies, it is necessary to combine the SFRs deduced from both the UV and the IR as:

$$SFR_{\text{Tot}} = SFR_{\text{UV}} + SFR_{\text{IR}}. \quad (10)$$

The SFR_{UV} , uncorrected for dust attenuation, is computed from L_{UV} (rest-frame 1500 Å UV luminosity) following Daddi et al. (2004):

$$SFR_{\text{UV}}[M_{\odot}\text{yr}^{-1}] = 2.17 \times 10^{-10} L_{\text{UV}}[L_{\odot}]. \quad (11)$$

For our catalogues, the L_{UV} were calculated for all individual galaxies from EAZY (Pannella et al. 2015). In this study, the SFR_{UV} was derived for each redshift and M_{\star} bin by averaging the SFR_{UV} of all individual galaxies in the bin. The L_{IR} was obtained from the SED fit of our stacks, by integrating the best-fit SED in the range 8–1000 μm rest frame, we deduced the SFR_{IR} following Kennicutt (1998a) (see Eq. 6).

The left panel of Fig. 5 displays our SFR for each bin of redshift and M_{\star} . The SFR follows a monotonic dependence with increasing M_{\star} , at fixed redshift; and with increasing redshift, at fixed M_{\star} . The high mass end presents a bending of the main sequence slope, which is more prominent as the redshift decreases.

Regarding the contribution of H -dropouts to our main sequence estimate, Wang et al. (2019) reported that ALMA-detected H -dropouts mostly fall within the main sequence at $z \sim 4$ (the version from S15). Moreover, as they represent only

Table 5: best-fit parameters of the main sequence of star-forming galaxies using Eq. 12

m_0	m_1	a_0	a_1	a_2
$9.36^{+0.02}_{-0.02}$	$8.52^{+0.26}_{-0.06}$	$1.34^{+0.09}_{-0.04}$	$0.241^{+0.018}_{-0.010}$	$3.42^{+0.11}_{-0.12}$

~ 7.1% of the galaxies at equivalent M_{\star} , their omission should not alter the overall shape of the main sequence.

The $SFR - M_{\star}$ correlation was then fitted using the formula introduced in S15 as it is able to capture the bending of the main sequence at the high-mass end (see Eq. 12).

$$\log_{10}(SFR_{\text{MS}}[M_{\odot}\text{yr}^{-1}]) = m - m_0 + a_0 r - a_1 [\max(0, m - m_1 - a_2 r)]^2, \quad (12)$$

where $r \equiv \log_{10}(1+z)$ and $m \equiv \log_{10}(M_{\star}/10^9 M_{\odot})$. It was shown in S15 that the main sequence has the shape in logarithmic space of a Gaussian distribution with a homogeneous scatter of $\sigma \simeq 0.3$ dex. Because we stacked our galaxies, via mean stacking, we actually recover the $\langle L_{\text{IR}} \rangle$ of our sample which is different from the mean of a Gaussian distribution in logarithmic space with a dispersion σ_{dist} , with, $\langle 10^X \rangle = \exp((\sigma_X \times \ln(10))^2/2) \times 10^{\langle X \rangle}$, $X = \log_{10}(SFR)$ following a Gaussian distribution. To correct for this, we assume that the dispersion of this Gaussian distribution in logarithmic space is $\sigma_{\text{dist}} = 0.3$ dex (S15). Our best-fit parameters are given in Table 5, and displayed on the left panel of Figure 5 (left panel).

The shape chosen for the fit sets a slope of one, which is broadly consistent with our data points. The normalisation of the main sequence increases significantly with redshift. As we have already pointed out in the study of T_{dust} , at the highest redshift (i.e., $3.9 \leq z \leq 5.0$) and the two highest M_{\star} bins (i.e., $10.5 \leq \log_{10}(M_{\star}) \leq 11$ and $11 \leq \log_{10}(M_{\star}) \leq 12$), appear to be highly star-forming and are above our main sequence by a factor of two. This suggests that these bins include a significant fraction of galaxies with high SFR relative to the main sequence (i.e., high R_{SB}).

We compare our results with several versions of the main sequence from the literature in Figure 6. Compared to Speagle et al. (2014), who did not fit any bending, our best-fit is consistent with the general trend and evolution of the normalisation. However, our work suggests that the bending is real and becomes stronger at low redshift. Overall, our best-fit remains close to what was found by S15 at $z \geq 0.7$. As already confirmed by Delvecchio et al. (2021), the trend of S15 main sequence holds when constructed mainly from FIR data. Nevertheless, we find a stronger curvature of the main sequence at $z \leq 0.7$ compared to what we could extrapolate from S15. This is probably due in part to the fact that they did not probe the main sequence for $z \leq 0.3$. The version of the main sequence by Leslie et al. (2020) was derived from a study of the radio continuum at 3 GHz, which may explain the differences in slope, normalisation and bending. But both roughly agree on the same evolutionary trend and on a bending of the main sequence with marginal differences. The bending of the main sequence being at the high mass end, it suggests that it is triggered by some mass driven physical processes.

We have also followed the evolution of the stellar mass knee M_0 marking the bending point of the main sequence by following Daddi et al. (2022) (see Eq. 13).

$$\frac{SFR}{SFR_0} = \frac{1}{1 + (M_0/M_{\star})^{\gamma}}. \quad (13)$$

Table 6: best-fit parameters of the main sequence of star-forming galaxies using Eq. 13.

Redshift bin	$\langle z \rangle$	$\log_{10}(M_0/M_\odot)$	$\log_{10}(SFR_0/M_\odot \text{yr}^{-1})$
$0.1 \leq z \leq 0.4$	0.19	$9.36^{+0.04}_{-0.04}$	$0.49^{+0.03}_{-0.03}$
$0.4 \leq z \leq 0.7$	0.59	$10.13^{+0.02}_{-0.02}$	$1.13^{+0.01}_{-0.01}$
$0.7 \leq z \leq 1.0$	0.87	$10.36^{+0.01}_{-0.01}$	$1.49^{+0.01}_{-0.01}$
$1.0 \leq z \leq 1.3$	1.16	$10.60^{+0.03}_{-0.02}$	$1.76^{+0.02}_{-0.02}$
$1.3 \leq z \leq 1.8$	1.52	$10.86^{+0.02}_{-0.02}$	$2.12^{+0.02}_{-0.02}$
$1.8 \leq z \leq 2.3$	2.02	$11.10^{+0.02}_{-0.02}$	$2.48^{+0.02}_{-0.02}$
$2.3 \leq z \leq 3.1$	2.70	$11.03^{+0.05}_{-0.04}$	$2.63^{+0.04}_{-0.03}$
$3.1 \leq z \leq 3.9$	3.37	$11.65^{+0.35}_{-0.23}$	$3.25^{+0.08}_{-0.11}$
$3.9 \leq z \leq 5.0$	4.30	$11.92^{+0.07}_{-0.11}$	$3.84^{+0.08}_{-0.11}$

not change our conclusions because for our sample, the relative median difference in linear scale between the two estimates is $(M_{\text{gas}}^{\text{MZR-Leroy11}} - M_{\text{gas}}^{\text{MZR-Magdis12}})/M_{\text{gas}}^{\text{MZR-Magdis12}} = 0.14^{+0.05}_{-0.08}$.

Another way to calculate the metallicity is the fundamental metallicity relation (FMR; Mannucci et al. 2010, see Eq. 17). It differs from the MZR by adding some dependence on the SFR.

$$12 + \log_{10}(O/H) = 8.90 + 0.37m - 0.14s - 0.19^2 + 0.12ms - 0.054s^2, \quad (17)$$

where $m = \log_{10}(M_\star/1.7) - 10$ and $s = \log_{10}(SFR/1.7)$. These metallicities are calibrated for the KD02 photoionization models (Kewley & Dopita 2002). We used the recipe from Kewley & Ellison (2008) to convert it into a PP04 N2 scale. But once again the differences in metallicities between the MZR and FMR method does not impact our conclusions, as for our sample, the relative median is $(M_{\text{gas}}^{\text{FMR-Magdis12}} - M_{\text{gas}}^{\text{MZR-Magdis12}})/M_{\text{gas}}^{\text{MZR-Magdis12}} = -0.16^{+0.16}_{-0.06}$.

The previous methods are only reliable when the SED peak is well defined (i.e., T_{dust} and M_{dust}), which is not the case in our bins. The only two bins concerned are $10.0 \leq \log_{10}(M_\star) \leq 10.5$ for $3.1 \leq z \leq 3.9$ and $3.9 \leq z \leq 5.0$. In this situation, we can also estimate M_{gas} from a single band measurement located in the Rayleigh-Jeans part of the SED (e.g. Scoville et al. 2014; Groves et al. 2015; Schinnerer et al. 2016). The main limitation is that it does not take into account the evolution with redshift of the M_{gas} metallicity and T_{dust} (e.g. Genzel et al. 2015; Berta et al. 2016; Schinnerer et al. 2016; Magdis et al. 2017; Harrington et al. 2021). However, this is a reliable way of estimating M_{gas} at low cost (25% uncertainties; Scoville et al. 2016) and especially when there is only one band measured in the Rayleigh-Jeans tail. For these reasons, while we favoured $\delta_{\text{GDR}} - \text{MRZ}$ methods to deduce M_{gas} as long as the T_{dust} was well defined. In the opposite case, and when an ALMA measurement is available, we calculated M_{gas} by the method described in Scoville et al. (2016), i.e.,

$$M_{\text{gas}} = 1.78S_{v_{\text{obs}}} [\text{mJy}] (1+z)^{-4.8} \left(\frac{\nu_{850\mu\text{m}}}{\nu_{\text{obs}}} \right)^{3.8} (d_L[\text{Gpc}])^2 \times \frac{6.7 \times 10^{19}}{\alpha_{850}} \frac{\Gamma_0}{\Gamma_{\text{RJ}}} 10^{10} M_\odot \quad \text{for } \lambda_{\text{rest}} > 250\mu\text{m}, \quad (18)$$

$$\Gamma(z) = \frac{h\nu_{\text{obs}}(1+z)}{k_B T_d} \frac{1}{\left(\exp\left(\frac{h\nu_{\text{obs}}(1+z)}{k_B T_d}\right) - 1 \right)}, \quad (19)$$

where d_L is the luminosity distance, $\alpha_{850} = 6.2 \times 10^{19} \text{erg sec}^{-1} \text{Hz}^{-1} M_\odot^{-1}$, $\Gamma_0 = \Gamma(z=0)$ and $\Gamma_{\text{RJ}} = \Gamma(z)$, h is Planck's constant, k_B is Boltzmann's constant, $T_d = 25\text{K}$ and $\nu_\lambda = \frac{c}{\lambda}$. We note that this technique provides, for our sample, consistent results with those of the MZR method, with a relative median $(M_{\text{gas}}^{\text{Scoville16}} - M_{\text{gas}}^{\text{MZR-Magdis12}})/M_{\text{gas}}^{\text{MZR-Magdis12}} = 0.19 - 0.32^{+0.35}$ when both $\delta_{\text{GDR}} - \text{MRZ}$ and Scoville et al. (2016) could be performed.

In summary, we chose to calculate our M_{gas} using Magdis et al. (2012) for $\delta_{\text{GDR}}(Z)$ (Eq. 15) and Genzel et al. (2015) MZR for the metallicities (Eq. 16). When the peak of the SED is poorly constrained and an ALMA flux is available, we chose to calculate M_{gas} from Scoville et al. (2016) method. For the rest of the paper, we will refer to $M_{\text{gas}}^{\text{MZR-Magdis12}}$, or $M_{\text{gas}}^{\text{Scoville16}}$ simply as M_{gas} .

Here M_{gas} represents the total gas budget of a galaxy including both molecular gas (M_{H_2}) and atomic gas (M_{HI}), i.e.,

Following recommendations from Daddi et al. (2022), we set $\gamma = 1.1$, which should help to reduce the errors and should not affect the result much. If γ was defined as a free parameter in the fit, the $\langle \gamma \rangle$ would be close to 1.1 anyway. Our best-fit parameters are given in Table 6, and displayed on the right panel of Figure 5. Overall, our results are quite comparable to the evolution of the bending found by Lee et al. (2015) and Daddi et al. (2022) (i.e., a decrease in M_0 as we move to a lower redshift). However, we see little or no evidence of a bending for $z > 3$. We suggest that this may be because the physical processes that trigger the main sequence bending have not had enough time to impact the main sequence trend at the high mass end at $z > 3$. Another possibility is that the bending still occurs at high redshifts, but only for very high mass galaxies ($M_\star > 2 - 3 \times 10^{11} M_\odot$), which we could not probe with this study because they are extremely rare.

5.3. Gas mass

We chose to calculate M_{gas} from M_{dust} deduced from our stacked SEDs. We can link M_{gas} to M_{dust} by a gas-to-dust mass ratio (δ_{GDR}) that depends only on the metallicity Z ($\log Z = 12 + \log_{10}(O/H)$) of the galaxy,

$$M_{\text{gas}} = \delta_{\text{GDR}}(Z) M_{\text{dust}}. \quad (14)$$

Multiples studies (e.g. Leroy et al. 2011; Magdis et al. 2012; Rémy-Ruyer et al. 2014; Genzel et al. 2015) show consistent $\delta_{\text{GDR}} - Z$ relations that hold at both low and high redshift. We chose here to use the relation from Magdis et al. (2012):

$$\log \delta_{\text{GDR}} = 10.54 - 0.99 \times (12 + \log_{10}(O/H)). \quad (15)$$

As for most galaxies we do not have UV or optical spectra, we do not have a direct measurement of their metallicity. To go around this problem, we use the mass-metallicity relation (MZR; Erb et al. 2006) and follow its redshift dependent version from Genzel et al. (2015),

$$12 + \log_{10}(O/H) = a - 0.087 \times (\log_{10}(M_\star/1.7) - b)^2, \quad (16)$$

where $a = 8.74$ and $b = 10.4 + 4.46 \log_{10}(1+z) - 1.78(\log_{10}(1+z))^2$. We note that Genzel et al. (2015) use a Chabrier (2003) IMF to define the MZR. In order to use it correctly, our M_\star must first be divided by a factor of 1.7. We chose to adopt an uncertainty of 0.2 dex for our metallicity following the recommendation from Magdis et al. (2012). These latter metallicities are calibrated in the PP04 N2 scale ($N_2 = [N_{\text{H}}] \lambda 6583/\text{H}_\alpha$; Pettini & Pagel 2004). We note that by using the δ_{GDR} relation of Leroy et al. (2011), instead of Magdis et al. (2012), would

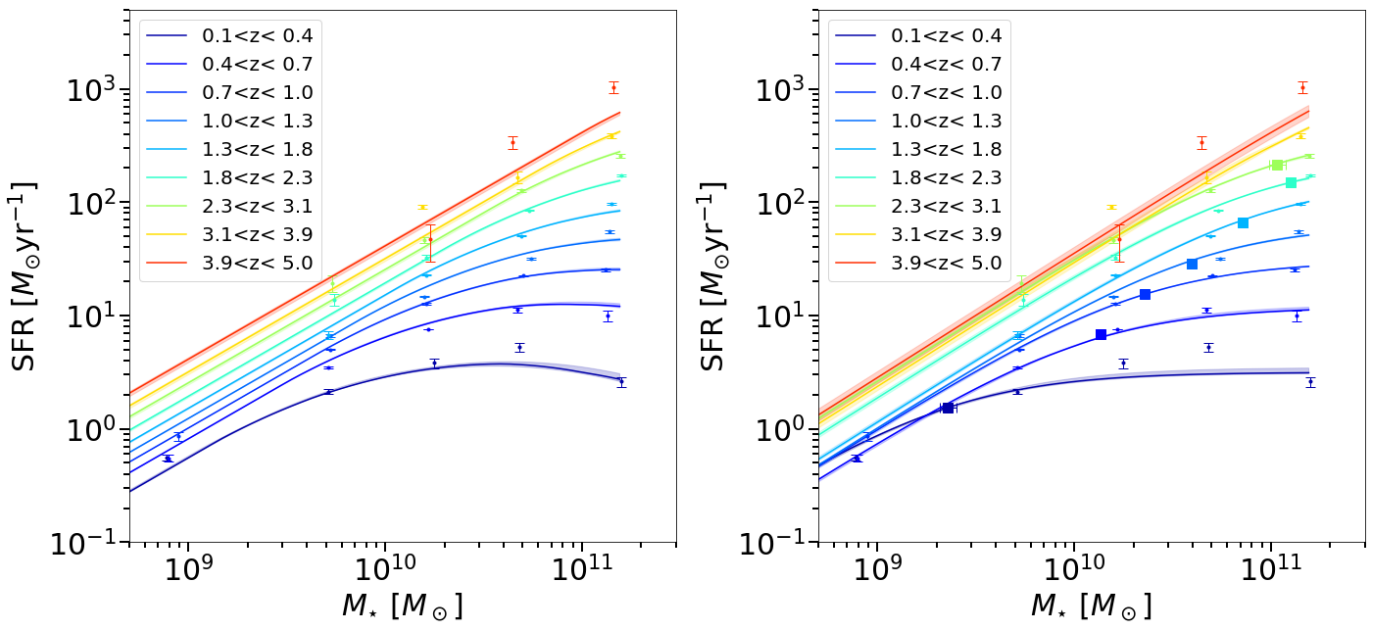


Fig. 5: SFR_{MS} as a function of M_* over different redshift bins. The dots represent data from this work. The upper limits were used to perform the fit but are not shown here to avoid overloading the figure. Left panel: fitted by the Eq. 12, the shaded area the 68% uncertainty of the fit. Right panel: fitted by the Eq. 13, the shaded area the 68% uncertainty of the fit. The squares represent the best-fit parameter M_0 . No bending was detected for $z > 3.1$ and therefore no square error bars are displayed.

$M_{\text{gas}} = M_{\text{H}_2} + M_{\text{HI}}$. The HI content of galaxies is still poorly known outside the local universe because the 21cm emission line is difficult to detect with current facilities. However, Bauermeister et al. (2010) showed that it is unlikely that the HI content of galaxies varies strongly with redshift. In contrast, the H₂ content evolves strongly with redshift (e.g. Daddi et al. 2010; Tacconi et al. 2010, 2013; Lagos et al. 2015; Genzel et al. 2015; Tacconi et al. 2018). In Tacconi et al. (2018), it was concluded that the assumption $M_{\text{gas}} \sim M_{\text{H}_2}$ should hold for $z > 0.4$. Therefore, we decided not to consider our M_{gas} for $z < 0.4$ (i.e., our first redshift bin), as we could not probe the HI content of the galaxy at these redshifts. In order to add some reliable measurements of M_{H_2} to our study at $z < 0.4$, we used data points from Saintonge et al. (2017) that come from very local measurements ($0.01 \leq z \leq 0.05$).

Our M_{gas} measurements are displayed in Fig. 7. We observe a rapid rise with redshift from Saintonge et al. (2017) data at low redshift, to our first data points at $z \geq 0.4$. Then, at fixed M_* , M_{gas} reach a maximum at $z \sim 1 - 2$ and remains relatively constant as the redshift increases. At fixed redshift, M_{gas} gradually increase with M_* .

We examined the contribution of the H -dropouts to M_{gas} in order to have the most unbiased view possible. Here, we have simply calculated the M_{gas} , associated with each H -dropout in the sample of Wang et al. (2019), using their ALMA measurement at 870 μm and following Scoville et al. (2016) method. The final contribution of the H -dropout to the total M_{gas} within each bin is $M_{\text{gas}}^{H\text{-dropout}} \times N_{\text{gal}}^{H\text{-dropout}} \times \epsilon / (M_{\text{gas}}^{H\text{-dropout}} \times N_{\text{gal}}^{H\text{-dropout}} \times \epsilon + M_{\text{gas}} \times N_{\text{gal}})$ = 19%^{+7%}_{-17%} on average (only the bins with at least one H -dropout are taken into account), where $\epsilon = \text{Area}_{\text{Leroy+23}} / \text{Area}_{\text{Wang+19}} \sim 1.8$. The contribution of H -dropouts can represent up to ∼32% for some bins, hence we chose to add it to our data. The seven bins that have been corrected for the H -dropout contribution are circled Fig. 7.

Table 7: best-fit parameters of M_{gas} evolution of the main sequence using Eq. 20. * indicates that this parameter was fixed during the fit.

A	B	F	D	β^*
$0.0453^{+0.146}_{-0.036}$	$-1.61^{+0.73}_{-2.87}$	$0.901^{+0.362}_{-0.373}$	$-0.306^{+0.929}_{-0.718}$	2

Tacconi et al. (2018) combined M_{gas} from stacks in the IR and M_{gas} from CO emission. We try to fit our data using the formula of Tacconi et al. (2018):

$$\log_{10}(M_{\text{gas}}) = A + B(\log_{10}(1+z) - F)^{\beta} + D(\log_{10}(M_*/1.7) - 10.7) + \log_{10}(M_*/1.7), \quad (20)$$

where the factor 1.7 represents the conversion of M_* from a Salpeter (1955) to Chabrier (2003) IMF. As our data points represent main sequence galaxies, we cannot probe the C_{μ} term in Tacconi et al. (2018), that represents the evolution with respect to the distance to the main sequence $sSFR/sSFR_{MS}$. And we do not explore the morphology of galaxies in this study, which makes it impossible to probe the term E_{μ} , which compares the effective radius of galaxies (R_e) to the mean effective radius of the star forming population R_{e_0} . The results are displayed in Fig. 7, and our best-fit parameters are given in Table 7.

Looking at Fig. 7, we notice that M_{gas} observed at low redshift ($0.4 \leq z \leq 1$) tends to be higher than the best-fit trend (even though it is in most cases within the error bars), and the trends from literature such as Tacconi et al. (2018). A similar effect has been observed by Tacconi et al. (2018) who measured higher depletion times (τ_{dep}) deduced from dust observations compared to the ones deduced from CO line fluxes. The effect observed in Tacconi et al. (2018) decreases slowly with redshift (about 0.3 dex at $z \sim 0.4$ to 0 at $z \sim 1.5$) and roughly matches the effect observed here. We conclude that this effect, which was solved

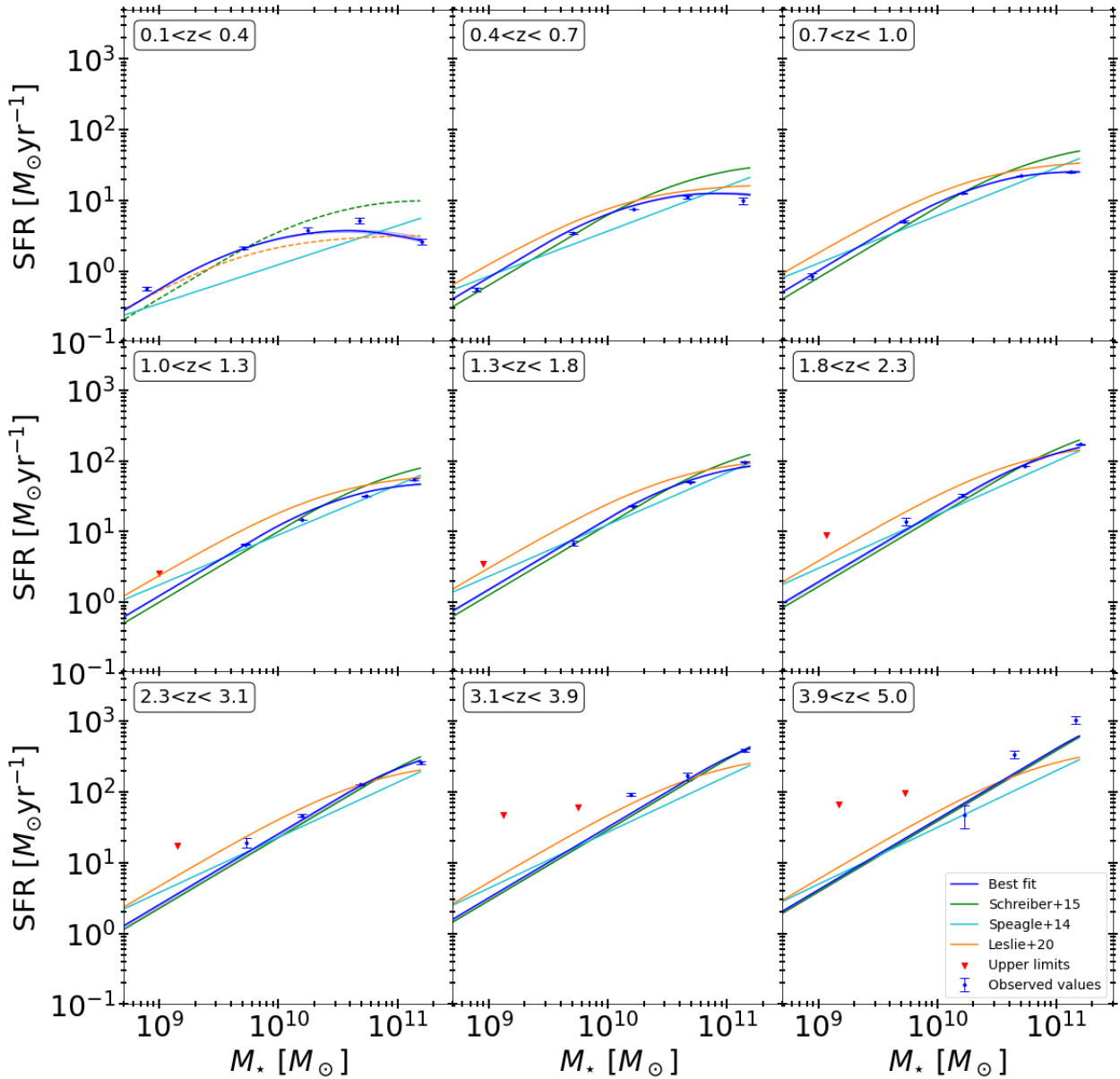


Fig. 6: SFR_{MS} as a function of M_* . The red triangles represent upper limits, the blue dots are the observed values from this work and shaded area the 68% uncertainty of the fit. The blue lines represent the best-fit from this work. The green, cyan and orange lines represents the main sequence from S15, Speagle et al. (2014) and Leslie et al. (2020), respectively. The dashed lines represent extrapolated main sequences to redshifts that were not investigated in their respective studies.

in Tacconi et al. (2018) by matching the zero-point for each method, arises when deducing M_{gas} from dust observations. It feels that the form use in Tacconi et al. (2018) to fit M_{gas} fails to properly recover the form of our measurements. In a way to provide for a better fit, we chose to also fit our data using a formula of the form:

$$\log_{10}(M_{\text{gas}}) = \begin{cases} m_0 + m_1 m + a_1 r + a_2 r^2 & \text{for } z < z_0 \\ m_0 + m_1 m + a_1 r_0 + a_2 r_0^2 & \text{for } z \geq z_0, \end{cases} \quad (21)$$

where $m = \log_{10}(M_*)$, $r = \log_{10}(1+z)$, $r_0 = \log_{10}(1+z_0)$ and $z_0 = -a_1/2a_2$. The best-fit parameters, using Eq. 21 are given in Table 8.

We compare our results to the trends observed by Tacconi et al. (2018) and Wang et al. (2022) in Fig. 8. The trend observed by Wang et al. (2022) M_{gas} comes from millimetre fluxes used to deduce M_{gas} using the method from Scoville et al. (2016).

Table 8: best-fit parameters of M_{gas} evolution of the main sequence using Eq. 21.

m_0	m_1	a_1	a_2
$1.93^{+0.18}_{-0.23}$	$0.69^{+0.02}_{-0.01}$	$3.53^{+0.33}_{-0.56}$	$-2.96^{+0.92}_{-0.71}$

Overall, our trend is much more similar to that found in Wang et al. (2022) than Tacconi et al. (2018), but tends to yield slightly lower M_{gas} at high redshift compared to what is reported by Wang et al. (2022). Differences between trends might just ensue from the variation in the methods and data sets used to deduce M_{gas} .

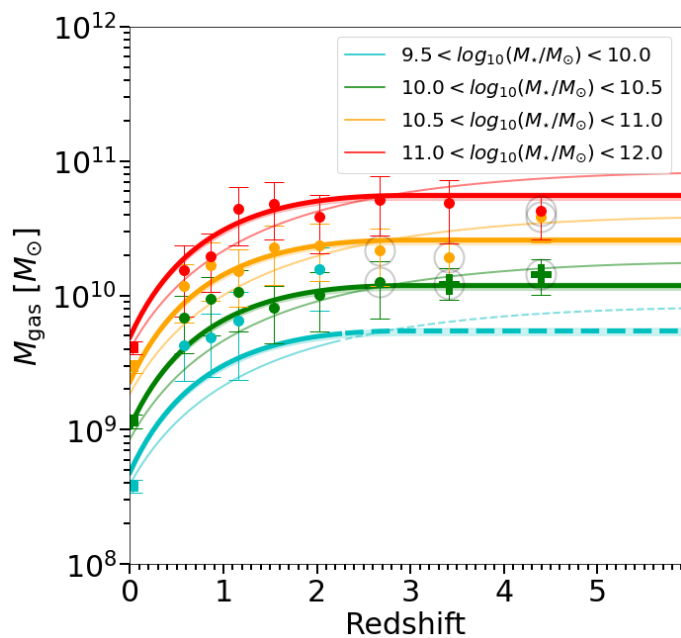


Fig. 7: M_{gas} as a function of redshift for different M_{\star} . The dots represent M_{gas} estimates from this work using the $\delta_{\text{GDR}} - \text{MRZ}$ method, the crosses represent M_{gas} estimates from this work following the method from Scoville et al. (2016). The squares are measurements from Saintonge et al. (2017). The bins that have been corrected for the H -dropout contribution are circled. The thick and thin solid colour lines represent the best-fit from this work, using Eq. 21 and Eq. 20, respectively. The dashed lines are the fits extrapolation. The shaded area the 68% uncertainty of the fit.

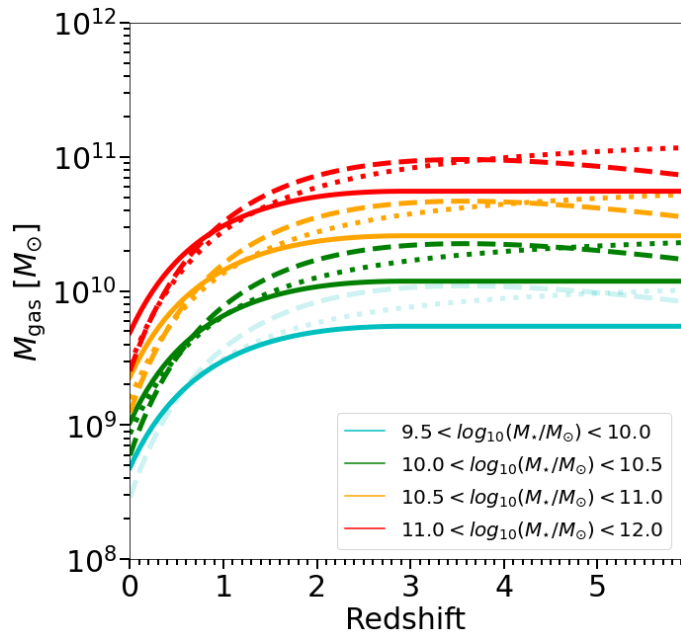


Fig. 8: M_{gas} as a function of redshift and M_{\star} . The solid lines represent the best-fit from this work colour-coded by M_{\star} (using Eq. 21), the dashed lines represent the trend from Tacconi et al. (2018), the dotted lines are from Wang et al. (2022). The faded lines represent an extrapolation from their respective laws.

As mentioned in Sect. 4, we chose to work with M_{dust} from amorphous silicate and graphitic grains (Draine & Li 2007) instead of amorphous carbon (Galliano et al. 2011; S18). We investigated what the impact would have been on M_{gas} if we had chosen a model based on amorphous carbon such as Galliano et al. (2021). Although the results are quite comparable, using the model from Galliano et al. (2021), would translate into slightly lower M_{gas} ($\sim -10\%$ at $z = 4$). These differences would not have changed the conclusions drawn in this paper.

6. Cosmic star formation history

In this section, we present the redshift evolution of ρ_{SFR} , i.e., the cosmic star formation history. To calculate the ρ_{SFR} , we start from the stellar mass function of SFGs of Davidzon et al. (2017), that is given for different redshift bins. For each redshift bin, we generated galaxies with uniform redshift distribution within the bin, and a M_{\star} distribution following these stellar mass functions. From the redshift and M_{\star} , we then assigned a SFR using the same method as in Sect. 4.3. In summary, $S\text{F}\text{R} = R_{\text{SB}} \times S\text{F}\text{R}_{\text{MS}}$, where $S\text{F}\text{R}_{\text{MS}}$ is calculated from the main sequence evolution found in this work (See Eq. 12 and parameters Table 5). And a R_{SB} is randomly drawn from a double Gaussian distribution representing the position of normal and starbursting galaxies relative to the main sequence (Eq. 3). Then ρ_{SFR} is calculated by summing the SFR of galaxies down to $M_{\star}^{\text{lim}} = 3 \times 10^9 M_{\odot}$. Errors were generated by varying the $S\text{F}\text{R}_{\text{MS}}$ trend of Eq. 12 within the errors of the fit, a 100 times.

The study of Wang et al. (2019) presents the contribution to ρ_{SFR} of H -dropout galaxies, which can reach up to 10% at $z \sim 4 - 5$. We have therefore added the contribution of H -dropout galaxies of Wang et al. (2019) to our ρ_{SFR} considering the sample of H -dropout galaxies have a median stellar mass of $M_{\star} \sim 10^{10.6} M_{\odot}$ (Wang et al. 2019).

We compare the ρ_{SFR} evolution with that of Madau & Dickinson (2014) who integrate UV and IR luminosity functions down to $L_{\min} = 0.03 L_{\star}$. Deducing ρ_{SFR} by integrating luminosity functions down to $0.03 L_{\star}$, or the mass function down to $3 \times 10^9 M_{\odot}$ should yield, to the first order, similar results (Schreiber et al. 2015). We chose for the rest of the paper to derive our ρ_{SFR} by integrating the mass function down to $3 \times 10^9 M_{\odot}$. Thus, all conclusions on the evolution of the ρ_{SFR} in this paper should be understood in this framework, as integrating the luminosity function down to lower luminosities, or the mass function down to lower masses, must yield a higher total ρ_{SFR} .

The total ρ_{SFR} is displayed in Fig. 9 along with some examples from the literature, and the data points from this work are summarised in Table 9. We observe a rise of ρ_{SFR} from $z \sim 5$ to $z \sim 2$, and then it gradually decreases down to $z \sim 0.35$. The high masses (i.e., $\log_{10}(M_{\star}/M_{\odot}) > 10$) account for most of the ρ_{SFR} until $z \sim 4$. On the other hand the ρ_{SFR} associated to low mass galaxies (i.e., $\log_{10}(M_{\star}/M_{\odot}) < 10$) is roughly constant over $0 \leq z \leq 5$.

We can see that our estimate of the total ρ_{SFR} is close to what has been observed by Leslie et al. (2020) and to the evolution of Madau & Dickinson (2014). On the other hand, the measurements from Gruppioni et al. (2020) are mostly in disagreement with our results at high redshift (i.e., $z \geq 2$). The ρ_{SFR} from Gruppioni et al. (2020) is deduced from the integration of the IR-luminosity function (which make it $\rho_{\text{SFR}}^{\text{IR}}$) down to $10^8 L_{\odot}$.

In Fig. 10, we show the contribution to the total ρ_{SFR} of the full range of stellar masses. We observe that the increase in the total ρ_{SFR} , from $z \sim 5$ to $z \sim 2$, comes from the growing number of massive galaxies (i.e., $\log_{10}(M_{\star}/M_{\odot}) > 10$), which can

Table 9: ρ_{SFR} as a function of redshift from this work. Here, ρ_{SFR} values include the H -dropout contribution from Wang et al. (2019).

Redshift	0.35	0.65	0.95	1.3	1.75	2.25	2.75	3.25	3.75	5.00
$\log_{10} \left(\frac{\rho_{\text{SFR}}}{M_{\odot} \text{yr}^{-1} \text{Mpc}^{-3}} \right)$	$-1.41^{+0.01}_{-0.01}$	$-1.22^{+0.01}_{-0.01}$	$-1.01^{+0.01}_{-0.01}$	$-0.90^{+0.01}_{-0.01}$	$-0.84^{+0.01}_{-0.01}$	$-0.92^{+0.01}_{-0.01}$	$-0.97^{+0.01}_{-0.01}$	$-1.11^{+0.01}_{-0.02}$	$-1.26^{+0.01}_{-0.02}$	$-1.39^{+0.02}_{-0.03}$
$\log_{10} \left(\frac{\rho_{\text{SFR}}^{M_{\star} > 10^{10} M_{\odot}}}{M_{\odot} \text{yr}^{-1} \text{Mpc}^{-3}} \right)$	$-1.60^{+0.01}_{-0.01}$	$-1.37^{+0.01}_{-0.01}$	$-1.13^{+0.01}_{-0.01}$	$-1.00^{+0.01}_{-0.01}$	$-0.92^{+0.01}_{-0.01}$	$-1.00^{+0.01}_{-0.01}$	$-1.08^{+0.01}_{-0.01}$	$-1.25^{+0.01}_{-0.02}$	$-1.41^{+0.02}_{-0.02}$	$-1.55^{+0.02}_{-0.02}$
$\log_{10} \left(\frac{\rho_{\text{SFR}}^{M_{\star} < 10^{10} M_{\odot}}}{M_{\odot} \text{yr}^{-1} \text{Mpc}^{-3}} \right)$	$-1.88^{+0.03}_{-0.03}$	$-1.74^{+0.02}_{-0.03}$	$-1.62^{+0.02}_{-0.02}$	$-1.60^{+0.02}_{-0.02}$	$-1.60^{+0.03}_{-0.04}$	$-1.67^{+0.04}_{-0.05}$	$-1.61^{+0.04}_{-0.05}$	$-1.65^{+0.03}_{-0.07}$	$-1.77^{+0.05}_{-0.07}$	$-1.91^{+0.05}_{-0.09}$

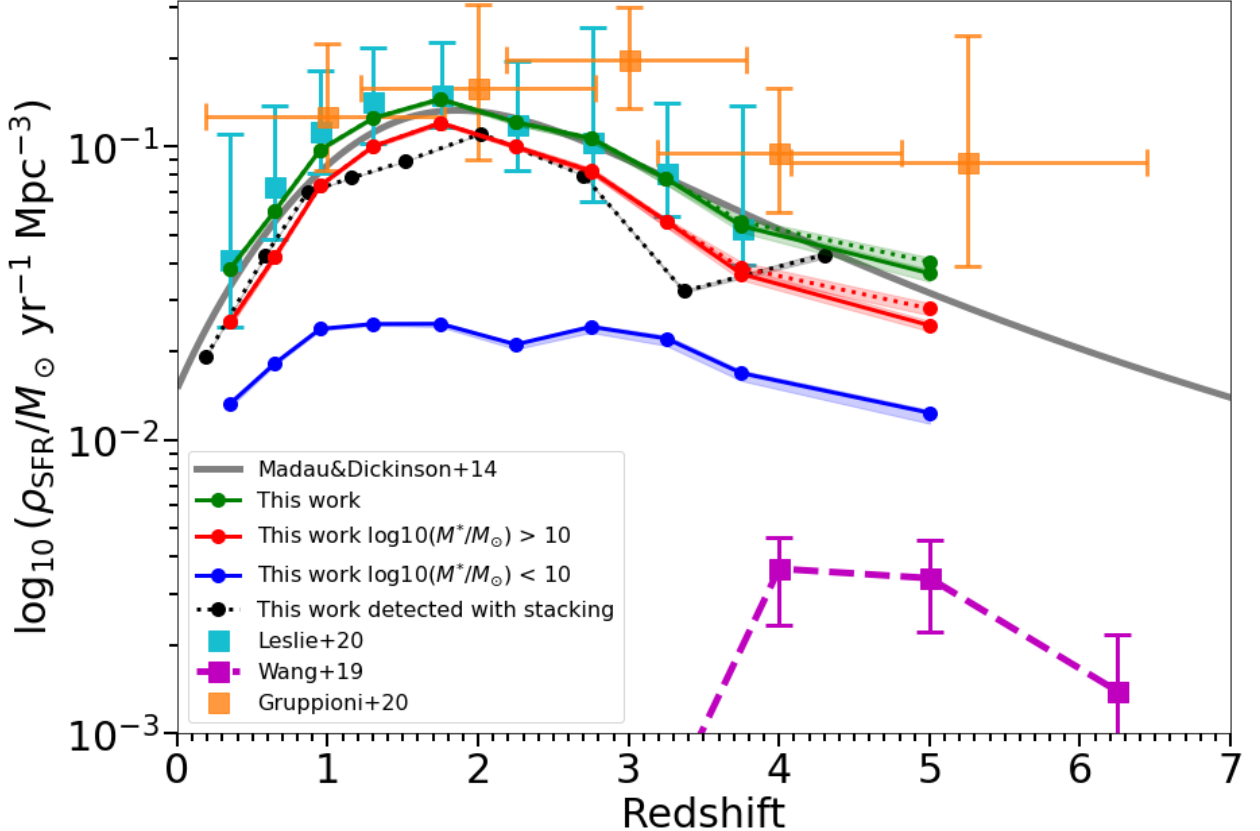


Fig. 9: Cosmic star formation rate density (ρ_{SFR}) as a function of redshift. The green line represents the total ρ_{SFR} trend from this work (i.e., integrating the stellar mass function down to $3 \times 10^9 M_{\odot}$). The red and blue lines represent the contribution of galaxies with $\log_{10}(M_{\star}/M_{\odot}) > 10$ and $\log_{10}(M_{\star}/M_{\odot}) < 10$, respectively. The black dotted line represents the ρ_{SFR} detected with stacking. The purple squares show the contribution of H -dropout from Wang et al. (2019). The dotted green and red lines show the trend once H -dropout contribution from Wang et al. (2019) has been added to the respective coloured solid lines. The grey line represents the trend from Madau & Dickinson (2014). The cyan and orange squares represent ρ_{SFR} estimate from Leslie et al. (2020) and Gruppioni et al. (2020), respectively.

be seen in the evolution of the stellar mass function at these redshifts (Davidzon et al. 2017). Downsizing and the bending of the main sequence explain the fall of the contribution of massive galaxies from $z \sim 2$ to $z \sim 0$. We again observe that massive galaxies (i.e., $\log_{10}(M_{\star}/M_{\odot}) > 10$) dominate the total ρ_{SFR} at all redshifts (i.e., they account for more than 70%). In particular, it appears that galaxies with $11.25 > \log_{10}(M_{\star}/M_{\odot}) > 10.5$ account for more than $\sim 55\%$ of the total ρ_{SFR} at $z = 2$, making them the main driver of the peak in the observed cosmic star formation history at this redshift.

7. Cosmic evolution of the gas mass density

In Sect. 6, we have simulated a catalogue of galaxies where for each of them, we calculated M_{\star} and R_{SB} . From these properties, we now infer M_{gas} by expanding Eq. 21 as:

$$\log_{10}(M_{\text{gas}}) = \begin{cases} m_0 + m_1 m + a_1 r + a_2 r^2 \\ + C \times \log_{10}(R_{\text{SB}}(z, M_{\star})) & \text{for } z < z_0 \\ m_0 + m_1 m + a_1 r_0 + a_2 r_0^2 \\ + C \times \log_{10}(R_{\text{SB}}(z, M_{\star})) & \text{for } z \geq z_0, \end{cases} \quad (22)$$

where $m = \log_{10}(M_{\star})$, $r = \log_{10}(1+z)$, $r_0 = \log_{10}(1+z_0)$ and $z_0 = -a_1/2a_2$. Here, m_0 , m_1 , a_1 and a_2 are taken from Table 8,

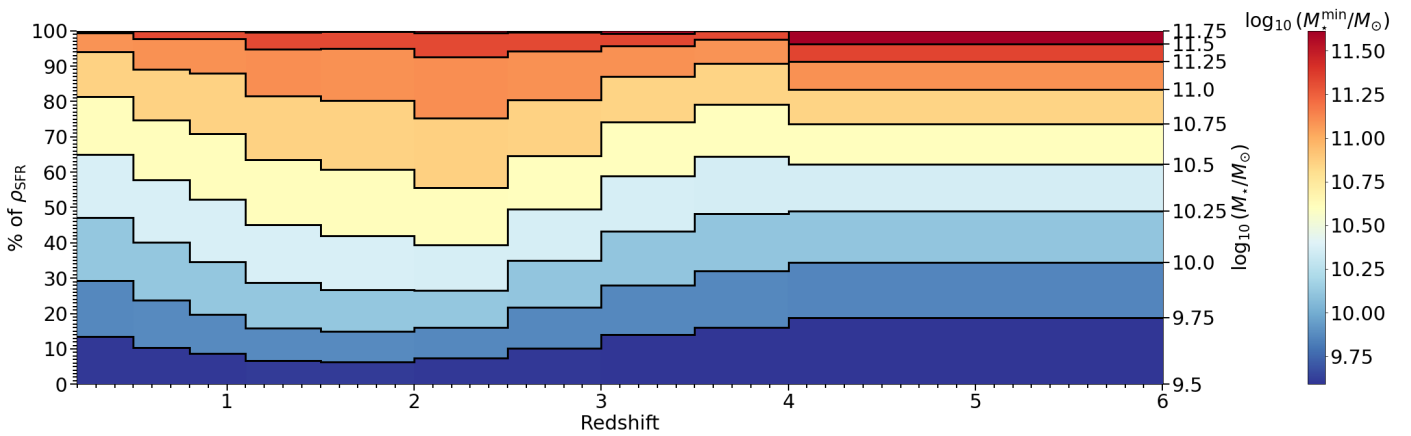
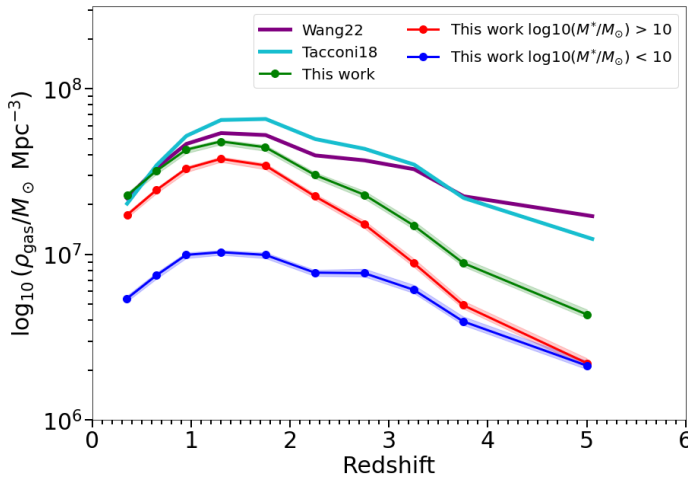
Fig. 10: Contributions over the whole range of stellar masses to the total ρ_{SFR} as a function of redshift for SFGs.

Fig. 11: ρ_{gas} as a function of redshift. The green line represents the total ρ_{gas} inferred from this work (i.e., integrating the stellar mass function down to $3 \times 10^9 M_{\odot}$). The red and blue lines represent the contribution to the total ρ_{gas} of galaxies with $\log_{10}(M_{\star}) > 10$ and $\log_{10}(M_{\star}) < 10$, respectively. The purple, orange and cyan lines represent ρ_{gas} deduced from the M_{gas} definition of Wang et al. (2022), Liu et al. (2019a,b) and Tacconi et al. (2018), respectively

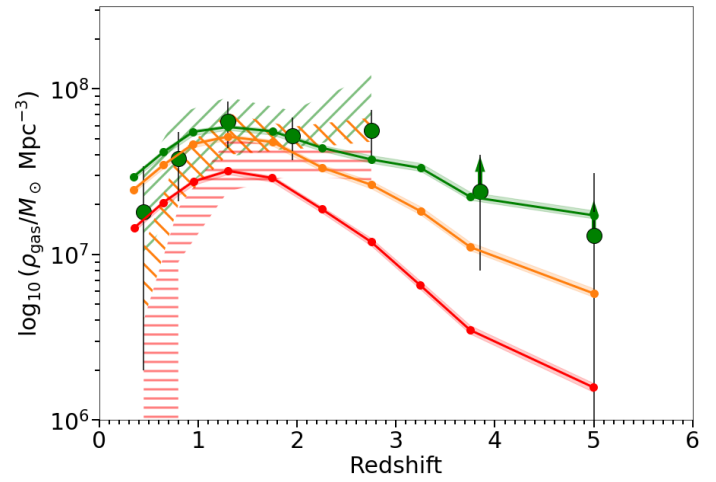


Fig. 12: ρ_{gas} as a function of redshift. The green, orange and red lines represent ρ_{gas} derived from this work with M_{\star}^{lim} of 1.7×10^8 , 1.7×10^9 and $1.7 \times 10^{10} M_{\odot}$, respectively. The green, orange and red hatches represent estimates of ρ_{gas} from Magnelli et al. (2020) with M_{\star}^{lim} of 1.7×10^8 , 1.7×10^9 and $1.7 \times 10^{10} M_{\odot}$, respectively. The green dots with black circles depict the estimate of ρ_{gas} from Magnelli et al. (2020) for $M_{\star} > M_{\text{limit}}$, M_{limit} being the stellar mass completeness limit from Magnelli et al. (2020).

and $C = 0.53$ is taken from Tacconi et al. (2018). Next, the cosmic evolution of gas density (ρ_{gas}) is calculated by summing the M_{gas} of galaxies down to $M_{\star}^{\text{lim}} = 3 \times 10^9 M_{\odot}$. Errors were generated by varying our best-fit of $M_{\text{gas}}^{\text{MS}}$ within its errors, one hundred times. Defined this way, ρ_{gas} directly represents the gas content of galaxies contributing to the ρ_{SFR} presented in Fig. 9. We display the evolution of ρ_{gas} as a function of redshift in Fig. 11. We can see the same kind of features as for the evolution of ρ_{SFR} : a rise and fall with redshift with a maximum around $z \sim 2$; a dominance across all redshifts of the high mass galaxies (i.e., $\log_{10}(M_{\star}/M_{\odot}) > 10$) contribution; and a relatively flat evolution of the low mass galaxies (i.e., $\log_{10}(M_{\star}/M_{\odot}) < 10$). This shows that the SFE of both high and low mass galaxies are not drastically changing with time, and thus that the gas content of galaxies (i.e., the accretion) is the primary driver of their SFRs: high mass galaxies have higher SFR at fixed redshift because they have more gas. However, comparing the relative evolution of ρ_{gas} (see Fig. 11) and ρ_{SFR} (see Fig. 9) shows that $\rho_{\text{gas}}^{z=5}/\rho_{\text{gas}}^{z=0}$

(and in particular the high mass contribution) is lower by a factor $\sim 3 - 4$ compared to $\rho_{\text{SFR}}^{z=5}/\rho_{\text{SFR}}^{z=0}$. This hints that one unit of gas leads to more stars being formed at $z \sim 5$ compared to $z \sim 0$ (i.e., a higher SFE at $z \sim 5$ compared to $z \sim 0$).

We substituted, in our later method to estimate ρ_{gas} , M_{gas} from this work, for best-fit of M_{gas} from the literature and compared it to our estimate of ρ_{gas} . We can see in Fig. 11, that the redshift evolution of ρ_{gas} from Tacconi et al. (2018) or Wang et al. (2022) are higher compared to the one from this work. These are simply resulting from discrepancies already observed in the respective M_{gas} trend they were built from. As already pointed out in Liu et al. (2019b), the form of the formula chosen to fit M_{gas} can have a significant impact on the resulting ρ_{gas} trend, and could be the cause of what is observed here.

We also computed ρ_{gas} by summing M_{gas} of all galaxies down to several different M_{\star}^{lim} ($M_{\star}^{\text{lim}} = 1.7 \times 10^8$, 1.7×10^9 and $1.7 \times 10^{10} M_{\odot}$). We compared it to Magnelli et al. (2020) where a ρ_{gas} was computed for the same M_{\star}^{lim} from the stacking of H -

band selected galaxies in ALMA and through the method from Scoville et al. (2016). The results are displayed in Fig. 12. Here, our work agrees quite well with that of Magnelli et al. (2020) for the total ρ_{gas} (i.e., $M_{\star}^{\text{lim}} = 1.7 \times 10^8$). However, the mass distribution is not similar: massive galaxies (i.e., $M_{\star}^{\text{lim}} = 1.7 \times 10^{10}$) contribute more at low redshift (i.e., $z \leq 0.7$) in this work as compared to Magnelli et al. (2020); conversely, their contribution is smaller at higher redshift (lower by a factor ~ 3 at $z \sim 2.8$ compared to Magnelli et al. 2020).

8. Discussion

Here, when we discuss the evolution of galaxies, it should be understood that we are discussing the evolution of main sequence galaxies, as all scaling relations of SFR, M_{gas} and T_{dust} with M_{\star} and redshift have been deduced for main sequence galaxies.

8.1. Cosmic densities of star formation and gas density as a function of stellar mass

An interesting feature of Fig. 9 is the fact that the contribution to ρ_{SFR} of galaxies with $M_{\star} \leq 10^{10} M_{\odot}$ appears to be constant over $1 \leq z \leq 5$. This means that the balance of the number of these galaxies and their efficiency in producing stars remains constant with cosmic time. This feature can also be seen in Fig. 11, where the contribution to ρ_{gas} is also quite stable for galaxies with $M_{\star} \leq 10^{10} M_{\odot}$.

On the other hand, galaxies with $M_{\star} \geq 10^{10} M_{\odot}$ account for most stars formed up to $z \sim 5$. This shows that it is galaxies with $M_{\star} \geq 10^{10} M_{\odot}$ that are responsible for the observable shape on the ρ_{SFR} , especially at the cosmic noon at $z \sim 2$. In Fig. 13a, we can see that the 10% (of the total number of galaxies contributing to ρ_{SFR}) most massive galaxies contribute to a large fraction of the ρ_{SFR} at all redshifts. This contribution goes from $\sim 24\%$ at $z \sim 0$ to $\sim 48\%$ at $z \sim 5$. In particular, this means that by considering only 10% (in number) of the most massive galaxies, we can deduce a relatively good estimation of the total ρ_{SFR} at intermediate and high redshifts. From these numbers, we can also recognise some hierarchical growth effect, as bins gradually rise in M_{\star} over time.

We find that H -dropout galaxies account for 13 % of the total cosmic SFR density (CSFD) at $z=4-6$. This is in agreement with the value of 10 % found in Wang et al. (2019). We note that H -dropout galaxies account for ~ 23 % of the stars formed in massive galaxies (i.e., $M_{\star} \geq 10^{10.3} M_{\odot}$). This is a large contribution but not a dominant one, as opposed to the claim of Wang et al. (2019) that " H -dropouts dominate the SFR density in massive galaxies". This discrepancy results from our use of a fully complete sample of galaxies selected in stellar mass, whereas Wang et al. (2019) compared H -dropouts to UV-selected and similarly massive Lyman-break (LBG) galaxies.

We observe a decline in star formation in massive galaxies that mirrors that of the total star formation density. This is an illustration of the bending effect of the MS at high-mass (see Fig. 13a). The use of the depletion time in Fig. 13b illustrates this clearly: the depletion time of massive galaxies varies from $\tau_{\text{dep}} \lesssim 200$ Myr at $z > 4$ to $\tau_{\text{dep}} \gtrsim 600$ Myr at $z < 1$.

In Fig. 13c, we show that the contribution of the most massive galaxies (e.g., $M_{\star} \sim 10^{11} M_{\odot}$) to the CSFD is nearly flat, meaning that they tightly follow the global history of cosmic star formation.

Let us consider a typical galaxy with $M_{\star}=M_{\text{star}}$, such that 50 % of ρ_{\star} (cosmic stellar mass density) is made of galaxies

above and below M_{star} . We can follow the contribution of such typical galaxy to the cosmic SFR density by following the line where the Y-axis on the right of Fig. 13c equals 50 %. We find that galaxies with $M_{\star} > M_{\text{star}}$ contribute to ~ 50 % of ρ_{SFR} at $z > 3$ and drops to only ~ 25 % at $z \sim 0$. This decrease of the relative contribution of massive galaxies to ρ_{\star} illustrates the impact on the cosmic SFR history of the bending of the MS. The fact that this happens continuously with cosmic time, supports a scenario of a slow downfall of star formation rather than a rapid quenching of the most massive galaxies.

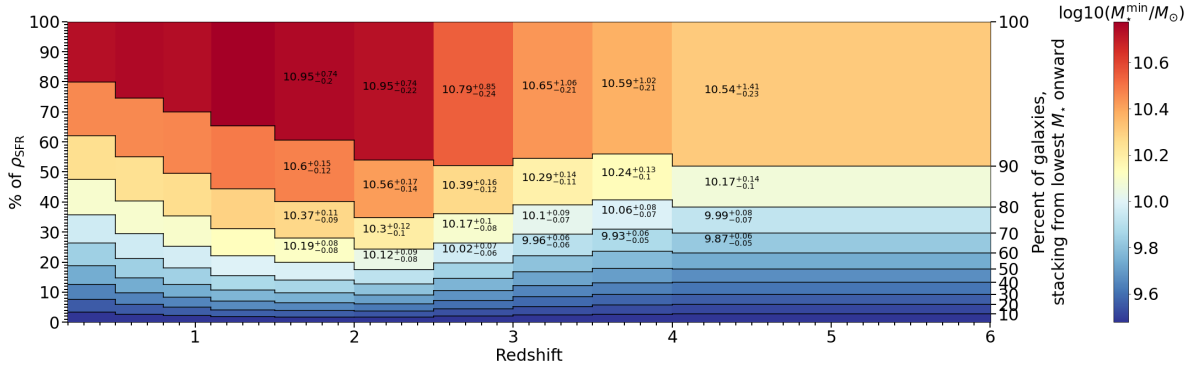
8.2. Comparison with the TNG100 simulation

Here we compare our results with cosmological simulations. In particular, we have investigated whether current simulations are able to reproduce the contribution of the different stellar mass bins to the total ρ_{SFR} . We chose to examine the TNG100 simulation (Nelson et al. 2019, 2018; Springel et al. 2018; Marinacci et al. 2018; Naiman et al. 2018; Pillepich et al. 2018b,a; Weinberger et al. 2017) of the IllustrisTNG project.

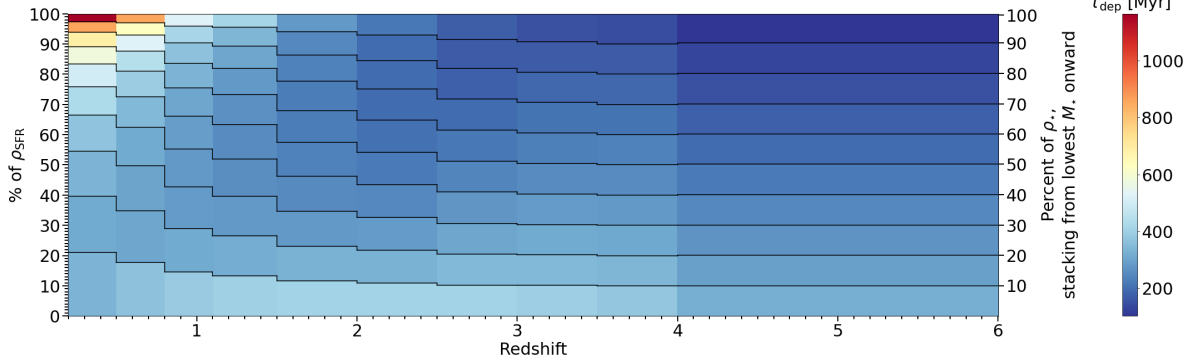
We retrieved the ρ_{SFR} of TNG100 using the same method as the one with which we calculate the ρ_{SFR} in this work, i.e., by integrating down to $3 \times 10^9 M_{\odot}$. In order to compare the trends with our work, this was also done by integrating only galaxies with $\log_{10}(M_{\star}/M_{\odot}) > 10$ and $\log_{10}(M_{\star}/M_{\odot}) < 10$. We display the evolution of ρ_{SFR} with redshift retrieved from the TNG100 simulation in Fig. 14. By comparing the trends of the TNG100 simulation with our results, we can see clear discrepancies. The ρ_{SFR} of the low masses in TNG100 (i.e., $\log_{10}(M_{\star}/M_{\odot}) < 10$) is not nearly as flat as observed (especially at $z \leq 2$). On the other hand, the ρ_{SFR} of the high masses in TNG100 (i.e., $\log_{10}(M_{\star}/M_{\odot}) > 10$) does not account for as large a part of the total ρ_{SFR} for $z < 3$. The high masses account for less than half of the total ρ_{SFR} at $z \sim 1.7$ in the simulation compared to the observations. As a result, the ρ_{SFR} peak is reached too early (i.e., at $z \sim 3$ instead of the observed at $z \sim 1.7$) in the simulation. The disparities between the two total ρ_{SFR} trends can be almost exclusively associated with the contribution of massive galaxies being off in the TNG100 simulation.

Another way to show the difference in behaviour between the TNG100 simulation and our observations for the two mass bins, is to look at the evolution over redshift of $\rho_{\text{SFR}}^{M_{\star}>10^{10}} / \rho_{\text{SFR}}^{M_{\star}<10^{10}}$ (see Fig. 15). We can see that the ratio decreases continuously with increasing redshift in the simulation, while observations show a clear peak in the ratio around $z \sim 1.7$ (i.e., the cosmic noon) where the amount of stars formed in high-mass galaxies (i.e., $\log_{10}(M_{\star}/M_{\odot}) > 10$) exceeds by a factor up to ~ 5.6 the one from low mass galaxies (i.e., $\log_{10}(M_{\star}/M_{\odot}) < 10$).

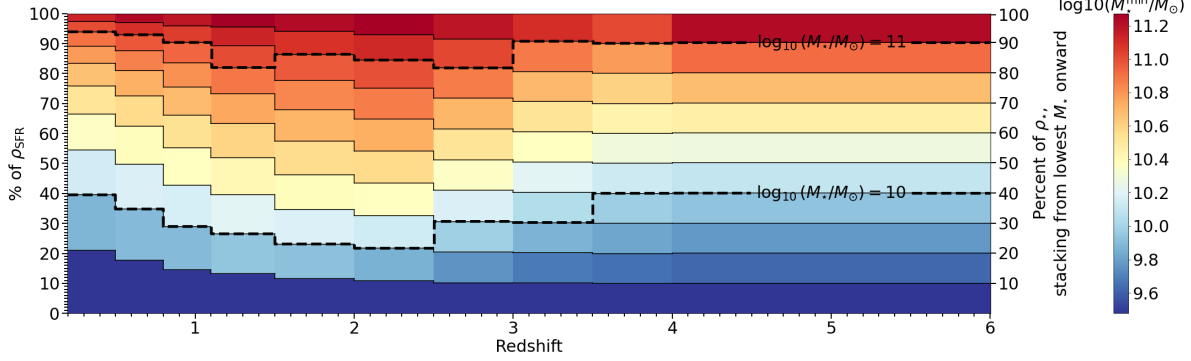
In addition to underestimating the contribution of massive galaxies to ρ_{SFR} , these simulations tend to recover, for SFGs, lower gas fractions (see Fig. 16) and SFR (see Fig. 17) compared to observations. In TNG100, $f_{\text{gas}} < 15\%$ for $M_{\star} > 10^{10} M_{\odot}$ at all redshifts (Fig. 16), as it was already addressed in Pillepich et al. (2019). Moreover, the SFR of massive individual galaxies is lower in the TNG100 simulation than in observations at e.g. $z > 4$ (see Fig. 17). Lewis et al. (2023) shows a lack of metal content in IllustrisTNG simulations at $z = 1$, that might be due to AGN feedback that removes large quantities of metal-rich gas from the centres of massive galaxies. The lower metallicities observed by Lewis et al. (2023) in IllustrisTNG simulations at $z = 1$ could be a residual memory of how AGN affected star-formation at higher z , which matches the lack of star formation we observe in Fig. 17. This could indicate flaws in the way gas



(a) Each bin includes 10% of the galaxies in number, picking from the lowest M_{\star} onwards. The minimum M_{\star} in the bin defines the colour. The numbers give the median M_{\star} within the bin along with the lower and maximum extension of the bin.



(b) Each bin includes 10% of the total M_{\star} of all galaxies, picking from the lowest M_{\star} onwards. The median τ_{dep} in the bin defines colour.



(c) Each bin includes 10% of the total M_{\star} of all galaxies, picking from the lowest M_{\star} onwards. The minimum M_{\star} in the bin defines the colour. Contours of $\log_{10}(M_{\star}/M_{\odot}) = 10$ and $\log_{10}(M_{\star}/M_{\odot}) = 11$ are added as black dashed lines.

Fig. 13: Contribution to ρ_{SFR} of SFGs as a function of redshift. Catalogues were binned through different methods and a specific property is displayed through colours: see each sub-figure for specifics.

accretion, the efficiency of galaxies to form stars from their gas content, or the ejection of gas through galactic winds is treated in the simulations. This shows that the problems encountered in the simulations may be due to the feedback processes used to regulate star formation and the gas reservoir of galaxies. In particular, the impact of AGN feedback may be overestimated to regulate star formation and kill massive galaxies. It has been shown that AGN feedback does not have much impact on quenching galaxies. High-resolution simulations (i.e., with maximum spatial resolution $\sim 100-5\text{pc}$) show that the AGN feedback tends to have little or no effect on the dense gas inside the galactic disc, because most of the out-flowing winds escape perpendicular to the galactic disc (Gabor & Bournaud 2014). AGN-driven outflows (i.e., ejective feedback), if sustained, could only quench

a galaxy after a long time scale, i.e., more than one Gyr (Gabor & Bournaud 2014; Biernacki & Teyssier 2018). These high-resolution simulations favour preemptive feedback (i.e., cutting out inflows of gas into the disc), though AGN-driven winds, to quench a galaxy (Gabor & Bournaud 2014; DeGraf et al. 2017; Biernacki & Teyssier 2018). However, even strong AGN-driven winds (i.e., $\sim 2500\text{km/s}$) would only reduce star formation in the galaxy by a factor of 2 (DeGraf et al. 2017). The TNG100 simulation has a much lower spatial resolution (i.e., a softening length of $\sim 0.74\text{kpc}$ at $z = 1$), and is therefore not able to resolve the AGN-feedback interactions correctly. The sub-grid model of AGN feedback used in the *IllustrisTNG* has already been advocated to be responsible for a lower submillimetre galaxies (SMGs) number counts compared to observations

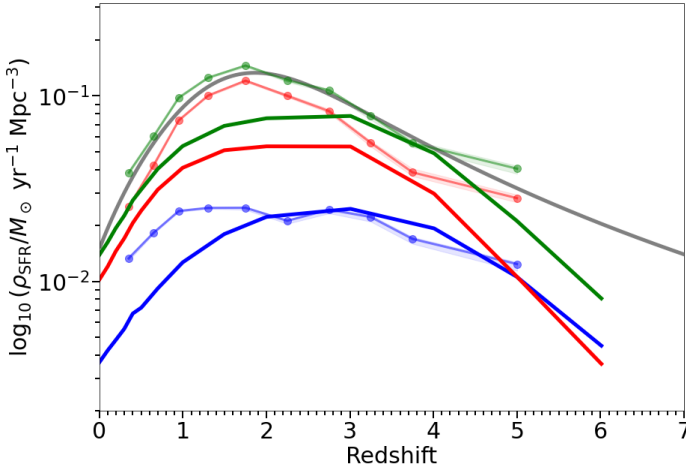


Fig. 14: Cosmic star formation rate density (ρ_{SFR}) as a function of redshift. The green, red and blue lines represent ρ_{SFR} deduced from the TNG100 simulation integrated from $3 \times 10^9 M_\odot$, including all galaxies, galaxies with $\log_{10}(M_\star/M_\odot) > 10$, and galaxies with $\log_{10}(M_\star/M_\odot) < 10$, respectively. The green, red and green faded dots represent the total ρ_{SFR} trend, ρ_{SFR} of galaxies with $\log_{10}(M_\star/M_\odot) > 10$, and galaxies with $\log_{10}(M_\star/M_\odot) < 10$, respectively (including H -dropout contribution from Wang et al. (2019)), from this work. The grey line represents the trend from Madau & Dickinson (2014) for reference.

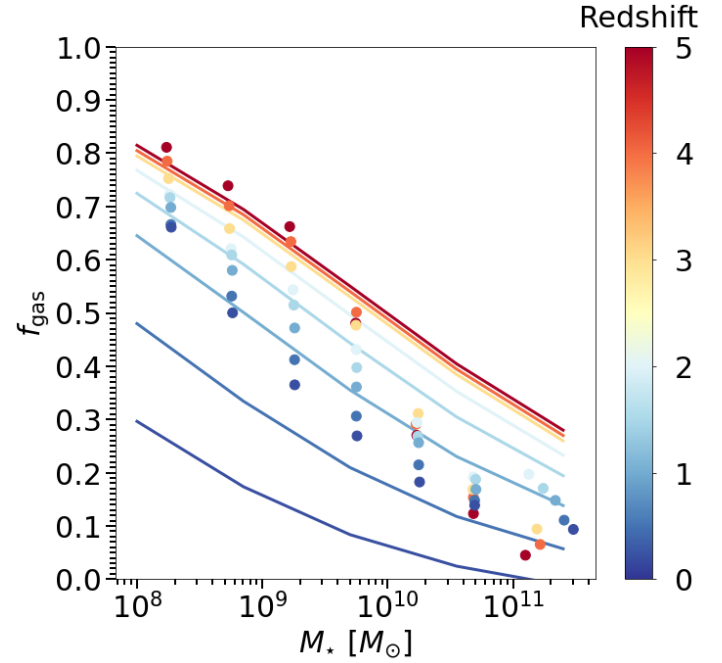


Fig. 16: f_{gas} as a function of M_\star for SFGs in TNG100. Coloured lines represent the evolution deduced from the best-fit of M_{gas} from this work (see Table 7).

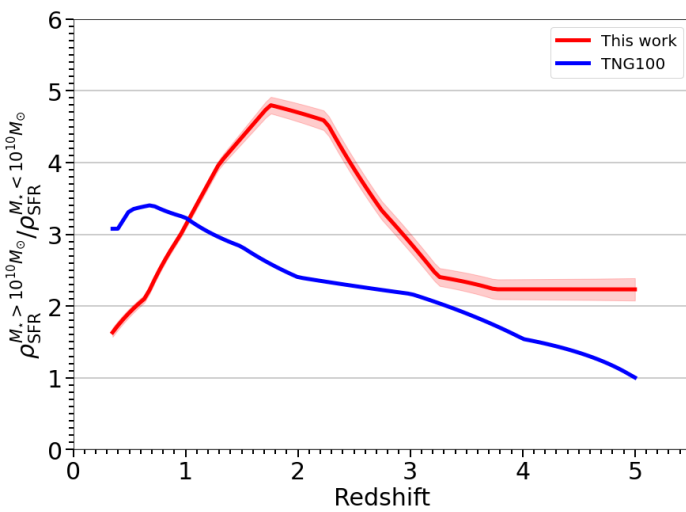


Fig. 15: Ratio of the ρ_{SFR} of high mass ($M_\star > 10^{10} M_\odot$) over low mass ($M_\star < 10^{10} M_\odot$) galaxies, as a function of redshift. The red line represents the ratio deduced from this work (i.e., from observations). The blue line represents the ratio deduced from the TNG100 simulation.

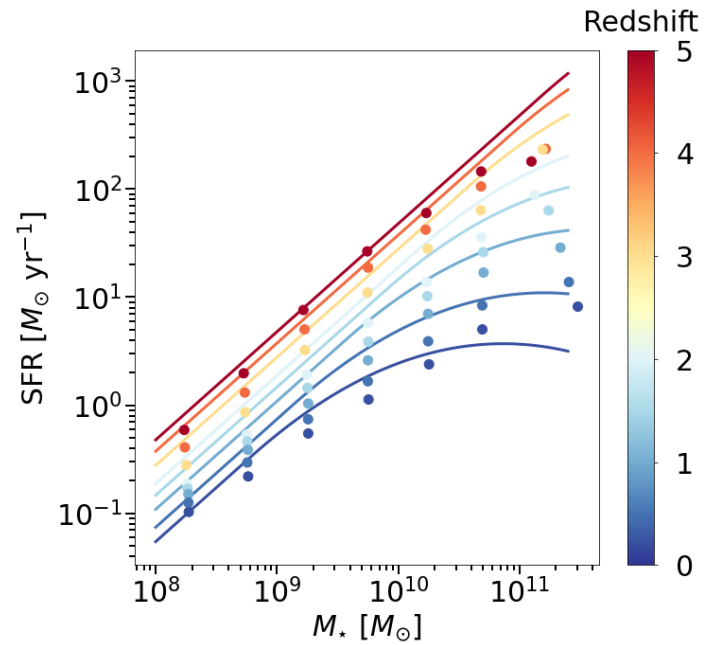


Fig. 17: SFR as a function of M_\star for SFGs in TNG100. Coloured lines represent the best-fit from this work (see Table 5).

(Hayward et al. 2021). The first *James Webb* Space Telescope (JWST) results interestingly go in the same direction: the number of bright, possibly massive, galaxies is found to exceed predictions at high z (Finkelstein et al. 2022; Donnan et al. 2023; Mason et al. 2023). This discrepancy on ρ_{SFR} could be a starting point to the underestimation of the global ρ_{SFR} in TNG100 for $(1 \leq z \leq 2)$ reported early by Donnari et al. (2019) or non-trivial issues in the simulated galaxy and halo populations found in the Illustris simulation (Nelson et al. 2015).

8.3. The Kennicutt-Schmidt relation and SFE

Through this work, we have obtained a measurement of both SFR and M_{gas} of main sequence galaxies over various redshift and M_\star bins. We can thus deduce the corresponding SFE of main sequence galaxies (i.e., examine the $SFR-M_{\text{gas}}$ plane) and its evolution as a function of redshift and M_\star . The Kennicutt-Schmidt relation (Kennicutt 1998b) illustrates similar properties by examining SFR and M_{gas} surface density (i.e., Σ_{SFR} and Σ_{gas}

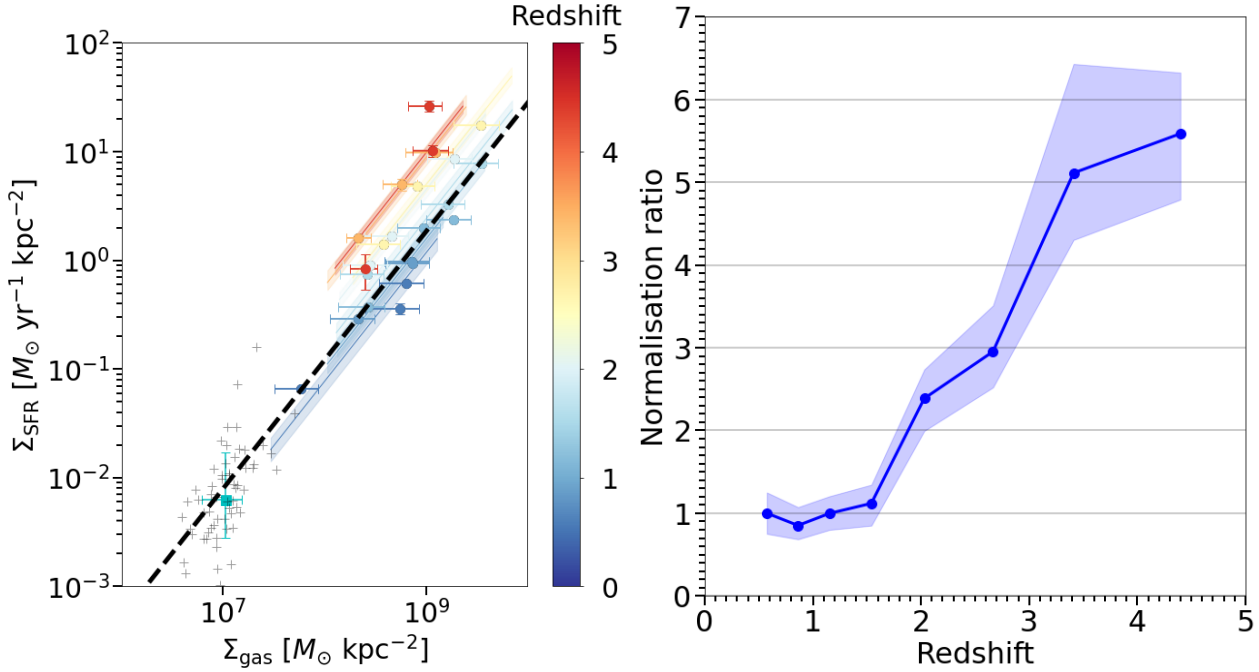


Fig. 18: Left panel: the Kennicutt-Schmidt relation: Σ_{SFR} as a function of Σ_{gas} . The dots represent the data from this work, and are colour coded by redshift. The cyan squared error bar represents the median of the sample distribution from Kennicutt (1998b), with individual galaxies displayed as grey crosses. The dashed black line represents the best-fit of all points. Coloured lines represent the best-fit, by fixing the slope to the all points best-fit value (i.e., $N = 1.18^{+0.01}_{-0.01}$), at fix redshift. Right panel: redshift evolution of the normalisation when fitting at fix slope for each redshift bin.

respectively):

$$\Sigma_{\text{SFR}} = \text{SFR}/(2\pi R_e^2), \quad (23)$$

$$\Sigma_{\text{gas}} = M_{\text{gas}}/(2\pi R_e^2), \quad (24)$$

and links them such as:

$$\log_{10}(\Sigma_{\text{SFR}}) = A + N \times \log_{10}(\Sigma_{\text{gas}}). \quad (25)$$

We do not probe R_e in this study, thus, we chose to use $R_e(z, M_*)$, for galaxies with $M_* \geq 10^{10}$, from Wang et al. (2022). We divided galaxies into bins of redshift ($0 \leq z \leq 6$) and M_* ($10 \leq \log_{10}(M_*) \leq 12$). When fitting all bins, we added the sample with low redshift and low M_* from Kennicutt (1998b). Then, we fitted the evolution of the normalisation at fixed redshift (i.e., by fixing the slope to the value of the best-fit of all bins : $N = 1.18^{+0.01}_{-0.01}$). The errors on the fits were generated by randomly varying the bin values within the uncertainties of the corresponding bin. We display the Schmidt-Kennicutt relation deduced from this work in Fig. 18.

All studies agree on a linear dependence of $\log_{10}(\Sigma_{\text{SFR}})$ as a function of $\log_{10}(\Sigma_{\text{gas}})$ with an overall slope ranging from 1 to 1.5 (e.g. Kennicutt 1998b; Wang et al. 2022), with no evolution of the slope or normalisation with redshift or M_* . Our best-fit, over all redshifts and M_* bins, also suggests a power-law scaling with a slope of $N = 1.18^{+0.01}_{-0.01}$. However, in Fig. 18, we observe an increase of the normalisation parameter A when we examine the dependence at a fixed redshift. The normalisation increases when fitting individual redshift bins (i.e., high-redshift galaxies tend to be above the line of the best-fit and low redshift galaxies below). We can see two regimes for $z \leq 2$ and $z > 2$. At $z \leq 2$ the normalisation barely evolves (i.e., the SFE does not evolves

with redshift), and at $z > 2$ the normalisation greatly evolves (i.e., SFE increase with redshift).

At $z \leq 2$, in Fig. 18, the normalisation does not evolve much with redshift. On the other hand, in Fig. 7, M_{gas} increases with redshift and M_* at $z \leq 2$. This means that an increase in SFR as a function of redshift or stellar mass, at $z \leq 2$, is mainly due to the variation of M_{gas} .

At $z > 2$, in Fig. 18, the normalisation increases with redshift: by a factor ~ 4 between $z \sim 2$ and $z \sim 4.3$. On the other hand, in Fig. 7, M_{gas} remains roughly constant for $z > 2$. This means that the SFE plays a non-negligible role in increasing the normalisation of the main sequence SFR between $2 \leq z \leq 4.3$.

We found that $\Sigma_{\text{SFR}} = A \times (\Sigma_{\text{gas}})^N$ with $N \sim 1.18$ which means that an increase in M_{gas} induces some increase in SFE (i.e., $\text{SFE} \sim (M_{\text{gas}})^{0.18}$). It would not be the case if the slope of the Kennicutt-Schmidt relation was $N = 1$ as in Tacconi et al. (2013). In our case, it means that, we need to differentiate two effects: an increase of SFE due to the increase of M_{gas} , and an intrinsic increase in SFE. For example, at fixed stellar mass for $10.5 \leq \log_{10}(M_*/M_\odot) \leq 11$ between $z = 1.15$ and $z = 2$, SFR increase by a factor ~ 4 (see Fig. 5), while M_{gas} increase by a factor ~ 1.6 (see Fig. 7): it means that SFE increase by a factor ~ 2.5 , which reflects the increase of the normalisation in Fig. 18 by ~ 2.5 for the same redshift range. The first effect in an increase of SFE due to the increase of M_{gas} (i.e., resulting from the Kennicutt-Schmidt relation of slope $N \sim 1.18$): $\alpha_{\text{SFE}}^{\text{due to } M_{\text{gas}}} \sim \alpha_{M_{\text{gas}}}^{N_1} = (1.6)^{0.18} \sim 1.09$. The second effect is an intrinsic increase in SFE between the two redshifts (i.e., independent of the increase of M_{gas}): $\alpha_{\text{SFE}}^{\text{intrinsic}} \sim \alpha_{\text{SFE}}/\alpha_{\text{SFE}}^{\text{due to } M_{\text{gas}}} \sim 2.3$. Finally, we could conclude by saying that a factor ~ 2.3 is solely due to an increase of SFE, and a factor $\sim \alpha_{M_{\text{gas}}} \times \alpha_{\text{SFE}}^{\text{due to } M_{\text{gas}}} = 1.75$ is due to the increase of M_{gas} .

We note that this effect is not inherent to our specific data points, or even best-fit evolution laws of SFR and M_{gas} , as a similar evolution could be observed if we were to generate catalogues from the laws of S15 for SFR, and Wang et al. (2022) or Tacconi et al. 2018 for M_{gas} (following the method used to generate ρ_{SFR} and ρ_{gas} see Sect. 6 and 7). If we were to choose laws from Speagle et al. 2014 for SFR and Tacconi et al. (2018) for M_{gas} , this effect would disappear completely, and we would end up with a linear non-evolving slope depending on redshift or M_{\star} . We conclude, in this case, that the correct normalisation and the presence of the bending of the main sequence – which are lacking in the study of Speagle et al. (2014)) – are essential to observe this effect. One could advocate that the observation of an increase in efficiency with redshift when generating catalogues, for example, from S15 for SFR, and Tacconi et al. 2018 for M_{gas}), comes from the fact that the M_{gas} fitting form from Tacconi et al. (2018), or the one use in this work, do not allow a bending or an evolution of it. However, we found no evidence of a bending or its evolution at high-mass when we tried to fit our data using various forms allowing them. Overall, it suggests that some physical processes limit the star formation efficiency in low-redshift galaxies, as compared to high-redshift galaxies, beyond the simple fact that they have less available gas.

Overall, even though the evolution of the normalisation is not well constrained, this study suggests that galaxies at high-redshift form stars more efficiently at a fixed gas surface density. This excess cannot be explained by a universal Kennicutt-Schmidt relation over all redshifts. This may partly explain the early results of JWST: a higher ρ_{UV} at $z \geq 8$ (Finkelstein et al. 2023; Donnan et al. 2023; Mason et al. 2023) compared to pre-JWST extrapolation Oesch et al. (2018); more massive galaxies at $z \geq 7$ (Labbe et al. 2022). This may be explained by the model proposed by Dekel et al. (2023) who showed that the environment of the most massive dark-matter haloes at $z \geq 10$ favour high star-formation efficiencies.

In conclusion, the gradual appearance of the bending of the main sequence with redshift appears to result from a reduction of the SFE, i.e., a gradual disappearance of this extra factor affecting the SFE (observed at $z \sim 4.3$ and absent at $z \sim 2$). Then, at a fixed lower redshift (i.e., $z < 2$), the bending of the main sequence (as M_{\star} increases) is mainly due to a decrease in M_{gas} with stellar mass, and to second order, to a decrease in SFE with stellar mass. This characteristics is also observed in the local universe (i.e., for $0.01 < z < 0.05$) in Saintonge et al. (2016): when the stellar mass increases by a factor 10, the SFR increases by a factor ~ 1.4 , which is due to an increase of M_{gas} by a factor ~ 1.8 and a decrease in SFE by a factor ~ 1.25 . Saintonge et al. (2016) reach the same conclusion in the local universe: at a fixed redshift, M_{gas} is the main reason for the bending of the main sequence. The slow downfall of the star formation efficiency in the most massive galaxies (i.e., $M_{\star} \geq 10^{11} M_{\odot}$) observed between $0.1 \leq z \leq 4.3$, was also observed in Schreiber et al. (2016). It seems that a discontinuation of gas accretion cannot be the only reason for the bending of the SFR main sequence (Daddi et al. 2022). It must be coupled with other effects that prevent the gas in high M_{\star} galaxies from cooling and collapsing into stars (i.e., an evolution of the SFE). The main driver of the bending could be the quenching of galaxies due to environmental effects, as massive galaxies populate denser environments where they suffer from ram pressure stripping, galaxy harassment (e.g., Kalita et al. 2022).

9. Summary and conclusions

In this work we gather catalogues of H -band selected SFGs over four fields (GOODS-South, GOODS-North, COSMOS, UDS). This sample is stacked over 7 wavelengths ($24 \mu\text{m}$, $100 \mu\text{m}$, $160 \mu\text{m}$, $250 \mu\text{m}$, $350 \mu\text{m}$, $500 \mu\text{m}$ and 1.13 mm). The main addition to this work, compared to previous studies, is the use of the GOODS-ALMA survey (Gómez-Guijarro et al. 2022b), which helps to reach lower M_{\star} and higher redshifts, when combined with *Herschel*. We combine the stacking of H -band selected galaxies with H -dropout galaxy properties to obtain a complete view of the cosmic history of galaxies. We derive the evolution of main sequence galaxy properties such as SFR, T_{dust} , M_{gas} through a consistent analysis. We generate a detailed view of ρ_{SFR} and ρ_{gas} depending on key galaxy properties such as M_{\star} , L_{IR} and τ_{dep} .

This study allowed us to confirm several feature of galaxies, the main ones being summarised as follows:

- T_{dust} evolves linearly with redshift. There is no clear evidence for a dependence of T_{dust} depending on M_{\star} at a fixed redshift, when considering main sequence galaxies.
- The SFR- M_{\star} MS has a slope close to unity at low masses (i.e., $M_{\star} \lesssim 10^{10} - 10^{11} M_{\odot}$), with a bending appearing below $z \sim 2$ on the high-mass end. The bending of the MS corresponds to the slow downfall of star-formation in massive galaxies.
- The total ρ_{SFR} follows a form close to the one presented in Madau & Dickinson (2014), at least up to $z = 5$. As a result, the contribution of H -dropout galaxies to the total ρ_{SFR} is $\sim 13\%$ at $z = 5$.

The main new results from this paper can be summarised as follows:

- We measure the contribution of galaxies of different M_{\star} to the total ρ_{SFR} over the cosmic time. We find that massive galaxies (i.e., $M_{\star} \geq 10^{10} M_{\odot}$) account for most of the ρ_{SFR} up to $z \sim 5$. Low-mass galaxies (i.e., $M_{\star} \leq 10^{10} M_{\odot}$) contribute a roughly constant fraction to the total ρ_{SFR} at $0.4 \leq z \leq 5$.
- The TNG100 simulation fails to reproduce the contributions of the different bins of M_{\star} to the total ρ_{SFR} . In particular, in the TNG100 simulation, massive galaxies do not form enough stars around cosmic noon, when the cosmic SFR density peaks. We conclude that the mechanisms used to regulate star formation (in particular feedback from AGNs) are possibly too strong in this simulation, namely too efficient in producing a drop of the gas content in massive galaxies.
- We estimate H -dropout galaxies (as defined in Wang et al. (2019)) contribute to $\sim 23\%$ of the ρ_{SFR} of galaxies with $M_{\star} \geq 10^{10.3} M_{\odot}$ at $z=4-6$.
- We find hints that high-redshift galaxies convert their gas reservoirs more efficiently than local galaxies, i.e., suggesting a possible evolution of the Kennicutt-Schmidt relation with redshift.

Acknowledgements. This work was supported by the Programme National Cosmology et Galaxies (PNCG) of CNRS/INSU with INP and IN2P3, co-funded by CEA and CNES. C.G.G. acknowledges support from CNES.

References

- Barro, G., Pérez-González, P. G., Cava, A., et al. 2019, ApJS, 243, 22
- Bauermeister, A., Blitz, L., & Ma, C.-P. 2010, ApJ, 717, 323
- Bavouzet, N., Dole, H., Le Floc'h, E., et al. 2008, A&A, 479, 83

- 1313 Berta, S., Lutz, D., Genzel, R., Förster-Schreiber, N. M., & Tacconi, L. J. 2016, A&A, 587, A73 1394
 1314 Béthermin, M., Daddi, E., Magdis, G., et al. 2015, A&A, 573, A113 1395
 1315 Béthermin, M., Dole, H., Cousin, M., & Bouvouzet, N. 2010, Astronomy and 1396
 1316 Astrophysics, 516, A43 1397
 1317 Béthermin, M., Fudamoto, Y., Ginolfi, M., et al. 2020, A&A, 643, A2 1398
 1318 Béthermin, M., Kilbinger, M., Daddi, E., et al. 2014, A&A, 567, A103 1399
 1319 Béthermin, M., Le Floc'h, E., Ilbert, O., et al. 2012, A&A, 542, A58 1400
 1320 Biernacki, P. & Teyssier, R. 2018, MNRAS, 475, 5688 1401
 1321 Bigiel, F., Leroy, A., Walter, F., et al. 2008, AJ, 136, 2846 1402
 1322 Bourne, A. D., Wolfire, M., & Leroy, A. K. 2013, ARA&A, 51, 207 1403
 1323 Bourne, N., Maddox, S. J., Dunne, L., et al. 2012, MNRAS, 421, 3027 1404
 1324 Bouwens, R., González-López, J., Aravena, M., et al. 2020, ApJ, 902, 112 1405
 1325 Bouwens, R. J., Illingworth, G. D., Oesch, P. A., et al. 2015a, ApJ, 811, 140 1406
 1326 Bouwens, R. J., Illingworth, G. D., Oesch, P. A., et al. 2012a, ApJ, 754, 83 1407
 1327 Bouwens, R. J., Illingworth, G. D., Oesch, P. A., et al. 2015b, ApJ, 803, 34 1408
 1328 Bouwens, R. J., Illingworth, G. D., Oesch, P. A., et al. 2012b, ApJ, 752, L5 1409
 1329 Brammer, G. B., van Dokkum, P. G., & Coppi, P. 2008, ApJ, 686, 1503 1410
 1330 Bruzual, G. & Charlot, S. 2003, MNRAS, 344, 1000 1411
 1331 Calzetti, D., Kinney, A. L., & Storchi-Bergmann, T. 1994, ApJ, 429, 582 1412
 1332 Casey, C. M., Zavala, J. A., Spilker, J., et al. 2018, ApJ, 862, 77 1413
 1333 Chabrier, G. 2003, PASP, 115, 763 1414
 1334 da Cunha, E., Groves, B., Walter, F., et al. 2013, ApJ, 766, 13 1415
 1335 Daddi, E., Cimatti, A., Renzini, A., et al. 2004, ApJ, 617, 746 1416
 1336 Daddi, E., Delvecchio, I., Dimauro, P., et al. 2022, A&A, 661, L7 1417
 1337 Daddi, E., Dickinson, M., Morrison, G., et al. 2007, ApJ, 670, 156 1418
 1338 Daddi, E., Elbaz, D., Walter, F., et al. 2010, ApJ, 714, L118 1419
 1339 Davidzon, I., Ilbert, O., Laigle, C., et al. 2017, A&A, 605, A70 1420
 1340 de los Reyes, M. A. C. & Kennicutt, Robert C., J. 2019, ApJ, 872, 16 1421
 1341 DeGraf, C., Dekel, A., Gabor, J., & Bournaud, F. 2017, MNRAS, 466, 1462 1422
 1342 Dekel, A., Sarkar, K. S., Birnboim, Y., Mandelker, N., & Li, Z. 2023, arXiv 1423
 1343 e-prints, arXiv:2303.04827 1424
 1344 Delvecchio, I., Daddi, E., Sargent, M. T., et al. 2021, Astronomy & Astrophysics, 647, A123 1425
 1345 Donnan, C. T., McLeod, D. J., Dunlop, J. S., et al. 2023, MNRAS, 518, 6011 1426
 1346 Donnari, M., Pillepich, A., Nelson, D., et al. 2019, MNRAS, 485, 4817 1427
 1347 Draine, B. T., Aniano, G., Krause, O., et al. 2014, ApJ, 780, 172 1428
 1348 Draine, B. T. & Li, A. 2007, ApJ, 657, 810 1429
 1349 Drew, P. M. & Casey, C. M. 2022, ApJ, 930, 142 1430
 1350 Elbaz, D., Daddi, E., Le Borgne, D., et al. 2007, A&A, 468, 33 1431
 1351 Elbaz, D., Dickinson, M., Hwang, H. S., et al. 2011, A&A, 533, A119 1432
 1352 Elbaz, D., Leiton, R., Nagar, N., et al. 2018, A&A, 616, A110 1433
 1353 Erb, D. K., Shapley, A. E., Pettini, M., et al. 2006, ApJ, 644, 813 1434
 1354 Finkelstein, S. L., Bagley, M. B., Ferguson, H. C., et al. 2022, CEERS Key Paper 1435
 1355 I: An Early Look into the First 500 Myr of Galaxy Formation with JWST 1436
 1356 Finkelstein, S. L., Bagley, M. B., Ferguson, H. C., et al. 2023, ApJ, 946, L13 1437
 1357 Franco, M., Elbaz, D., Béthermin, M., et al. 2018, A&A, 620, A152 1438
 1358 Franco, M., Elbaz, D., Zhou, L., et al. 2020, A&A, 643, A53 1439
 1359 Fritz, J., Franceschini, A., & Hatziminaoglou, E. 2006, MNRAS, 366, 767 1440
 1360 Gabor, J. M. & Bournaud, F. 2014, MNRAS, 441, 1615 1441
 1361 Galametz, A., Grazian, A., Fontana, A., et al. 2013, ApJS, 206, 10 1442
 1362 Galliano, F., Hony, S., Bernard, J. P., et al. 2011, A&A, 536, A88 1443
 1363 Galliano, F., Nersesian, A., Bianchi, S., et al. 2021, A&A, 649, A18 1444
 1364 Genzel, R., Tacconi, L. J., Lutz, D., et al. 2015, ApJ, 800, 20 1445
 1365 Gómez-Guijarro, C., Elbaz, D., Xiao, M., et al. 2022a, A&A, 658, A43 1446
 1366 Gómez-Guijarro, C., Elbaz, D., Xiao, M., et al. 2022b, A&A, 659, A196 1447
 1367 Griffin, M. J., Abergel, A., Abreu, A., et al. 2010, A&A, 518, L3 1448
 1368 Grogin, N. A., Kocevski, D. D., Faber, S. M., et al. 2011, ApJS, 197, 35 1449
 1369 Groves, B. A., Schinnerer, E., Leroy, A., et al. 2015, ApJ, 799, 96 1450
 1370 Gruppioni, C., Béthermin, M., Loiacono, F., et al. 2020, A&A, 643, A8 1451
 1371 Guo, K., Zheng, X. Z., & Fu, H. 2013, ApJ, 778, 23 1452
 1372 Hao, L., Strauss, M. A., Fan, X., et al. 2005, AJ, 129, 1795 1453
 1373 Harrington, K. C., Weiss, A., Yun, M. S., et al. 2021, ApJ, 908, 95 1454
 1374 Hatziminaoglou, E., Omont, A., Stevens, J. A., et al. 2010, A&A, 518, L33 1455
 1375 Hayward, C. C., Sparre, M., Chapman, S. C., et al. 2021, MNRAS, 502, 2922 1456
 1376 Hodge, J. A. & da Cunha, E. 2020, Royal Society Open Science, 7, 200556 1457
 1377 Kaasinen, M., Scoville, N., Walter, F., et al. 2019, ApJ, 880, 15 1458
 1378 Kalita, B. S., Daddi, E., Bournaud, F., et al. 2022, A&A, 666, A44 1459
 1379 Kennicutt, Robert C., J. 1998a, ARA&A, 36, 189 1460
 1380 Kennicutt, Robert C., J. 1998b, ApJ, 498, 541 1461
 1381 Kewley, L. J. & Dopita, M. A. 2002, ApJS, 142, 35 1462
 1382 Kewley, L. J. & Ellison, S. L. 2008, ApJ, 681, 1183 1463
 1383 Koekemoer, A. M., Faber, S. M., Ferguson, H. C., et al. 2011, ApJS, 197, 36 1464
 1384 Kurczynski, P. & Gawiser, E. 2010, AJ, 139, 1592 1465
 1385 Labbe, I., van Dokkum, P., Nelson, E., et al. 2022, arXiv e-prints, 1466
 1386 Lagache, G. 2018, in Peering towards Cosmic Dawn, ed. V. Jelić & T. van der 1467
 1387 Hulst, Vol. 333, 228–233 1468
 1388 Lagos, C. d. P., Crain, R. A., Schaye, J., et al. 2015, MNRAS, 452, 3815 1469
 1389 Lee, N., Sanders, D. B., Casey, C. M., et al. 2015, ApJ, 801, 80 1470
 1390 LeFloc'h, E., Aussel, H., Ilbert, O., et al. 2009, ApJ, 703, 222 1471
 1391 Leroy, A. K., Bolatto, A., Gordon, K., et al. 2011, ApJ, 737, 12 1472
 1392 Leroy, A. K., Walter, F., Brinks, E., et al. 2008, AJ, 136, 2782 1473
 1393 Leslie, S. K., Schinnerer, E., Liu, D., et al. 2020, ApJ, 899, 58 1474
 1394 Lewis, Z. J., Andrews, B. H., Bezanson, R., et al. 2023, arXiv e-prints, 1475
 1395 arXiv:2304.12343 1476

BIBLIOGRAPHY

- Aufort, G., Ciesla, L., Pudlo, P., & Buat, V. 2020, , 635, A136
- Barro, G., Pérez-González, P. G., Cava, A., et al. 2019, , 243, 22
- Barrufet, L., Oesch, P. A., Weibel, A., et al. 2023, , 522, 449
- Bauermeister, A., Blitz, L., & Ma, C.-P. 2010, , 717, 323
- Bavouzet, N., Dole, H., Le Floc'h, E., et al. 2008, , 479, 83
- Berta, S., Lutz, D., Genzel, R., Förster-Schreiber, N. M., & Tacconi, L. J. 2016, , 587, A73
- Béthermin, M., Daddi, E., Magdis, G., et al. 2015, , 573, A113
- Béthermin, M., Dole, H., Beelen, A., & Aussel, H. 2010a, *Astronomy and Astrophysics*, 512, A78
- Béthermin, M., Dole, H., Cousin, M., & Bavouzet, N. 2010b, *Astronomy and Astrophysics*, 516, A43
- Béthermin, M., Fudamoto, Y., Ginolfi, M., et al. 2020, , 643, A2
- Béthermin, M., Kilbinger, M., Daddi, E., et al. 2014, , 567, A103
- Béthermin, M., Le Floc'h, E., Ilbert, O., et al. 2012, , 542, A58
- Biernacki, P. & Teyssier, R. 2018, , 475, 5688
- Bigiel, F., Cormier, D., & Schmidt, T. 2014, *Astronomische Nachrichten*, 335, 470
- Bigiel, F., Leroy, A., Walter, F., et al. 2008, , 136, 2846
- Bisigello, L., Gandolfi, G., Grazian, A., et al. 2023, , 676, A76
- Bolatto, A. D., Wolfire, M., & Leroy, A. K. 2013, , 51, 207
- Boquien, M., Burgarella, D., Roehlly, Y., et al. 2019, , 622, A103
- Boselli, A., Cortese, L., Boquien, M., et al. 2014a, , 564, A66
- Boselli, A., Cuillandre, J. C., Fossati, M., et al. 2016, , 587, A68
- Boselli, A., Voyer, E., Boissier, S., et al. 2014b, , 570, A69
- Bourne, N., Maddox, S. J., Dunne, L., et al. 2012, , 421, 3027
- Bouwens, R., González-López, J., Aravena, M., et al. 2020, , 902, 112
- Bouwens, R. J., Illingworth, G. D., Oesch, P. A., et al. 2015a, , 811, 140
- Bouwens, R. J., Illingworth, G. D., Oesch, P. A., et al. 2012a, , 754, 83
- Bouwens, R. J., Illingworth, G. D., Oesch, P. A., et al. 2015b, , 803, 34

- Bouwens, R. J., Illingworth, G. D., Oesch, P. A., et al. 2012b, , 752, L5
- Brammer, G. B., van Dokkum, P. G., & Coppi, P. 2008, , 686, 1503
- Bruzual, G. & Charlot, S. 2003, , 344, 1000
- Buat, V., Heinis, S., Boquien, M., et al. 2014, , 561, A39
- Calzetti, D., Kinney, A. L., & Storchi-Bergmann, T. 1994, , 429, 582
- Carnall, A. C., Leja, J., Johnson, B. D., et al. 2019, , 873, 44
- Casey, C. M., Zavala, J. A., Spilker, J., et al. 2018, , 862, 77
- Castellano, M., Fontana, A., Treu, T., et al. 2022, , 938, L15
- Chabrier, G. 2003, , 115, 763
- Chiang, Y.-K., Overzier, R. A., Gebhardt, K., & Henriques, B. 2017, , 844, L23
- Ciesla, L., Buat, V., Boquien, M., et al. 2021, , 653, A6
- Ciesla, L., Charmandaris, V., Georgakakis, A., et al. 2015, , 576, A10
- Ciesla, L., Elbaz, D., & Fensch, J. 2017, , 608, A41
- Ciesla, L., Elbaz, D., Schreiber, C., Daddi, E., & Wang, T. 2018, , 615, A61
- Cowie, L. L., Songaila, A., Hu, E. M., & Cohen, J. G. 1996, , 112, 839
- Cucciati, O., Tresse, L., Ilbert, O., et al. 2012, , 539, A31
- Curtis-Lake, E., Carniani, S., Cameron, A., et al. 2023, Nature Astronomy, 7, 622
- da Cunha, E., Groves, B., Walter, F., et al. 2013, , 766, 13
- da Cunha, E., Walter, F., Smail, I. R., et al. 2015, , 806, 110
- Daddi, E., Cimatti, A., Renzini, A., et al. 2004, , 617, 746
- Daddi, E., Delvecchio, I., Dimauro, P., et al. 2022, , 661, L7
- Daddi, E., Dickinson, M., Morrison, G., et al. 2007, , 670, 156
- Daddi, E., Elbaz, D., Walter, F., et al. 2010, , 714, L118
- Davé, R., Anglés-Alcázar, D., Narayanan, D., et al. 2019, , 486, 2827
- Davidzon, I., Ilbert, O., Laigle, C., et al. 2017, , 605, A70
- de los Reyes, M. A. C. & Kennicutt, Robert C., J. 2019, , 872, 16
- DeGraf, C., Dekel, A., Gabor, J., & Bournaud, F. 2017, , 466, 1462
- Dekel, A., Birnboim, Y., Engel, G., et al. 2009, , 457, 451

- Dekel, A., Sarkar, K. S., Birnboim, Y., Mandelker, N., & Li, Z. 2023, arXiv e-prints, arXiv:2303.04827
- Delvecchio, I., Daddi, E., Sargent, M. T., et al. 2021, *Astronomy Astrophysics*, 647, A123
- Donnan, C. T., McLeod, D. J., Dunlop, J. S., et al. 2023, , 518, 6011
- Donnari, M., Pillepich, A., Nelson, D., et al. 2019, , 485, 4817
- Draine, B. T., Aniano, G., Krause, O., et al. 2014, , 780, 172
- Draine, B. T. & Li, A. 2007, , 657, 810
- Dressler, A. 1980, , 236, 351
- Dressler, A., Oemler, Augustus, J., Couch, W. J., et al. 1997, , 490, 577
- Drew, P. M. & Casey, C. M. 2022, , 930, 142
- Einstein, A. 1915, *Sitzungsberichte der Königlich Preussischen Akademie der Wissenschaften*, 844
- Elbaz, D., Daddi, E., Le Borgne, D., et al. 2007, , 468, 33
- Elbaz, D., Dickinson, M., Hwang, H. S., et al. 2011, , 533, A119
- Elbaz, D., Leiton, R., Nagar, N., et al. 2018, , 616, A110
- Erb, D. K., Shapley, A. E., Pettini, M., et al. 2006, , 644, 813
- Fabian, A. C. 2012, , 50, 455
- Fine, S., Croom, S. M., Miller, L., et al. 2006, , 373, 613
- Finkelstein, S. L., Bagley, M. B., Ferguson, H. C., et al. 2023, , 946, L13
- Finkelstein, S. L., Ryan, Russell E., J., Papovich, C., et al. 2015, , 810, 71
- Franco, M., Elbaz, D., Béthermin, M., et al. 2018, , 620, A152
- Franco, M., Elbaz, D., Zhou, L., et al. 2020, , 643, A53
- Fritz, J., Franceschini, A., & Hatziminaoglou, E. 2006, , 366, 767
- Gabor, J. M. & Bournaud, F. 2014, , 441, 1615
- Galametz, A., Grazian, A., Fontana, A., et al. 2013, , 206, 10
- Galliano, F., Galametz, M., & Jones, A. P. 2018, , 56, 673
- Galliano, F., Hony, S., Bernard, J. P., et al. 2011, , 536, A88
- Galliano, F., Nersesian, A., Bianchi, S., et al. 2021, , 649, A18
- Gavazzi, G., Catinella, B., Carrasco, L., Boselli, A., & Contursi, A. 1998, , 115, 1745

- Genzel, R., Tacconi, L. J., Lutz, D., et al. 2015, , 800, 20
- Gómez-Guijarro, C., Elbaz, D., Xiao, M., et al. 2022a, , 658, A43
- Gómez-Guijarro, C., Elbaz, D., Xiao, M., et al. 2022b, , 659, A196
- Gómez-Guijarro, C., Magnelli, B., Elbaz, D., et al. 2023, arXiv e-prints, arXiv:2304.08517
- González, V., Labbé, I., Bouwens, R. J., et al. 2010, , 713, 115
- Griffin, M. J., Abergel, A., Abreu, A., et al. 2010, , 518, L3
- Grogin, N. A., Kocevski, D. D., Faber, S. M., et al. 2011, , 197, 35
- Groves, B. A., Schinnerer, E., Leroy, A., et al. 2015, , 799, 96
- Gruppioni, C., Béthermin, M., Loiacono, F., et al. 2020, , 643, A8
- Gunn, J. E. & Gott, J. Richard, I. 1972, , 176, 1
- Guo, K., Zheng, X. Z., & Fu, H. 2013, , 778, 23
- Hao, L., Strauss, M. A., Fan, X., et al. 2005, , 129, 1795
- Harikane, Y., Inoue, A. K., Mawatari, K., et al. 2022, , 929, 1
- Harrington, K. C., Weiss, A., Yun, M. S., et al. 2021, , 908, 95
- Harrison, C. M. 2017, Nature Astronomy, 1, 0165
- Hatziminaoglou, E., Omont, A., Stevens, J. A., et al. 2010, , 518, L33
- Hayward, C. C., Sparre, M., Chapman, S. C., et al. 2021, , 502, 2922
- Heinis, S., Buat, V., Béthermin, M., et al. 2013, , 429, 1113
- Heinis, S., Buat, V., Béthermin, M., et al. 2014, , 437, 1268
- Helou, G., Soifer, B. T., & Rowan-Robinson, M. 1985, , 298, L7
- Herschel, W. 1786, Philosophical Transactions of the Royal Society of London Series I, 76, 457
- Herschel, W. 1789, Philosophical Transactions of the Royal Society of London Series I, 79, 212
- Herschel, W. 1802, Philosophical Transactions of the Royal Society of London Series I, 92, 477
- Hopkins, P. F., Cox, T. J., Kereš, D., & Hernquist, L. 2008a, , 175, 390
- Hopkins, P. F., Hernquist, L., Cox, T. J., & Kereš, D. 2008b, , 175, 356
- Hubble, E. 1929, Proceedings of the National Academy of Science, 15, 168
- Hubble, E. P. 1925, The Observatory, 48, 139
- Hubble, E. P. 1936, Realm of the Nebulae

- Iyer, K. & Gawiser, E. 2017, , 838, 127
- Iyer, K. G., Gawiser, E., Faber, S. M., et al. 2019, , 879, 116
- Jacobs, C., Glazebrook, K., Calabro, A., et al. 2023, , 948, L13
- Kalita, B. S., Daddi, E., Bournaud, F., et al. 2022, , 666, A44
- Kartaltepe, J. S., Rose, C., Vanderhoof, B. N., et al. 2023, , 946, L15
- Kennicutt, Robert C., J. 1998a, , 36, 189
- Kennicutt, Robert C., J. 1998b, , 498, 541
- Kennicutt, R. C. & Evans, N. J. 2012, , 50, 531
- Kewley, L. J. & Dopita, M. A. 2002, , 142, 35
- Kewley, L. J. & Ellison, S. L. 2008, , 681, 1183
- Koekemoer, A. M., Faber, S. M., Ferguson, H. C., et al. 2011, , 197, 36
- Kriek, M., van Dokkum, P. G., Labb  , I., et al. 2009, , 700, 221
- Kroupa, P. 2001, , 322, 231
- Kurczynski, P. & Gawiser, E. 2010, , 139, 1592
- Labbe, I., van Dokkum, P., Nelson, E., et al. 2022, arXiv e-prints, arXiv:2207.12446
- Lagache, G. 2018, in Peering towards Cosmic Dawn, ed. V. Jeli   & T. van der Hulst, Vol. 333, 228–233
- Lagos, C. d. P., Crain, R. A., Schaye, J., et al. 2015, , 452, 3815
- Le Borgne, D., Elbaz, D., Ocvirk, P., & Pichon, C. 2009, , 504, 727
- Lee, N., Sanders, D. B., Casey, C. M., et al. 2015, , 801, 80
- LeFloc'h, E., Aussel, H., Ilbert, O., et al. 2009, , 703, 222
- Leja, J., Carnall, A. C., Johnson, B. D., Conroy, C., & Speagle, J. S. 2019, , 876, 3
- Lema  tre, G. 1927, Annales de la Soci  t   Scientifique de Bruxelles, 47, 49
- Leroy, A. K., Bolatto, A., Gordon, K., et al. 2011, , 737, 12
- Leroy, A. K., Walter, F., Brinks, E., et al. 2008, , 136, 2782
- Leslie, S. K., Schinnerer, E., Liu, D., et al. 2020, , 899, 58
- Lewis, I., Balogh, M., De Propris, R., et al. 2002, , 334, 673
- Lewis, Z. J., Andrews, B. H., Bezanson, R., et al. 2023, arXiv e-prints, arXiv:2304.12343

- Liu, D., Daddi, E., Dickinson, M., et al. 2018, , 853, 172
- Liu, D., Schinnerer, E., Groves, B., et al. 2019, , 887, 235
- Liu, G., Koda, J., Calzetti, D., Fukuhara, M., & Momose, R. 2011, , 735, 63
- Lower, S., Narayanan, D., Leja, J., et al. 2020, , 904, 33
- Lutz, D., Poglitsch, A., Altieri, B., et al. 2011, , 532, A90
- Madau, P. & Dickinson, M. 2014, , 52, 415
- Madau, P., Pozzetti, L., & Dickinson, M. 1998, , 498, 106
- Magdis, G. E., Daddi, E., Béthermin, M., et al. 2012, , 760, 6
- Magdis, G. E., Daddi, E., Elbaz, D., et al. 2011, , 740, L15
- Magdis, G. E., Rigopoulou, D., Daddi, E., et al. 2017, , 603, A93
- Magnelli, B., Boogaard, L., Decarli, R., et al. 2020, , 892, 66
- Magnelli, B., Elbaz, D., Chary, R. R., et al. 2009, , 496, 57
- Magnelli, B., Elbaz, D., Chary, R. R., et al. 2011, , 528, A35
- Magnelli, B., Gómez-Guijarro, C., Elbaz, D., et al. 2023, arXiv e-prints, arXiv:2305.19331
- Magnelli, B., Lutz, D., Saintonge, A., et al. 2014, , 561, A86
- Magnelli, B., Popesso, P., Berta, S., et al. 2013, , 553, A132
- Magnelli, B., Saintonge, A., Lutz, D., et al. 2012, , 548, A22
- Man, A. & Belli, S. 2018, Nature Astronomy, 2, 695
- Mannucci, F., Cresci, G., Maiolino, R., Marconi, A., & Gnerucci, A. 2010, , 408, 2115
- Marinacci, F., Vogelsberger, M., Pakmor, R., et al. 2018, , 480, 5113
- Mason, C. A., Trenti, M., & Treu, T. 2023, , 521, 497
- McLure, R. J. & Dunlop, J. S. 2004, , 352, 1390
- Messier, C. 1781, Catalogue des Nébuleuses et des Amas d’Étoiles (Catalog of Nebulae and Star Clusters), Connoissance des Temps ou des Mouvements Célestes, for 1784, p. 227-267
- Molnár, D. C., Sargent, M. T., Leslie, S., et al. 2021, , 504, 118
- Moore, B., Katz, N., Lake, G., Dressler, A., & Oemler, A. 1996, , 379, 613
- Moore, B., Lake, G., & Katz, N. 1998, , 495, 139
- Morokuma-Matsui, K. & Muraoka, K. 2017, , 837, 137

- Moustakas, J., Kennicutt, Robert C., J., & Tremonti, C. A. 2006, , 642, 775
- Murphy, E. J., Condon, J. J., Schinnerer, E., et al. 2011, , 737, 67
- Muzzin, A., Marchesini, D., Stefanon, M., et al. 2013, , 777, 18
- Naiman, J. P., Pillepich, A., Springel, V., et al. 2018, , 477, 1206
- Nayyeri, H., Hemmati, S., Mobasher, B., et al. 2017, , 228, 7
- Nelson, D., Pillepich, A., Genel, S., et al. 2015, *Astronomy and Computing*, 13, 12
- Nelson, D., Pillepich, A., Springel, V., et al. 2018, , 475, 624
- Nelson, D., Springel, V., Pillepich, A., et al. 2019, *Computational Astrophysics and Cosmology*, 6, 2
- Noeske, K. G., Weiner, B. J., Faber, S. M., et al. 2007, , 660, L43
- Novak, M., Smolčić, V., Delhaize, J., et al. 2017, , 602, A5
- Oesch, P. A., Bouwens, R. J., Illingworth, G. D., et al. 2013, , 773, 75
- Oesch, P. A., Bouwens, R. J., Illingworth, G. D., Labbé, I., & Stefanon, M. 2018, , 855, 105
- Oh, K., Choi, H., Kim, H.-G., Moon, J.-S., & Yi, S. K. 2013, , 146, 151
- Opik, E. 1922, , 55, 406
- Pannella, M., Elbaz, D., Daddi, E., et al. 2015, , 807, 141
- Pannella, M., Gabasch, A., Goranova, Y., et al. 2009, , 701, 787
- Peng, Y.-j., Lilly, S. J., Kovač, K., et al. 2010, , 721, 193
- Pettini, M. & Pagel, B. E. J. 2004, , 348, L59
- Pillepich, A., Nelson, D., Hernquist, L., et al. 2018a, , 475, 648
- Pillepich, A., Nelson, D., Springel, V., et al. 2019, , 490, 3196
- Pillepich, A., Springel, V., Nelson, D., et al. 2018b, , 473, 4077
- Popesso, P., Concas, A., Cresci, G., et al. 2023, , 519, 1526
- Popesso, P., Magnelli, B., Buttiglione, S., et al. 2012, arXiv e-prints, arXiv:1211.4257
- Postman, M., Franx, M., Cross, N. J. G., et al. 2005, , 623, 721
- Reddy, N. A., Steidel, C. C., Erb, D. K., Shapley, A. E., & Pettini, M. 2006, , 653, 1004
- Rémy-Ruyer, A., Madden, S. C., Galliano, F., et al. 2014, , 563, A31
- Richards, G. T., Lacy, M., Storrie-Lombardi, L. J., et al. 2006, , 166, 470
- Rodighiero, G., Daddi, E., Baronchelli, I., et al. 2011, , 739, L40

- Rosse, E. O. 1844, Philosophical Transactions of the Royal Society of London Series I, 134, 321
- Rosse, T. E. O. 1850, Philosophical Transactions of the Royal Society of London Series I, 140, 499
- Rubin, V. C., Ford, W. K., J., & Thonnard, N. 1980, , 238, 471
- Rubin, V. C., Ford, W. K., J., Thonnard, N., & Burstein, D. 1982, , 261, 439
- Rubin, V. C. & Ford, W. Kent, J. 1970, , 159, 379
- Rubin, V. C. & Ford, W. Kent, J. 1971, , 170, 25
- Saintonge, A. & Catinella, B. 2022, , 60, 319
- Saintonge, A., Catinella, B., Cortese, L., et al. 2016, , 462, 1749
- Saintonge, A., Catinella, B., Tacconi, L. J., et al. 2017, , 233, 22
- Saintonge, A., Tacconi, L. J., Fabello, S., et al. 2012, , 758, 73
- Salim, S., Charlot, S., Rich, R. M., et al. 2005, , 619, L39
- Salpeter, E. E. 1955, , 121, 161
- Santini, P., Castellano, M., Fontana, A., et al. 2022, , 940, 135
- Santini, P., Fontana, A., Castellano, M., et al. 2017, , 847, 76
- Santini, P., Fontana, A., Grazian, A., et al. 2009, , 504, 751
- Santini, P., Fontana, A., Grazian, A., et al. 2012, , 538, A33
- Sarazin, C. L. 1986, Reviews of Modern Physics, 58, 1
- Sargent, M. T., Béthermin, M., Daddi, E., & Elbaz, D. 2012, , 747, L31
- Schenker, M. A., Robertson, B. E., Ellis, R. S., et al. 2013, , 768, 196
- Schiminovich, D., Ilbert, O., Arnouts, S., et al. 2005, , 619, L47
- Schinnerer, E., Groves, B., Sargent, M. T., et al. 2016, , 833, 112
- Schreiber, C., Elbaz, D., Pannella, M., et al. 2018, , 609, A30
- Schreiber, C., Elbaz, D., Pannella, M., et al. 2016, , 589, A35
- Schreiber, C., Pannella, M., Elbaz, D., et al. 2015, , 575, A74
- Scoville, N., Aussel, H., Sheth, K., et al. 2014, , 783, 84
- Scoville, N., Sheth, K., Aussel, H., et al. 2016, , 820, 83
- Sevilla-Noarbe, I., Bechtol, K., Carrasco Kind, M., et al. 2021, , 254, 24
- Shirley, R., Duncan, K., Campos Varillas, M. C., et al. 2021, , 507, 129

- Silk, J. 2011, in Tracing the Ancestry of Galaxies, ed. C. Carignan, F. Combes, & K. C. Freeman, Vol. 277, 273–281
- Silk, J. 2013, , 772, 112
- Silk, J. & Rees, M. J. 1998, , 331, L1
- Slipher, V. M. 1912, Lowell Observatory Bulletin, 2, 26
- Slipher, V. M. 1913, Lowell Observatory Bulletin, 2, 56
- Slipher, V. M. 1915, Popular Astronomy, 23, 21
- Slipher, V. M. 1917, Proceedings of the American Philosophical Society, 56, 403
- Speagle, J. S., Steinhardt, C. L., Capak, P. L., & Silverman, J. D. 2014, , 214, 15
- Springel, V., Pakmor, R., Pillepich, A., et al. 2018, , 475, 676
- Springel, V., White, S. D. M., Tormen, G., & Kauffmann, G. 2001, , 328, 726
- Steidel, C. C., Adelberger, K. L., Giavalisco, M., Dickinson, M., & Pettini, M. 1999, , 519, 1
- Suess, K. A., Kriek, M., Price, S. H., & Barro, G. 2019, , 885, L22
- Tacchella, S., Johnson, B. D., Robertson, B. E., et al. 2023, , 522, 6236
- Tacconi, L. J., Genzel, R., Neri, R., et al. 2010, , 463, 781
- Tacconi, L. J., Genzel, R., Saintonge, A., et al. 2018, , 853, 179
- Tacconi, L. J., Neri, R., Genzel, R., et al. 2013, , 768, 74
- Tomczak, A. R., Quadri, R. F., Tran, K.-V. H., et al. 2014, , 783, 85
- Torrey, P., Vogelsberger, M., Marinacci, F., et al. 2019, , 484, 5587
- Trump, J. R., Arrabal Haro, P., Simons, R. C., et al. 2023, , 945, 35
- Viero, M. P., Moncelsi, L., Quadri, R. F., et al. 2013, , 779, 32
- Wang, T., Schreiber, C., Elbaz, D., et al. 2019, , 572, 211
- Wang, T.-M., Magnelli, B., Schinnerer, E., et al. 2022, , 660, A142
- Weaver, J. R., Kauffmann, O. B., Ilbert, O., et al. 2022, , 258, 11
- Weinberger, R., Springel, V., Hernquist, L., et al. 2017, , 465, 3291
- Welikala, N., Béthermin, M., Guery, D., et al. 2016, , 455, 1629
- Whitaker, K. E., Franx, M., Leja, J., et al. 2014, , 795, 104
- Whitaker, K. E., Labb  , I., van Dokkum, P. G., et al. 2011, , 735, 86

- Whitaker, K. E., van Dokkum, P. G., Brammer, G., & Franx, M. 2012, , 754, L29
- White, R. L., Helfand, D. J., Becker, R. H., Glikman, E., & de Vries, W. 2007, , 654, 99
- Whitmore, B. C., Gilmore, D. M., & Jones, C. 1993, , 407, 489
- Williams, R. J., Quadri, R. F., Franx, M., van Dokkum, P., & Labbé, I. 2009, , 691, 1879
- Wuyts, S., Labbé, I., Franx, M., et al. 2007, , 655, 51
- Xiao, M. Y., Elbaz, D., Gómez-Guijarro, C., et al. 2023, , 672, A18
- Yun, M. S., Reddy, N. A., & Condon, J. J. 2001, , 554, 803
- Zhou, L., Elbaz, D., Franco, M., et al. 2020, , 642, A155
- Zubovas, K., Nayakshin, S., King, A., & Wilkinson, M. 2013, , 433, 3079